Quantum Trajectories with Incompatible Decoherence Channels

Quentin Ficheux

THÈSE DE DOCTORAT

de l'Université de recherche Paris Sciences et Lettres
PSL Research University

École Normale Supérieure

QUANTUM TRAJECTORIES WITH INCOMPATIBLE DECOHERENCE CHANNELS

Ecole doctorale n°564

PHYSIQUE EN ÎLE DE FRANCE

Spécialité PHYSIQUE

COMPOSITION DU JURY :

M. BERNARD Denis
École Normale Supérieure, Membre du jury

M. GOUGH John
Aberystwyth University, Rapporteur

M. JORDAN Andrew
University of Rochester, Membre du jury

M. LEEK Peter
University of Oxford, Rapporteur

M. ROCH Nicolas
Institut Néel, Membre du jury

Soutenue par Quentin **FICHEUX**
le 7 Décembre 2018

Dirigée par **Benjamin HUARD**
et codirigée par **Zaki LEGHTAS**

M. HUARD Benjamin
École Normale Supérieure de Lyon, Directeur de thèse

M. LEGHTAS Zaki
Mines ParisTech, Co-directeur de thèse

ENS PSL RESEARCH UNIVERSITY PARIS

À celle qui se reconnaitra.

ABSTRACT

In contrast with its classical version, a quantum measurement necessarily disturbs the state of the system. The projective measurement of a spin-1/2 in one direction maximally randomizes the outcome of a following measurement along a perpendicular direction. In this thesis, we discuss experiments on superconducting circuits that allow us to investigate this measurement back-action. In particular, we measure the dynamics of a superconducting qubit whose three Bloch x, y and z components are simultaneously recorded.

Two recent techniques are used to make these simultaneous recordings. The x and y components are obtained by measuring the two quadratures of the fluorescence field emitted by the qubit. Conversely, the z component is accessed by probing an off-resonant cavity dispersively coupled to the qubit. The frequency of the cavity depends on the energy of the qubit and the strength of this last measurement can be tuned from weak to strong in situ by varying the power of the probe. These observations are enabled by recent advances in ultra-low noise microwave amplification using Josephson circuits. This thesis details all these techniques, both theoretically and experimentally, and presents various unpublished additional results.

In the presence of the simultaneous measurements, we show that the state of the system diffuses inside the sphere of Bloch by following a random walk whose steps obey the laws of the backaction of incompatible measurements. The associated quantum trajectories follow a variety of dynamics ranging from diffusion to Zeno blockade. Their peculiar dynamics highlights the non-trivial interplay between the back-action of the two incompatible measurements. By conditioning the records to the outcome of a final projective measurement, we also measure the weak values of the components of the qubit state and demonstrate that they exceed the mean extremal values. The thesis discusses in detail the statistics of the obtained trajectories.

RÉSUMÉ

Au contraire de sa version classique, une mesure quantique perturbe nécessairement l'état du système. Ainsi, la mesure projective d'un spin-1/2 selon une direction rend parfaitement aléatoire le résultat d'une mesure successive de la composante du même spin le long d'un axe orthogonal. Dans cette thèse, nous discutons des expériences basées sur les circuits supraconducteurs qui permettent de mettre en évidence cette action en retour de la mesure. Nous mesurons en particulier la dynamique d'un qubit supraconducteur dont on révèle simultanément les trois composantes de Bloch x, y et z.

Deux techniques récentes sont utilisées pour réaliser ces enregistrements simultanés. Les composantes x et y sont obtenues par la mesure des deux quadratures du champ de fluorescence émis par le qubit. La composante z est quant à elle obtenue en sondant une cavité non résonante couplée de manière dispersive au qubit. La fréquence de la cavité dépend de l'énergie du qubit et la force de cette dernière mesure peut être ajustée in situ en faisant varier la puissance de la sonde. Ces observations sont rendues possibles grâce aux avancées récentes dans l'amplification ultrabas bruit des signaux micro-onde grâce aux circuits Josephson. Cette thèse détaille toutes ces techniques à la fois théoriquement et expérimentalement et présente différents résultats annexes inédits.

En présence des mesures simultanées, nous montrons que l'état du système diffuse à l'intérieur de la sphère de Bloch en suivant une marche aléatoire dont les pas obéissent aux lois de l'action en retour de mesures incompatibles. Les trajectoires quantiques associées ont des dynamiques allant du régime diffusif au régime de blocage de Zénon soulignant l'interaction non-triviale des actions en retours des deux mesures incompatibles effectuées. En conditionnant les enregistrements aux résultats d'une mesure projective finale, nous mesurons également les valeurs faibles des composantes de notre qubit et démontrons qu'elles dépassent les valeurs extrémales moyennes. La thèse discute en détail de la statistique des trajectoires obtenues.

Notre seul pouvoir véritable consiste à aider autrui.

— **Tenzin Gyatso**

REMERCIEMENTS

Mon nom est sur ce manuscrit mais ce travail de thèse est le fruit d'une *intelligence collective*. Ma *trajectoire* professionnelle et personnelle est le résultat d'un grand nombre d'interactions et de rencontres.

Certaines interactions sont de vraies *forces motrices*. Merci à Benjamin Huard de m'avoir fait confiance en me prenant dans le groupe. Benjamin est un chef prolifique, bienveillant et ambitieux. Il consacre beaucoup de temps à ses étudiants ce qui m'a permis de bénéficier de sa clairvoyance en physique et de ses talents de meneur. J'espère pouvoir m'inspirer de sa réussite pour trouver ma voie dans le monde de la recherche. Notre équipe a été en constante évolution pendant ces trois années avec le départ de François Mallet, l'arrivée de Zaki Leghtas et enfin notre départ à Lyon. Merci à François pour ses explications très précises et ses bonnes idées lorsque je découvrais le domaine des circuits supraconducteurs. Zaki est un physicien et une personne que j'admire. Je le remercie pour l'influence positive qu'il a sur moi. J'exprime toute ma gratitude à Sébastien Jezouin qui m'a instruit au quotidien dès mon arrivée dans le groupe. Il m'a appris aussi bien les bases du métier de chercheur que les techniques les plus avancées de ce manuscrit.

D'autres rencontres ont un effet *stochastique* dont le bilan est parfois productif et parfois égayant. L'atmosphère dans l'équipe est familiale et bon enfant. L'entraide, la fumisterie et l'autodérision sont toujours de mise. Merci Nathanaël Cottet avec qui j'ai échangé bien plus que des frisbees et des avions en papier, Danijela Marković notre grande sœur de thèse qui a su nous supporter, Théau Peronnin l'éternel stagiaire de 3$^{\text{ème}}$ accro au Coca-Cola et abonné aux allers-retours Paris-Lyon, Raphaël Lescanne que l'on a laissé à Paris mais qui nous manque, Jeremy Stevens pour qui "ça joue" toujours et qui assure, avec Antoine Essig, une relève d'un excellent niveau. Que ce soit à la Montagne, au Mayflower, au Ninkasi ou au labo, cela a été et cela sera toujours un plaisir.

Afin de profiter au maximum de ces interactions, il est crucial d'évoluer dans un bon *environnement*. Le laboratoire Pierre Aigrain constitue un écosystème de choix pour faire de la recherche. Merci à Michael Rosticher et José Palomo pour leurs conseils et leur bonne humeur dans la salle blanche. Merci à Takis Kontos dont la "funkytude" n'est plus à démontrer. Merci à l'équipe HQC et à tous les doctorants du LPA pour leur sympathie lors des pauses café. Merci à Jean-Marc Berroir, Jérôme Tignon et Jean-François Allemand qui sont des leaders sur qui nous pouvons compter. Le vendredi était le jour des pizzas avec l'équipe Quantic de l'INRIA lors du "Tuesday Lunch Seminar". Merci à Mazyar Mirrahimi, Alain Sarlette, Pierre Rouchon et leurs étudiants qui maintiennent un très bon niveau dans le groupe. Merci à Olivier Andrieu pour les nombreux footings au jardin du Luxembourg. Merci à l'équipe de mécanique de l'ENS Paris qui nous a fourni les pièces nécessaires à nos expériences.

Je remercie également tous les membres du laboratoire de physique de l'ENS de Lyon qui nous a accueilli à bras ouverts. Il y règne une atmosphère très conviviale et stimulante propice à l'activité et la créativité. Merci à Thierry Dauxois qui est un directeur de laboratoire modèle. Merci à Nadinne Clervaux et Fatiha Boucheneb qui ont été d'un support administratif aussi agréable qu'efficace. Merci aux doctorants du labo avec qui j'ai passé de très bons moments. Merci aux camarades de promotion retrouvés, Valentin, Charles-Edouard et Vincent. Merci aux services électroniques et mécaniques qui nous ont beaucoup aidé lors de notre installation.

Le déménagement à Lyon a affecté ma vie *personnelle* en m'éloignant de Nolwenn. L'amour a su trouver un chemin au prix de long trajets qui étaient une bien maigre peine comparée au plaisir de se retrouver. Merci à toi d'avoir toujours été là pour moi.

Je remercie mes parents, mon frère et ma famille qui ont su donner une excellente *condition initiale* à ma trajectoire avec l'*impulsion* nécessaire pour aller toujours plus loin. Merci aux familles Morin et Laennec qui m'ont très rapidement considéré comme un des leurs. Merci à mes amis et colocataires qui ont vécu à mes côtés pendant ces trois années.

Merci enfin aux membres du jury qui ont accepté d'évaluer mon travail de thèse.

Lyon, octobre 2018 *Quentin Ficheux*

CONTENTS

LIST OF FIGURES

LIST OF TABLES

1 INTRODUCTION

1.1 BACKGROUND

I recall that during one walk Einstein suddenly stopped, turned to me and asked whether I really believed that the moon exists only when I look at it.

— **Abraham Pais [1]**

Albert Einstein came up with numerous memorable questionings when trying to understand the *concept of reality*. He wanted physical objects to have objective properties, whether or not they were measured. For this ontological reason, the quantum origin of the classical world was incredibly difficult to concede for the founding fathers of quantum mechanics. On top of the singular role played by measurement, the quantum theory exhibits many 'strange' features such as *entanglement* and *state superposition*. In an effort to replace quantum theory by a more complete description of reality with classical underpinnings Einstein, Podolsky and Rosen expressed the influential EPR paradox [2] in 1935 while de Broglie and Bohm suggested an interpretation in terms of 'hidden variables' [3], to name but a few. In 1964, Bell showed that a quantitative numerical prediction of the quantum theory entails the nonexistence of these kinds of local variables. This prediction was experimentally confirmed by Freedman and Clauser [4] and later by Alain Aspect et al. [5]. The conclusion of this test is independent of whether one believes or not in the interpretation of quantum mechanics. Bell's test shows that the very counterintuitive notion of *entanglement* or *non locality* if we insist on classical realism is required to describe the world we live in.

One can even set up quite ridiculous cases ... The psi-function of the entire system would express this by having in it the living and dead cat (pardon the expression) mixed or smeared out in equal parts.

— **Erwin Schrödinger [6]**

According to the rules of quantum mechanics, one can imagine a scenario where a cat is simultaneously both dead and alive, a state known as a *quantum superposition*. Quantum superpositions can, in principle, be exploited to encode information into ensembles of individually accessible degrees of freedom by associating the 0 and the 1 values of the usual binary code to the dead and alive states of the cat. Since there are many possible Schrödinger-cat states, the size of the total set of states in the Hilbert space is prodigious compared to size of the set of 'classically legal' states. One has to explain the selection rule that prevents the existence of most states in the Hilbert space in the classical world. *Decoherence* and *einselection* account for the transition between the quantum and classical world. As Zurek explains [7], classicality is an emergent

property induced in a system by its interaction with the environment. During the interaction, the system transmits *information* into its environment through *quantum channels*. In these conditions, the information on the quantum state is lost in the many degrees of freedom of the bath except for a preferred set of *pointer states* (or *classical states*) that survive the interaction. Since information is exchanged, decoherence can be seen as a continuous *observation* of the system by its environment.

Observations not only disturb what has to be measured, they produce it. We compel to assume a definite position... We ourselves produce the results of measurements.

— **Pascual Jordan [8]**

As Pascual Jordan puts it, information is acquired by an observer only when *measurement records* are produced by observation. The state of a system is encoded in a *density matrix* which refers to an *observer's knowledge* about the system. More precisely, the density matrix contains the probability of outcomes of any future measurements that an observer can perform on the system *conditioned on* her knowledge about the system at that time. Every time a measurement is performed, the observer *updates* his knowledge on the state of the system to take into account the measurement record, this effect is known as *measurement back-action*. To go back to Einstein's questioning, in general we cannot answer *deterministically* if the moon was there or not without the intervention of an observer. Different observers with different knowledge may assign simultaneously different density matrices to a same system revealing the observer-dependent character of the quantum state. One of the main results of this thesis is to demonstrate this fact experimentally with continuous measurement.

Shut up and calculate!

— **David Mermin**

David Mermin beautifully epitomized the general attitude adopted by most physicists toward the philosophical questions raised by quantum theory. In this thesis, we suggest the alternative approach "Shut up and contemplate!" [9] by providing textbook experimental observations of measurement and decoherence 'in action' on a quantum system. Directly accessible macroscopic systems, on which one makes up one's intuition, never display entanglement, state superposition or measurement back-action. The 'intriguing' aspects of quantum mechanics are more easily observed in systems made of a limited number of well-defined quantum degrees of freedom.

1.2 INDIVIDUAL QUANTUM SYSTEMS

... it is fair to state that we are not experimenting with single particles, any more than we can raise Ichthyosauria in the zoo.

— **Erwin Schrödinger [10]**

As a matter of fact, experiments involving single particles such as electrons, atoms or photons are nowadays routinely realized all over the world. A lot of different technologies are found in the zoo of experiments involving only a small number of quantum degrees of freedom including trapped ions [11], cavity quantum electrodynamics [12], circuit quantum electrodynamics [13], quantum dots [14], cavity optomechanics [15], etc ...

In this thesis, we manipulate quantum devices constructed from superconducting electrical circuits [16, 17, 18] (introduced in chapter 2). These circuits are composed of a large number of *microscopic* particles that exhibits a very simple set of *macroscopic* collective degrees of freedom. They form resonators and transmission lines that can be combined together in a modular manner. The insertion of non linear components such as *Josephson junctions* enables us to mimic the non linearity introduced by matter in quantum electrodynamics. However, in contrast with real atoms, superconducting device parameters can be tuned during their fabrication by design.

We use one particular kind of superconducting device dubbed the *transmon* [19, 20] (section 2.2). At a temperature of a few tens of mK, the transmon behaves as an *artificial atom* with independently addressable levels. The first two levels $|g\rangle$ and $|e\rangle$ are usually used as a *qubit* (two-dimensional Hilbert space) but there is no restriction to use it as *qutrit* (three dimensions) as in chapter 4 by addressing the third level $|f\rangle$ or even as *qudit* (N dimensions) (see Fig. 1.1) to encode more information.

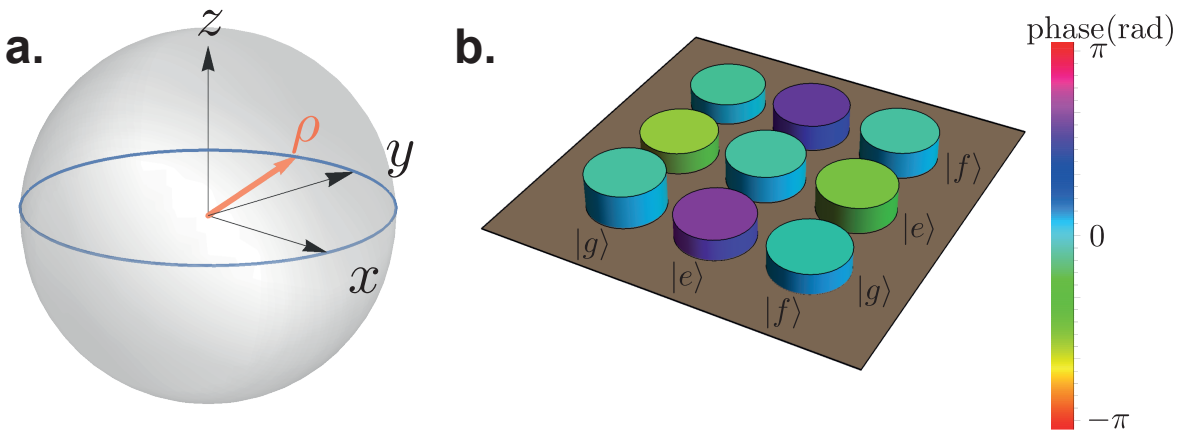

Figure 1.1: **a.** Bloch sphere representation of a quantum state $\rho = \frac{1}{2}(\mathbb{1} + x\sigma_x + y\sigma_y + z\sigma_z)$ of a qubit. The ground state is the south pole $z = -1$ and the excited state is the north pole $z = +1$. Only the poles of the sphere correspond to 'classically legal' states while all the other states correspond to quantum superpositions of classical states. **b.** Experimental density matrix of the superposed state $|\psi\rangle \approx (|g\rangle + i\,|e\rangle + |f\rangle)/\sqrt{3}$ of a qutrit (section 4.2).

These circuits provide an excellent test-bed for the *Gedanken experiments* envisioned by the founding father of quantum mechanics and quantum optics. Quantum circuits are also among the many promising candidate platforms that could lead to the advent of a universal quantum computer [13, 21].

1.3 DECOHERENCE AND READOUT OF A SUPERCONDUCTING QUBIT

The electromagnetic environment of the transmon is controlled by placing it into a cavity (see Fig. 1.2). The macroscopic size of the artificial atom allows a coupling to the cavity much larger than the rate of the dissipation processes [22] enabling us to explore the light-matter interaction at the most fundamental level. The qubit is manipulated with *microwave photons* at the frequency of the qubit f_q sent at the input port of the system. The electromagnetic environment induces decoherence on the qubit either by extracting information via photons temporarily stored inside the cavity (section 3.2.2), or by collecting photon spontaneously emitted by the artificial atom or even by exciting the qubit. This last mechanism can be neglected in our systems by making sure that the environment is almost in a vacuum state.

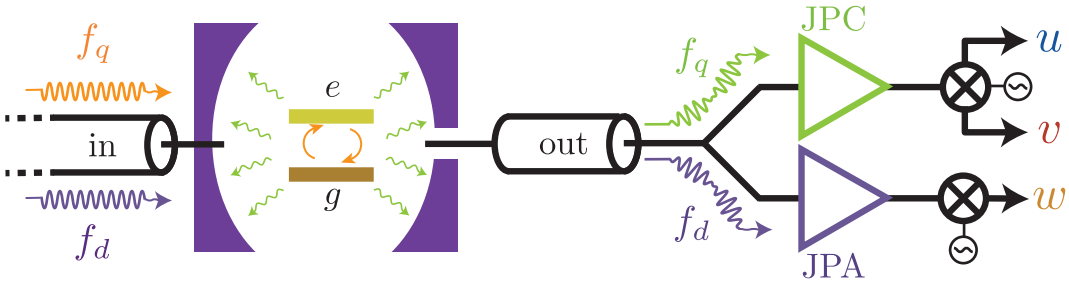

Figure 1.2: We place an artificial atom inside a cavity that is connected to the rest of the electrical circuit via two ports. We monitor the spontaneous emission of the transmon (in green) at f_q while concurrently probing the state of the cavity (in purple) at f_d that is coupled to the qubit. The photons are amplified with a Josephson parametric amplifier (at the frequency of the cavity) and a Josephson parametric converter (at the frequency of the qubit). Qubit rotations are performed by sending a resonant drive at the input.

We said earlier that decoherence can be seen as the action of an observer on the system (chapter 3). Let us be that observer. We monitor the *decoherence channel* associated with the energy relaxation of the qubit by measuring the complex amplitude of the outgoing field in green on Fig. 1.2. We obtain information on the real and imaginary parts of the *lowering operator* of the qubit $\sigma_- = (\sigma_x - i\sigma_y)/2$. Therefore, the associated *continuous measurement records* $u(t)$ and $v(t)$ reveal respectively the information on the σ_x and σ_y components of the qubit [23, 24, 25]. This detection is called *fluorescence measurement* (section 3.3).

When the qubit-cavity detuning is much larger than their interaction rate, the natural dipolar interaction between the qubit and the cavity couples the σ_z component of the qubit to the average number of excitations stored inside the cavity. Probing the state of the cavity leads to a *continuous measurement record* $w(t)$ which yields the σ_z component of the qubit [26, 27, 28, 29]. This very standard readout procedure is known as *dispersive measurement* (section 3.2).

By raw averaging the measurement records $u(t)$, $v(t)$ and $w(t)$, genuine quantum effects caused by measurement back-action vanish. In this case, monitoring both decoherence channels of the qubit is equivalent to imaging the average evolution of the

quantum state in the Bloch sphere (see Fig. 1.3) under the influence of *decoherence* induced by the coupling to the environment. By doing so, we obtain in section 3.4 a gate-free *full quantum tomography* of the system.

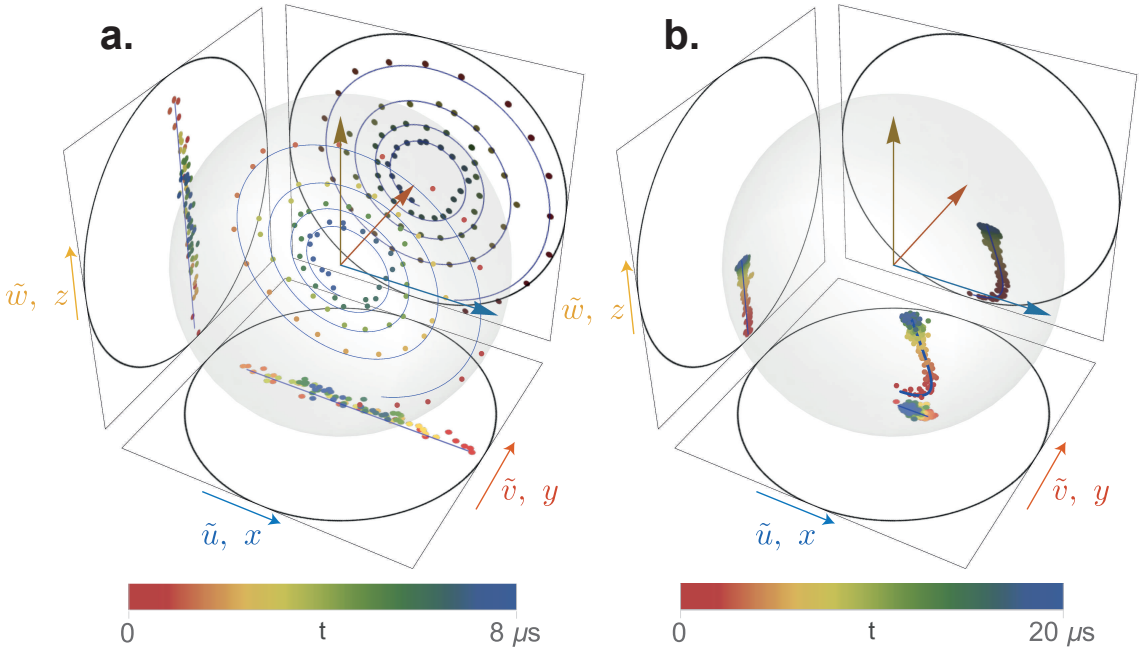

Figure 1.3: Rabi oscillations in the presence of decoherence observed with our quantum tomography method. The speed of the circular motion is large compared to the damping induced by decoherence in Fig. **a** while the opposite situation is depicted in Fig. **b.** The situation in Fig. **a** corresponds to the usual Rabi oscillation whereas the situation of Fig. **b** is in the *Zeno regime* [30, 31].

If the signal goes through a very noisy *quantum channel*, most of the information is dismissed preventing an observation of the impact of measurement performed by the observer on a single realization of the experiment. Owing to the recent development of quantum-limited microwave amplification, the observation of measurement back-action of either *strong* or *weak* measurement is within experimental reach. A *weak measurement* corresponds to the situation where the observer did not extract all the information on the quantum state. The state of the system is thus *slightly perturbed* by measurement back-action and it experiences a '*random kick*' instead of a *collapse* on one of the *pointer states* of the measurement. Microwave signals can be detected with an *efficiency* of the order of unity thanks to the Josephson parametric amplifier (JPA on Fig. 1.2) [32, 33, 34, 35, 36, 37] that amplifies the signal at the frequency of the cavity and a Josphson parametric converter (JPC on Fig. 1.2) [38, 39, 40] that amplifies the signal at the frequency of the qubit. These amplifiers are crucial to reach the *extreme sensitivity* required to investigate *measurement back-action* on individual open quantum systems. Microwave amplification at the quantum limit is the subject of chapter 5.

1.4 QUANTUM TRAJECTORIES

When continuously monitoring a qubit, its quantum state undergoes a non trivial stochastic evolution but the experimentalist can use the measurement outcomes to reconstruct *a posteriori* the evolution of the system. The density matrix of the system is updated at each time step *conditioned* on the *random* measurement outcome to take into account the succession of non-projective 'kicks' caused by the measurement. The resulting path in the Hilbert space is called a *quantum trajectory* (see Fig. 1.4) [41, 42, 43, 44, 45, 46, 26, 27, 47, 48, 28, 23, 29, 49, 25]. Chapter 6 contains an in-depth description of fundamental concepts and experimental implementation of quantum trajectories.

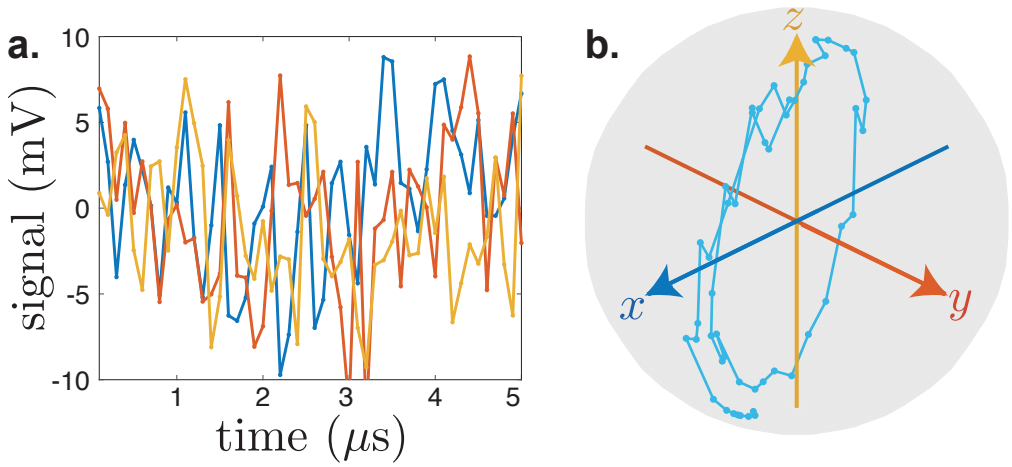

Figure 1.4: A 5 μs-long tracking of a quantum state. **a.** Raw (not normalized) measurement records $u(t)$ (blue), $v(t)$ (red) and $w(t)$ (yellow) as a function of time for one realization of the experiment. **b.** Bloch sphere representation of the reconstructed *quantum trajectory*.

The inherent back-action of a quantum measurement is better discussed by representing distributions of states at a given time (see Fig. 1.5) as the randomness of the measurement back-action *spreads* apart quantum states corresponding to different realizations of the experiment. We can isolate the contribution of *dispersive measurement* (Fig. 1.5 **a b c**) [26, 27] from the contribution of the energy relaxation (Fig. 1.5 **d e f**) [23, 25] or we can combine the effect of both measurements at the same time (Fig. 1.5 **g h i**) by collecting the records of one or the two detectors. While both measurements lead to the same average trajectory, their back-action differ. The uniqueness of perception of the three observers has its roots in the records stored in the *observer's memory* and it leads to the distinct statistics of Fig. 1.5. We prove in section 6.2.4 that every observers can safely use their density matrices to predict the results of an independent tomography.

The asymmetry of Fig. 1.5 **g** reveals the *incompatibility* of the dispersive measurement and fluorescence measurement (section 6.3.2). Monitoring dynamics of a system undergoing incompatible measurements provides a test of *quantum foundations* by exposing the *subtle interplay* between different back-action at the single quantum system level. The possibility to achieve simultaneous incompatible measurements was only very

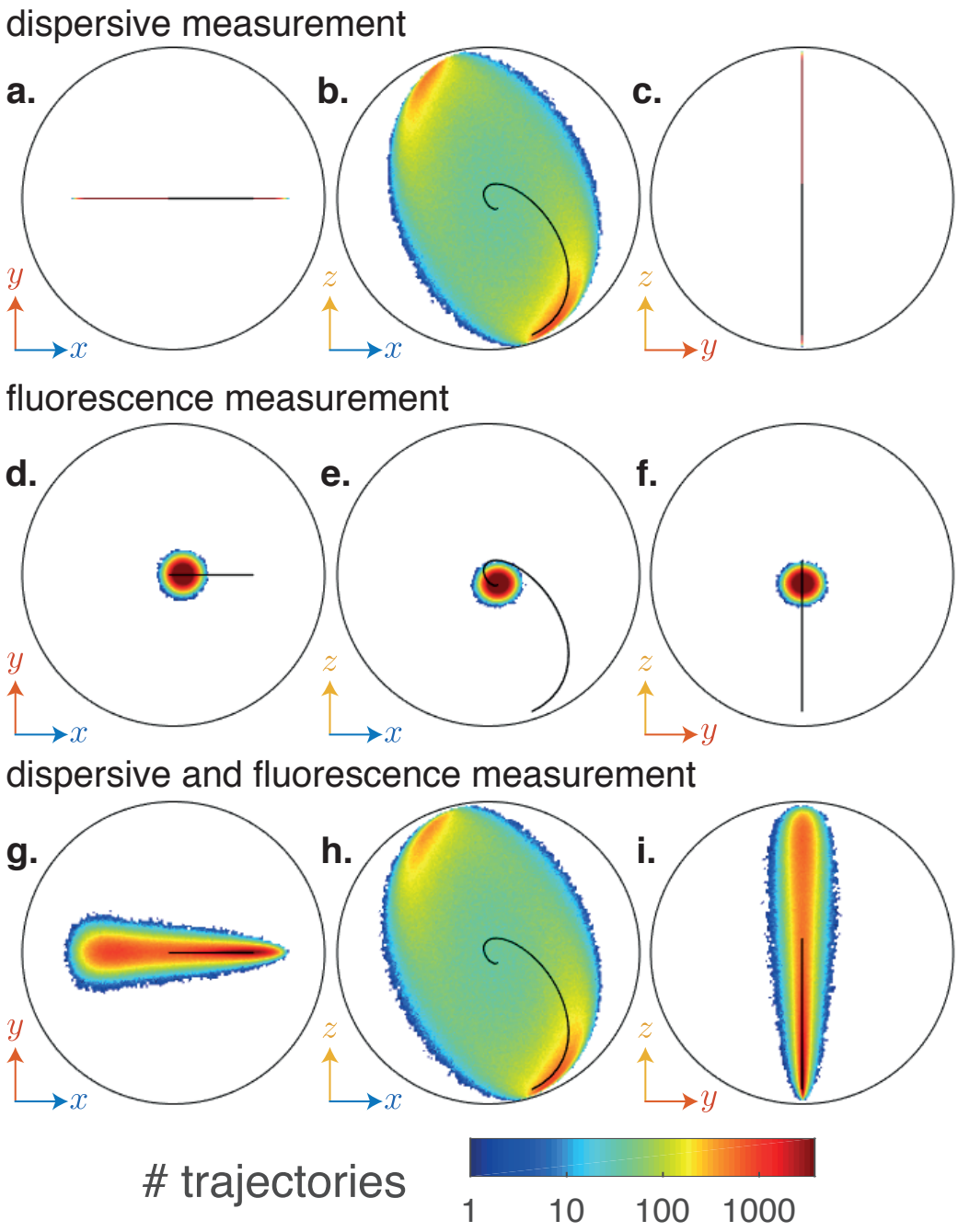

Figure 1.5: Impact of the type of detector on the distribution of quantum states in the *Zeno regime* of Fig. 1.3 **b**. **a**,**b**,**c** Marginal distribution in the $x-y$ (**a**), $x-z$ (**b**) and $y-z$ (**c**) planes of the Bloch sphere of the qubit states ρ_τ corresponding to 1.5 millions of measurement records $\{w(t)\}$ at the cavity frequency only. The information about $\{u(t), v(t)\}$ is here discarded. The boundary of the Bloch sphere is represented as a black circle and the average quantum trajectory as a solid line. **d**,**e**,**f** Case where the states are conditioned on fluorescence records $\{u(t), v(t)\}$ instead while discarding the information on $\{w(t)\}$. **g**,**h**,**i** Case where the states are conditioned on both fluorescence and dispersive measurement records $\{u(t), v(t), w(t)\}$.

recently demonstrated by Hacohen-Gourgy et al. [49] in the case of a qubit with two dephasing channels. Jordan and Bütikker [50] proposed such an experiment theoretically in 2005. By monitoring both decoherence channels, we take the place of the *environment* in this experiment and we reveal the knowledge that only the bath acquires in most experiments.

The quantum state *diffuses* inside the Bloch sphere, which is reminiscent of the *Brownian motion* [51] of a *particle* inside a colloid as explained in section 6.4. In this case, the measurement back-action plays the role of the *Langevin force*. The probability distribution of quantum trajectories obeys the celebrated *Fokker-Planck* equation. We gain insight into the physics of the diffusion of the quantum trajectories by analyzing the different terms of the Fokker-Planck equation. We find that our experiment is the first observation of a genuine 3D diffusion inside the Bloch sphere (section 6.4.6) and we explain the deep link between diffusion and back-action. The incompatibility of our measurement is encoded in a *persistant diffusion* enforced by a *Heinsenberg-like inequality* on the *diffusivity* of quantum states (section 6.4.8).

1.5 POST-SELECTED EVOLUTION

In the 50s, von Neumann and Bohm [52, 53] suggested that the irreversible collapse of a wave packet of the state of a system under the influence of measurement introduces a fundamental *time asymmetry* at the microscopic level. The *measurement back-action* was thus thought of as a time asymmetric element in quantum theory. Nevertheless, the symmetry of the rules of quantum mechanics is fully restored when specifying both the initial state and the final state of a closed system. The symmetric role of *preparation* or *pre-selection* and *post-selection* was enlightened by Aharonov et al. in 1964 [54]. While the density matrix ρ_t is the quantum state of the system conditioned on the *past* measurement records, the *effect matrix* E_t [55, 56, 57, 58] is the quantum state conditioned on the information available in the *future* (chapter 7). Taking into account the *forward* and *backward* estimation of the quantum state at the same time provides a so-called *past quantum state* that encapsulates all the information available from past and future measurements (section 7.1).

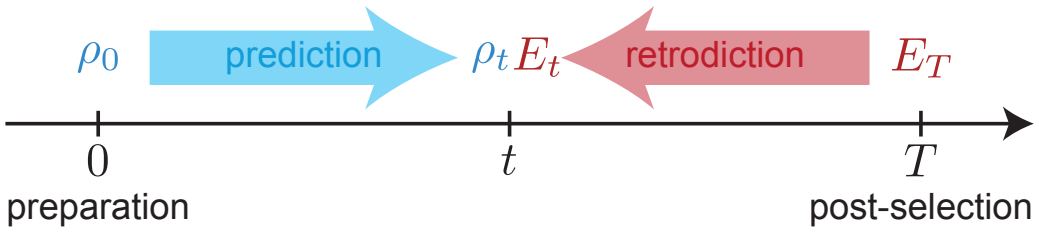

Figure 1.6: The state of the system can be *predicted* conditioned on *past* measurement records using the density matrix ρ_t or *rectrodicted*, *a posteriori*, conditioned on the *future* measurement records by unravelling the effect matrix E_t. The past quantum state (ρ_t, E_t) uses the complete measurement records to give an estimate of the distribution of any measurement performed on the system at time t.

In the presence of both *preparation* and *post-selection*, the measured expectation values of the signal can spread outside of the eigenvalue range defined by the corresponding observable. These anomalous values were called *weak values* [59, 60] and they can, in principle, reach arbitrarily large values. In this thesis, we present the results of an experiment illustrating this fact. By combining preparation and post-selection, the Bloch vector imaged with our direct quantum tomography method exceeds the boundary of the unit sphere [61, 62, 63, 64] in section 7.2.2.

1.6 OUTLINE

This thesis is organized as follows. Chapter 2 gives an introduction to the field of superconducting circuits. It aims at bridging the gap from the condensed matter aspect of superconducting circuits to the open quantum mechanics description of qubits and harmonic oscillators. In chapter 3 we describe a novel gate-free tomography method. The x and y components of the qubit are obtained by measuring the two quadratures of the fluorescence field emitted by the artificial atom while the z component is accessed by probing an off-resonant cavity dispersively coupled to the qubit. The experimentalist is not restricted to the first two levels of the transmon. We demonstrate in chapter 4 the coherent control and readout of a transmon qutrit. We give a general explanation of the most commonly used near quantum limited amplifiers in the microwave range in chapter 5. These amplifiers are instrumental to observe the partial collapse of the density matrix under the influence of weak measurement. Measurement back-action and quantum trajectories are at the heart of chapter 6. We investigate the case of multiple simultaneous observers monitoring incompatible operators on the same quantum bit. Impressively, the random walk of the state of the system in the Bloch sphere can be studied with the tools of classical diffusion physics. Finally chapter 7 investigates the behavior of post-selected quantum trajectories revealing weak values of our detection signals that exceed the boundary of the unit sphere.

The White Rabbit put on his spectacles. "Where shall I begin, please your Majesty ?" he asked. " Begin at the beginning," the King said, gravely, " and go on till you come to the end : then stop."

— **Lewis Carroll**, Alice's Adventures in Wonderland

Part I

MEASUREMENT AND CONTROL OF SUPERCONDUCTING CIRCUITS

2

INTRODUCTION TO SUPERCONDUCTING CIRCUITS

The goal of this first part is to give an up-to-date introduction to the field of superconducting circuits from an experimentalist perspective while focusing on the devices that are used in this thesis work. The first chapter will focus on the transmon qubit, which is the most widespread qubit in the superconducting circuit community. A lot of other types of qubits have very promising performances but they are not the subject of this thesis. The second chapter is dedicated to the readout of superconducting qubits with a particular emphasis on dispersive and fluorescence readout that are crucial to the second part of this thesis. The third chapter is dedicated to three-level systems. Most applications of superconducting circuits rely on quantum operations on two-level systems while transmons offer many more levels that are individually addressable. Increasing the size of the Hilbert space for quantum operations or quantum algorithms opens up new perspectives for quantum physics and quantum information processing. The fourth chapter is dedicated to pumped microwave circuits and more specifically to linear microwave amplifiers. Three kinds of amplifiers were used in this work and a non-exhaustive review is given on the current state-of-the-art of microwave amplification at the quantum level.

In this first chapter, we will introduce the transmon as an elementary unit instrumental to circuit QED. We will start by introducing quantum circuits from the solid-state physics perspective and then we combine it with the universal quantum mechanics description valid for a wide range of platforms dealing with single quantum systems.

2.1 CIRCUIT QUANTUM ELECTRODYNAMICS

2.1.1 *Introduction*

The goal of *cavity quantum electrodynamics* (CQED) is to study the properties of light (photons) coupled to matter (electrons, atoms, ...). This field has led to numerous ground-breaking experiments [12, 65] well described in books and reviews such as *Exploring the quantum* by Serge Haroche and Jean-Michel Raimond [66]. Subsequently, a new branch of this field emerged in 1999 with the invention of the first superconducting qubit [17] later followed by the demonstration of strong coupling regime between a transmon and a resonator [22] and was dubbed *circuit QED*. This first section is dedicated to the quantum optics of microwave circuits with superconducting artificial atoms.

A first striking property of these circuits is that they are macroscopic quantum systems. While they contain a large number of microscopic particles, they host macroscopic degrees of freedom that behave quantum-mechanically. Secondly, their properties are not set by fundamental constants like the Rydberg energy. They are engineered at will by design with the technology of microelectronic chips. Lastly, a truly remarkable level

of control was achieved in these systems thanks to the exponential growth of coherence times of these devices known as *Schoelkopf's Law* [13]. The system used throughout this thesis is the *transmon*[1], which is nowadays the most commonly used superconducting qubit. This qubit was originally envisioned to be coupled to a 2D resonator connected to a transmission line [19] but it can also be embedded into a 3D electromagnetic or into a lumped mode [67] in order to straightforwardly increase the quality factor of the LC resonator.

Transmons are usually made of a Josephson junction shunted by a large capacitance [20] and the circuit is shielded and anchored to the base plate of a dilution refrigerator at about 20 mK so that the energy of the thermal fluctuations is much smaller than the energy quantum at a few GHz $\hbar\omega \gg k_B T$.

Another important thing to mention about superconducting circuits is that it is one of the many candidate platforms that could lead to the advent of a universal quantum computer thanks to quantum error correction [68, 69]. A lot of landmarks were achieved such as the implementation of multi qubit algorithms [70] or gate fidelities sufficient for error correction [71] and few small uncorrected quantum processors are already available online but the race is still ongoing.

2.1.2 *Quantum LC oscillator*

A quantum LC oscillator is the simplest circuit element that can be built with capacitors and inductors [73, 74] as depicted in Fig. 2.1 **a**. In practice, the dynamics of a cavity mode is modeled by a harmonic oscillator. The most commonly used resonators in circuit QED are 3D rectangular cavities machined out of aluminum (Fig. 2.1 **b**), 3D coaxial $\lambda/4$ cavities (Fig. 2.1 **c**) and $\lambda/2$ coplanar-wave-guide (CPW) resonators (Fig. 2.1 **d**). There are no resistors in the circuit representation because the cavities are made out of superconducting materials that ensure that the supercurrent flows with negligible dissipation in the circuit. Losses will be introduced as a perturbation. In the case of a rectangular cavity of dimensions $l_x,\ l_y,\ l_z$, the limit conditions impose that the resonant frequency of the $\mathrm{TE}_{\mathrm{mnl}}$ and $\mathrm{TM}_{\mathrm{mnl}}$ modes are given by [75]

$$f_{nml} = \frac{c}{2\pi}\sqrt{\left(\frac{m\pi}{l_x}\right)^2 + \left(\frac{n\pi}{l_y}\right)^2 + \left(\frac{l\pi}{l_z}\right)^2} \tag{2.1}$$

where the indices $n,\ m,\ l$ refer to the number of anti-nodes in standing wave pattern in the $x,\ y,\ z$ directions. A cavity with dimensions $(l_x, l_y, l_z) = (26.5 \times 26.5 \times 9.6)\ \mathrm{mm}^3$ has a first TE_{110} mode at $f_{1,1,0} = 8$ GHz. Similarly, a coaxial $\lambda/4$ cavity has a fundamental resonance frequency $f_0 \simeq 4.25$ GHz for $l = 20$ mm [76] well separated from its first harmonic frequency $f_1 = 3f_0 = 12.75$ GHz. Finally, $\lambda/2$ CPW resonators are planar transmission lines terminated by two open circuits loads. The two terminations are sufficient to create a standing wave as in a Fabry-Pérot cavity and a $l = 20$ mm resonator will have a fundamental mode at $f_0 = 8.5$ GHz. The first harmonic is $f_1 = 2f_0 = 17$ GHz.

1 The original name comes from transmission-line shunted plasma oscillation qubit [19].

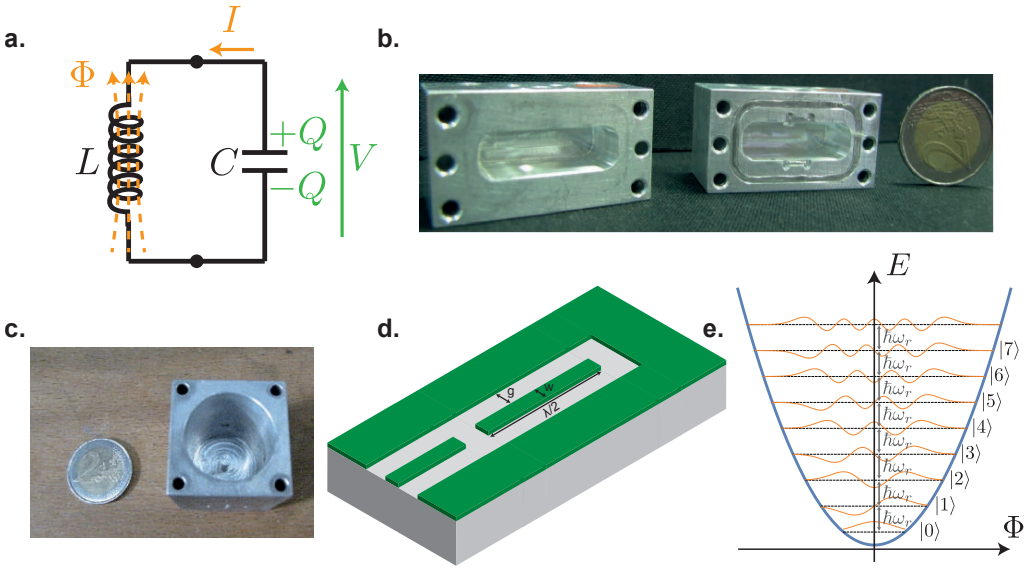

Figure 2.1: **a.** Electrical circuit of an LC oscillator. This system is analogous to a mass-spring system in mechanics with position coordinate taken to be Φ, the magnetic flux through the coil and the momentum variable is Q, the charge accumulated on the capacitor. The role of the spring constant is played by $1/L$ and the mass is C. The standard electrical variable V and I are obtained by Hamilton's equation (2.5). **b.** Picture of two blocks of aluminum forming a microwave cavity resonating at 8 GHz [67]. The cavity is created with a drilling machine from a raw block of aluminum. A qubit can be inserted in the cavity before closing it with an indium seal. **c.** Picture of a 3D coaxial $\lambda/4$ cavity [72]. The length of the central pin determines the resonant frequency of the cavity. The electromagnetic mode is confined at the bottom of the cavity and it is evanescent from the pin to the top opening. **d.** Schematics of a $\lambda/2$ coplanar waveguide (CPW) resonator surrounded by its ground plane. A superconducting material (in our group Nb or TiN) in green is deposited on a silicon substrate in gray. The impedance of the resonator is determined by the width of the resonator w, the size of the gap g, the height of the superconducting material and the nature of the substrate. **e.** Energy levels of an harmonic oscillator. The energy levels in dashed line are evenly spaced by $\hbar\omega_r$. The wavefunction amplitudes of the different Fock states are represented in orange as a function of the flux Φ. The number of nodes of the wave function is equal to the number of photons in the cavity.

The Lagrangian of the classical system is readily written as the difference of the potential energy stored in the capacitor and the kinetic energy stored in the inductor

$$\mathcal{L} = \frac{Q^2}{2C} - \frac{\Phi^2}{2L} \tag{2.2}$$

by defining the flux threading the coil Φ and the charge on the capacitor Q according to

$$\begin{cases} \Phi = \int_{-\infty}^{t} V(t')dt' \\ Q = \int_{-\infty}^{t} I(t')dt' \end{cases}. \tag{2.3}$$

And the Hamiltonian can be written

$$\mathcal{H} = Q\dot{\Phi} - \mathcal{L} = \frac{\Phi^2}{2L} + \frac{Q^2}{2C}. \tag{2.4}$$

Hamilton's equations of motion give us the current crossing the inductor and the voltage applied across the leads of the capacitor

$$\begin{cases} \dot{\Phi} = \dfrac{\partial H}{\partial Q} = \dfrac{Q}{C} = V \\ \dot{Q} = -\dfrac{\partial H}{\partial \Phi} = -\dfrac{\Phi}{L} = I \end{cases} \tag{2.5}$$

Remarkably the whole complexity of the system containing an enormous number of electrons boils down to a system with a *single* position degree of freedom. We choose the flux threading the coil Φ as the position coordinate. The system is simply analogous to a spring with mass[2] C, spring constant $1/L$ and momentum Q. The two variables Φ and Q can be promoted to quantum operators $\hat{\Phi}$ and $\hat{Q}$ that obey the canonical commutation relation

$$[\hat{\Phi}, \hat{Q}] = i\hbar. \tag{2.6}$$

The Hamiltonian now reads

$$\hat{H} = \frac{\hat{\Phi}^2}{2L} + \frac{\hat{Q}^2}{2C}. \tag{2.7}$$

We can diagonalize it in the usual form

$$\boxed{\hat{H} = \hbar\omega_r \left(\hat{a}^\dagger \hat{a} + \frac{1}{2}\right)} \tag{2.8}$$

in terms of the ladder operators

$$\begin{cases} \hat{a} = \dfrac{1}{\sqrt{2\hbar L\omega_r}}\hat{\Phi} + i\dfrac{1}{\sqrt{2\hbar C\omega_r}}\hat{Q} \\ \hat{a}^\dagger = \dfrac{1}{\sqrt{2\hbar L\omega_r}}\hat{\Phi} - i\dfrac{1}{\sqrt{2\hbar C\omega_r}}\hat{Q} \end{cases}, \tag{2.9}$$

2 Note that it is also possible to choose the charge accumulated on the capacitor as the position coordinate but with a 'mass' L and 'spring constant' $1/C$.

with $\omega_r = 1/\sqrt{LC}$. And the creation and annihilation operators obey the usual bosonic relation $[\hat{a}, \hat{a}^\dagger] = 1$. The number operator $\hat{n} = \hat{a}^\dagger \hat{a}$ gives the number of quanta in the mode that we dub *photons*. We can think of these quanta as collective excitations of both the electrical field and the Cooper pairs inside the materials[3].

The energy spectrum of the harmonic oscillator is represented in Fig 2.1**e**. The energy levels of the harmonic oscillator are evenly spaced as predicted from (2.8). Sending a cold enough classical microwave radiation at energy $\hbar\omega_r$ inevitably populates all the levels of the Hilbert space with a Poisson distribution leaving the cavity in a coherent state. In order to prepare other states, one needs to couple the oscillator to a non linear element or to perform postselection or non-Gaussian measurements. This will be the role of the Josephson junction in the following.

The charge and flux operators can then be expressed as

$$\begin{cases} \hat{\Phi} = \Phi_{\text{ZPF}}(\hat{a} + \hat{a}^\dagger) \\ \hat{Q} = -iQ_{\text{ZPF}}(\hat{a} - \hat{a}^\dagger) \end{cases}, \tag{2.10}$$

where the zero-point fluctuations are defined as a function of the characteristic impedance of the resonator $Z = \sqrt{L/C}$ by $Q_{\text{ZPF}} = \sqrt{\frac{\hbar}{2Z}}$ and $\Phi_{\text{ZPF}} = \sqrt{\frac{\hbar Z}{2}}$. Notice that the Heisenberg minimal uncertainty product is given by $Q_{\text{ZPF}}\Phi_{\text{ZPF}} = \frac{\hbar}{2}$.

Equation (2.5) allows to estimate the zero-point voltage fluctuations of a cavity mode in the ground state

$$V_{\text{ZPF}} \sim \frac{Q_{\text{ZPF}}}{C} \sim \omega_r \sqrt{\frac{\hbar}{2} Z} \sim 0.4\ \mu\text{V} \tag{2.11}$$

with $\omega_r = 2\pi \times 8$ GHz and $Z = 100\ \Omega$.

2.1.3 *Open quantum systems*

In practice our microwave circuits are open quantum systems and the above groundwork has to be completed by connecting the harmonic oscillator to the rest of the circuitry to enable coherent control and measurement of the system. The dynamics of an open system of Hamiltonian $\hat{H}$ is governed by the Lindblad equation

$$\boxed{\frac{d\rho_t}{dt} = -\frac{i}{\hbar}[\hat{H}, \rho_t] + \sum_k \mathcal{D}_k(\rho_t)dt,} \tag{2.12}$$

where ρ_t is the density matrix of the cavity at time t, $\mathcal{D}_k(\rho_t) = L_k \rho_t L_k^\dagger - \frac{1}{2}\rho_t L_k^\dagger L_k - \frac{1}{2} L_k^\dagger L_k \rho_t$ is the dissipation super-operator and $\{L_k\}$ are the *jump operators*. Each index k is associated to an irreversible quantum channel and the effect of the interaction between the bath and the system is encoded in L_k.

This very general differential equation describes the decoherence of an open quantum system by extending the Schrödinger equation to *Markovian* open systems, that is,

3 Note that usually physicists rigorously speak about photons only as excitations of a free propagating electromagnetic mode but our denomination is legitimized by the fact that the stationary photons that we defined above can fully be converted into propagating excitations of a transmission line whose limit conditions can be continuously impedance matched to infinity.

local in time [77]. Local in time means that ρ_{t+dt} must be entirely determined by ρ_t. Dissipation originates from the fact that energy and information can flow from the system to the bath however if this is a two-way process, information can also flow back in the system and give rise to a non-Markovian evolution of the system since we need to know the value of ρ at earlier times.

In order to derive the Lindblad Eq. (2.12) the following hypotheses are required [66]

- We usually deal with Eq. (2.12) by dividing the time into 'slices' of duration dt and every evolution ρ_t from time t to $t + dt$ is incremental. This 'coarse-grained' description of the first order differential Eq. (2.12) screens out high frequency component of the dynamics with $\omega \gg 1/dt$. We thus perceive the dynamics of the studied system through a filter and this description will be accurate only for $dt \ll T_H$ where T_H is the typical time scale of evolution of the observables of ρ due to unitary evolutions or damping processes.

- The environment must be a 'sink'. We assume that this large system has a great number of degrees of freedom (represented by the collection of discrete electromagnetic modes in Fig. 2.2 b) and that the dynamics of the bath does not impact the dynamics of the system. This amounts to neglect the *memory effects* of the *bath* (also called *reservoir* in statistical physics). Mathematically we denote by τ_E the time scale of the fluctuations and correlations of the environment. The inequality $\tau_E \ll dt$ is required to ensure that the environment is amnesic at the scale dt. We thus renounce to the microscopic description of fluctuations much faster than dt.

- There is no notion of quantum measurement in the derivation of Eq. (2.12). Continuous quantum measurement will be introduced in Chapter 3 and the dynamics of the quantum state will be predicted by the *stochastic master equation* in chapter 6.

In the case of a cavity losing photons 'one-by-one' via a coupling to a transmission line, only one jump operator is non zero $L = \sqrt{\kappa}\hat{a}$ where κ is the coupling rate to the transmission line. We will see the jump operators associated to a qubit in a following section and for any given system that satisfies the above-listed conditions, there exists a set of jump operators describing the decoherence of the system.

2.1.4 *Cavity coupled to two transmission lines*

In this thesis, we used two-port cavities with jump operators $\hat{L}_1 = \sqrt{\kappa_1}\hat{a}$ and $\hat{L}_2 = \sqrt{\kappa_2}\hat{a}$. The input-output relation (see appendix A)

$$\boxed{\sqrt{\kappa_i}\hat{a} = \hat{a}^i_{\text{in}} + \hat{a}^i_{\text{out}}} \tag{2.13}$$

relates the input and output propagating modes of the transmission line to the stationary mode $\hat{a}$ of the device. In the case of 3D resonators, the value of the coupling is determined by the length of the pins of the SMA connectors mounted on the cavity, while the coupling is given by a planar capacitance in the case of 2D resonators. In our

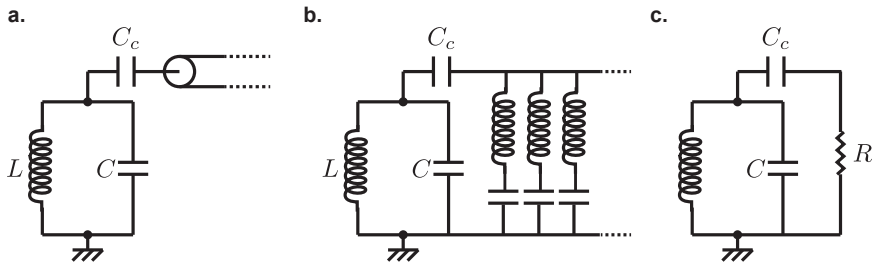

Figure 2.2: **a.** Example of an open quantum system: a cavity is connected to the transmission line. The coupling capacitance C_c sets the value of κ in the input-output relation (2.13). **b.** By discretizing the modes of the transmission line, we find an equivalent description: the quantum system is coupled to an infinite number of LC modes. **c.** The impedance of the infinite ensemble of LC resonators can be represented by a purely reactive dissipative element whose Caldeira-Leggett representation is the ensemble of modes.

case, we have $\kappa \sim 2\pi \times 2.3$ MHz for the most coupled port that will be used to collect the outgoing signals.

Equivalently to (2.12), operators evolve in time in the Heisenberg picture according to the quantum Langevin equation

$$\frac{d\hat{a}}{dt} = \frac{i}{\hbar}[\hat{H}, \hat{a}] - \frac{\kappa_1 + \kappa_2 + \kappa_L}{2}\hat{a} + \sqrt{\kappa_1}\hat{a}_{\text{in},1} + \sqrt{\kappa_2}\hat{a}_{\text{in},2} + \sqrt{\kappa_L}\hat{a}_{\text{in,L}} \tag{2.14}$$

with an additional κ_L term that models the internal losses of the cavity by a zero-temperature dissipative mode. Adding an external driving force of amplitude A_d and angular velocity ω_d on the system amounts to add the following Hamiltonian [78]

$$\hat{H}_{\text{drive}} = \hbar(A_d(t)e^{-i\omega_d t}\hat{a}^\dagger + A_d^*(t)e^{i\omega_d t}\hat{a}) \tag{2.15}$$

By driving the system with a coherent field on port 1, Eq. (2.14) becomes on average

$$\frac{d\alpha(t)}{dt} = -i\omega_r\alpha(t) - \frac{\kappa_1 + \kappa_2 + \kappa_L}{2}\alpha(t) + \sqrt{\kappa_1}\alpha_{\text{in},1} \tag{2.16}$$

where $\alpha(t)$ is the complex amplitude of the coherent field stored in the cavity at time t. We can then write the reflection coefficient $S_{11}(\omega) = \frac{\alpha_{\text{out},1}(\omega)}{\alpha_{\text{in},1}(\omega)}$ and the transmission coefficient $S_{21}(\omega) = \frac{\alpha_{\text{out},2}(\omega)}{\alpha_{\text{in},1}(\omega)}$ in the spectral domain as

$$\begin{cases} S_{11}(\omega) = \dfrac{\kappa_1 - \kappa_2 - \kappa_L + 2i(\omega - \omega_r)}{\kappa_1 + \kappa_2 + \kappa_L - 2i(\omega - \omega_r)} \\ S_{21}(\omega) = \dfrac{2\sqrt{\kappa_1\kappa_2}}{\kappa_1 + \kappa_2 + \kappa_L - 2i(\omega - \omega_r)} \end{cases}. \tag{2.17}$$

We often denote $\kappa_{\text{tot}} = \kappa_1 + \kappa_2 + \kappa_L$ the total damping rate of the system, $Q = \omega_r/\kappa_{\text{tot}}$ the quality factor of the resonator and $Q_{\text{int}} = \omega_r/\kappa_L$ its internal quality factor. Internal quality factors as high as 10^8 are reported for 3D cavities [76] in presence of a superconducting qubit and 10^{10} for experiments with flying Rydberg atoms [79]. In our experiment we used a 3D rectangular copper cavity with $\kappa_{\text{tot}} = 2\pi \times 2.3$ MHz and

a total quality factor of ~ 500 dominated by the coupling to one of the transmission line to enhance photon collection by the so-called *Purcell effect* explained below.

From Eq. (2.17), we can see that the transmission profile is always a Lorentzian in amplitude accompanied with a π phase shift (see Fig 2.3). The width of Lorentzian and the phase shift is always given by κ_{tot}. In reflection on port 1, three regimes are observed.

- The over-coupled regime is defined by $\kappa_1 \gg \kappa_L + \kappa_2$. In this regime the losses are negligible so in reflection $|S_{11}(\omega)| = 1$ and a 2π phase shift is observed (blue curve in Fig 2.3).
- The critical coupling corresponds to $\kappa_1 = \kappa_L + \kappa_2$. In this regime a π phase shift is observed in reflection while the amplitude vanishes at resonance (green curve in Fig 2.3).
- The under-coupled regime corresponds to $\kappa_L + \kappa_2 \gg \kappa_1$. A bigger dip in amplitude is observed in reflection due to the important losses with a phase shift $\leq \pi$ (red curve in Fig 2.3).

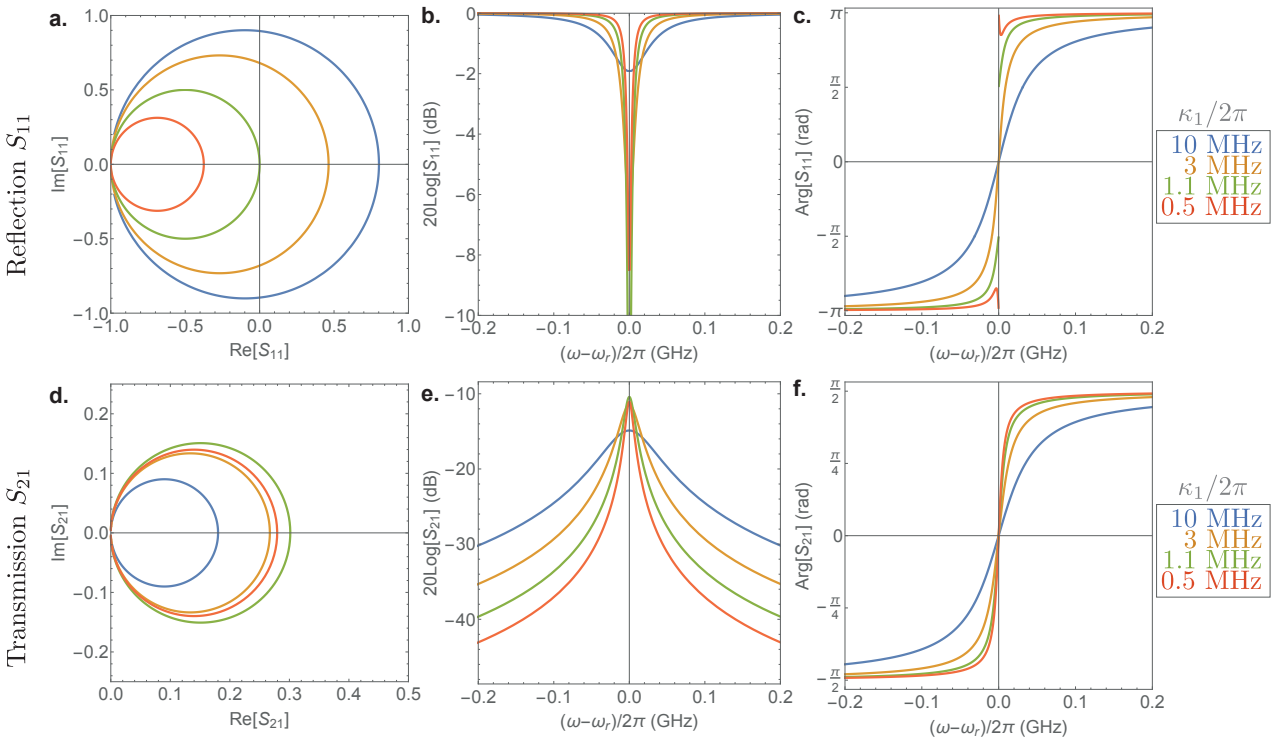

Figure 2.3: Reflection (**a**, **b** and **c**) and transmission (**d**, **e** and **f**) signal through the cavity given by Eq. (2.17) for $\kappa_2 = 2\pi \times 100$ kHz, $\kappa_L = 2\pi \times 1$ MHz and various κ_1 (indicated by color). The distinct over-coupled (blue line), critical (green curve) and under-coupled (red curve) regimes are observed in the reflected signal whereas the transmitted signals are all Lorentzian resonances.

2.2 TRANSMON QUBIT

Now that we know how to deal with open quantum systems, we need to add a non linear element to complete the cQED toolbox. The transmon is an artificial atom made of a Josephson junction connected to two superconducting islands. In our case the aluminum/alumina/aluminum junction is typically 250 × 200 nm and the associated tunnel resistance at room temperature of the order of 2 to 8 kΩ (see appendix B). The coupling Hamiltonian associated to the coherent tunneling of a Cooper pair through the barrier reads

$$\hat{H}_{\text{tunneling}} = -\frac{E_J}{2} \sum_{N=-\infty}^{+\infty} \left(|N\rangle \langle N+1| + |N+1\rangle \langle N| \right) \tag{2.18}$$

where E_J is a macroscopic parameter, which is proportional to the DC conductance G_n of the junction in the normal state, which can be adjusted during the fabrication process and to the superconducting gap Δ of the material $E_J = \Delta G_n \frac{h}{8e^2}$. The state $|N\rangle$ corresponds to exactly N Cooper pairs having passed through the junction.

We can define a new 'plane wave' basis

$$|\varphi\rangle = \sum_{N=-\infty}^{+\infty} e^{iN\varphi} |N\rangle . \tag{2.19}$$

The number φ can be thought of as an angle since $\varphi \to \varphi + 2\pi$ leaves $|\varphi\rangle$ unaffected. The variable φ corresponds to the superconducting phase difference across the junction and the Josephson relation relates to the electromagnetic flux by $\varphi = \frac{\hat{\Phi}}{\varphi_0} \pmod{2\pi}$ with the reduced flux quantum $\varphi_0 = \frac{\hbar}{2e}$. The tunneling Hamiltonian (2.18) is formally a hopping Hamiltonian in a 1D tight-binding model, so we get the usual cosine dispersion relation

$$\hat{H}_{\text{tunneling}} |\varphi\rangle = -E_J \cos(\varphi) |\varphi\rangle . \tag{2.20}$$

On top of this tunneling energy, one has to consider the charging energy. The potential energy associated with the transfer of a single electron is $E_C = \frac{e^2}{2C}$ with C the capacitance between the two superconducting islands so the energy operator associated with the transfer of a Cooper pair is four times larger. We obtain the Cooper Pair Box (CPB) Hamiltonian [80]

$$\hat{H} = 4E_C(\hat{N} - N_g)^2 - E_J\widehat{\cos(\varphi)}. \tag{2.21}$$

where we added N_g called the dimensionless *gate charge*. It represents either the effect of a voltage applied across the junction or a junction asymmetry that breaks the symmetry between positive and negative charge transfer [73]. We define the number operator $\hat{N} = \sum_{N=0}^{+\infty} N |N\rangle \langle N|$. The number operator $\hat{N}$ has integer eigenvalues whereas N_g is a continuous variable. The Hamiltonian (2.21) is formally identical to the Hamiltonian of a 'quantum rotor' in a gravity field with the charging energy playing the role of 'moment of inertia' and the Josephson energy as the torque produced by gravity.

Unfortunately, the gate charge uncontrollably fluctuates and this is what limited the interest of the CPB as a qubit [17, 81]. However when $E_J/E_C \sim 50$ or above, the energy

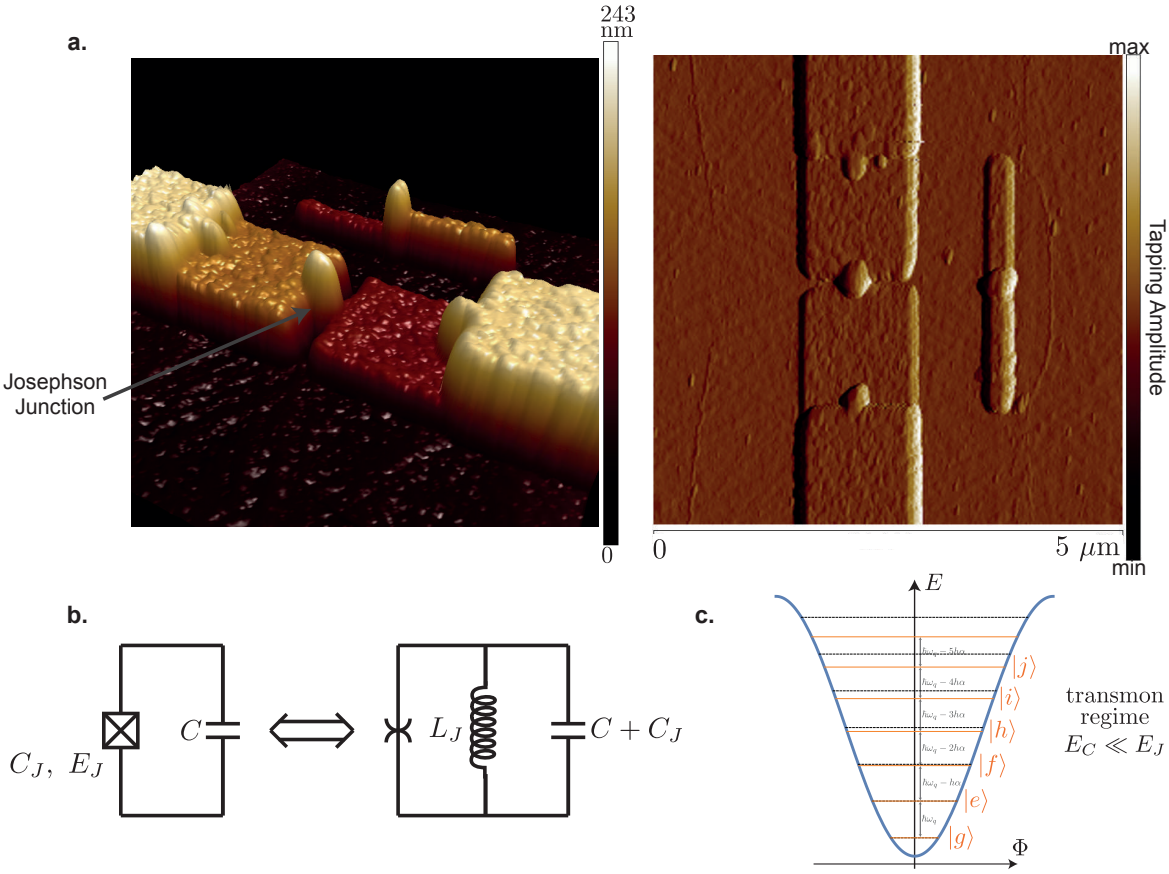

Figure 2.4: **a.** Atomic force microscope image of a Josephson junction in 3D and in 2D. The amplitude of the signal in tapping mode is shown. The height of the different layers of superconductor is coming from the double angle evaporation in the fabrication recipe (see Appendix B). A small 'diving platform' can be seen next to the junction. In fact this small additional Josephson junction is not connected to the rest of the circuit. It is used to release the strain on the Dolan bridge during fabrication. **b.** Schematics of a Josephson junction with Josephson energy E_J and intrinsic capacitance $C_J(\sim$ fF) in parallel with a large capacitance C that ensures that this Cooper pair box operates in the transmon regime $E_J > 50E_C$. The CPB Hamiltonian (2.21) can be expanded in an LC circuit in parallel with a non linear element (2.22) represented by the 'spider' symbol. **c.** Energy diagram of a transmon with $E_J = \hbar \times 20$ GHz and $E_C = \hbar \times 200$ MHz. The energy levels of the transmon are represented in orange while the energy levels of the corresponding harmonic oscillator are in dashed lines. At low temperature $k_B T \ll h f_q$, a single level of the qubit can be occupied. The frequency of the qubit transition is given by $h f_q \simeq \sqrt{8 E_J E_C}$ and the anharmonicity of the qubit is $h\alpha \simeq -E_C$.

spectrum of the CPB becomes almost independent of N_g, this is the so-called *transmon regime* [19, 20]. In our design, we make sure to operate in this regime by shunting the junction by a large enough capacitance that is obtained by connecting the junction to large enough pads (see Fig. 2.5). From the Hamiltonian (2.21), we see that in this regime eigenstates have a well defined phase $\hat{\Phi}$ and a large $\hat{Q}$ uncertainty in charge $\hat{Q}$.

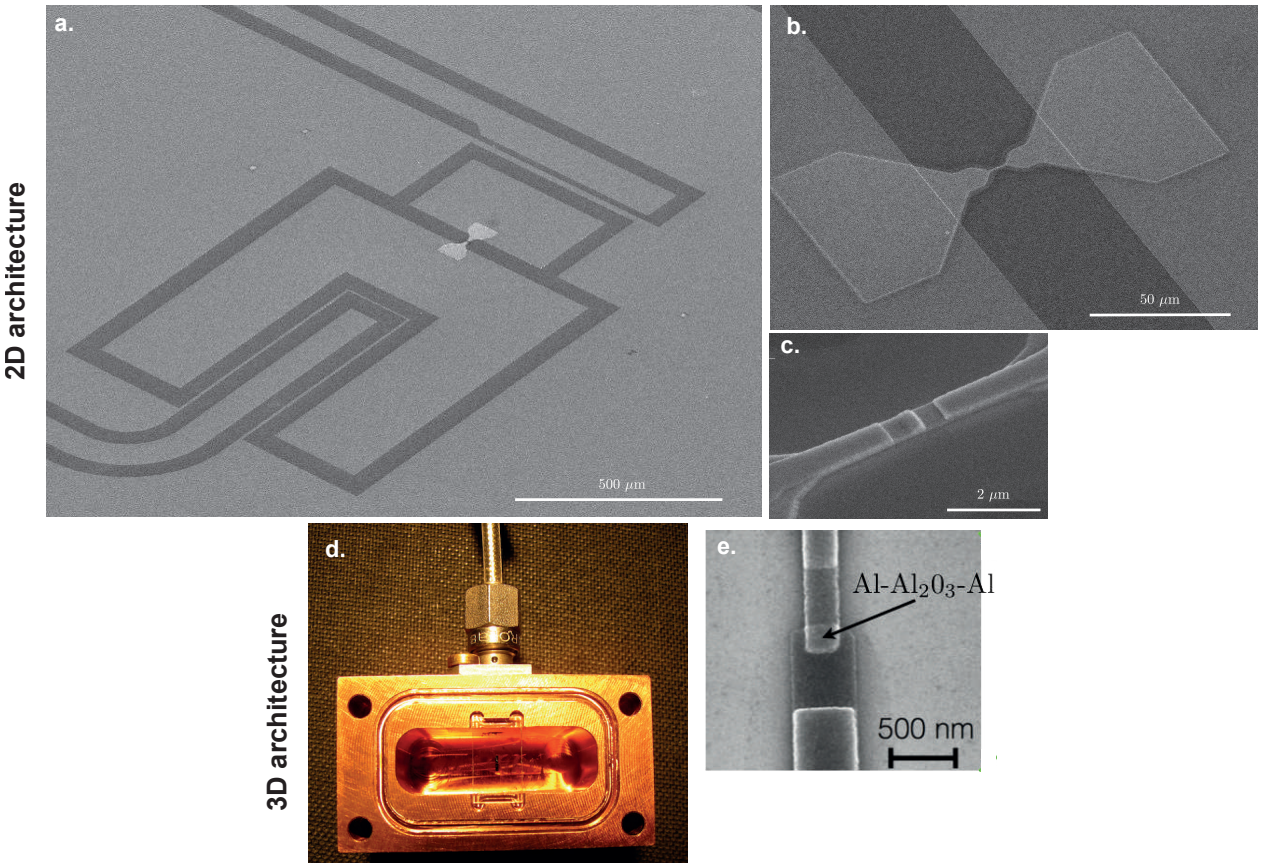

Figure 2.5: **a.** Scanning electron microscope image under an angle of a 2D transmon embedded in a niobium CPW circuit. The Josephson junction made out of aluminum is connected to two large pads forming a large capacitance that lowers the charging energy $E_C = \hbar\frac{e^2}{2C} \simeq \hbar \times 234$ MHz. **b.** and **c.** Zooms on the Josephson junction deposited by double angle evaporation with the Dolan bridge technique (see appendix B). **d.** 3D aluminum cavity with a sapphire chip. The chip is gripped on its two edges between two blocks of aluminum to ensure that the substrate is thermalized. We measured $E_J = \hbar \times 20.588$ GHz and $E_C = \hbar \times 174$ MHz for this chip so we are deeply in the tranmson regime. **e.** SEM image of the Josephson junction of the $3D$ transmon device, which is very similar to the one on silicon in Fig. **c**.

By reording the terms in (2.21), we obtain

$$\hat{H} = \underbrace{\left(4E_C(\hat{N} - N_g)^2 + \frac{1}{2}E_J\hat{\varphi}^2\right) - E_J}_{\hat{H}_{\text{HO}}} \underbrace{-E_J\left(\widehat{\cos(\varphi)} + \frac{\hat{\varphi}^2}{2} - 1\right)}_{\hat{H}_{NL}} \tag{2.22}$$

where $\hat{H}_{\text{HO}}$ is the Hamiltonian of the harmonic oscillator $\hat{H}_{\text{HO}} = hf_q(\hat{a}^\dagger\hat{a} + 1/2)$ at frequency $f_q = \frac{1}{h}\sqrt{8E_JE_C}$, which is of the order of ~ 5 GHz in our systems. In the limit $\varphi \ll 1$, the purely non-linear term reads

$$\hat{H}_{NL} = -E_J(\widehat{\cos(\varphi)} + \hat{\varphi}^2/2 - 1) \simeq -E_J(\varphi^4/4! - \varphi^6/6! + \varphi^8/8! + ...). \tag{2.23}$$

This term is symbolized by the spider element in Fig. 2.4 and is responsible for the non evenly spaced distribution of the energy levels. This anharmonicity is crucial to selectively manipulate a limited number of levels and effectively truncate the Hilbert space. Specifically, the first two levels $|g\rangle$ and $|e\rangle$ are used as a *two-level system* or *qubit* throughout this thesis and in the third chapter we additionally used the third level $|f\rangle$ to work with a *qutrit*.

The basics features of the transmon circuit (Fig. 2.4**b**) were explained in this section without taking into consideration the cavity. Introducing it at this stage becomes quite technical since the geometry of the transmon and cavity modes are affected and distorted by one another to become *dressed states*, which both inherit some non linearity of the junction. The complexity increases further by including the harmonics of the cavity. We rather derive an effective Hamiltonian with the *Black-box quantization method*.

2.2.1 *Black-box quantization of a transmon embedded in a cavity*

2.2.1.1 *General theory with a single junction*

Typical circuits used in our experiments have more degrees of freedom than a simple harmonic oscillator and all the complexity of the system can be captured in a 'black box'. The *black box quantization method* was originally introduced by Nigg et al. [82]. Generalizations of this method have been proposed by Solgun *et. al.* [83] and Malekakhlagh *et. al.* [84] to model more complex environment but we restrict the discussion to the Foster decomposition of the environment. Its principle relies on solving the linearized problem and treat the non linearity perturbatively. In the case of a linear circuit, knowing the impedance $Z(\omega)$ or admittance $Y(\omega) = Z^{-1}(\omega)$ of a dipole black box connected as a function of frequency completely characterizes its quantum properties.

We start by decomposing the impedance seen by the junction into M RLC-oscillators in series[4] $Z(\omega) = \sum_{p=1}^{M}(j\omega C_p + \frac{1}{j\omega L_p} + \frac{1}{R_p})^{-1}$ (Fig. 2.6). First, neglecting the dissipation associated to the R_p elements, the Hamiltonian of the linear system reads [85]

$$\hat{H}_{\text{linear}} = \sum_{p=1}^{M} \hbar\omega_p(\hat{a}_p^\dagger\hat{a}_p + 1/2) \tag{2.24}$$

with $\omega_p = 1/\sqrt{L_pC_p}$ (for weak dissipation i.e. $R_P \gg \sqrt{L_P/C_p}$). This Foster decomposition is equivalent to diagonalizing coupled modes into M uncoupled *hybrid* or *dressed* modes which are collective excitations of the linear circuit. The ladder operators of each mode p are defined as $\hat{a}_p = \sqrt{\frac{1}{2\hbar Z_p}}\hat{\Phi}_p + i\sqrt{\frac{Z_p}{2\hbar}}Q_p$ with $Z_p = \sqrt{L_p/C_p}$. We obtain

4 It is important to understand that usually the circuit elements drawn in electrical circuits have no physical counter part in the actual device.

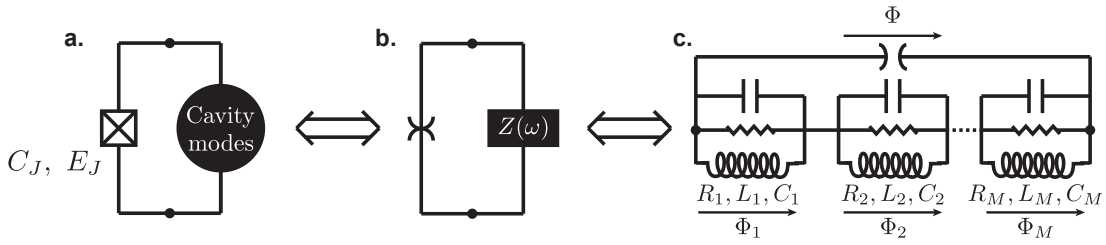

Figure 2.6: **a.** Schematics of a Josephson junction coupled to an arbitrary linear circuit dubbed 'cavity modes' for the transmon. **b.** The Josephson element is replaced by a purely non linear element (spider symbol) the linear inductance L_J and capacitance C_j of the junction together with the cavity modes are encapsulated in an impedance $Z(\omega)$ seen by the spider element. **c.** The impedance is replaced by its pole decomposition (Foster-equivalent) $Z(\omega) = \sum_{p=1}^{M}(j\omega C_p + \frac{1}{j\omega L_p} + \frac{1}{R_p})^{-1}$. We also introduce the fluxes Φ_p used in the text.

the expression of the flux across the junction $\hat{\Phi} = \sum_{p=1}^{M} \hat{\Phi}_p$ that can be reinjected in the non linear Hamiltonian (2.23). By restricting ourselves to the first non linear term, we obtain

$$\hat{H}_{\mathrm{NL}} = \sum_p \Delta_p \hat{n}_p + \frac{1}{2}\sum_{pp'} \hbar\chi_{pp'}\hat{n}_p\hat{n}'_p \tag{2.25}$$

with the excitation number operator $\hat{n}_p = \hat{a}_p^\dagger \hat{a}_p$ of mode p. The Lamb-shift of mode p is $\Delta_p = -\frac{e^2}{2L_J}(Z_p \sum_{p'} Z_{p'} - Z_p^2/2)$ expressing a frequency 'renormalization' due to the presence of the other modes. The expressions of the self-Kerr χ_{pp} and cross-Kerr $\chi_{pp'}$ constants are given by

$$\begin{cases} \hbar\chi_{pp} = -\dfrac{L_p}{L_J}\dfrac{C_\parallel}{C_p}E_C = -Z_p^2\dfrac{C_\parallel}{L_J}E_C \\ \hbar\chi_{pp'} = -2\sqrt{\chi_{pp}\chi_{p'p'}} \end{cases} \tag{2.26}$$

where $C_\parallel$ is the capacitance shunting the junction. Lastly, the finite width of the resonances are given by the imaginary part of the zeros of the admittance $Y(\omega) = Z^{-1}$ of the Black-box. The quality factor of mode p is given by

$$Q_p = \frac{\omega_p}{2}\frac{\mathrm{Im}[Y'(\omega_p)]}{\mathrm{Re}[Y(\omega_p)]}. \tag{2.27}$$

Similarly to the non-linearity, dissipation is spread over all effective modes. This method can be extended to multiple non linearities coupled to an arbitrary black box but it requires heavier equations [82]. We will know apply it to the case of a transmon coupled to a cavity.

2.2.1.2 *Application to the transmon*

For a transmon inside a cavity, the qubit and cavity are treated as electromagnetic modes on equal footing and then we account for the weak non linearity of the Josephson potential perturbatively[5]. As depicted above, there is no clear separation between

5 Note that this method is applicable to transmon qubits because they exhibit a weak anharmonicity that allow the perturbative treatment.

the qubit and the cavity in this model and one mode with a strong (resp. weak) anharmonicity is called qubit-like (resp. cavity like). Mathematically speaking the qubit-like mode has a much higher impedance seen by the junction $Z_q \gg Z_p$ for all p. By restricting ourselves to one cavity mode, we obtain a total Hamiltonian similar with a non linear part given by Eq. (2.25)

$$\hat{H}_{BBQ} = \hbar\omega_q \hat{a}_q^\dagger \hat{a}_q + \hbar\omega_c \hat{a}_c^\dagger \hat{a}_c - \hbar\chi \hat{a}_c^\dagger \hat{a}_c \hat{a}_q^\dagger \hat{a}_q - \hbar\frac{\alpha}{2}\hat{a}_q^{\dagger 2}\hat{a}_q^2 + \hbar\frac{K}{2}\hat{a}_c^{\dagger 2}\hat{a}_c^2 \tag{2.28}$$

where ω_q and ω_c are the dressed qubit and cavity frequencies, a_q and a_c are the annihilation operators of the qubit-like and cavity-like modes. The non-linear terms reads

$$\begin{cases} \alpha = -\chi_{qq}/\hbar = \dfrac{E_C}{\hbar} \text{ (anharmonicity of the transmon)} \\ \chi = -2\chi_{qc}/\hbar = 2\alpha\left(\dfrac{g}{\Delta}\right)^2 \text{ (cavity pull)} \\ K = \chi_{cc}/\hbar = -\left(\dfrac{Z_c}{Z_q}\right)^2 \dfrac{E_C}{\hbar} \text{ (self} - \text{Kerr of the cavity mode)} \end{cases} . \tag{2.29}$$

In practice the anharmonicity of the cavity K is negligible because $Z_q \gg Z_c$ and in our system $|K| \sim 2\pi \times 40$ kHz so we will neglect this term in the rest of the thesis. The interaction strength is given by cavity pull[6] χ as a function of the dipolar coupling constant g between the artificial atom and the electrical field and the detuning $\Delta = |\omega_q - \omega_c|$ [86]. The cavity pull is of the order of a few MHz in our experiments and it may be enhanced by increasing the length of the antenna to obtain a greater dipole moment. The anharmonicity of the transmon α is of the order of $\alpha \sim 2\pi \times 100 - 200$ MHz. Its value is controlled by the charging energy which is set by the antenna area.

The cavity mode is connected to a resistor (Fig. 2.7) modeling the coupling to an external transmission line. Photons leak out of the cavity on a time scale κ^{-1} and Eq. (2.27) predicts a finite quality factor Q_q for the qubit-like mode and thus a finite decay rate known as *Purcell rate* $\Gamma_{1,\text{Purcell}} = \omega_q/Q_q$. We obtain the Purcell decay rate that limits the lifetime of the transmon

$$\Gamma_{1,\text{Purcell}} = 2\frac{\text{Re}[Y'(\omega_q)]}{\text{Im}[Y'(\omega_q)]} \simeq \kappa\frac{g^2}{\Delta^2}. \tag{2.30}$$

In practice with typical values $g/2\pi = 290$ MHz, $\kappa/2\pi = 2.3$ MHz and $\Delta/2\pi = 2.4$ GHz, we obtain $\Gamma_{1,\text{Purcell}} = (4.7\ \mu\text{s})^{-1}$ which is much higher than the experimental value. This known discrepancy [86] could be due to one of the approximations of the model and it is nonetheless possible to get a good approximation of $\Gamma_{1,\text{ Purcell}}$ by simulating directly the admittance seen by the junction with finite-element simulations. However we make sure that the relaxation time of the qubit is limited by Purcell effect in this thesis to be able to collect a significant part of the spontaneous emission in the output line (see chapter 3).

6 The cavity-pull of the transmon is reduced by a factor $1/\Delta$ compared to a Jaynes-Cummings hamiltonian due to higher levels.

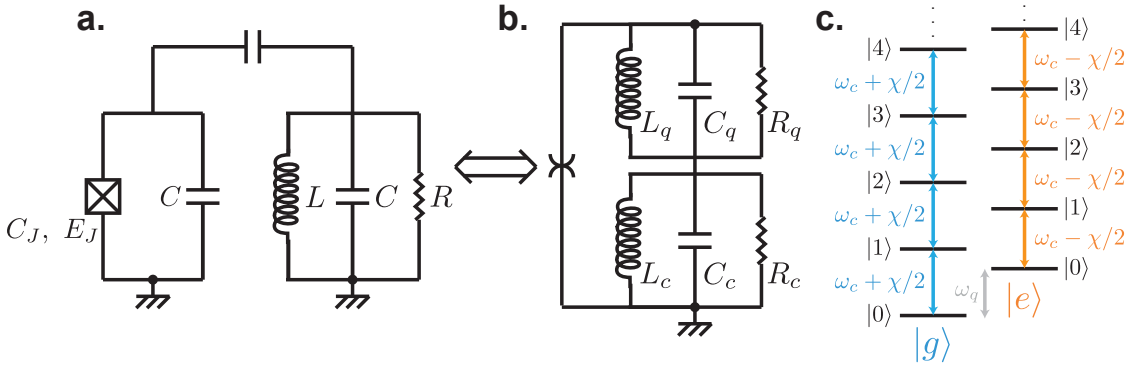

Figure 2.7: **a.** Schematics of the system. A capacitively shunted Josephson junction is coupled to an harmonic oscillator with a small dissipative element $R \ll \sqrt{L/C}$ used to model the coupling to a transmission line. **b.** Equivalent decription with the Black-box quantization method. A purely non-linear element is connected to an impedance whose Foster decomposition contain a qubit-like mode and a cavity-like mode. The non linearity is distributed over the two modes depending on their impedance Z_p according to Eq. (2.26). The dissipation is also distributed over the modes and in particular the qubit-like mode acquires a dissipative element R_q resulting in the Purcell effect. **c.** Energy ladder for the Hamiltonian (2.32) of transmon-cavity system in the two-level limit approximation. The energy diagram is composed of two harmonic oscillator ladders with a transition frequency $\omega_c+\chi/2$ (resp. $\omega_c-\chi/2$) if the qubit is in $|g\rangle$ (resp. $|e\rangle$).

In this formalism all modes are bosons but we usually think about fermions when talking about qubits. The last step that we have to make is to confine the number of excitations in the transmon[7] to one photon. In this case, we can safely replace

$$\hbar\omega_q \hat{a}_q^\dagger \hat{a}_q - \hbar\alpha \hat{a}_q^{\dagger 2}\hat{a}_q^2 \to \hbar\omega_q \frac{\sigma_z + 1}{2} \tag{2.31}$$

with the Pauli matrix $\sigma_z = \begin{pmatrix} 1 & 0 \\ 0 & -1 \end{pmatrix}$ expressed in the basis $\{|e\rangle, |g\rangle\}$. We end up with the circuit QED Hamiltonian in the dispersive regime

$$\boxed{\hat{H} = \hbar\frac{\omega_q}{2}\sigma_z + \hbar\omega_c \hat{a}_c^\dagger \hat{a}_c - \hbar\frac{\chi}{2}\sigma_z \hat{a}_c^\dagger \hat{a}_c.} \tag{2.32}$$

We recover the energy ladder of this Hamiltonian in Fig. 2.7 for the hybrid levels of the transmon-cavity system.

The previous derivation is universal in the sense that we only dealt with lumped elements regardless of the structure of the actual device (metallic tracks, bulk metal, dielectric substrates and tunnel junctions) whose geometry may be planar (2D CPW architecture) or three-dimensional. This formalism becomes particularly powerful to design an experiment with targeted parameters values by looking at the electromagnetic energy distribution in the actual device thanks to finite element simulation.

7 We implicitly assume that we drive the qubit with pulses with a duration much longer than h/α to ensure that the higher levels of the transmon are not excited.

2.2.2 *Finite element simulation - Energy participation ratios*

In order to predict the values of the frequencies $\{\omega_p\}$ in (2.24) and χ's in (2.26), we perform classical finite element simulation of our devices[8]. We replace the Josephson element by a lumped[9] electromagnetic element of inductance L_J and capacitance[10] C_j and the solver extracts the electromagnetic eigenmodes of the linear problem (2.24). The frequency of the eigenmode p is ω_p and even its quality factor Q_p (see Eq. (2.27)) can be predicted by introducing losses in the simulation.

The solver gives the stationary electric and magnetic eigenfields $\vec{E}_m(\vec{r})$ and $\vec{H}_m(\vec{r})$ of mode m where $\vec{r}$ indicates the spatial coordinates. The total electromagnetic energy of the system breaks down in the sum of its inductive energy $\mathcal{E}_{\text{inductive}}$ and its capacitive energy $\mathcal{E}_{\text{capacitive}}$. The inductive energy originates from the magnetic fields and from the kinetic energy stored in the lumped linear inductance of the junction $\mathcal{E}_{\text{inductive}} = \mathcal{E}_{\text{mag fields}} + \mathcal{E}_{\text{kinetic}}$ whereas the capacitive energy is solely stored in the electrical fields $\mathcal{E}_{\text{capacitive}} = \mathcal{E}_{\text{elec fields}}$. When a stationary mode m is excited on resonance the total energy equilibrates between inductive and capacitive energy $\mathcal{E}_{\text{capacitive}} = \mathcal{E}_{\text{inductive}}$ because of the equipartition theorem.

We introduce the *energy participation ratios* of the junction to the mode m as the fraction of inductive energy stored in the junction when exciting mode m

$$p_m = \frac{\mathcal{E}_{\text{kinetic}}}{\mathcal{E}_{\text{inductive}}}\bigg|_m \underset{equipartition}{=} \frac{\mathcal{E}_{\text{elec fields}} - \mathcal{E}_{\text{mag fields}}}{\mathcal{E}_{\text{elec fields}}} \tag{2.33}$$

where the electromagnetic energies are computed as [87]

$$\begin{cases} \mathcal{E}_{\text{elec fields}} = \dfrac{1}{2}\displaystyle\int d^3\vec{r}\left(\vec{E}(\vec{r}).\underline{\underline{\epsilon}}(\vec{r}).\vec{E}(\vec{r})\right) \\ \mathcal{E}_{\text{mag fields}} = \dfrac{1}{2}\displaystyle\int d^3\vec{r}\left(\vec{H}(\vec{r}).\underline{\underline{\mu}}(\vec{r}).\vec{H}(\vec{r})\right) \end{cases} \tag{2.34}$$

where $\underline{\underline{\epsilon}}$ (resp. $\underline{\underline{\mu}}$) denotes the electric-permittivity tensor (resp. magnetic-permeability tensor).

Interestingly the list of participation ratio $\{p_m\}$ is sufficient to characterize the non-linearity of a multi-mode circuit hosting one Josephson junction. It is easy to show that they are real numbers between 0 and 1 and that they sum up to one $\sum_{m=1}^{M} p_m = 1$. We typically obtain participation ratios of the order of ~ 0.9 for qubit-like modes and ≤ 0.1 for cavity-like modes. It is possible to show that[11] the impedance of mode m seen by the junction is simply $Z_m = \frac{\omega_m}{E_J} p_m$ and from Eq. (2.26) we obtain the non linear terms of the Hamiltonian as a function of the participation ratios

$$\begin{cases} \chi_{mm} = -\hbar\dfrac{\omega_m^2 p_m^2}{8E_J} \\ \chi_{mn} = -\dfrac{\hbar\omega_m\omega_n}{4E_J} p_m p_n \text{ (for n} \neq \text{m)} \end{cases} \tag{2.35}$$

8 These simulations are performed using HFSS or Sonnet.

9 The lumped approximation is justified by the fact the size of the junction $\sim$ hundreds nm is very small compared to the wavelength $\sim$ cm of the electromagnetic modes.

10 In practice, we forget about this capacitance because it is negligible in the transmon regime.

11 Zlatko Minev *et al.* in preparation.

In practice, we use an open-source package pyEPR[12] developed by Zlatko Minev and Zaki Leghtas which automates the energy participation ratio approach with HFSS. The package allows to compute the non linear couplings between electromagnetic modes with more than one junction and at an arbitrary order in the expansion of the cosine potential (2.23). This package was tested in the design of several experiments [88, 89, 90] and it fills the need for a simple and systematic method to predict the non-linear interaction of the increasingly complex and diverse architecture of circuit QED.

2.3 OPEN SYSTEM DYNAMICS OF A QUBIT

Now that we understand the transmon, we can forget about the solid-state description of the device and replace it with the quantum physics representation of a two states system called *qubit* or spin system. The qubit is the quantum analog of 'bit' or 'binary digit' that can only have two distinct logical values. In the quantum world, the qubit is a superposition of two distinct states $|g\rangle$ (ground state) and $|e\rangle$ (excited state). The formalism described in this section is widely used in the field of nuclear magnetic resonance to describe the dynamics of nuclear spins in the presence of time dependent magnetic fields as well as in the fields of quantum computing and quantum communication. We will introduce the Bloch decomposition of the density matrix on the Pauli matrices, the Bloch sphere that is extensively used in this thesis, the concept of entropy and purity of a spin 1/2 and finally we will discuss the decoherence mechanisms proper to a two-level system.

2.3.1 *Qubits*

We consider that the qubit is in a perfectly known state or *pure state* such that we can write it as a superposition of ground and excited state $|\psi\rangle = \alpha|g\rangle + \beta|e\rangle$ with α and β two complex coefficients satisfying $\sqrt{|\alpha|^2 + |\beta|^2} = 1$. In this case, the density matrix ρ associated to $|\psi\rangle$ is simply

$$\rho = |\psi\rangle\langle\psi| = \begin{pmatrix} |\beta|^2 & \alpha^*\beta \\ \alpha\beta^* & |\alpha|^2 \end{pmatrix}. \tag{2.36}$$

The density matrix is a generic object used to encapsulate an observer's knowledge about the state of the system [91] and more general states known as *mixed states* or *statistical mixtures* can be cast in a density matrix. We consider a statistical mixture of states $|\psi_i\rangle$ with probability p_i,

$$\rho = \sum_i p_i |\psi_i\rangle\langle\psi_i| \tag{2.37}$$

12 http://github.com/zlatko-minev/pyEPR

where p_i is a set of classical probabilities such that $\sum_i p_i = 1$. Since ρ is Hermitian, positive and of trace 1, it can be decomposed on the Pauli matrix basis

$$\boxed{\rho = \frac{1}{2}(\mathbb{1} + x\sigma_x + y\sigma_y + z\sigma_z) = \frac{1}{2}\left(\mathbb{1} + \begin{pmatrix} x & y & z \end{pmatrix}\begin{pmatrix} \sigma_x \\ \sigma_y \\ \sigma_z \end{pmatrix}\right) = \frac{1}{2}(\mathbb{1} + \vec{r}.\vec{\sigma})} \quad (2.38)$$

with the useful Pauli matrices

$$\mathbb{1} = \begin{pmatrix} 1 & 0 \\ 0 & 1 \end{pmatrix}, \quad \sigma_x = \begin{pmatrix} 0 & 1 \\ 1 & 0 \end{pmatrix}, \quad \sigma_y = \begin{pmatrix} 0 & -i \\ i & 0 \end{pmatrix}, \quad \sigma_z = \begin{pmatrix} 1 & 0 \\ 0 & -1 \end{pmatrix}. \quad (2.39)$$

The state of a qubit ρ is represented by its Bloch vector $\vec{r} = (x, y, z)^T$ in the *Bloch sphere*, which is a ball of radius 1 (see Fig. 2.8). Every coordinate $i \in \{x, y, z\}$ is the averaged result of the measurement of the observable σ_i, $i = \langle\sigma_i\rangle_\rho = \mathrm{Tr}(\rho\sigma_i)$. The excited state is the north pole ($\langle\sigma_z\rangle = +1$) of the sphere and the ground state is the south pole of the sphere ($\langle\sigma_z\rangle = -1$). Given Eq. (2.38), a non zero x or y coordinate is equivalent to quantum states with coherences between $|g\rangle$ and $|e\rangle$. A state ρ is said to be pure if and only if $||\vec{r}||^2 = 1$ and in this case the density matrix has exactly the same information content as a state vector. The surface of the ball is thus composed of pure states whereas the inner of the ball is composed of mixed states.

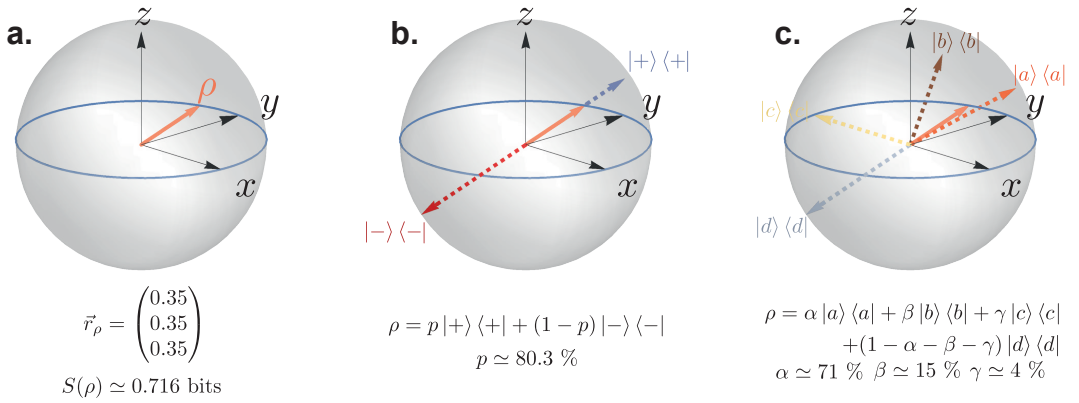

Figure 2.8: **a.** A mixed state ρ is represented by its Bloch vector $\vec{r}$ inside the Bloch sphere. We compute the entropy $S \simeq 0.716$ bits of this quantum state from Eq. (2.41). **b.** Decomposition of ρ on to orthogonal pure states[13] $|+\rangle$ and $|-\rangle$. This decomposition is in fact unique and the $\{p, 1-p\}$ are the eigenvalues of the density matrix used to compute the entropy. **c.** Another decomposition of ρ on 4 arbitrary chosen non orthogonal pure states denoted by $|x\rangle\langle x|$ for $x \in \{a, b, c, d\}$. The decomposition of a mixed state is not unique and there is no way to recover the initially prepared states with the associated classical probabilities $\{p_i\}$. For instance, from a maximally mixed state $\rho = \mathbb{1}/2$ there is no way to tell if the operator prepared a statistical mixture of $|g\rangle$ and $|e\rangle$ with probability 1/2 or a statistical mixture of $\{|g\rangle, |e\rangle, (|g\rangle + |e\rangle)/\sqrt{2}, (|g\rangle - |e\rangle)/\sqrt{2}\}$ with probability 1/4 each.

It is easy to notice that $||\vec{r}||^2 = x^2 + y^2 + z^2 = 2\mathrm{Tr}(\rho^2) - 1 = 2\gamma(\rho) - 1$ where the purity γ of the quantum state ρ is defined as

$$\gamma(\rho) = \mathrm{Tr}(\rho^2). \quad (2.40)$$

For a qubit[14] the purity is bounded $1/2 < \gamma < 1$ and its extrema $\gamma = 1$ and $\gamma = 1/2$ correspond to the surface of the ball (pure states) and the center of the ball (maximally mixed state).

2.3.2 *Entropy of a qubit*

Entropy is a key concept used to measure how much information is lacking about the state of a physical system. This lack of information comes from the classical uncertainty of Eq. (2.37) where the set of probability and pure vectors are not uniquely defined as explained in Fig. 2.8. Several definitions exist and we will use *Von Neumann entropy*

$$\boxed{S(\rho) = \mathrm{Tr}(\rho \mathrm{Log}_2(\rho)) = -p\mathrm{Log}_2(p) - (1-p)\mathrm{Log}_2(1-p)} \tag{2.41}$$

where Log_2 is the binary logarithm, we define $0\mathrm{Log}_2(0) = 0$ and $\{p, 1-p\}$ are the eigenvalues of the qubit density matrix. The entropy of a qubit lies between 0 (pure state) and 1 (maximally mixed-state or center of the Bloch sphere)[15]. Interestingly, Von Neumann entropy can be seen as a generalization of the classical *Shannon entropy* of a probability distribution equal to the eigenvalues of the quantum state. It can be shown that the entropy of a quantum state increases after an unread projective measurement but it can decrease because of decoherence[16].

In addition to the previous definition, we define the quantum relative entropy between two quantum states σ and ρ as [92]

$$S(\rho||\sigma) = -\mathrm{Tr}(\rho \mathrm{Log}_2(\rho)) + \mathrm{Tr}(\rho \mathrm{Log}_2(\sigma)) \tag{2.42}$$

which is a measure of the 'distance' between the two quantum states. The definition (2.42) is symmetric $S(\rho||\sigma) = S(\sigma||\rho)$ and non-negative $S(\rho||\sigma) \geq 0$ (*Klein*'s inequality) with equality if and only if $\sigma = \rho$. The relative entropy of two quantum states is monotonic, it can only decrease when tracing out a 'part' of a bipartite system. For our open-system experiments, we will see that relative entropy can only decrease in time under the effect of unread measurements because a part of the information on the system is lost.

2.3.3 *Decoherence mechanisms*

Similarly to the case of a cavity, we can write a Lindblad equation for the density matrix ρ_t at time t of a qubit

$$\frac{d\rho_t}{dt} = -\frac{i}{\hbar}[\hat{H}, \rho_t] + \mathcal{L}(\rho_t). \tag{2.43}$$

The Hamiltonian $\hat{H}$ can describe any unitary evolution. The Lindbladian can be decomposed according to

$$\mathcal{L}(\rho_t) = \sum_{i=1}^{3} \mathcal{D}_i(\rho_t) \tag{2.44}$$

14 In general the purity satisfies $1/d < \gamma < 1$ where d is the dimension of the Hilbert space.
15 In dimension d, the entropy lies between 0 and $\mathrm{Log}_2[d]$.
16 An energy relaxation channel brings the quantum system in the ground state, which is a pure state of zero entropy.

with the dissipation super-operator $\mathcal{D}_i(\rho_t) = L_i\rho_t L_i^\dagger - \frac{1}{2}L_i^\dagger L_i\rho_t - \frac{1}{2}\rho_t L_i^\dagger L_i$. The L_i's are dubbed *jump operators*

- $L_1 = \sqrt{\Gamma_\downarrow}\sigma_-$ for relaxation
- $L_2 = \sqrt{\Gamma_\uparrow}\sigma_+$ for excitation
- $L_3 = \sqrt{\frac{\Gamma_\phi}{2}}\sigma_z$ for pure dephasing.

The *energy relaxation channel* or *amplitude damping channel* [93] is a model of the decay of an atom due to spontaneous emission of a photon in the environment. By 'detecting' the photon, the environment causes an exponential decay of the energy of the qubit driving the state of the qubit toward the ground state. In practice, this relaxation effect comes from spontaneous emission of the qubit into the output transmission line and other events associated to non radiative decay of the qubit such as dielectric losses in the substrate, interaction with a resonant two-level system, quasi-particles in the aluminum. We make sure that the predominant relaxation process is energy relaxation through the output transmission line by *Purcell effect* to be able to monitor this decoherence channel. The *excitation channel* or *heating channel* is due to the coupling to hot baths that induce thermal excitation. This could be substrate phonons, high frequency radiations routed via the transmission lines or trapped two-level systems. We can measure the typical time for energy decay to relax to thermal equilibrium, which is given by $T_1 = \frac{1}{\Gamma_\uparrow+\Gamma_\downarrow}$.

The *dephasing channel* or *phase damping channel* destroys the extra-diagonal terms of the density matrix of the qubit exponentially fast in the energy basis. In practice the Bloch sphere shrinks to a spheroid aligned with the z axis (see Fig. 2.9). This *decoherence mechanism* is a general feature of any system leaking information that is imprinted in auxiliary degrees of freedom [7]. In our system, dephasing is usually caused by residual thermal photons inside the cavity coupled to the qubit, by flux noise in the superconducting loops formed of Josephson junctions, interaction with non-resonant trapped two-level systems. It can be measured in Ramsey interference experiments by measuring $T_2 = \frac{1}{\frac{\Gamma_\uparrow+\Gamma_\downarrow}{2}+\Gamma_\phi}$, which is the typical time for coherence decay.

In both cases, decoherence shrinks the accessible volume of Hilbert space in time as depicted in Fig. 2.9 but no physical process described by Lindblad equation (2.43) can blow it up again. However, we will see that these channels can be monitored and that we can use the extracted information to recover knowledge on the state of the system which results in a purification of the density matrix during the evolution.

In term of Pauli coordinates the evolution during a time step dt due solely to dissipation reads

$$\begin{cases} dx_t^{\text{dissipation}} = -\left(\dfrac{\Gamma_1}{2} + \Gamma_\phi\right) x_t dt \\ dy_t^{\text{dissipation}} = -\left(\dfrac{\Gamma_1}{2} + \Gamma_\phi\right) y_t dt \\ dz_t^{\text{dissipation}} = -\Gamma_1(z_t - z_{\text{th}})dt \end{cases} \tag{2.45}$$

where $\Gamma_1 = 1/T_1 = \Gamma_\uparrow + \Gamma_\downarrow$ and $z_{\text{th}} = \frac{\Gamma_\uparrow - \Gamma_\downarrow}{\Gamma_\uparrow + \Gamma_\downarrow}$ is the z component of the qubit at thermal equilibrium.

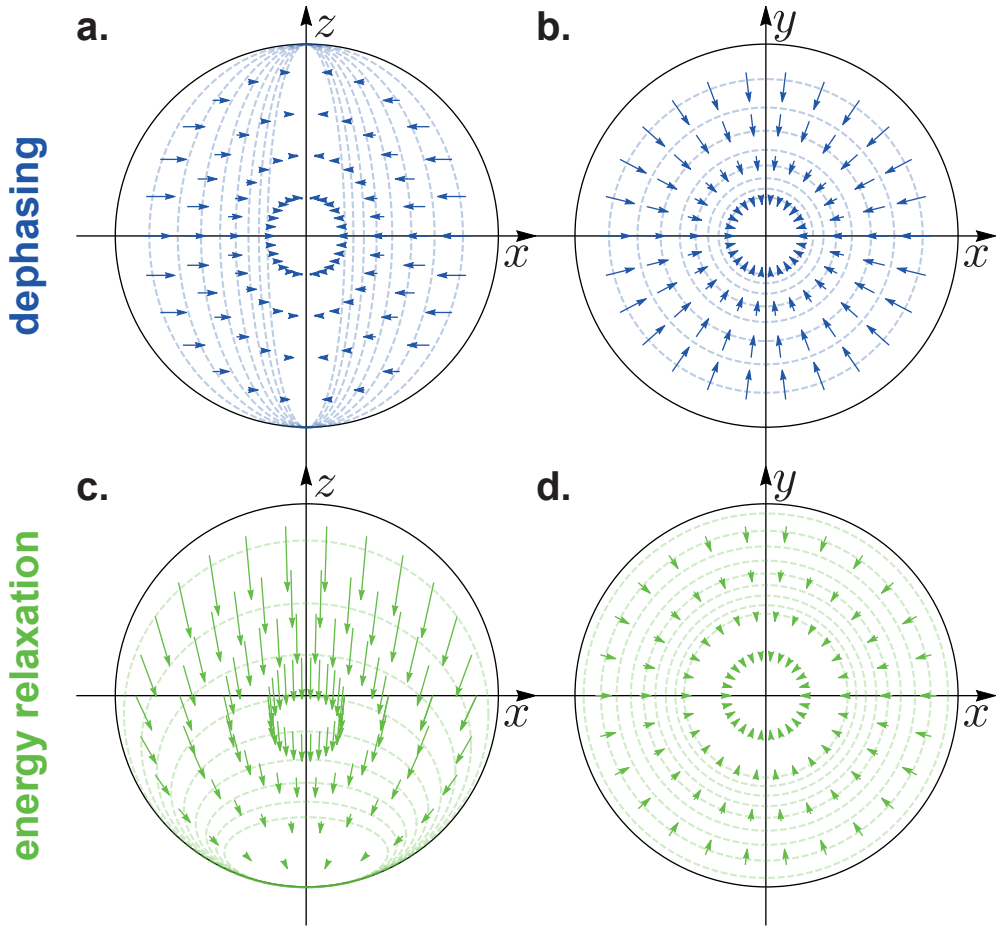

Figure 2.9: Representation of the dissipation evolution given in Eq. (2.45) in the $x-z$ (**a** and **c**) and $x-y$ (**b** and **d**) planes of the Bloch sphere. The arrows form a vector field that pushes the quantum states toward the z axis for dephasing (Fig. **a** and **b**) and toward the ground state $|g\rangle$ for energy relaxation (Fig. **c** and **d**). The vector fields are obtained by paving the Bloch sphere with quantum states that evolve according to Eq. (2.45) for a duration dt such that $\Gamma_1 dt = \Gamma_\phi dt = 0.2$. Ellipsoids corresponding to the boundary of reachable states at times $\Gamma t = 0.2, 0.4, ..., 1.6$ (in blue) and $\Gamma t = 0.1, 0.3, ..., 1.8$ (in green) are represented in dashed lines.

2.4 CONCLUSION

This introduction chapter was dedicated to

- quantum electrodynamics with superconducting circuits with a detailed treatment of linear and non-linear oscillators and their practical implementation in cQED.
- the black-box quantization method and its use for designing experiments with specified parameter values thanks to finite-element simulations.
- the dynamics of open quantum systems with a comprehensive list of decoherence channels for a qubit.
- the basic quantum mechanics toolbox to work with qubits including the Bloch sphere representation, the notion of purity and entropy.

3

READOUT OF A SUPERCONDUCTING QUBIT

The quantum state of a system is usually encoded in a density matrix which refers to an observer's knowledge about a system. More precisely, it is the knowledge that the observer has about the outcome of future measurements on this system conditioned on their observation and we will see that observers with different knowledge may assign simultaneously different density matrices to a single system. This apparent paradox is resolved when defining properly the crucial quantum operation performed by the observer when measuring a quantum system. In this chapter, we aim at clarifying this procedure and apply it to the measurement of the transmon qubit introduced in the previous chapter. Another consequence of these statements is that when performing repeated or continuous measurements, obtaining information on the system necessarily changes the state of the system in time depending on the measurement outputs. This is know as the *quantum back-action* of the measurement. For standard readout, we average a large number of realizations and this genuinely quantum effect vanishes. A detailed study of the back action of continuous quantum measurement in the framework of single *quantum trajectories* is the subject of chapter 6 and we will here focus on different kinds of tomography protocols.

Measuring the state of a qubit is a fundamental operation of quantum physics that is still actively developed in circuit-QED. The duration and fidelity of qubit readout are of critical importance for quantum information processing. The fidelity of algorithms, which reuse qubits after measurement or apply feedback based on the measurement results are limited by readout performances [94, 71]. Most *quantum non-demolition* readout schemes in circuit QED are currently based on dispersive interaction [19]. Optimizing the parameters of the system with the addition of Purcell filters [95] leads to state-of-the-art fidelities as high as 99.2% in 88 ns [96, 97]. However, this approach is intrinsically limited since increasing the power of the readout pulse induces unwanted transitions preventing one from increasing significantly the fidelity of the measurement [98, 99]. Other measurement paradigm are readily available such as the readout by a bistable system [100, 101] or the so-called *High power readout* developed by Reed *et al.* [102], whose mechanism is still the subject of intense research [103, 104, 105]. Very recently Touzard *et al.* [106] proposed a novel readout technique by engineering an on-demand 'longitudinal coupling' with a cavity that would implement a fast and selective QND readout while minimizing decoherence effects. In this chapter, we do not aim to reach record-breaking fidelities. Instead, we present the physical mechanisms of two different kind of detections namely the usual dispersive readout and the fluorescence tomography. We implement them together to obtain the first implementation of a *gate-free full quantum tomography* of a qubit.

First, we recall a quantum measurement theory that goes beyond the Von Neumann projective measurement by introducing an intermediate *ancilla* or *probe* system. We take this formalism to the continuous time limit that describes our experiments. We

then apply this formalism to the *dispersive* readout of an atom via a coupled electromagnetic field and study the decoherence induced by probing the state of the qubit. The spontaneously fluoresced field of a spin-1/2 detected by an *heterodyne* apparatus fits in this formalism as well and it can be used as an alternative readout technique that amounts to take the place of the environment in which the system relaxes. Finally, we propose a novel readout method combining the two previous techniques that grants a direct access to the Bloch vector by raw averaging. All these concepts are explained by the formalism developed herein below.

3.1 MEASURING A QUANTUM SYSTEM

3.1.1 *Generalized measurement*

In textbook quantum mechanics [107, 66], we learn that the measurement of an observable[1] A leads to the collapse of the system into an eigenstate of A and the observer learns the corresponding eigenvalue a referred to as the *measurement outcome*. The quantum state prior to the measurement is ρ. We detect a with probability $p_a = \mathrm{Tr}(\Pi_a \rho)$ where Π_a is the projection operator[2] over the eigen-space associated to a. Immediately after the measurement, the density matrix conditioned on the outcome reads

$$\rho_a = \frac{\Pi_a \rho \Pi_a}{p_a} = \frac{\Pi_a \rho \Pi_a}{\mathrm{Tr}(\Pi_a \rho)}. \tag{3.1}$$

This process is known as a *Von Neumann* measurement. A first striking feature is that the transformation between ρ and ρ_a in Eq. (3.1) is non linear because of the normalisation coefficient that ensures that the process is trace preserving as opposed to the linear Hamiltonian and Lindbladian evolutions. Futhermore, the value of the density matrix is instantaneously updated to ρ_a with an evolution infinitely sharp in time so the system cannot evolve because of other causes during the measurement process and the information is transferred to the observer instantaneously as well[3].

Projective measurements are not the most general measurements possible on a quantum system and in general they are inadequate to describe actual measurements done in the lab. We introduce the concept of *generalized measurement* that is modeled by a unitary evolution of a total system composed of the studied physical system coupled to an *ancillary* or *probe* system (electromagnetic field, atoms, ...) followed by a Von Neumann measurement of the probe [108]. In order to formulate such a measurement paradigm we first assume that the system and the ancilla start in an initial separable pure state[4]. The density matrix of the total system is

$$\rho_{S+P} = \rho \otimes |\theta_P\rangle \langle\theta_P| \tag{3.2}$$

Let us denote by $U_{S,P}$ the unitary evolution of the system and ancilla during the measurement caused by the interaction between S and P and $O = I_S \otimes (\sum_\mu \lambda_\mu \Pi_\mu)$

1 An observable is a self-adjoint operator. In virtue of the spectral theorem, it can be diagonalized in an orthonormal basis and its eigenvalues are real numbers.

2 Π_a is not necessarily a rank-1 operator as the eigenvalues of A can be degenerate.

3 This can be a relativity issue if the observer and system do not occupy the exact same spatial position.

4 This is also possible to generalize further to the case where the meter is not initially in a pure state [44].

the final Von Neumann measurement of the probe with possible outcomes $\{\lambda_\mu\}_\mu$. We define here $\Pi_\mu = |\lambda_\mu\rangle\langle\lambda_\mu|$ as rank-1 operators so the λ's may be degenerate. We define the measurement operator M_μ as the operation on the system state resulting from the unitary evolution and the measurement of the probe in state $|\lambda_\mu\rangle$ i.e.

$$M_\mu = \langle\lambda_\mu| U_{S,P} |\theta_P\rangle \tag{3.3}$$

In this case, the probe yields the outcome λ_μ with an occurrence probability

$$p_\mu = \mathrm{Tr}\left((I_S \otimes \lambda_\mu\Pi_\mu)U_{S,P}(\rho \otimes |\theta_P\rangle\langle\theta_P|)U_{S,P}^\dagger(I_S \otimes \lambda_\mu\Pi_\mu)\right) = \mathrm{Tr}(M_\mu\rho M_\mu^\dagger) \tag{3.4}$$

After the measurement the conditional state of the system reads

$$\boxed{\rho_\mu = \frac{M_\mu\rho M_\mu^\dagger}{p_\mu} = \frac{M_\mu\rho M_\mu^\dagger}{\mathrm{Tr}(M_\mu\rho M_\mu^\dagger)}.} \tag{3.5}$$

This last equation is of the same form as Eq. (3.1) but the important difference is that the $\{M_\mu\}$ are no longer projectors but arbitrary operators called *measurement operators*. The operators $\{M_\mu^\dagger M_\mu\}$ are hermitian and positive and they form a *Positive Operator Valued Measure* (POVM). The occurence probability of outcome λ_μ is $p_\mu = \mathrm{Tr}(M_\mu^\dagger M_\mu\rho)$ and a consequence of the definition (3.3) is that

$$\sum_\mu M_\mu^\dagger M_\mu = 1 \tag{3.6}$$

which ensures the normalisation of the measurement probabilities $\sum_\mu p_\mu = 1$. In the rest of the manuscript we indistinctly talk about set of *measurement operators* or set of *Kraus operators*. Kraus operators describe the action of any *quantum map* or any physical *super-operator*[5] by a relation of the form

$$\mathcal{L}(\rho) = \sum_\mu A_\mu\rho A_\mu^\dagger, \tag{3.7}$$

where the operators $\{A_\mu\}$ are called *Kraus operators*. An example of such a *quantum map* is the action of unread measurements on the state of the system. Indeed, the relation (3.5) describes the evolution of a quantum state conditioned on the measurement records and its physical consequences are discussed in section 6.1. When discarding the measurement outcomes, the state of the system enters a statistical mixture after measurement

$$\sum_\mu p_\mu\rho_\mu = \sum_\mu M_\mu\rho M_\mu^\dagger = \mathcal{L}(\rho), \tag{3.8}$$

which amounts to tracing out the degrees of freedom of the environment. We find an expression of the form of Eq. (3.7). The measurement operators $\{M_\mu\}$ are thus an example of Kraus operators but they are not unique.

Physically this unread measurement is lost information and it decreases the relative entropy between two quantum states that are more and more likely to look alike.

5 Mathematically, the quantum map has to be trace-preserving, completely positive and convex linear see [92].

Lindblad and Uhlmann [109] showed the monotonicity of relative entropy defined in Eq. (2.42) i.e. for two quantum states ρ and σ,

$$S(\mathcal{L}(\rho)||\mathcal{L}(\sigma)) \leq S(\rho||\sigma). \tag{3.9}$$

This description corresponds to the common understanding of *decoherence*. The environment 'watches' the system but the information is lost for the observer and its density matrix - that only contains their knowledge on the state of the system - loses its distinguishability.

3.1.2 *Continuous measurement*

We will now apply the previous results to the continuous evolution of a quantum system between t and $t+dt$ where dt is a short time step compared to any other time scale of the problem. We use the set of assumptions exposed in section 2.1.3 namely we assume that the environment is Markovian and that the time scale hierarchy $\tau_E \ll dt \ll T_H$ is respected where τ_E is the correlation time of the bath and T_H is time scale of evolution of the observables of the system [66]. In this limit, it is possible to show that a single measurement operator is of order unity[6]

$$M_0 = \mathbb{1} - \frac{i}{\hbar} H dt - J dt \tag{3.10}$$

where H and J are Hermitian. Because of the normalisation condition $\sum_\mu M_\mu^\dagger M_\mu = 1$ are at best of order $\sqrt{dt}$ and we can write

$$\begin{cases} M_\mu = \sqrt{dt} L_\mu \text{ (for } \mu \neq 0) \\ \text{with } J = \dfrac{1}{2} \displaystyle\sum_{\mu \neq 0} L_\mu^\dagger L_\mu \end{cases} . \tag{3.11}$$

with the *jump operators* $\{L_\mu\}$ of order unity.

The meaning of the Kraus operators can be understood by examining a simple physical situation. Let us consider an excited qubit that spontaneously relaxes by emitting a propagating electromagnetic wave packet. The environment is modeled as a collection of photocounters. There are two Kraus operators in this case, M_0 for which no click was detected at all during dt and M_1 for which a click was recorded. Observing no click during dt leads to an evolution of the form $\frac{M_0 \rho M_0^\dagger}{\mathrm{Tr}(M_0 \rho M_0^\dagger)}$ which corresponds to the application of the Hamiltonian H concurrently with J that ensures the normalisation of the Kraus operators. The absence of a click during dt is an *information* on the energy state of the qubit whose state is updated by the operator J. When a click is recorded, the state of the system evolve according to $\frac{M_1 \rho M_1^\dagger}{\mathrm{Tr}(M_1 \rho M_1^\dagger)}$ that projects the state of the system in the ground state.

In the continuous time limit, the case of unread measurements (3.7) becomes

$$\rho_{t+dt} = \mathcal{L}(\rho_t) = \sum_\mu M_\mu \rho_t M_\mu^\dagger. \tag{3.12}$$

6 It is always possible to perform a unitary evolution of the system-apparatus so as to get a single operator M_0 of order unity

which becomes the so-called Lindblad equation with Eq. (3.10) and (3.11)

$$\boxed{\frac{d\rho_t}{dt} = -\frac{i}{\hbar}[H, \rho_t] + \sum_\mu \mathcal{D}[L_\mu]\rho_t} \tag{3.13}$$

with the Lindblad superopertator $\mathcal{D}[L](\rho_t) = L\rho_t L^\dagger - \frac{1}{2}\{L^\dagger L, \rho_t\}$. We see that the formalism above not only gives a more general definition of a quantum measurement but it also gives an interpretation of decoherence as unread measurements performed by the environment leading to a Lindbladian evolution. The formalism enables us to predict the system state conditioned on the measurement as will be show in section 6.1. The *records* read [110]

$$\boxed{y_\mu(t)dt = \sqrt{\eta}\mathrm{Tr}(L_\mu\rho + \rho L_\mu^\dagger)dt + dW_\mu(t).} \tag{3.14}$$

In this expression $dW_\mu(t)$ is a *Wiener process* accounting for noise, which includes the irreducible quantum fluctuations of the signal. It satisfies

$$\boxed{\begin{cases} \mathbb{E}[dW_\mu(t)] = 0 \\ dW_\mu(t)^2 = dt \end{cases}.} \tag{3.15}$$

Because of this Wiener process, the measured outcomes are random and updating our knowledge on the system creates a 'random kick' on the density matrix. The quantum state undergoes a non trivial stochastic evolution but the experimentalist can use the measurement outcomes to reconstruct a posteriori the evolution of the system and avoid the decrease of relative entropy associated to the case of unread measurement. To do so, the stochastic master equation is used and it is the subject of chapter 6. For now, we are going to apply this formalism to understand the dispersive measurement of a cavity coupled to a transmon for qubit state tomography.

3.2 DISPERSIVE READOUT

3.2.1 *Homodyne detection of the cavity field*

We call *homodyne detection* the measurement of one quadrature of an oscillating signal that can be performed by demodulating that signal with a standard oscillation of exactly the same frequency that can be produced by a *local oscillator* (LO). This technique is very general with applications ranging from direct-conversion radio receiver to quantum optics [111] and it can be understood in classical physics as the multiplication of a signal $s(t) = I(t)\cos(\omega_s t) + Q(t)\sin(\omega_s t)$ with slow varying quadratures $I(t)$ and $Q(t)$ by a tone $A\cos(\omega_{\mathrm{LO}} t + \phi)$ produced by the local oscillator with $\omega_s = \omega_{\mathrm{LO}}$. By filtering out the fast oscillating components, the resulting signal is $\frac{AI}{2}\cos(\phi) + \frac{AQ}{2}\sin(\phi)$ so by varying the phase of the local oscillator, one can choose the measured quadrature. In the microwave domain, the homodyne detection is performed using a commercial mixer (represented on Fig. 3.1**a**). A microwave source provides both the carrier frequency of the signal and the LO to minimize relative phase fluctuation of the two signals and the signal is digitized by an acquisition board[7].

7 see appendix B for details on the experimental techniques.

The signal that we detect is coming from our quantum system in cavity. The Hamiltonian (2.32) of the qubit-cavity device in the dispersive regime can be rewritten

$$\hat{H} = \hbar\frac{\omega_q}{2}\sigma_z + \hbar(\omega_c - \chi\frac{\sigma_z}{2})\hat{a}_c^\dagger\hat{a}_c \tag{3.16}$$

so the interaction term can be seen as a qubit-state dependent frequency of the cavity $\omega_c^g = \omega_c + \chi/2$ and $\omega_c^e = \omega_c - \chi/2$. When probing the state of the cavity at the center frequency ω_c, the input signal acquires a phase shift $\pm\theta/2$ as it is transmitted through the cavity that depends on the state of the qubit (Fig. 3.1**c**), this is known as *dispersive readout* [112, 19]. The information on the state of the system is thus encoded in the phase of the propagating signal a_{out}.

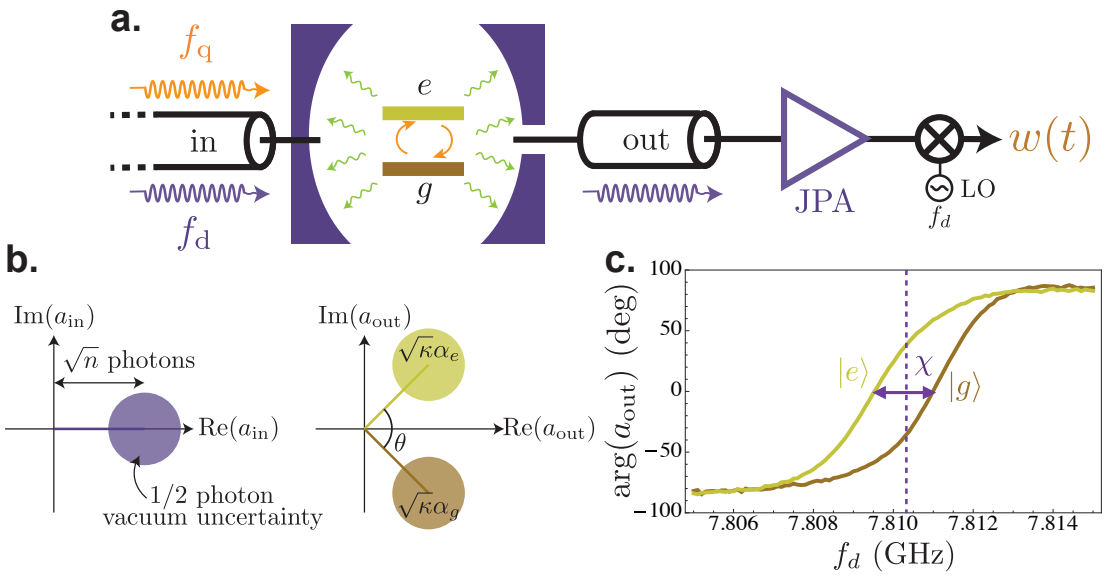

Figure 3.1: **a.** Schematics of the measurement setup for the homodyne detection of a dispersively coupled electromagnetic field. Microwave light at frequency f_d close to f_c is sent at the input of the cavity. The field interacts with the qubit according to Hamiltonian (3.16) and the signal is amplified by a *Josephson parametric amplifier* (JPA), routed out of the refrigerator and detected by mixing it with a *local oscillator* (LO) before digitization. **b.** Fresnel plane representation of the signal in a plane rotating at f_c. On the left, the signal at the input of the system is represented. The input field is a *displaced vacuum field* or *coherent field* generated by a classical microwave source represented by a distribution (circle) caused by irreducible quantum fluctuations. On the right, the outgoing signal is represented. The initial field acquired a phase shift $+\theta/2$ if the qubit is in $|e\rangle$ and $-\theta/2$ if the qubit is in $|g\rangle$ according to Eq. (3.18). Note that this representation is valid only if the system is probed at f_c. Formally, the Gaussian distributions are the Wigner functions of the field. **c.** Measured phase of the transmitted signal $a_{\text{out}}$when the qubit is in $|g\rangle$ (brown) or $|e\rangle$ (yellow) as a function of probe frequency f_d. The central frequency of the cavity is displaced as $\omega_c \to \omega_c + \chi/2$ for a qubit in the ground state and as $\omega_c \to \omega_c - \chi/2$ for a qubit in the excited state.

More quantitatively, Gambetta *et al.* have shown in a seminal paper [113] that the field inside the driven cavity evolves depending on the qubit state according to the first order equations

$$\begin{cases} \dfrac{d\alpha_g(t)}{dt} = i(\omega_d - \omega_c - \dfrac{\chi}{2})\alpha_g(t) - \dfrac{\kappa}{2}\alpha_g(t) + \epsilon_d \\ \dfrac{d\alpha_e(t)}{dt} = i(\omega_d - \omega_c + \dfrac{\chi}{2})\alpha_e(t) - \dfrac{\kappa}{2}\alpha_e(t) + \epsilon_d \end{cases} . \tag{3.17}$$

Here κ is the decay rate of the cavity, χ is the cavity pull and ϵ_d is the drive strength. The steady state values of the field are obtained by canceling the left side of (3.17)

$$\alpha_g = \frac{2\epsilon_d}{\kappa + i\chi - 2i(\omega_d - \omega_c)} \quad \text{and} \quad \alpha_e = \frac{2\epsilon_d}{\kappa - i\chi - 2i(\omega_d - \omega_c)} \tag{3.18}$$

In transmission, the output field is related to the intra cavity field by $\langle a_{\text{out}} \rangle = \sqrt{\kappa_{\text{out}}} \langle a \rangle$ where κ_{out} is the damping rate of the cavity mode through the output port. In our setup, the decay rate of the cavity is dominated by its coupling to the output port so $\kappa_{\text{out}} \simeq \kappa$. The two corresponding outgoing field amplitudes are represented on Fig 3.1**b** when the cavity is in a steady state. By detecting $\text{Im}(a_{\text{out}})$ we can reveal the information on the energy of the qubit and conversely the quadrature $\text{Re}(a_{\text{out}})$ does not depend on the qubit state, an homodyne detection is thus well-suited. We use a home made quantum-limited *phase-preserving amplifier* called *Josephson parametric amplifier* (JPA in Fig 3.1**a**) that amplifies the quadrature of interest at the expense of the other quadrature[8] followed by commercial amplifiers that are not represented on the figure for simplicity.

By using the measurement theory developed hereabove, the continuous time measurement record reads [44]

$$w(t)dt = \sqrt{\eta_d} \langle 2\text{Im}(a_{\text{out}}) \rangle \, dt + dW_w(t) \tag{3.19}$$

where $\eta_d = 34\%$ is the measurement efficiency of the detection setup. By assuming that the cavity field reached the steady state and that $\omega_d = \omega_c$, we can express

$$\langle 2\text{Im}(a_{\text{out}}) \rangle = \sqrt{\kappa} \langle 2\text{Im}(a) \rangle = \sqrt{\kappa} \langle \sigma_z \rangle \frac{\alpha_e - \alpha_g}{i} = 2 \langle \sigma_z \rangle \sqrt{\frac{\kappa n \chi^2}{\kappa^2 + \chi^2}} \tag{3.20}$$

where $n = \frac{4|\epsilon_d|^2}{\kappa^2 + \chi^2}$ is the average number of photon stored in the cavity. The signal to noise ratio (SNR) of the measurement record (3.19) during dt is defined as

$$\text{SNR}(dt) = \left(\frac{\sqrt{\eta_d} \langle 2\text{Im}(a_{\text{out}}) \rangle \, dt}{dW_w(t)} \right)^2 = \eta_d \kappa |\alpha_e - \alpha_g|^2 \langle \sigma_z \rangle^2 \, dt \tag{3.21}$$

since $dW_w(t)^2 = dt$. The measurement rate Γ_m can be defined as half the signal to noise ratio per unit of time when $\langle \sigma_z \rangle = \pm 1$

$$\Gamma_m = \frac{\text{SNR}(t)}{2t} = \frac{\eta_d \kappa}{2} |\alpha_e - \alpha_g|^2 = \frac{2\eta_d n \kappa \chi^2}{\kappa^2 + \chi^2} \tag{3.22}$$

8 See chapter 5 for a complete description of this amplifier.

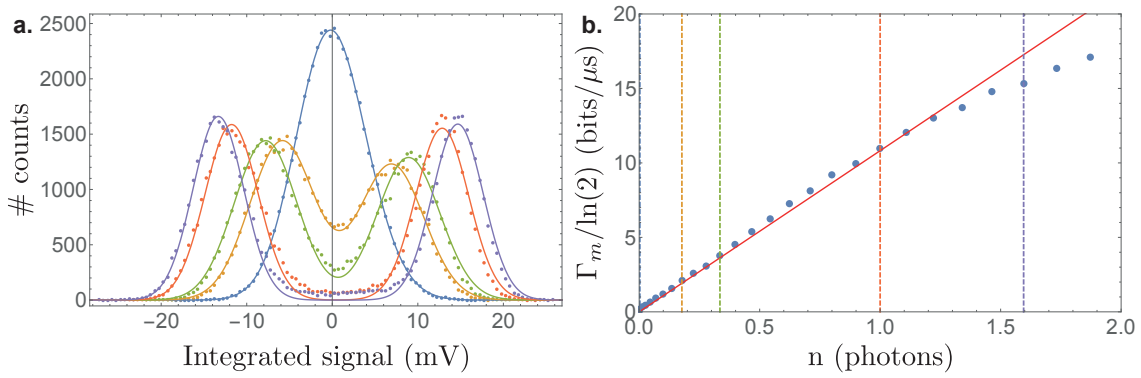

Figure 3.2: **a.** Histograms of 5×10^4 integrated measurement records $\alpha \int_0^T w(t)dt$ for various numbers of photons n indicated by the colors. The photon numbers are reported as dashed lines in **b**. The integration time is $T = 1$ μs and α is a proportionality constant in mV that depends on the detection setup. The qubit is initialized in $(|g\rangle + |e\rangle)/\sqrt{2}$ and we observe the progressive separation of two peaks corresponding to the qubit in either $|g\rangle$ or $|e\rangle$. Their width is given by the combined effect of zero-point fluctuations and the noise added by the detection setup. If the two peaks do not overlap, the spin state is projected and the measurement is *strong*. When the two peaks overlap, the experimentalist cannot distinguish between $|g\rangle$ and $|e\rangle$ and the measurement is *weak*. **b.** Number of bits of information gained on the qubit state by unit of time as a function of the stationary number of photons stored in the cavity. We observe a linear dependence of Γ_m in the number of photons n in agreement with Eq. (3.22) up to ~ 1.5 photons. Beyond this number, the JPA placed after the cavity (see Fig. 3.1) becomes non-linear because the high photon flux at the amplifier input 'exhausts' the pump.

The scale factor 2 is arbitrary in (3.22), this particular choice is motivated because as defined $\Gamma_m/\ln(2)$ is the number of bits of information gained from the measurement per unit of time [114] (see Fig. 3.2**b**).

The measurement record thus takes the form

$$\boxed{w(t)dt = \sqrt{2\Gamma_m}\,\langle\sigma_Z\rangle\,dt + dW_w(t),} \tag{3.23}$$

which exactly corresponds to (6.29) with a jump operator $L_w = \sqrt{\Gamma_d/2}\sigma_z$ with $\Gamma_m = \eta_d\Gamma_d$. According to equation (3.22), the measurement rate can be varied by tuning the input power of the readout field a_{in} that changes the stationary number of photon n in the cavity. In Fig 3.2 are represented histograms of the integrated output signal $\int_0^T w(t)dt$ for an increasing stationary number of photons in the cavity. When the two distributions in Fig. 3.1 and 3.2 are well-separated, we can resolve the qubit state in a *single-shot* manner, that is in one realization of the experiment. In this case, we know if the qubit is in $|g\rangle$ or $|e\rangle$ and the qubit state is projected because we extract more than one bit of information during the measurement time T. The measurement is then said to be *strong*. By increasing Γ_m well above any other time scale of the system, we enter the *quantum jump* regime [115]. The measurement records are discontinuous in time because the qubit state 'jumps' between the two pointer state values $|g\rangle$ and $|e\rangle$ and any unitary departure from this point is suppressed by Zeno effect [116]. When the two distributions overlap, the qubit state is not projected onto $|e\rangle$ or $|g\rangle$, we talk about

weak measurement. However, the density matrix of the system is updated conditioned on the measurement outcome to take into account the non-projective 'kick' caused by the measurement.

Finally, we mention that this measurement scheme is routinely used in circuit QED to perform a quantum tomography of a qubit state. In Fig. 3.3, we prepare arbitrary pure states on the surface of the Bloch sphere by applying a pulse θ_ϕ on the qubit where $\theta \in [0, 2\pi]$ is the rotation angle of the unitary transformation and ϕ is the phase of the preparation pulse. We then perform a quantum tomography of each prepared state by measuring the qubit strongly after having mapped σ_x, σ_y or σ_z onto σ_z by a $\frac{\pi}{2}$ pulse. The measurement outputs span a sphere proving that any state on the Bloch surface can be faithfully extracted with this technique. Here, the fidelity of the tomography is $F = 98\%$ for an integration time of 2 μs.

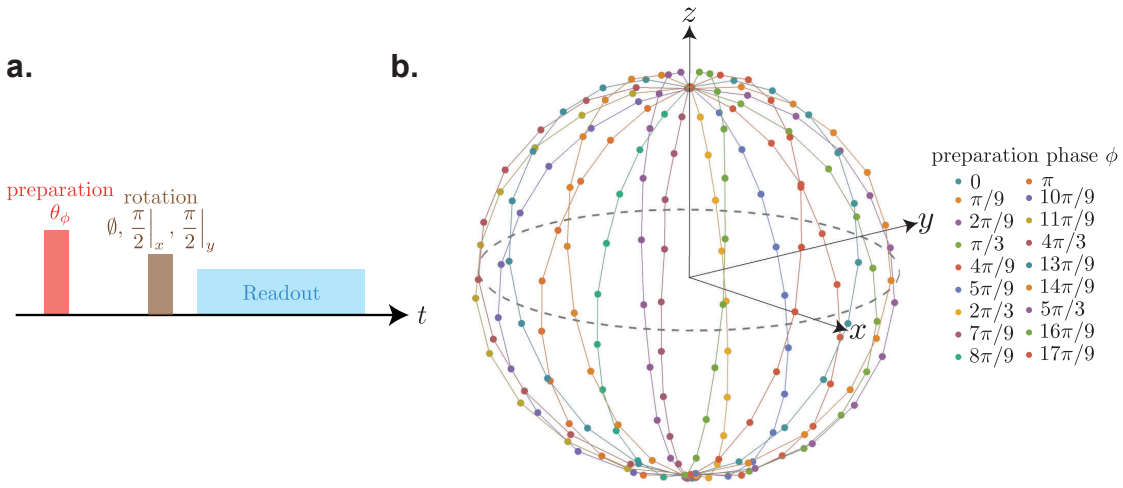

Figure 3.3: Quantum tomography by dispersive measurement **a.** Pulse sequence used for the measurement. We prepare the qubit with a pulse θ_ϕ with $\theta = k\pi/12$ for $k = 0, 1, ..., 11$ and $\phi = n\pi/9$ for $n = 0, 1, ...8$ and then perform a quantum tomography with a fast gate $\emptyset$, $\frac{\pi}{2}\big|_x$ or $\frac{\pi}{2}\big|_y$ followed by a strong dispersive readout of the cavity. **b.** The raw averaged measurement outputs given by the 3 rotations correspond to the three Bloch coordinates and they span a Bloch sphere when displayed in 3 dimensions.

3.2.2 *AC stark shift and measurement induced dephasing*

A direct measurable consequence of the dispersive interaction Hamiltonian is that increasing the average population of the cavity shifts the measured frequency of the qubit, this is known as the *AC Stark shift*. When driving the cavity with a coherent field at f_d close to f_c, the field produced in the cavity follows a Poisson statistics so the qubit frequency itself follows a Poisson statistics. The average density matrix of the qubit is the weighted mean of Bloch vectors rotating at different angular velocities $f_{q,n} = f_q - n\chi\hbar$. This loss of purity is dubbed *measurement induced dephasing*[9] because this effect can

9 This phenomenon originates from noise in the qubit frequency which matches the *photon shot noise*.

be seen as an unread measurement of the qubit state by the cavity field described by a quantum map of the form (3.12). In this section we give the expression of the frequency shift of the qubit and dephasing associated to this decoherence mechanism as a function of the drive parameters in the steady state regime.

In the case of unread measurements performed by the cavity, we can model the decoherence by the interaction Hamiltonian (3.16) and then trace out the electromagnetic field stored in the cavity. The resulting qubit dynamics is of the Lindblad form as shown at the beginning of this chapter with renormalized qubit frequency $\omega_q \to \omega + \omega_{\text{stark}}$ and a jump operator $L_\varphi = \sqrt{\Gamma_d/2}\sigma_z$. The Stark-shift frequency and measurement induced dephasing rate read [113]

$$\begin{cases} \Gamma_d(t) = \chi \text{Im}[\alpha_g^*(t)\alpha_e(t)] \\ \omega_{\text{stark}}(t) = \chi \text{Re}[\alpha_g^*(t)\alpha_e(t)] \end{cases} \tag{3.24}$$

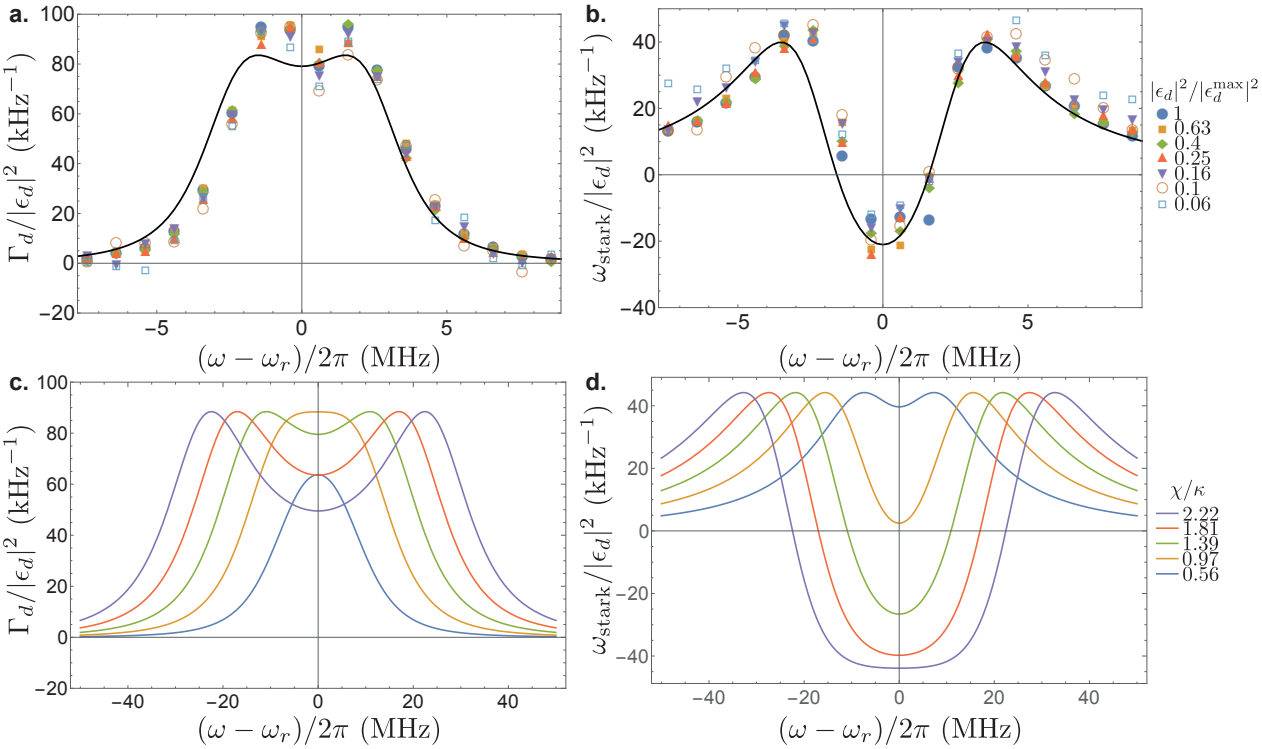

Figure 3.4: **a.** and **b.** Measured induced dephasing and Stark-shift as a function of the detuning between the probe and the cavity for various input powers. The dephasing rates are obtained by Ramsey interferometry in the presence of an electromagnetic field that creates an extra dephasing and a frequency shift. We normalize the measurement rate and Stark-shift by the relative dimensionless power of the input drive $|\epsilon_d|^2$ to show the validity of Eq. (3.25) up to $\epsilon_d^{\max} = 40$ MHz^2. We superimpose a theoretical curve in black given by Eq. (3.25) with independently measured parameters $\chi = 2\pi \times 4.9$ MHz and $\kappa = 2\pi \times 3.6$ MHz. **c.** and **d.** Numerical simulations of the Stark-shift and dephasing rate given by Eq. (3.25) for various χ/κ ratios ranging from 0.56 to 2.22 and $\kappa = 2\pi \times 3.6$ MHz. Note also that the Stark shift can become negative for some χ/κ ratios.

In the steady state regime, we can use Eq. (3.18) and we obtain the explicit expressions

$$\begin{cases} \Gamma_d = -\dfrac{8\kappa\chi^2|\epsilon_d|^2}{(\kappa^2+4(\omega_d-\omega_c)^2-\chi^2)^2+4\chi^2\kappa^2} \\ \omega_{\text{stark}} = \dfrac{4\chi|\epsilon_d|^2\left(\kappa^2+4(\omega_d-\omega_c)^2-\chi^2\right)}{(\kappa^2+4(\omega_d-\omega_c)^2-\chi^2)^2+4\chi^2\kappa^2} \end{cases} \tag{3.25}$$

These frequencies are measured by performing a Ramsey interferometry experiment with a populated cavity. We prepare the qubit in the $(|g\rangle+|e\rangle)/\sqrt{2}$ superposition with a $\pi/2$ detuned pulse, wait for a given amount of time and then readout the cavity just after a fast $\pi/2$ rotation. We observe an exponentially decaying oscillation with a decay rate $\Gamma_d+\Gamma_2$ and the frequency allows a precise measurement of $\omega+\omega_{\text{stark}}$. We performed such a measurement for a range of drive frequencies and input powers gathered in Fig. 3.4. Another important remark is that we use these measurements to calibrate the attenuation of the line and convert an input power at the input of the dilution refrigerator in dBm into a number of photons[10] $n=\frac{\kappa^2+\chi^2}{2\kappa\chi^2}\Gamma_d$ in the cavity as shown in Fig. 3.2. We can thus prepare a coherent field containing on average a 'fraction' of a photon in the cavity with our system with a predictable frequency shift and coherence time reduction for the qubit.

3.3 MEASUREMENT OF FLUORESCENCE

3.3.1 *Heterodyne detection of the fluorescence of a qubit*

We call *heterodyne* detection, the simultaneous measurement of the two quadratures of an oscillating signal. It can be performed by down-conversion to a lower frequency range (compatible with the bandwidth of the digitization boards) using the mixing with a tone produced by a *local oscillator* at a frequency close to the carrier frequency of the signal. Similarly to the homodyne detection, the heterodyne detection is widely used in signal processing and applications range from the celebrated superheterodyne radio receiver to current quantum optics experiments [111]. We propose here to collect the fluorescence of a spin-1/2 by heterodyne detection [117, 23].

In our experiments, qubit pulses are generated by a microwave source modulated at a few tens of MHz (typically 50 MHz, orange drive in Fig. 3.5), the spontaneous emission of the qubit is collected in the output port. The coupling rate of the input port of the cavity and the internal loss rate of the cavity are much smaller than the coupling rate to the output port of the cavity as depicted on Fig. 3.5. By doing so, we ensure that the large majority of the fluoresced field goes in the ouput port owing to Purcell effect. Indeed, coupling the cavity to a transmission line reduces the lifetime of the qubit (see chapter 2). It is also much more 'likely' that the qubit emits a photon in the output port than into the input port because of the coupling rate asymmetry.

10 It is important to understand that an external drives populate the cavity in a coherent state of average photon number n and not a Fock state with a perfectly defined number of photons.

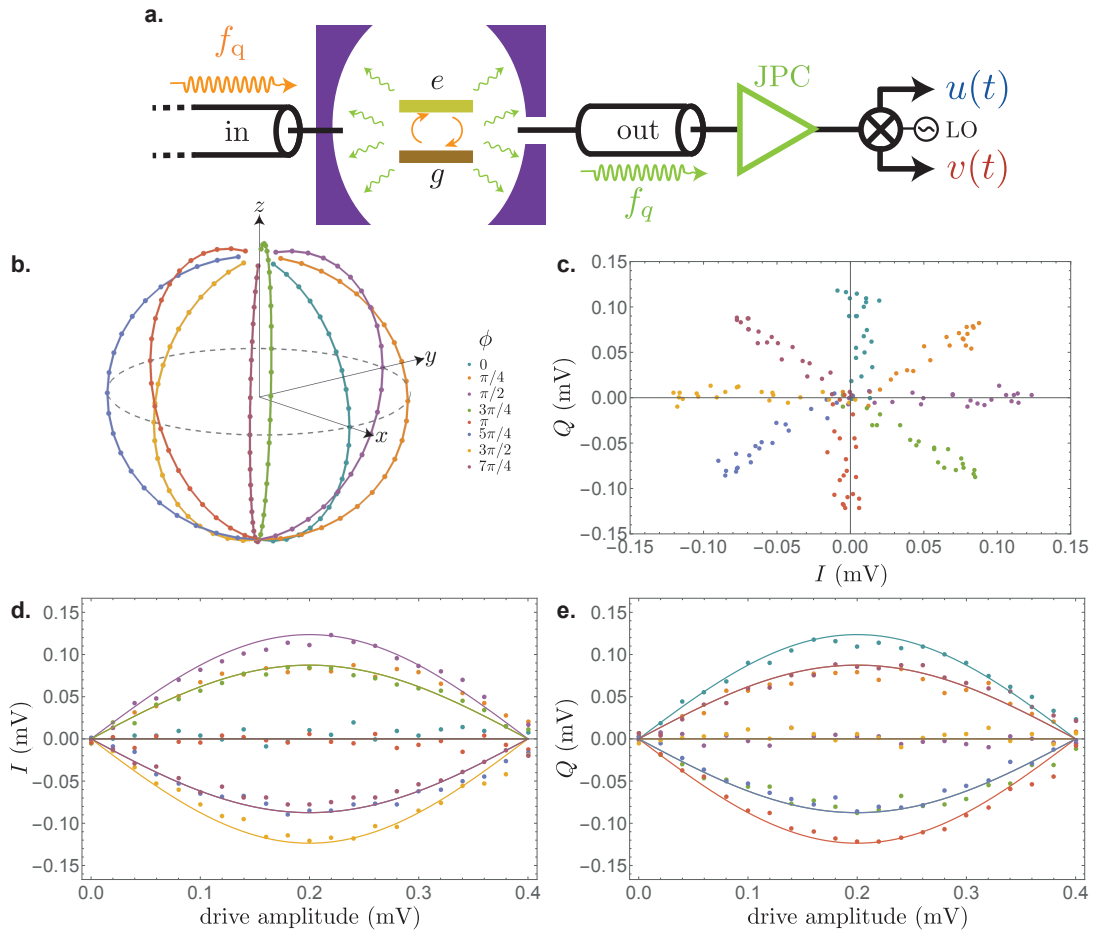

Figure 3.5: **a.** Schematics of the heterodyne detection of the fluorescence field emitted by an atom. We monitor the light emitted in the output port at f_q. The signal goes through the *Josephson parametric converter* (JPC) that amplifies both quadratures of the signal followed by commercial amplifiers (not represented in the figure). The signal is down-converted by mixing with a *local oscillator* detuned of a few tens of MHz from f_q and before digitization and numerical demodulation. The two extracted measurement records dubbed u and v are given by Eq. (3.26). **b.** Bloch sphere representation of the targeted states (theory). We span the Bloch sphere with a pulse θ_ϕ pulse where θ is proportional to the drive amplitude and $\phi = 0, \pi/4, \pi/2, ..., 7\,\pi/4$ is the phase of the pulse indicated by the color. **c.** Average on 10^6 realization of the integrated quadratures $I \propto \int_0^T u(t)dt$ and $Q \propto \int_0^T v(t)dt$ for $T = 2\ \mu$s for every prepared state of **b**. According to Eq. (3.26), the integrated records reveal $\langle\sigma_x\rangle$ and $\langle\sigma_y\rangle$ up to a prefactor. This IQ plane representation is thus a projection of the Bloch sphere in the $x - y$ plane. **d.** and **e.** Average integrated quadratures as a function of drive amplitude at f_q. The drive amplitude is proportional to the angle θ of the pulse. The solid lines correspond to the solid lines of **b**.

The signal is then amplified by a *phase-preserving* amplifier named *Josephson parametric converter* (JPC)[11]. In this process the phase of the signal is preserved by amplification and we detect both observables $\mathrm{Re}(a_{\mathrm{out}})$ and $\mathrm{Im}(a_{\mathrm{out}})$ associated with the two quadratures[12] The amplified field is mixed with the signal of the same microwave source that is used to generate the carrier of the input drive to avoid phase drifts. The resulting signal is a low frequency field oscillating at 50 MHz that is digitized with an acquisition board and numerically demodulated to recover the I and Q quadratures.

In this case, the system is probed by the vacuum fluctuations of the electromagnetic fields that can be viewed as triggering the emission of photons by the atom. So we can apply the generalized measurement theory (6.29) with two jump operators $L_u = \sqrt{\Gamma_\downarrow/2}\sigma_-$ and $L_v = iL_u$ corresponding to the two detected quadratures [85] where $\Gamma_\downarrow$ is the de-excitation rate of the qubit and $\sigma_- = (\sigma_x - i\sigma_y)/2$ is the lowering operator of the qubit. The measurement records read

$$\boxed{\begin{cases} u(t)dt = \sqrt{\eta_f \Gamma_\downarrow/2}\,\langle\sigma_x\rangle\, dt + dW_u(t) \\ v(t)dt = \sqrt{\eta_f \Gamma_\downarrow/2}\,\langle\sigma_y\rangle\, dt + dW_v(t) \end{cases}} \tag{3.26}$$

where $\eta_f = 14$ % is the efficiency of the detection setup. Similarly to the homodyne detection, we can define a signal to noise ratio and the measurement rate of the fluorescence detection.

We show the integrated signals $\int u(t)dt$ and $\int v(t)dt$ during $T = 2$ μs in Fig. 3.5 of an undriven qubit relaxing after a θ_ϕ preparation pulse for various θ and ϕ. As can be seen, this detection technique leads to the x and y Bloch coordinates of the qubit state. However the measurement rate associated to this tomography is set by the relaxation rate of the artificial atom $\Gamma_\downarrow = 50 - 100$ kHz (variable from one run to the other). It is not tunable *in situ* in contrast with the dispersive readout.

3.3.2 *Destructive and QND measurements*

In this section, we introduce the concepts of *destructive* measurement as opposed to *quantum non-demolition* measurement (QND). A QND measurement intuitively means that we are able to probe a quantum state without 'destroying' it [66]. For instance, when one photon is detected in a transmission line by heterodyne detection or by photocounting the state of the wave packet carrying the photon is not projected, it is altogether 'demolished'. Instead of erasing the entire information on the state of the system, a QND measurement projects the state of the system in one of the pointer states of the measurement and thus preserving information for subsequent quantum operations. A second key ingredient of the definition is that two successive strong QND measurements should yield the same outcome. In the case of Von Neumann measurement a second measurement of the same observable immediately after the first

11 See chapter 5 for a detailed description of this amplifier.

12 The two quadratures $\mathrm{Re}(a)$ and $\mathrm{Im}(a)$ of a quantum electromagnetic field do not commute. Pleasingly, on top of amplifying the signal the JPC mixes the quadratures with an extra *idler* mode that transforms the quadratures of the field in a set of commuting observables [26] at the price of adding an extra noise to the signal corresponding to the zero-point fluctuations of this idler mode.

projection leads to the same outcome[13]. In the generalized measurement formalism, a sufficient condition for QND measurement is that the interaction Hamiltonian between the probe and the system commutes with the projector operator of the Von Neumann measurement performed on the probe [66]. But it is not necessary.

In the case of the dispersive interaction, information on the state of the qubit is imprinted in the phase of the electromagnetic field without destroying the state of the qubit. For large values[14] of Γ_d, the measurement is repeatable and the state of the system is projected in $|g\rangle$ or $|e\rangle$, which are the pointer states of the measurement. This process is thus QND even if the interaction Hamiltonian $\sigma_z \hat{a}^\dagger \hat{a}$ does not commute with the measured observable $\mathrm{Im}(\hat{a} + \hat{a}^\dagger)$.

In the case of energy relaxation, one photon is emitted at the frequency of the qubit and we detect it by heterodyne detection. The interaction Hamiltonian and the measured observables do not commute either. In this case the measurement erases the information on the quantum state by reseting the qubit in its ground state. In the strong measurement limit *i.e.* $\Gamma_\downarrow$ much larger than any other inverse time scale, the measurement has two possible outcomes corresponding to qubit having relaxed in its ground state after emitting one photon or no photons were emitted. The measurement cannot be repeated immediately after the emission of a photon without re-excitation of the qubit preventing this process to be a *QND* measurement. Lastly, we note that we monitor the expectation value of the operator σ_- which is not an observable[15]. The fact that we are not 'measuring' an observable of the system can be understood by the open nature of the system and in this case the quantum state of the system is converted into a propagating photon whose detection 'destroys' the state of the qubit.

3.4 FULL QUANTUM TOMOGRAPHY

In this section, we propose a novel detection setup combining the two previous ones. As we saw an heterodyne monitoring of the spontaneous emission of an atom divulges information on its $\langle\sigma_x\rangle$ and $\langle\sigma_y\rangle$ components while an homodyne monitoring of the cavity in the dispersive regime reveals information on $\langle\sigma_z\rangle$. First, we show that performing the two detections concurrently over a large number of realizations amounts to imaging the Bloch vector. This technique is then used to monitor Rabi oscillations in the presence of decoherence and our method is validated by comparison with the solution of Lindblad equation. Finally, we compare the fidelity of this quantum tomography with the usual tomography protocol obtained from successive strong measurements of x,y and z components of the qubit.

3.4.1 *Direct access to the Bloch vector*

In the actual detection setup, we combine the two previous measurements[16] (see Fig. 3.6). The spontaneous emission is at the frequency of the qubit $f_q \simeq 5.3$ GHz while the

13 This not the case if we let the system evolve or relax between the two measurements.
14 Much larger than any other time scale of the system.
15 In particular, it is not Hermitian $\sigma_-^\dagger = \sigma_+ = (\sigma_x + i\sigma_y)/2$.
16 We can retrieve any of the previous situations by discarding the outputs of one of the detector.

dispersive readout is at the frequency of the cavity $f_c \simeq 7.8$ GHz. The two signals are spatially separated by a commercial frequency diplexer TIGER TGF-A4214-001 placed in the output line[17] (see Fig. 3.6). The signal is then routed out of the fridge via two detection setups described in the previous sections namely two quantum limited amplifiers are used to perfom an homodyne detection of the field at the frequency of the cavity and an heterodyne detection of the spontaneous emission at the frequency of the spin. The signal is then down-converted by mixing it with local oscillators before digitization and numerical demodulation.

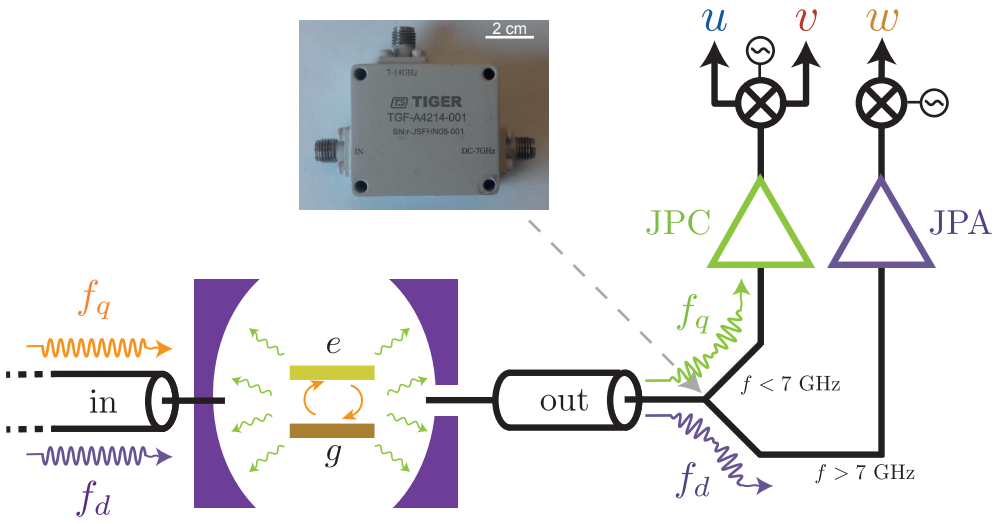

Figure 3.6: Schematics of the complete detection setup. We concurrently monitor the spontaneous emission of the atom at f_q (green) and we probe the state of the cavity at $f_d \simeq f_c$ (purple). The two signals are spatially separated based on their frequencies thanks to a commercial frequency diplexer. The complete measurement output is a vector (u, v, w) given by Eq. (3.27) and its raw average scaled by the appropriate prefactors is directly the Bloch vector (x, y, z). This method enables us to perform a complete quantum tomography of the system without performing any gate on the system.

We obtain simultaneously three measurement records

$$\boxed{\begin{cases} u(t)dt = \sqrt{\eta_f \Gamma_\downarrow/2}\,\langle\sigma_x\rangle\,dt + dW_u(t) \\ v(t)dt = \sqrt{\eta_f \Gamma_\downarrow/2}\,\langle\sigma_y\rangle\,dt + dW_v(t)\,\cdot \\ w(t)dt = \sqrt{2\eta_d \Gamma_d}\,\langle\sigma_Z\rangle\,dt + dW_w(t) \end{cases}} \tag{3.27}$$

17 This is a key ingredient of our detection setup. It is in principle possible to replace the diplexer by a beam splitter but by doing so we would lose 'half of the signal' resulting in halving the detection efficiencies.

A simple raw averaging provides a full quantum tomography of the system according to

$$\begin{pmatrix} x(t) \\ y(t) \\ z(t) \end{pmatrix} = \begin{pmatrix} \bar{u}(t)/\sqrt{\eta_f \Gamma_1/2} \\ \bar{v}(t)/\sqrt{\eta_f \Gamma_1/2} \\ \bar{w}(t)/\sqrt{2\eta_d \Gamma_d} \end{pmatrix} \tag{3.28}$$

where $\bar{\cdot}$ denotes the average over many realizations of the experiments. In order to obtain the Bloch vector, the two prefactors $\sqrt{\eta_f \Gamma_1/2}$ and $\sqrt{2\eta_d \Gamma_d}$ must be determined. The rates $\Gamma_1 \sim (15\ \mu\text{s})^{-1}$ and Γ_d are respectively inferred from energy relaxation measurement and Ramsey oscillations in the presence of a populated cavity (see section 3.2.2). The quantum efficiency η_f and η_d are obtained by SNR estimation or by reckoning the back-action of the measurement[18]. In the actual experiments, the signal is integrated during time steps $dt = 100$ ns and the records are amplified and filtered by the detection chains[19] so that we obtain $(\alpha u, \alpha v, \beta w)$ where α and β are the amplitude gains of the two chains. These scaling factors are precisely measured by looking at the amplitude of Rabi oscillations[20]. We can thus image the Bloch vector in time without performing any quantum gates on the system in contrast with the usual tomography protocol of Fig. 3.3. This 'gate free' tomography is robust to any systematic errors on pulse calibration and relies instead on the estimation of the normalization constant of the chains.

In the following section, we confirm the validity of this readout technique in the case of Rabi oscillation in the presence of decoherence by comparing the raw average of the measurement records with the prediction of Lindblad equation.

3.4.2 *Tomography of a qubit undergoing Rabi oscillations*

In this experiment, the qubit is initialized in its thermal state close to the ground state with an excitation probability of 2%. We apply a microwave drive on the device at the frequency of the qubit, which acts as a driving torque of amplitude Ω around the σ_Y axis. We use the detection setup of Fig. 3.6 to observe the dynamics of the system in the presence of weak decoherence (see Fig. 3.7).

The evolution of the state of the system is predicted by Lindblad equation

$$\frac{d\rho_t}{dt} = i[\frac{\Omega}{2}\sigma_y, \rho_t] + \frac{\Gamma_\text{d} + \Gamma_\varphi}{2}\mathcal{D}[\sigma_z](\rho_t) + \Gamma_\downarrow \mathcal{D}[\sigma_-](\rho_t) + \Gamma_\uparrow \mathcal{D}[\sigma_+](\rho_t) \tag{3.29}$$

where $\Gamma_\uparrow = \frac{1+z_\text{th}}{2}\Gamma_1 \simeq 0.75$ ms is the thermal excitation rate of the qubit, $\mathcal{D}[L](\rho) = L\rho L^\dagger - \frac{1}{2}(\rho L^\dagger L + L^\dagger L \rho)$ is the Lindblad super-operator, $z_\text{th} = -0.96$ is the z component of the qubit at equilibrium and $\Gamma_\downarrow = \frac{1-z_\text{th}}{2}\Gamma_1 \simeq \Gamma_1 = (15\ \mu\text{s})^{-1}$ is the decay rate of the qubit. The dephasing rates $\Gamma_d = (5.0\ \mu\text{s})^{-1}$ and $\Gamma_\varphi = (17.9\ \mu\text{s})^{-1}$ are respectively the measurement induced dephasing rate and the pure dephasing rate. For an initial state

18 See chapter 6.

19 In this chapter we make sure that dt is much smaller than any evolution and relaxation rate of the system. We also take it greater than the inverse bandwidth of the amplifiers to avoid any time filtering of the signal by finite bandwidth of the JPA and JPC.

20 They can be equivalently inferred from noise correlations, see chapter 6 for details.

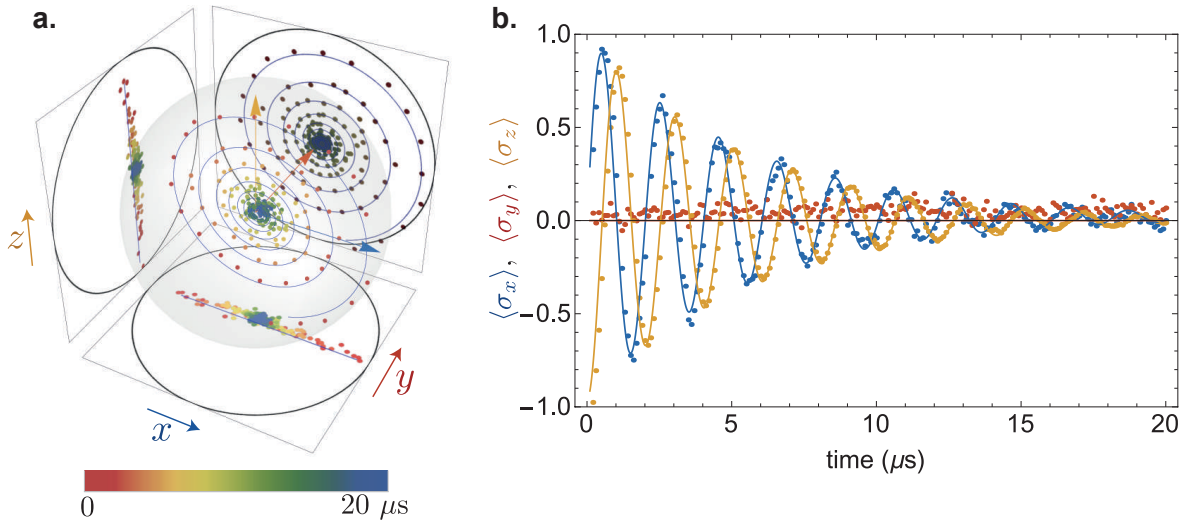

Figure 3.7: Dynamics of a qubit undergoing a Rabi oscillation around the y axis from a thermal state with 2% of excitation probability. The dots are the full quantum tomography on the system obtained by raw averaging the measurement records given in Eq. (3.28). The solid lines correspond to solutions of Eq. (3.29) with the parameters $\Gamma_1 = (15\ \mu\text{s})^{-1}$, $\Gamma_\phi = (17.9\ \mu\text{s})^{-1}$, $\Gamma_d = (5.0\ \mu\text{s})^{-1}$ and $\Omega/2\pi = (2\ \mu\text{s})^{-1}$ determined by independent projective measurements. **a.** Bloch sphere representation of the evolution of the density matrix of the system. The color of the dots encodes the evolution time $0 < t < 20\ \mu$s. **b.** Projections along the axes of the Bloch sphere as a function of time, the color now encodes the axis of the projection. We observe a good agreement between the continuous tomography and the solution of Lindblad equation.

$\rho_0 = \frac{1}{2}(\mathbf{1} + x_0\sigma_x + z_0\sigma_z)$, the time evolution of the component of the Bloch vector is confined in the $x - z$ plane and its components read

$$\begin{cases} x(t) = x_{\text{inf}} + e^{-(3\Gamma_1+2\Gamma_\varphi+2\Gamma_\text{d})\frac{t}{4}}[(x_0 - x_{\text{inf}})(\cos(\nu t) + \sin(\nu t)\dfrac{\Gamma_1 - 2\Gamma_\varphi - 2\Gamma_\text{d}}{4\nu} + (z_0 - z_{\text{inf}})\dfrac{\sin(\nu t)\Omega}{\nu}] \\ z(t) = z_{\text{inf}} + e^{-(3\Gamma_1+2\Gamma_\varphi+2\Gamma_\text{d})\frac{t}{4}}[(z_0 - z_{\text{inf}})(\cos(\nu t) - \sin(\nu t)\dfrac{\Gamma_1 - 2\Gamma_\varphi - 2\Gamma_\text{d}}{4\Omega}) - (x_0 - x_{\text{inf}})\dfrac{\sin(\nu t)}{\nu}\Omega], \end{cases} \tag{3.30}$$

where rotation speed in the Bloch sphere around σ_y is given by $\nu = \sqrt{\Omega^2 - \frac{(\Gamma_1 - 2\Gamma_\varphi - 2\Gamma_\text{d})^2}{16}}$ and the quantum state converges toward

$$x_{\text{inf}} = \frac{2z_{\text{th}}\Omega\Gamma_1}{\Gamma_1(\Gamma_1 + 2\Gamma_\varphi + 2\Gamma_\text{d}) + 2\Omega^2} \qquad z_{\text{inf}} = \frac{z_{\text{th}}\Gamma_1(\Gamma_1 + 2\Gamma_\varphi + 2\Gamma_\text{d})}{\Gamma_1(\Gamma_1 + 2\Gamma_\varphi + 2\Gamma_\text{d}) + 2\Omega^2} \tag{3.31}$$

in the long time limit.

As depicted in Fig. 3.7, because of decoherence the state of the system experiences under-damped oscillation toward the center of the Bloch sphere which is the *maximally mixed* state or *most entropic* state of the Bloch sphere. This damping is caused by the fact that we lose a part of our knowledge on the state of the system with time resulting in an increase of the entropy of the system. A good agreement between our tomography and the solution of the Lindblad equation is found in Fig. 3.7 proving the validity of our tomography. However it is interesting to compare the effectiveness of our tomography with the usual tomography based on strong measurements.

3.4.3 *Comparing the fidelities of a weak and projective quantum tomography*

Our tomography protocol is a direct averaging of the measurement records (u, v, w) on a large number of experiments N. Our tomography protocol highly differs from the usual technique that consists in measuring the three components of the qubit in separate experiments by projective measurements and it is thus interesting to compare the effectiveness of the two methods.

For the case of projective tomography, let us assume that we are able to measure any axis of the bloch sphere with a fast and single-shot readout of fidelity $F = 1$. After $3N$ measurements, the probability distributions of the measurement records are given by a binomial distribution of $+1$ and -1 and the variance of the estimated Bloch coordinates are $\mathrm{Var}(\langle\sigma_x\rangle_{\mathrm{estimated}}) = \frac{1-x^2}{N}$, $\mathrm{Var}(\langle\sigma_y\rangle_{\mathrm{estimated}}) = \frac{1-y^2}{N}$ and $\mathrm{Var}(\langle\sigma_z\rangle_{\mathrm{estimated}}) = \frac{1-z^2}{N}$. Three million experiments are thus needed to estimate an arbitrary state with a standard deviation lower than 10^{-3}. For our detection setup, the measurement records integrated during a time dt are given by Eq. (3.27). In the limit of a large number N of experiments $\mathrm{Var}(\langle\sigma_x\rangle_{\mathrm{estimated}}) = \mathrm{Var}(\langle\sigma_y\rangle_{\mathrm{estimated}}) = \frac{2}{N\eta_f\Gamma_1 dt}$ and $\mathrm{Var}(\langle\sigma_z\rangle_{\mathrm{estimated}}) = \frac{1}{2N\eta_d\Gamma_{\mathrm{d}}dt}$. Thus, with the parameters of Fig. 3.7, 2×10^9 experiments are needed to estimate an arbitrary state with a standard deviation lower than 10^{-3}. For these parameters, our method is much slower than the standard tomography to reconstruct a density matrix at least for the small integration time $dt = 100$ ns chosen in our experiment.

Nevertheless, the average evolution of a quantum state evolving in time can only be accessed by doing a set of quantum tomography at successive time steps. In Fig. 3.7, there are 198 time steps so reconstructing the evolution of the state of the qubit by projective tomography would require 6×10^8 experiments while 2×10^9 experiments are still required for tomography based on weak measurements. The signal to noise ratio of the tomography based on weak measurements is thus independent on the number of successive tomography and it becomes favorable in order to reconstruct lengthy evolution of a qubit. More precisely, our method becomes more effective when reconstructing more than 660 successive time steps. Alternatively, increasing the integration time dt to higher values is straightforward with our setup[21] and the variance of the outcomes is reduced as $1/dt$. There is trade-off between the SNR of the measurement during a single time-step and the number of time-step required to resolve the dynamics of the qubit.

Moreover, the convergence of the result of the projective tomography depends on the state of the qubit and the variances of the signal vanish when the quantum state is in a pointer state of the measured observable. The reconstruction of the time evolution of an oscillating qubit thus leads to a time varying uncertainty on the quantum state for a given number of realizations with the usual method. On the other hand, in the case of weak tomography, the variance of the measurement records is independent of the state of the system so our technique provides a uniform signal to noise ratio regardless of the state of the system.

21 Note that the expression of the records (3.27) is only valid in the small dt regime. One has to integrate this expression to obtain the measurement outcomes integrated over time-scales that are not negligible compared to the characteristic time of evolution of the system.

Finally, we assumed that the fidelity of the strong measurement is $F = 1$ but in practice is it often limited by the fidelity of the readout process as well as the fidelity of the quantum gates. With our qubit parameters, even 100 ns long gates have a fidelity lower than 99 % because of the large dephasing on the qubit[22]. Our method does not rely on any quantum gates and therefore avoids this limitation.

3.5 CONCLUSION

In this chapter we demonstrated

- a general theory for quantum measurement in continuous time limit with Kraus operators.
- the readout of a superconducting qubit by dispersive measurement both for weak measurement and tomography with the unavoidable decoherence associated to the photon shot-noise of the cavity.
- the monitoring of the fluorescence field spontaneously emitted by an atom.
- a measurement scheme combining the monitoring of the two above mentioned decoherence channels allowing for a continuous full quantum tomography of the qubit by direct raw averaging.

22 This rough estimation only takes into account Γ_φ which is the fastest decoherence mechanism in our experiment.

4

QUTRITS

4.1 INTRODUCTION

As we saw in chapter 2 the transmon hosts about 10 levels inside the cosine potential so the quantum physicist is not restricted to the first two levels of the artificial atom to store information and manipulate quantum states. This section is dedicated to the coherent manipulation and readout of a three level system.

Morse code is based on a three letter alphabet: dashed, dot and space. This encoding was widely used with the advent of the telegraph but modern communications use binary signals. The quantum equivalent of Morse code is quantum communication with three-state systems dubbed *qutrits*. A very good level of control was achieved with superconducting qutrits [118, 119] suggesting qutrits as a building block to achieve universal quantum computation [120]. Moreover, they are useful in communication protocols such as quantum key distribution [121] and they are known to be more robust to certain class of eavesdropping attacks [122]. Besides, they are routinely used in the superconducting circuits community to shape the temporal profile of single photons [123], to implement a quantum random generator [124] or to realize geometric phases [125]. More broadly, multi level systems have many applications including the simplification of quantum gates [126, 127, 119], the simulation and investigation of quantum chaos [128] or even for metrology [129].

4.2 PREPARATION OF AN ARBITRARY QUANTUM SUPERPOSITION OF THREE LEVELS

If we go back to the BBQ formalism explained in section 2.2.1, we can write the Hamiltonian of a transmon coupled to a cavity

$$\hat{H} = \hbar\tilde{\omega}_c \hat{a}_c^\dagger \hat{a}_c + \hbar\tilde{\omega}_t \hat{a}_t^\dagger \hat{a}_t - E_J \cos_4(\varphi_t(\hat{a}_t + \hat{a}_t^\dagger) + \varphi_c(\hat{a}_c + \hat{a}_c^\dagger)) \tag{4.1}$$

where $\cos_4(x) = \cos(x) - 1 + \frac{x^2}{2}$, $\hat{a}_c$ and $\hat{a}_c$ (resp. $\hat{a}_t$ and $\hat{a}^\dagger$) are the annihilation and creation operators of the cavity (resp. transmon). In the case of small zero point fluctuation amplitudes $\varphi_t, \varphi_c \ll 1$, we can restrict the cosine expansion to 4^{th} order. In the dispersive regime, the Hamiltonian of a qutrit dispersively coupled to a cavity reads

$$\boxed{\hat{H} = \hbar\omega_{01} |1\rangle\langle 1| + \hbar(\omega_{01} + \omega_{12}) |2\rangle\langle 2| - \hbar\chi \sum_{i=0}^{3} i |i\rangle\langle i| \hat{a}_c^\dagger \hat{a}_c} \tag{4.2}$$

where we denote by $|0\rangle$, $|1\rangle$, $|2\rangle$[1] the quantum states corresponding to a well defined number of excitations in the transmon. The frequency of the $g \leftrightarrow e$ qubit transition is

1 We equivalently use the notation $|0\rangle$, $|1\rangle$, $|2\rangle$ or $|g\rangle$, $|e\rangle$, $|f\rangle$ throughout this chapter.

$\omega_{01} = \omega_q$, the frequency of the $1 \leftrightarrow 2$ transition is $\omega_{12} = \omega_q - \alpha$ with α the anharmonicity and χ is the cavity pull[2].

The addition of a drive on the system results in a driven Hamiltonian of the form

$$H_{\text{drive}} = \epsilon_{01} |0\rangle \langle 1| + \epsilon_{01}^* |1\rangle \langle 0| + \epsilon_{12} |1\rangle \langle 2| + \epsilon_{12}^* |2\rangle \langle 1| + \epsilon_d \hat{a}_c + \epsilon_d^* \hat{a}_c^\dagger. \tag{4.3}$$

Under the rotating wave approximation, only one of these terms will be resonant. The first term is resonant when the pump is applied around the angular frequency ω_{01}, the second term is resonant when the pump is applied at ω_{12} and finally the last term is kept when the pumped is applied around ω_c. As we can see we cannot directly drive the $0 \leftrightarrow 2$ transition. This 'selection rule' comes from the truncation of the expansion of the cosine that only allows the conversion of one pump photon in one qubit excitation. A higher expansion allows to convert one pump photon into two qubit excitations by driving the system at $f_q - \alpha/2$ but it requires a much higher pump power[3]. In practice, we used 100 ns long gaussian pulses to implement qutrit gates. We denote the qutrit gates by $(\theta)_a^{ij}$ where $\theta \in [0, 2\pi[$ is the rotation angle of the unitary transformation, ij denotes the addressed transition and $a \in \{x, -x, y, -y\}$ denotes the phase of the pulse. For instance, $\left(\frac{\pi}{2}\right)_x^{01}$ denotes a $\pi/2$ pulse around the x axis applied to the $0 \leftrightarrow 1$ transition. We now can easily compute the unitary transformation resulting in a sequence of pulses. Table 4.1 is a summary of the list of pulses used to prepare several different initial states starting with a qutrit in the ground state.

Targeted quantum state	Preparation pulse
$\frac{1}{\sqrt{3}}(\|g\rangle + \|e\rangle + \|f\rangle)$	$\left(\frac{\pi}{2}\right)_y^{12} \circ \left(2\arccos(\frac{1}{\sqrt{3}})\right)_y^{01}$
$\frac{1}{\sqrt{3}}(-\|g\rangle + \|e\rangle + \|f\rangle)$	$\left(\frac{\pi}{2}\right)_y^{12} \circ \left(-2\arccos(\frac{1}{\sqrt{3}})\right)_y^{01}$
$\frac{1}{\sqrt{3}}(\|g\rangle + \|e\rangle - \|f\rangle)$	$\left(-\frac{\pi}{2}\right)_y^{12} \circ \left(2\arccos(\frac{1}{\sqrt{3}})\right)_y^{01}$
$\frac{1}{\sqrt{3}}(\|g\rangle - \|e\rangle + \|f\rangle)$	$\left(-\frac{\pi}{2}\right)_y^{12} \circ \left(-2\arccos(\frac{1}{\sqrt{3}})\right)_y^{01}$
$\frac{1}{\sqrt{3}}(i\|g\rangle + \|e\rangle + \|f\rangle)$	$\left(\frac{\pi}{2}\right)_y^{12} \circ \left(2\arccos(\frac{1}{\sqrt{3}})\right)_x^{01}$
$\frac{1}{\sqrt{3}}(\|g\rangle + \|e\rangle + i\|f\rangle)$	$\left(-\frac{\pi}{2}\right)_x^{12} \circ \left(2\arccos(\frac{1}{\sqrt{3}})\right)_y^{01}$
$\frac{1}{\sqrt{3}}(\|g\rangle + i\|e\rangle + \|f\rangle)$	$\left(\frac{\pi}{2}\right)_x^{12} \circ \left(-2\arccos(\frac{1}{\sqrt{3}})\right)_x^{01}$

Table 4.1: List of pulses to prepare an arbitrary superposition of three levels, see text for notation details.

4.3 PROJECTIVE TOMOGRAPHY OF A THREE-LEVEL SYSTEM

This section is dedicated to the projective tomography of a three-level atom. Similarly to the qubit case, the dispersive interaction couples the qubit to the cavity and permits to

2 The cavity pull is the same for the two transition when expanding the cosine at 4^{th} order. Expanding it further reveals transition dependent cavity pull.

3 This actually extends to any order [105].

readout the energy state of the system. However it does not provide any information on the relative phases of a superposition of states. It is in principle possible to reconstruct the full density matrix of a quantum system by placing a complete set of independent quantum operations ahead of a dispersive readout pulse.

4.3.1 *From the measurement output to the density matrix*

The density matrix of a qutrit is a 3×3 matrix positive and self-adjoint matrix ρ of trace one. The state of the system is thus fully determined by 9 independent real numbers. Our tomography is achieved by 9 independent measurements with the set of following rotations prior to measurement

$$\mathbb{1}, \left(\frac{\pi}{2}\right)_x^{01}, \left(\frac{\pi}{2}\right)_y^{01}, \left(\frac{\pi}{2}\right)_x^{12}, \left(\frac{\pi}{2}\right)_y^{12}, \left(\frac{\pi}{2}\right)_x^{12}\left(\frac{\pi}{2}\right)_x^{01}, \left(\frac{\pi}{2}\right)_y^{12}\left(\frac{\pi}{2}\right)_x^{01}. \tag{4.4}$$

Other sets of pulses are possible [118] but we found this list to have the best fidelity with our measurement setup and to be the least sensitive to pulse calibration errors[4]. The tomography protocols give a list of 9 complex outputs $(s_1, ..., s_9)$. Each output s_i corresponds to pulse i in (4.4). We can decompose

$$s_i = c_{g,i}\alpha_g + c_{e,i}\alpha_e + c_{f,i}\alpha_f \tag{4.5}$$

with $c_{g,i}, c_{e,i}, c_{f,i} \geq 0$ and $c_{g,i} + c_{e,i} + c_{f,i} = 1$. The complex amplitudes $\alpha_g, \alpha_e, \alpha_f$ represent the coherent state of the cavity in steady state regime when the qutrit is prepared in $|g\rangle, |e\rangle, |f\rangle$. More quantitatively Gambetta *et al.* have shown [113] that in the frame rotating at $\omega_c - \chi$ the stationary coherent field inside the cavity reads

$$\begin{cases} \alpha_g = \dfrac{-i\epsilon_d}{\kappa/2 - i(\omega_c - \omega_r - \chi)} \\ \alpha_e = \dfrac{-i\epsilon_d}{\kappa/2 - i(\omega_c - \omega_r)} \\ \alpha_f = \dfrac{-i\epsilon_d}{\kappa/2 - i(\omega_c - \omega_r + \chi)} \end{cases} \tag{4.6}$$

where ϵ_d is the amplitude of the readout tone and ω_r its angular velocity. The complex amplitudes α_i's are represented in the quadrature plane in Fig. 4.1. Transmission signals of the cavity are also shown for the parameters of the experiment.

Simple arithmetic manipulations show that the density matrix of the qutrit ρ can be expressed in terms of the measurement outputs

$$\begin{cases} \rho_{11} = c_{g,1} \qquad \rho_{22} = c_{e,1} \qquad \rho_{33} = c_{f,1} \\ \rho_{12} = \rho_{21}^* = (c_{e,3} - c_{g,3})/2 - i(c_{g,2} - c_{e,2})/2 \\ \rho_{13} = \rho_{31}^* = (c_{e,6} - c_{f,6} + c_{f,4} - c_{e,4})/\sqrt{2} - i(c_{e,7} - c_{f,7} + c_{f,5} - c_{e,5})/\sqrt{2} \\ \rho_{23} = \rho_{32}^* = (c_{f,5} - c_{e,5})/2 - i(c_{e,4} - c_{f,4})/2 \end{cases} \tag{4.7}$$

where we assumed that $\rho_{ii} \in \mathbb{R}$ and $\rho_{ij} = \rho_{ji}^*$.

4 This is due to the symmetry of Eq. (4.7) that cancels out any systematic measurement error.

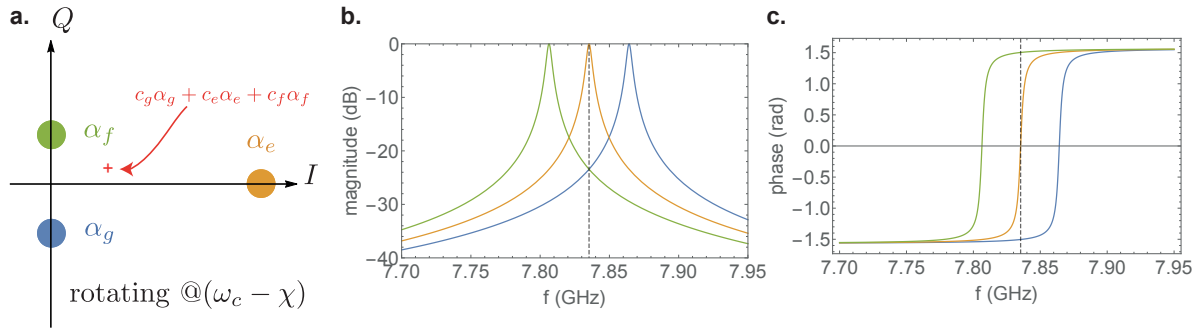

Figure 4.1: Readout signals given by (4.6) for the parameters of the experiment $\kappa = 3.9$ MHz and $\chi = 2\pi \times 4.6$ MHz. **a.** Quadrature plane representation of the signal. The complex amplitudes $\alpha_g, \alpha_e, \alpha_f$ correspond to the coherent fields populating the cavity when the qutrit is in the state $|g\rangle, |e\rangle, |f\rangle$. A red cross embodies a measurement record $s = c_g\alpha_g + c_e\alpha_e + c_f\alpha_f$. **b.** and **c.** Expected amplitude and phase of the transmitted signal through the cavity as a function of the frequency of the probe. The dashed line represents the measurement frequency of **a**.

4.3.2 *Representation of the density matrix of a qutrit*

In the case of a qutrit, there are no simple geometric representation such as the Bloch sphere for a qubit so we represent each element of the density matrix with a cylinder whose height and color encode the magnitude and phase of the tomographically reconstructed matrix element. Fig. 4.2 represents the density matrices obtained for an arbitrary list of prepared quantum states. We calculate the fidelity $F = \left[\mathrm{Tr}(\sqrt{\sqrt{\rho_T}\rho\sqrt{\rho_T}})\right]^2$ to the target state ρ_T. The fidelities shown in Fig. 4.2 are lower than 90 % because of a calibration error on the angle of the $(2\arccos(\frac{1}{\sqrt{3}}))^{01}$ pulses.

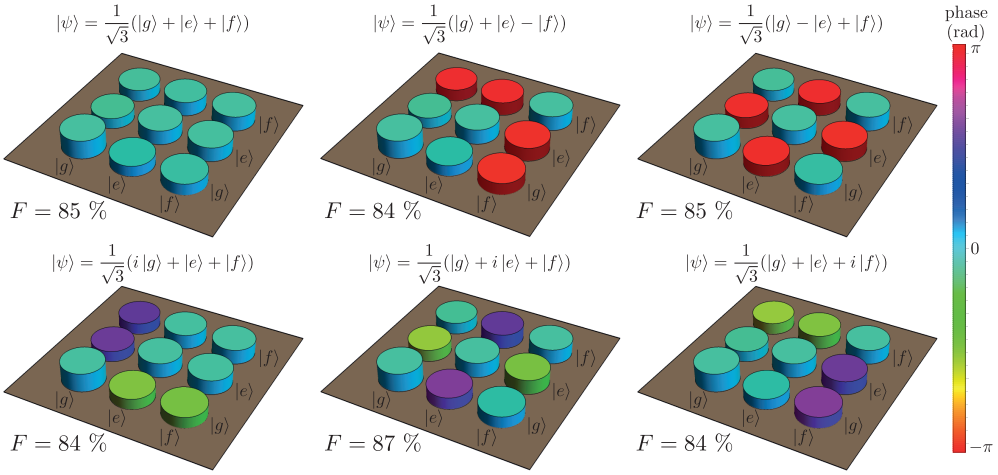

Figure 4.2: Tomography of a qutrit for several superposition of $|g\rangle$, $|e\rangle$ and $|f\rangle$. The height of the cylinders encodes the magnitude of the matrix elements, while the color encodes the phase of the superposition. We are able to prepare any desired state with an appropriate sequence of $0 \leftrightarrow 1$ and $1 \leftrightarrow 2$ pulses (see Table 4.1). The fidelity $F = \left[\mathrm{Tr}(\sqrt{\sqrt{\rho_T}\rho\sqrt{\rho_T}})\right]^2$ to the target state ρ_T is given on each panel. The fidelities are here limited by a pulse calibration error for this measurement.

The described projective tomography protocol can be used to track any operation on the qutrit. As an example we prepared a 'GEF' state $|\psi\rangle = (|g\rangle + |e\rangle + |f\rangle)/\sqrt{3}$ and we let it relax to the ground state of the transmon. The evolution of the density matrix over time can be visualized in Fig. 4.3.

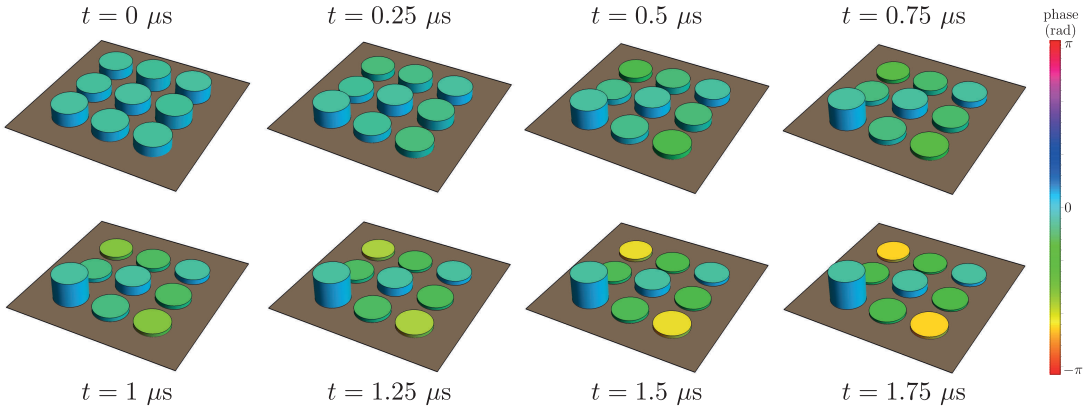

Figure 4.3: Tomography of the relaxation of a 'GEF' state. The qutrit is initialized in the $(|g\rangle + |e\rangle + |f\rangle)/\sqrt{3}$ state and a projective tomography is carried out every 250 ns after the preparation.

4.4 QUADRATURE PLANE CALIBRATION AND TEMPERATURE MEASUREMENT

In this section, we show how to calibrate the I, Q quadrature plane of the readout signal of a qutrit. This calibration is instrumental to convert the measured signal in milliVolts into the coefficients c_g, c_e, c_f in Eq. (4.5). We also give a simple protocol to estimate the temperature of a 3D transmon qubit thanks to the control of the third level.

4.4.1 *Calibration of the IQ plane*

In this run, we had a 'hot' transmon with an effective temperature of the order of 160 mK. The residual temperature of 3D transmons are commonly attributed to the coupling to unknown hot bath (phonons of the substrate, quasi-particles, ...) that randomly injects excitations in the transmon mode. This effect could be caused by a poor thermalisation of the substrate or of the complete device or by an irradiation of high frequency noise [130] routed by the microwave lines. Aluminum cavities usually have colder transmons than copper cavities and we noticed that by etching the inner surface of the cavity before placing it inside the fridge, the residual temperature population was reduced. The proposed method for the temperature measurement is very simple and efficient and it also gives an alternative way to measure gate fidelities for qubit and qutrit operations. At the end of the section, we compare this method with a 'direct' temperature measurement, which requires a single shot measurement with a good signal to noise ratio.

We cannot directly prepare a pure state $|g\rangle$ (resp. $|e\rangle$ or $|f\rangle$) and measure the corresponding cavity transmissions because of the initial temperature of the qubit and the

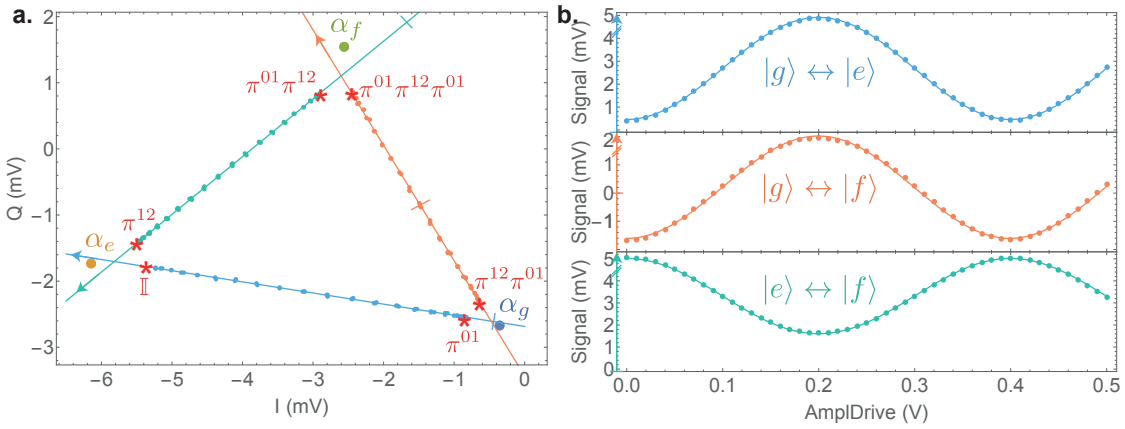

Figure 4.4: **a.** Determination of α_g, α_e and α_f. The 6 transmission amplitudes are indicated by red stars. The solution of the system (4.9) gives the values of α_g, α_e and α_f used for the tomography. We superimpose in blue, green and orange measured Rabi oscillations between the three levels of the qutrit along with linear interpolation (solid lines). **b.** Rabi oscillations as a function of drive amplitude between different levels projected along the lines drawn in **a**. The vertical axis origin matches the dash on each line in **a** and the arrow indicates the sign of the signal. The dots are the measured signal and the solid lines are sinusoidal fits. These Rabi oscillations are used to calibrate our qutrit gates.

finite fidelities of the gates. We measure transmissions of the cavity having prepared the qutrit in 6 different initial states with the following pulses

$$\mathbb{1},\ \pi^{01},\ \pi^{12}\circ\pi^{01},\ \pi^{12},\ \pi^{01}\circ\pi^{12},\ \pi^{01}\circ\pi^{12}\circ\pi^{01}. \tag{4.8}$$

The measurements are represented by red stars on Fig 4.4. We propose a simplified model to find the complex values of α_g, α_e and α_f that relies on the following assumptions

- We operate in a Hilbert space of dimension 3 namely $p_g + p_e + p_f = 1$ where p_i is the probability to find the qutrit in state $|i\rangle$ after a measurement. There is no leakage to states $|h\rangle$ or higher.
- The qutrit is initially in a thermal state ρ_{th} corresponding to a Boltzmann distribution with a well-defined temperature T.
- We model the finite fidelity of the π pulses of the transitions $0 \leftrightarrow 1$ and $1 \leftrightarrow 2$ by two numbers F and F'. The density matrix $\alpha\,|g\rangle\langle g| + \beta\,|e\rangle\langle e|$ becomes $(\beta F + (1-F)\alpha)\,|g\rangle\langle g| + (\alpha F + \beta(1-F))\,|e\rangle\langle e|$ after a π^{01} pulse of fidelity F. And similarly the density matrix $\alpha\,|e\rangle\langle e| + \beta\,|f\rangle\langle f|$ becomes $(\beta F' + (1-F')\alpha)\,|e\rangle\langle e| + (\alpha F' + \beta(1-F'))\,|f\rangle\langle f|$ after a π^{12} pulse of fidelity F'. We thus assume that there are no leakage to the $|f\rangle$ state during a π^{01} pulse and no leakage to the $|g\rangle$ state during a π^{12} pulse.

We then solve the following system of coupled equations for the complex transmission $(t_1, ..., t_6)$ corresponding to the pulses (4.8)

$$\begin{cases} t_1 = p_g\alpha_g + p_e\alpha_e + p_f\alpha_f \\ t_2 = (Fp_e + (1-F)p_g)\alpha_g + (Fp_g + (1-F)p_e)\alpha_e + p_f\alpha_f \\ t_3 = (Fp_e + (1-F)p_g)\alpha_g + (F'p_f + (1-F')(Fp_g + (1-F)p_e))\alpha_e \\ \quad + (F'(Fp_g + (1-F)p_e) + (1-F')p_f)\alpha_f \\ t_4 = p_g\alpha_g + (F'p_f + (1-F')p_e)\alpha_e + (F'p_e + (1-F')p_f)\alpha_f \\ t_5 = ((1-F)p_g + F(F'p_f + (1-F')p_e))\alpha_g + (Fp_g + (1-F)(F'p_f + (1-F')p_e))\alpha_e \\ \quad + (F'p_e + (1-F')p_f)\alpha_f \\ t_6 = (F(F'p_f + (1-F')(Fp_g + (1-F)p_e)) + (1-F)(Fp_e + (1-F)p_g))\alpha_g \\ \quad + (F(Fp_e + (1-F)p_g) + (1-F)(F'p_f + (1-F')(Fp_g + (1-F)p_e)))\alpha_e \\ \quad + (F'(Fp_g + (1-F)p_e) + (1-F')p_f)\alpha_f \end{cases} \tag{4.9}$$

where $p_g = \frac{1}{1+b+b^2}$, $p_e = \frac{b}{1+b+b^2}$ and $p_f = \frac{b^2}{1+b+b^2}$ with the Boltzmann weight $b = e^{-\hbar\omega_q/k_BT}$. The resolution of (4.9) gives us the values of α_g, α_e, α_f, the temperature T and the fidelities F and F'.

From the measurements shown in Fig. 4.4, we extract the fidelities $F = 95$ % for π^{01} pusles and $F' = 94$ % for π^{12} pulses. We also obtain an 8 % probability to find the qubit in the $|e\rangle$ state and 0.8 % probability to find the qubit in the $|f\rangle$ state, which corresponds to a qubit temperature of 160 mK. We thus demonstrated that our model allowed us to infer the value of α_g, α_e and α_f at rest. This calibration is essential to obtain the density matrix of the qutrit by a projective tomography (see previous section). A similar temperature measurement method was used to measure the efficiency of a cooling protocol known as the double drive reset of population (DDROP) [86] in our group [85].

4.4.2 *Direct temperature measurement*

In this section, we show that etching the inner surface of the cavity reduces the residual temperature of the transmon. We also use this opportunity to introduce a new temperature measurement based on a single-shot heterodyne measurement of the qubit in its thermal state at the frequency $f_c - \chi/2$ (see chapter 3). For this measurement the lifetime of the qubit was increased to $T_1 = 15$ μs and the cavity linewidth to $(\sim 70$ ns$)^{-1}$ by closing the output port of the cavity. We observe two separated probability distributions corresponding to the qubit in state $|g\rangle$ or $|e\rangle$. The probability to find the qubit in the excited state is given by the relative weight of the two distributions, which has to be measured in a time much longer than the inverse linewidth of the cavity and much shorter than the lifetime of the qubit.

From Fig 4.5, we extract the probability to find the qubit in the excited state $p_e \simeq 1.8$ % $\pm$ 0.2 % corresponding to an equilibrium with a bath at $T \simeq 63 \pm 2$ mK. We checked that the two temperature measurement methods give compatible results during the same experimental run. Recently *Serniak et al.* [131] discovered that quasiparticles

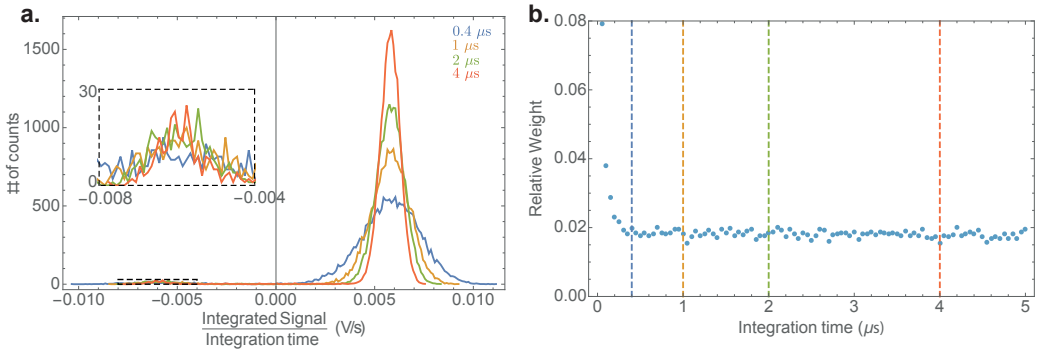

Figure 4.5: Measurement of the temperature of the qubit after etching the cavity (colder qubit temperature). **a.** A dispersive readout pulse is applied on the cavity and the in phase component of the signal is integrated for 0.4 μs (blue curve), 1 μs (yellow curve), 2 μs (green curve) and 4 μs (red curve). Two distinct probability distributions corresponding to the ground state (positive signal) and excited state (negative signal) can be distinguished. **b.** Owing to the finite relaxation time, the relative weight of the two distributions corresponds to the excitation probability only for integration times well below $T_1 = 15$ μs and well above both the inverse measurement rate $1/\Gamma_d = 0.025$ μs and the inverse cavity linewidth ~ 70 ns.

were for a good part responsible for a part of the thermal population of transmon but the generation mechanisms of non-equilibrium quasiparticles are not well understood yet.

4.5 OPEN-SYSTEM DYNAMICS OF A THREE-LEVEL ATOM

4.5.1 *Lindblad equation*

We can write a Lindblad equation for the qutrit

$$\frac{d\rho}{dt} = -\frac{i}{\hbar}[H, \rho] + \mathcal{L}(\rho) \tag{4.10}$$

where the Hamiltonian reads $H = \hbar\omega_{01} |1\rangle \langle 1| + \hbar(\omega_{01} + \omega_{12}) |2\rangle \langle 2|$ (plus a possible drive see Hamiltonian. (4.3)) and the Lindbladian reads

$$\mathcal{L}(\rho) = \sum_{i=1}^{6} \mathcal{D}_i(\rho). \tag{4.11}$$

The Lindblad super-operator[5] is $\mathcal{D}_i(\rho) = L_i \rho L_i^\dagger - \frac{1}{2} L_i^\dagger L_i \rho - \frac{1}{2} \rho L_i^\dagger L_i$ with the following jump operators $\{L_i\}_i$.

5 The Lindbladian of a qutrit can only take this form when the pure dephasing of the two transitions $0 \leftrightarrow 1$ and $1 \leftrightarrow 2$ are caused by uncorrelated frequency fluctuations. For a tunable transmon, unavoidable flux noise changes E_J resulting in correlated ω_{01} and ω_{12} fluctuations. In this case an extra term has to be added to the Lindbladian as explained by Li *et al* [132]. In the opposite case, the dephasing channels associated to L_5 and L_6 are not independent.

Symbol	Expression	Physical meaning
L_1	$\sqrt{\Gamma_{\downarrow}^{01}}\ \|0\rangle\langle 1\|$	spontaneous deexcitation $0 \to 1$
L_2	$\sqrt{\Gamma_{\uparrow}^{01}}\ \|1\rangle\langle 0\|$	spontaneous excitation $1 \to 0$
L_3	$\sqrt{\Gamma_{\downarrow}^{12}}\ \|1\rangle\langle 2\|$	spontaneous deexcitation $2 \to 1$
L_4	$\sqrt{\Gamma_{\uparrow}^{12}}\ \|2\rangle\langle 1\|$	spontaneous excitation $1 \to 2$
L_5	$\sqrt{\frac{\Gamma_{\phi}^{01}}{2}}\left(\|1\rangle\langle 1\| - \|0\rangle\langle 0\|\right)$	pure dephasing $0 \leftrightarrow 1$
L_6	$\sqrt{\frac{\Gamma_{\phi}^{12}}{2}}\left(\|2\rangle\langle 2\| - \|1\rangle\langle 1\|\right)$	pure dephasing $1 \leftrightarrow 2$

Table 4.2: List of jump operators of a qutrit. $\Gamma_{\uparrow(\downarrow)}^{ij}$ is the (de)excitation rate of the transition ij and Γ_{ϕ}^{ij} is the random AC Stark shift rate of transition ij, which can be modeled as fluctuations of ω_{ij}. We define the inverse lifetime of the $i \leftrightarrow j$ transition as $\Gamma_1^{ij} = \Gamma_{\downarrow}^{ij} + \Gamma_{\uparrow}^{ij}$.

From the expression of the jump operators 4.2, we can write the Lindbladian explicitly as follow

$$\mathcal{L}(\rho) = \frac{1}{2}\begin{pmatrix} 2(\Gamma_{\downarrow}^{01}\rho_{11} - \Gamma_{\uparrow}^{01}\rho_{00}) & -(\Gamma_{\downarrow}^{01}+\Gamma_{\uparrow}^{01}+\Gamma_{\uparrow}^{12}+2\Gamma_{\phi}^{01}+\Gamma_{\phi}^{12})\rho_{01} & -(\Gamma_{\uparrow}^{01}+\Gamma_{\downarrow}^{12}+\Gamma_{\phi}^{01}+\Gamma_{\phi}^{12})\rho_{02} \\ -(\Gamma_{\downarrow}^{01}+\Gamma_{\uparrow}^{01}+\Gamma_{\uparrow}^{12}+2\Gamma_{\phi}^{01}+\Gamma_{\phi}^{12})\rho_{10} & 2(\Gamma_{\uparrow}^{01}\rho_{00} - \Gamma_{\downarrow}^{01}\rho_{11}) + 2(\Gamma_{\downarrow}^{12}\rho_{22} - \Gamma_{\uparrow}^{12}\rho_{11}) & -(\Gamma_{\downarrow}^{01}+\Gamma_{\downarrow}^{12}+\Gamma_{\uparrow}^{12}+2\Gamma_{\phi}^{12}+\Gamma_{\phi}^{01})\rho_{12} \\ -(\Gamma_{\uparrow}^{01}+\Gamma_{\downarrow}^{12}+\Gamma_{\phi}^{01}+\Gamma_{\phi}^{12})\rho_{20} & -(\Gamma_{\downarrow}^{01}+\Gamma_{\downarrow}^{12}+\Gamma_{\uparrow}^{12}+2\Gamma_{\phi}^{12}+\Gamma_{\phi}^{01})\rho_{21} & 2(\Gamma_{\uparrow}^{12}\rho_{11} - \Gamma_{\downarrow}^{12}\rho_{22}) \end{pmatrix} \tag{4.12}$$

In the following section we will measure the different rates in 4.2 and check that the Eq. (4.10) indeed predicts the average evolution of the density matrix of the qutrit. Obviously the qubit case is recovered by setting all the relaxations rates Γ^{i2} and drives ϵ_{i2} to zero.

4.5.2 *Energy relaxation*

In this experiment, we first excite the qutrit with two successive drives at ω_{01} and ω_{12} (see Fig. 4.6) and we then monitor the evolution of the populations of the density matrix by tomographic reconstruction [118, 119]. The evolution of the populations reads

$$\begin{cases} \dfrac{d\rho_{00}}{dt} = \Gamma_{\downarrow}^{01}\rho_{11} - \Gamma_{\uparrow}^{01}\rho_{00} \\ \dfrac{d\rho_{11}}{dt} = \Gamma_{\uparrow}^{01}\rho_{00} - (\Gamma_{\downarrow}^{01} + \Gamma_{\uparrow}^{12})\rho_{11} + \Gamma_{\downarrow}^{12}\rho_{22} \\ \dfrac{d\rho_{22}}{dt} = \Gamma_{\uparrow}^{12}\rho_{11} - \Gamma_{\downarrow}^{12}\rho_{22} \end{cases} \tag{4.13}$$

This measurement allow us to extract the value of the matrix elements $(\Gamma_{\downarrow}^{01})^{-1} = (12 \pm 0.5)\ \mu$s and $(\Gamma_{\downarrow}^{12})^{-1} = (6 \pm 0.5)\ \mu$s as well as an estimation of the heating rates $(\Gamma_{\uparrow}^{01})^{-1} \sim 80\ \mu$s and $(\Gamma_{\uparrow}^{12})^{-1} > 100\ \ \mu$s. The heating rates can only be estimated asymptotically on time scales of the order of Γ^{-1} hence the previous estimation for this 30 μs long measurement (see previous sections for the temperature measurements with a good accuracy).

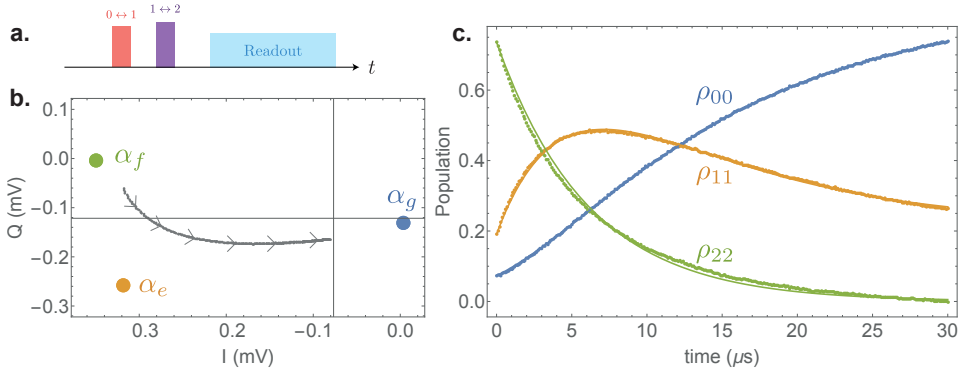

Figure 4.6: **a.** Pulse sequence. We successively excite the $0 \leftrightarrow 1$ and $1 \leftrightarrow 2$ transitions and then measure the population of the density matrix of the qubit by dispersive measurement. **b.** Raw signal in the IQ plane for 30 μs of relaxation. We observe a relaxation from α_f toward α_g. The line is curved in the direction of α_e because the matrix element $\Gamma_{\downarrow}^{02}$ is absent from (4.13). **c.** Extracted population as a function of time. The solid lines are the solution of Eq. (4.13).

4.5.3 *Ramsey experiments*

Similarly to the previous experiment we can realize any kind of experiment involving a unitary evolution and Lindbladian (4.12). By analogy with the qubit, we perfom Ramsey experiments [118, 119] between the two transitions by imprinting a rotation on the coherences of the density matrix. We initialized the qubit in a superposition of $|g\rangle$ and $|e\rangle$ (Fig. 4.7 **a**) or $|e\rangle$ and $|f\rangle$ (Fig. 4.7 **b**) and let the coherences of the density matrix rotate in order to measure the coherence times of the qutrit.

The Ramsey like experiments in Fig. 4.7 enable us to determine the decoherence times characterizing the qubit as well as the precise values of ω_{01} ans ω_{12} within an accuracy of few tens of kHz, which is below the typical fluctuation rate of transmon qubits. From Fig. 4.7, we extract the values of the coherence times of our qutrit $T_2^{01} = (\Gamma_{\downarrow}^{01} + \Gamma_{\uparrow}^{01} + \Gamma_{\uparrow}^{12} + 2\Gamma_{\phi}^{01} + \Gamma_{\phi}^{12})^{-1} = (10.0 \pm 0.2)$ μs and $T_2^{12} = (\Gamma_{\downarrow}^{01} + \Gamma_{\downarrow}^{12} + \Gamma_{\uparrow}^{12} + 2\Gamma_{\phi}^{12} + \Gamma_{\phi}^{01})^{-1} = (6.05 \pm 0.2)$ μs. Interestingly, we find that T_2^{01} (resp. T_2^{12}) has about the same value as T_1^{01} (resp. T_1^{12}) indicating that a quantum superposition of $|0\rangle$ and $|1\rangle$ (resp. $|1\rangle$ and $|2\rangle$) would decohere in twice this amount of time solely because of pure dephasing likely originating from residual thermal excitation of the cavity mode [133].

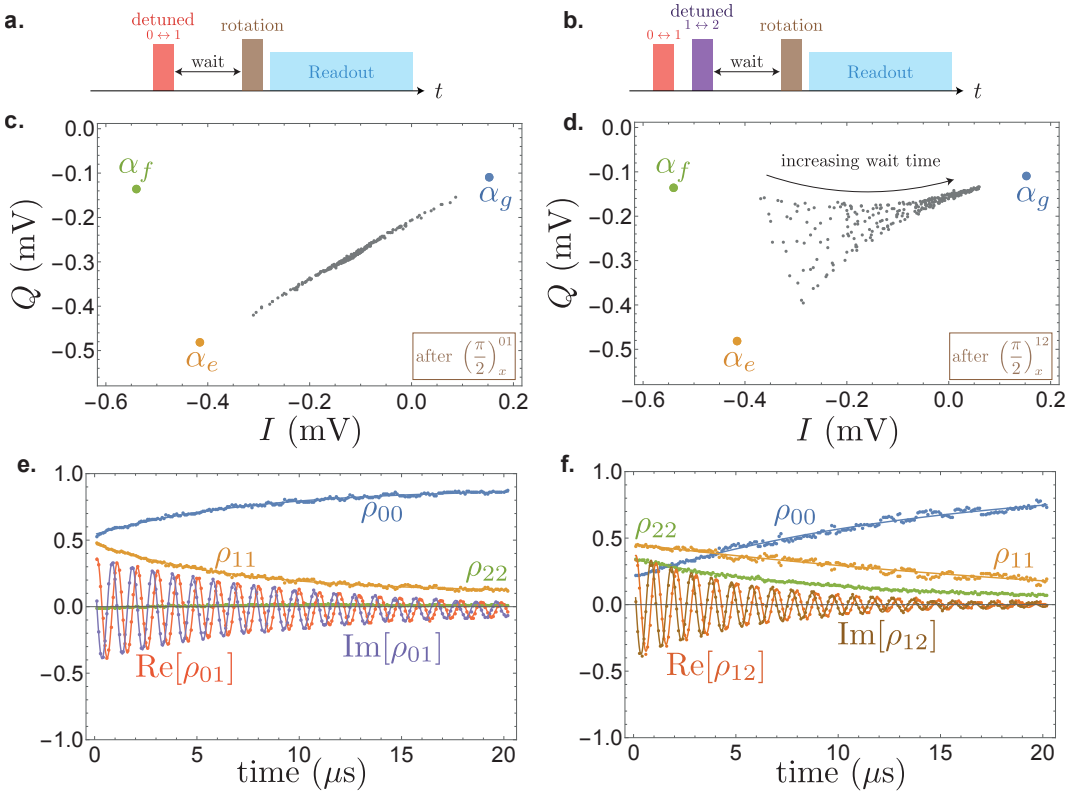

Figure 4.7: Ramsey experiments on a qutrit. **a.** and **b.** Pulse sequences for Ramsey experiments on the $0 \leftrightarrow 1$ and $1 \leftrightarrow 2$ transitions. In **a.** (resp. **b.**) we prepare $(|g\rangle + |e\rangle)/\sqrt{2}$ (resp. $(|e\rangle + |f\rangle)\sqrt{2}$) with a fast detuned $\left(\frac{\pi}{2}\right)_x^{01}$ (resp. $\left(\frac{\pi}{2}\right)_x^{12}$) pulse. After each waiting time $t \in [0, 20\ \mu\text{s}]$ a tomographic reconstruction of the density matrix is performed by applying the list of rotations (4.4) prior a dispersive measurement. **c.** (resp. **d.**) measurement outputs after a $\left(\frac{\pi}{2}\right)_x^{01}$ (resp. $\left(\frac{\pi}{2}\right)_x^{12}$) rotation. In **c.**, we observe oscillations of ρ_{12} along a line of the IQ (see temporal sgaoe in **e.** as $\text{Re}[\rho_{01}]$). In contrast in **d.** the coherence signal extends in both directions of the IQ plane owing to the relaxation $1 \to 0$. **e.** and **f.** selected density matrix elements reconstructed by tomography. The solid lines are given by Lindblad equation (4.10) with the coherence times $T_2^{01} = (\Gamma_\downarrow^{01} + \Gamma_\uparrow^{01} + \Gamma_\uparrow^{12} + 2\Gamma_\phi^{01} + \Gamma_\phi^{12})^{-1} = (10.0 \pm 0.2)\ \mu\text{s}$ and $T_2^{12} = (\Gamma_\downarrow^{01} + \Gamma_\downarrow^{12} + \Gamma_\uparrow^{12} + 2\Gamma_\phi^{12} + \Gamma_\phi^{01})^{-1} = (6.05 \pm 0.2)\ \mu\text{s}$.

4.6 CONTINUOUS MEASUREMENT OF A THREE-LEVEL SYSTEM

In this section, we show that it is possible to measure continuously a superconducting qutrit. We measured the transmitted signal of a dispersively coupled superconducting cavity hosting the device. The signal is measured in the I, Q quadrature plane. In order to readout the state of the qutrit with a sufficiently good signal to noise ratio, we use a Josephson parametric amplifier (see chapter 5 for more details). The amplifier is operated with a power gain $G_0 = 11$ dB and a dynamical bandwidth of 9 MHz. The center frequency of the amplifier is detuned by 2 MHz from the readout frequency

to avoid interferences between the signal and idler mode and thus operate is a phase preserving mode. We choose the highest readout power that does not affect the JPA[6].

We will first demonstrate that it is possible to separate the cavity states corresponding to $|g\rangle$,$|e\rangle$ or $|f\rangle$ in a time shorter than the transition rates of the qutrit. We will then show *quantum jumps* between the different energy levels of the qutrit.

4.6.1 *Dispersive measurement of a qutrit*

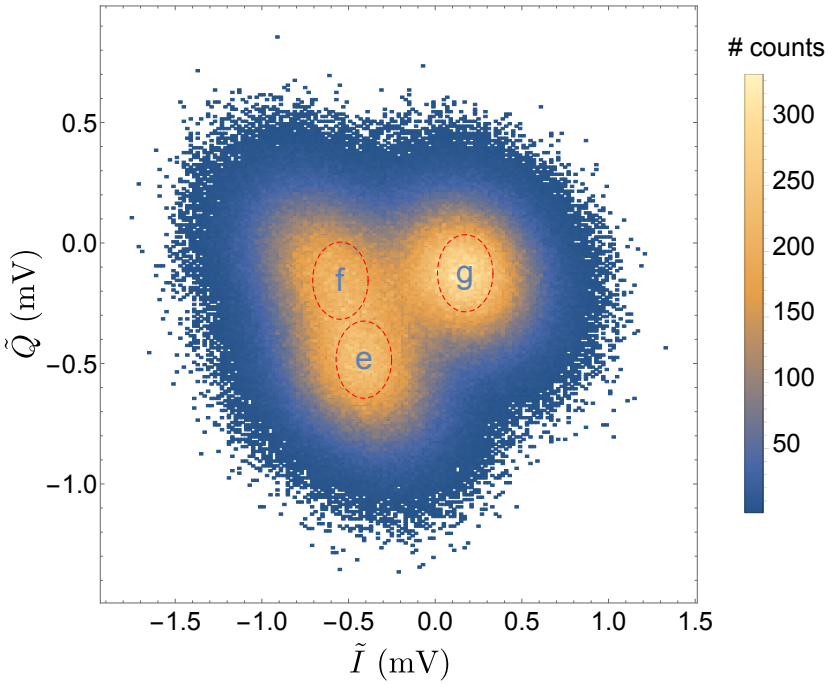

Figure 4.8: Density histogram of 10^6 digitized readout signals of a $(|g\rangle + |e\rangle + |f\rangle)/\sqrt{3}$ state integrated over $T = 2\ \mu\text{s} \sim \frac{1}{\Gamma_m}$. The signals are demodulated and they are equal to $\int_0^T (dI + idQ)$ (see Eq. (4.15)) up to a constant pre factor α. By optimizing the integration time and readout power, three maxima appear corresponding to the values α_g, α_e and α_f. The red dashed circles are 'guides for the eye' that indicate a confidence interval to assert that the qutrit is in a given state. We see that a lot of measurements fall outside of these region because the measurement time τ_m is a significant fraction of the inverse relaxation rates $(\Gamma_\downarrow^{01})^{-1} \simeq 12\ \mu\text{s}$ and $(\Gamma_\downarrow^{12})^{-1} \simeq 6\ \mu\text{s}$

In the continuous measurement limit, the measurement records at time t during a time dt are given by [118]

$$\boxed{\begin{cases} dI = \sqrt{2\eta\kappa}(\rho_{00}(t)x_g + \rho_{11}(t)x_e + \rho_{22}(t)x_f)dt + dW_{t,I} \\ dQ = \sqrt{2\eta\kappa}(\rho_{00}(t)y_g + \rho_{11}(t)y_e + \rho_{22}(t)y_f)dt + dW_{t,Q} \end{cases}} \tag{4.14}$$

6 When reading out the qutrit with a too large number of photon inside the cavity, the JPA is pumped by the readout signal itself and thus enter a phase sensitive mode. The 'stiff pump' approximation of the amplifier breaks down.

where $x_i = \mathrm{Re}(\alpha_i)$ and $y_i = \mathrm{Im}(\alpha_i)$, κ is the damping rate of the cavity mode and η is the quantum efficiency of the measurement. $dW_{t,I}$ and $dW_{t,Q}$ are two independent Wiener processes of variance dt accounting for the quantum fluctuations of the field.

In the present experiment (see Fig. 4.8), we integrate the signal during a time $T = 2\ \mu$s and we collect the digitized records[7]

$$\begin{cases} \tilde{I}(T) = \alpha \displaystyle\int_0^T dI \\ \tilde{Q}(T) = \alpha \displaystyle\int_0^T dQ \end{cases} \tag{4.15}$$

where α is a scaling factor in mV that takes into account the gain of the amplification chain.

4.6.2 *Quantum jumps between three levels*

This non demolition readout allows us to observe *quantum jumps* [115]. This kind of jumps appear when the total measurement rate Γ_m becomes much larger than any other spontaneous transition rate of the system. Similarly to the qubit case, we define a measurement rate $\Gamma_m^{ij} = \frac{\eta\kappa}{2}|\alpha_i - \alpha_j|^2$ to distinguish between states $|i\rangle$ and $|j\rangle$ and the total measurement rate reads $\Gamma_m = \min_{ij} \Gamma_m^{ij}$. After a typical time, Γ_m^{-1} we can distinguish any state from the others and if this timescale is much faster than the transition rates of the system, we observe jumps. In this case, the state of the system is one of the pointer states of the measurement and any coherent departure from a pointer state is suppressed. This effect is known as *Zeno effect* (see chapter 6 for more details). In this experiment, the qutrit in initialized in $(|g\rangle+|e\rangle+|f\rangle)/\sqrt{3}$ and then left undriven, while the cavity contains the same readout field used in Fig. 4.8. We are not deeply in the 'quantum jump regime' because the measurement time $T = 2\ \mu\mathrm{s} \sim \frac{1}{\Gamma_m}$ is not negligible compared to the relaxation times $(\Gamma_\downarrow^{01})^{-1}$ and $(\Gamma_\downarrow^{12})^{-1}$ of our device. However, the measurement records are mainly localized around α_g, α_e and α_f (maxima of the probability distribution of Fig. 4.8) and it is still possible to observe jumps between the surroundings of the maxima of the probability distribution.

In Fig. 4.9, we show three examples of such continuous measurements of an undriven transmon starting in $(|g\rangle+|e\rangle+|f\rangle)/\sqrt{3}$ exhibiting a blockade of the qutrit state in $|f\rangle$, jumps between $|f\rangle$ and $|e\rangle$ and between $|f\rangle$ and $|g\rangle$. For each measurement, we extract the coefficients c_g, c_e and c_f such that

$$\begin{cases} \tilde{I} + i\tilde{Q} = c_g\alpha_g + c_e\alpha_e + c_f\alpha_f \\ c_g + c_e + c_f = 1 \end{cases}. \tag{4.16}$$

An important difference with Eq. (4.5) is that the condition $c_g, c_e, c_f \geq 0$ is now relaxed and the coefficients are no longer bounded because of the noisy Wiener processes $dW_{t,I}$ and $dW_{t,Q}$ in Eq. (4.14). In the IQ plane, the signal is blurred and the complex output can fluctuate outside of the triangle formed by α_g, α_e and α_f contrary to an ideally averaged output s_i of Eq. (4.5). In practice, we are yet able to resolve jumps of the coefficients between 0 and 1 triggered by relaxation events of the system.

7 We assume here that the integration time T is much larger than the bandwidth of the detection setup.

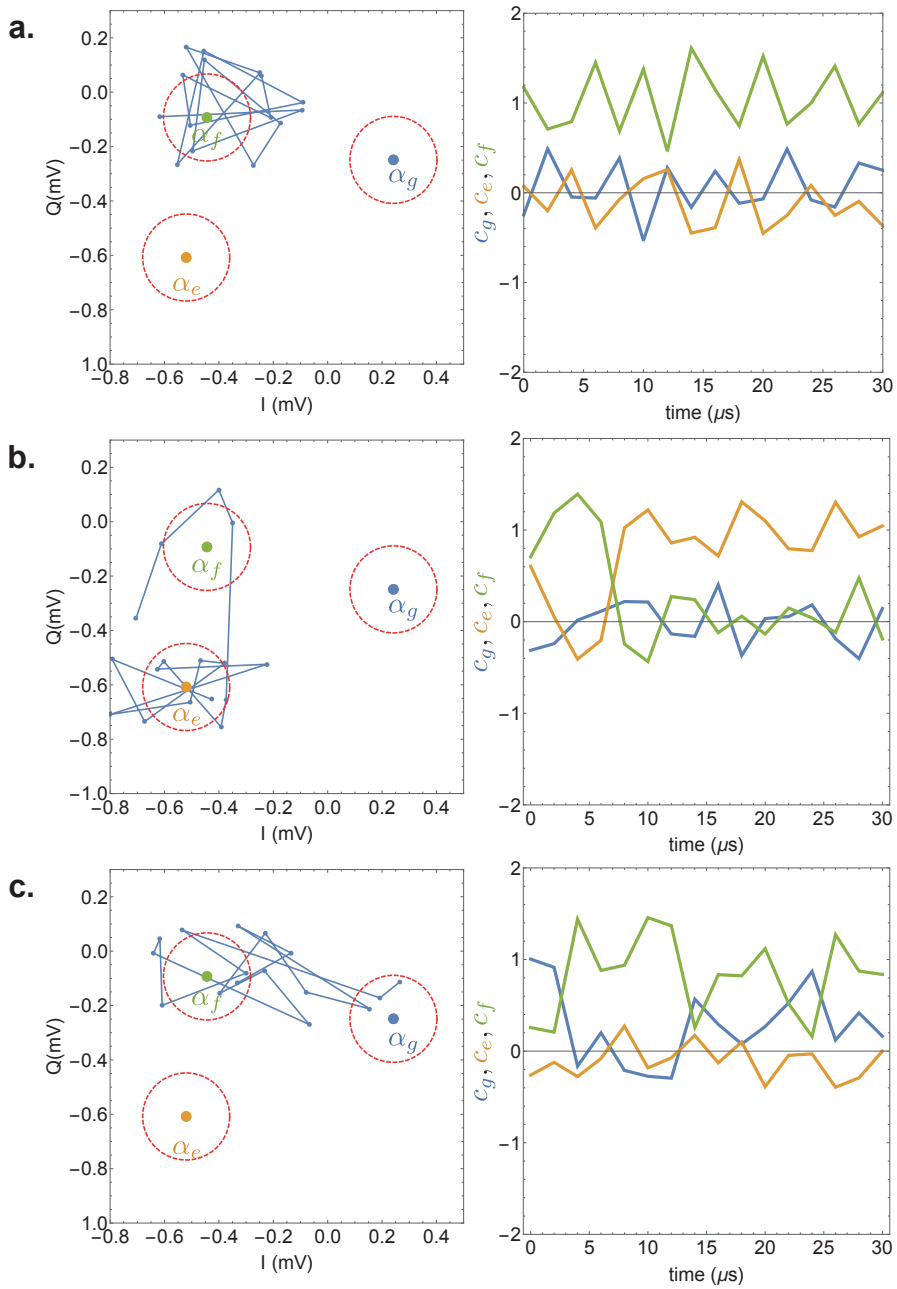

Figure 4.9: Continuous measurement of a qutrit. The qutrit is initialized in a pure 'GEF' state $(|g\rangle+|e\rangle+|f\rangle)/\sqrt{3}$ and the state of the qutrit is then continuously probed by heterodyne measurement for 30 μs and integrated over 2 μs time steps. The qutrit state can jump between different states because of thermal excitation and relaxation. We superimpose the values of α_g, α_e, α_f determined by an independent measurement. The red dashed circles are 'guides for the eye' that indicate a confidence interval to assert that the qutrit is in a given state similarly to Fig. 4.8. **a.** In this measurement, the output stays close to α_f indicating that the qutrit state was projected in the $|f\rangle$ state and is blocked there for the duration of the measurement. The c_f value of the state fluctuates around 1. **b.** The measurement output first reaches the α_f region ($c_f \simeq 1$) before jumping close to α_e ($c_e \simeq 1$). **c.** Jumps between α_g and α_f. The measurement outputs takes complex values between α_g and α_f because of relaxation events occurring during the measurement.

This measure can be improved by increasing the gain of the quantum amplifier that would increase the detection efficiency of the measurement resulting in a stronger separation of α_g, α_e and α_f. The readout power could also be increased and the measurement time decreased well below the characteristic times of the qutrit by increasing the pump power of the JPA and thus enforce the stiff pump approximation for the amplifier. However, it was not possible in our case to preserve a sufficient dynamical bandwidth to operate the JPA as a phase-preserving amplifier.

4.7 CONCLUSION

In this chapter, we demonstrated

- the coherent control of a three level system to prepare arbitrary superpositions of three quantum states.
- the dispersive measurement of a qutrit in its energy basis.
- the observation of quantum jumps by continuous monitoring of the system.
- a good understanding of decoherence mechanisms of the qutrit.
- a method to estimate the thermal population of a qubit and the gate fidelities of a qutrit.

These methods can readily be extended to populate and read out more than three levels of the transmon. Note that the protection of the transmon against charge noise requires larger and larger E_J/E_C as the level number increases. With our transmon $E_J/E_C = 140$ so all levels are addressable up to the 6^{th} level as explained in the supplementary material of [105]. The projective tomography method requires 3 measurements to reconstruct the density matrix of one qubit and 9 measurements for the density matrix of one qutrit. A 4 qutrits device has a Hilbert space of dimension $N = 3^4 = 81$ and $(N-1) + 2\frac{N(N-1)}{2} = 6560$ real coefficients to determine so the use of higher dimensional Hilbert space requires an exponential number of measurements to achieve the full quantum tomography of the system.

We presented only linear readout methods with superconducting amplifiers but a generalization to higher measurement power is an alternative way to obtain high fidelity single-shot measurements.

5

MICROWAVE AMPLIFIERS

5.1 INTRODUCTION

In the microwave domain, pumped circuits provide a complete toolbox to amplify signals [134, 135, 136], engineer non classical states of light [137, 138], catch and release quantum states [139], stabilize quantum states and manifolds [140, 88]. In this thesis I used three kinds of microwave amplifiers based on superconducting circuits namely the Josephson Parametric Amplifier (JPA), the Josephson Parametric Converter (JPC) and the Josephson Traveling Wave Parametric Amplifier (JTWPA). The following sections describe a general theory of quantum limited amplifiers and explain the operation principle of the above-mentioned amplifiers. Finally, we compare the figures of merit of the different amplifiers available in our laboratory.

The detailed fabrication processes of the JPA and JPC can be found in appendix B. The JTWPA was provided by the Lincoln Lab [136, 141] in 2017 and it was not used for the continuous time measurement presented in this thesis. At the end of this chapter, we compare the figure of merit of the different amplifiers namely gain, bandwidth, compression point, quantum efficiency and we explain the requirements for our experiments.

5.2 QUANTUM PARAMETRIC AMPLIFICATION

An amplifier can be modeled as a lumped device connected to two semi-infinite transmission lines that converts and amplifies an incoming quantum electromagnetic field $\hat{a}_{\text{in}}$ into an outgoing field $\hat{a}_{\text{out}}$. Note that we restrict the discussion to scattering amplifiers. The elementary excitations of these fields are the carriers of the information that we want to acquire. These electromagnetic modes are bosons so they verify the following commutation rule

$$[\hat{a}_{\text{in}}(t), \hat{a}^{\dagger}_{\text{in}}(t')] = [\hat{a}_{\text{out}}(t), \hat{a}^{\dagger}_{\text{out}}(t')] = \delta(t - t') \tag{5.1}$$

at all time t and t'. The nature of the amplifier is encoded in the scattering relation between the incoming field and the re-emitted outgoing field. Naively one could think that the simplest amplifier would correspond to $\hat{a}_{\text{out}}(t) = \sqrt{G}\hat{a}_{\text{in}}(t)$ but it is incompatible with (5.1) so it is forbidden by quantum mechanics.

5.2.1 *Phase preserving amplification*

By introducing an additional operator $\hat{b}_{\text{in}}$ called *idler* mode, one can write the relation

$$\boxed{\hat{a}_{\text{out}} = \sqrt{G}\hat{a}_{\text{in}} + \sqrt{G-1}\hat{b}^{\dagger}_{\text{in}}.} \tag{5.2}$$

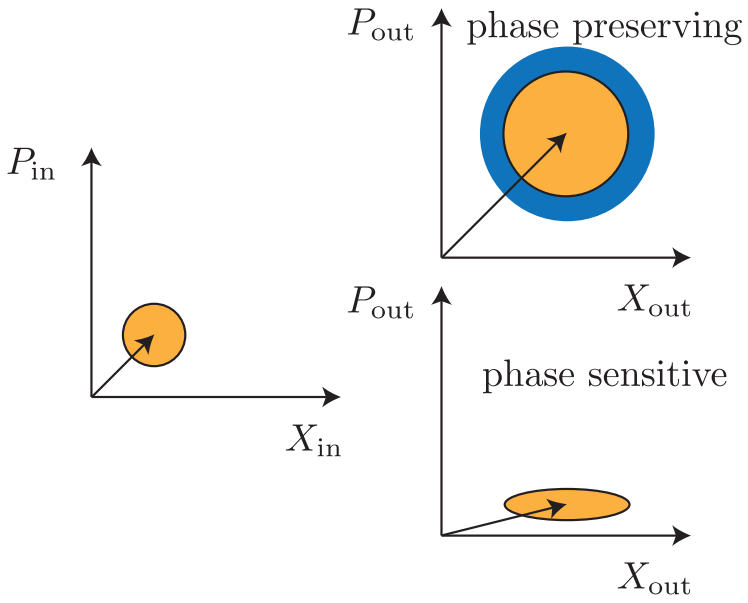

Figure 5.1: The contour of the Wigner distribution of an input field $\hat{a}_{\text{in}}$ represented in the complex plane on the left. The input field is converted in an output field $\hat{a}_{\text{out}}$ on the right. A phase preserving amplifier scales the incoming amplitude and add an *extra noise* (in blue) corresponding to the zero-point fluctuations of the idler mode. In contrast, a phase sensitive amplifier *squeezes* the input field. Namely one quadrature of the field is amplified while the other quadrature is deamplified.

With this new relation the commutation relation (5.1) can be satisfied both at the input and at the output. In the large gain limit $G \gg 1$ and for an idler port at zero temperature, this added noise boils down to half a photon at the signal frequency referred to the input. This is known as Caves' theorem [142]. This theorem can be expressed with the following relation

$$\frac{\langle \Delta X^2_{\text{a}_{\text{out}}} \rangle + \langle \Delta P^2_{\text{a}_{\text{out}}} \rangle}{G} \underset{G \gg 1}{\geq} \langle \Delta X^2_{\text{a}_{\text{in}}} \rangle + \langle \Delta P^2_{\text{a}_{\text{in}}} \rangle + \underbrace{(\langle \Delta X^2_{b_{\text{in}}} \rangle_{|0\rangle} + \langle \Delta P^2_{b_{\text{in}}} \rangle_{|0\rangle})}_{\geq \text{half a quantum}} \tag{5.3}$$

where $X_a = \text{Re}(a)$ and $P_a = \text{Im}(a)$ are the two quadratures of the electromagnetic mode.

This extra half photon can be seen as a requirement of the Heisenberg uncertainty principle. Since they are non-commuting observables, both quadratures of the field cannot be known simultaneously with an arbitrary precision. An amplifier in the regime where the degradation of the signal to noise ratio of the amplifier is only caused by irreducible quantum fluctuation is *a quantum limited amplifier*.

5.2.2 *Phase sensitive amplification*

Another way to satisfy the commutation relation (5.1) is to amplify one quadrature of the field while the corresponding conjugate quadrature is de-amplified

$$\boxed{\hat{a}_{\text{out}} = \sqrt{G}\hat{a}_{\text{in}} + e^{i\theta}\sqrt{G-1}\hat{a}^{\dagger}_{\text{in}}} \tag{5.4}$$

for a given *squeezing angle* θ. We can see that in the large gain regime $G \gg 1$ two quadratures of the field are given by $X^{\theta}_{\text{out}} = 2\sqrt{G}X^{\theta}_{\text{in}}$ and $P^{\theta}_{\text{out}} = \frac{1}{2\sqrt{G}}P^{\theta}_{\text{in}}$. If the input signal only consists in vacuum fluctuations, the amplifier squeezes the fluctuations making the quadrature P^{θ} less uncertain than the standard quantum limit (half a photon) while the uncertainty on X^{θ} is enhanced to preserve the Heisenberg uncertainty principle.

5.3 JOSEPHSON PARAMETRIC AMPLIFIER

The Josephson Parametric Amplifier (JPA) is a single-mode parametric amplifier connected to one transmission line via a non reciprocal device called a circulator [143]. It has recently known a strong revival decades after the seminal work of Yurke *et al.* [32]. This kind of device can be made out of a Josephson non linearity embedded into a $\lambda/2$ microwave resonator.

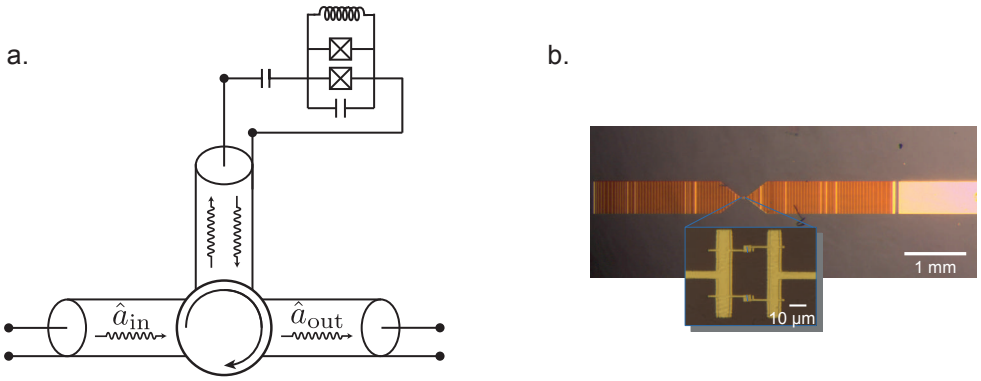

Figure 5.2: **a.** Circuit representation of the device. A SQUID composed of two Josephson junctions is embedded into a $\lambda/2$ resonator coupled to the transmission line via a microwave circulator. **b.** Optical image of the device. We evaporated a $\lambda/2$ microstrip aluminium resonator with a loop of two Josephson junctions forming a SQUID in its center.

Under the Markov approximation and the rotating-wave approximation, the dynamics of the amplifier is governed by the Quantum Langevin Equation (QLE) equation

$$\boxed{\frac{d\hat{a}}{dt} = \frac{i}{\hbar}[\hat{H}, \hat{a}] - \frac{\kappa}{2}\hat{a} + \sqrt{\kappa}\hat{a}_{\text{in}}(t)} \tag{5.5}$$

with $\hat{H} = \hbar\omega_r\hat{a}^{\dagger}\hat{a} + \hbar\frac{K}{2}(\hat{a}^{\dagger})^2(\hat{a})^2$ the lowest order approximation of the Hamiltonian where $\hat{a}$ and $\hat{a}^{\dagger}$ are the ladder operators of the oscillator with $[\hat{a}, \hat{a}^{\dagger}] = 1$, ω_r is the

pulsation of the oscillator, K is the Kerr constant and κ is the coupling rate to the bath.

Note that,

- The Hamiltonian of the JPA can be found by considering a 'BBQ' version of the JPA [144]

$$\hat{H}_{\text{JPA}}^{\text{lumped}} = \hbar\omega_0 \hat{a}^\dagger \hat{a} - E_J \sum_{n>1} \frac{(-\varphi_{\text{ZPF}}^2)^n}{(2n)!} (\hat{a} + \hat{a}^\dagger)^{2n} \tag{5.6}$$

  with the frequency of the lumped resonator $\omega_0 = \sqrt{8E_J E_C}/\hbar$ and $\varphi_{\text{ZPF}} = 2\sqrt{E_C/\hbar\omega}$ are the reduced zero-point fluctuations of the flux. The transmon qubit has the same Hamiltonian but with a much higher non linearity. By expanding the Hamiltonian to the first non-linear order, one obtains

$$\begin{aligned} \hat{H}_{\text{JPA}}^{\text{lumped}} &\simeq \hbar\omega_0 \hat{a}^\dagger \hat{a} - E_J \frac{\varphi_{\text{ZPF}}^4}{24} (\hat{a} + \hat{a}^\dagger)^4 \\ &\underset{\text{RWA}}{\simeq} \hbar\omega_r \hat{a}^\dagger \hat{a} - E_J \frac{\varphi_{\text{ZPF}}^4}{4} (\hat{a}^\dagger)^2 (\hat{a})^2. \end{aligned} \tag{5.7}$$

  This approximation is valid in the regime $E_C \ll \hbar\omega_r$ and the renormalized resonator frequency is $\omega_r = \omega_0 - E_J \frac{\varphi_{\text{ZPF}}^4}{2\hbar}$. Placing the junction in a resonator amounts to replace φ_{ZPF} by the total zero-point fluctuation of the flux but the non linear term in the expansion (5.6) are of the same form.

- This oscillator is know in classical physics as the Duffing oscillator. It exhibits an abrupt transition when driven above a critical power. The operation principle of the Josephson Bifurcation Amplifier [100] relies on this sharp transition.

- The so-called Markov approximation assumes that the environment is ohmic. That means that the density of modes can be considered constant around the transition frequencies of the circuit.

- The coupling constant to the bath κ is supposed to be small compared to any transition frequency in (5.5).

It is possible to integrate the QLE and express the circuit variable $\hat{a}(t)$ as a function of $\hat{a}_{\text{in}}(t)$. The output field is obtained via the Input-Output relation

$$\sqrt{\kappa}\hat{a}(t) = \hat{a}_{\text{in}}(t) + \hat{a}_{\text{out}}(t). \tag{5.8}$$

Let us introduce the Fourier transformed operator $\hat{a}[\omega] = \int_{-\infty}^{+\infty} dt e^{i\omega t} \hat{a}(t)$.
The QLE (5.5) now reads

$$\left(i(\omega - \omega_r) - \frac{\kappa}{2}\right) \hat{a}[\omega] - iK\hat{a}^\dagger[-\omega] * \hat{a}[\omega] * \hat{a}[\omega] + \sqrt{\kappa}\hat{a}_{\text{in}}[\omega] = 0 \tag{5.9}$$

We assume that the system receives a drive-tone at the input so intense that it can be modeled by a coherent field of amplitude α_{in}. The steady state of the intra-resonator field is then given by a coherent field α such that

$$\alpha = \frac{i\sqrt{\kappa}\alpha_{\text{in}}}{\frac{i\kappa}{2} + (\omega - \omega_r) - K|\alpha|^2} \tag{5.10}$$

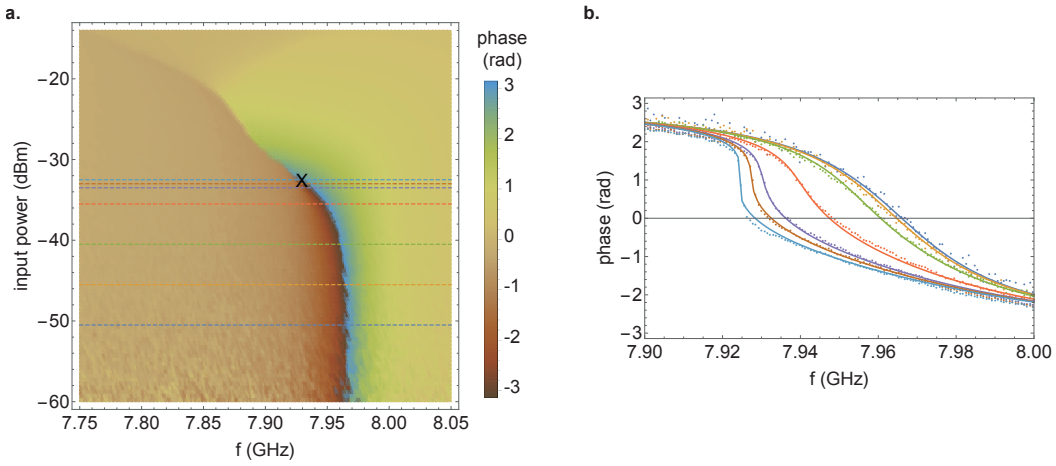

Figure 5.3: **a.** Phase of the reflected signal on an anharmonic oscillator as a function of input power and frequency of the probe drive. A black cross marks the position of the critical point of the oscillator. **b.** Horizontal cuts **a** for an input power $P = (-50.5, -45.5, -40.5, -32.5, -33.5, -33, -32.5)$ dBm from darkblue to lightblue (power is referred to the input of the dilution refrigerator). The dots are the measured phases and the solid lines correspond to a fit with equation (5.10) with $\omega_r = 2\pi \times 7.966$ GHz, $\kappa = 43$ MHz and the photon number calibration $K|\alpha|^2 = (50.77(\text{GHz}))10^{\text{P(dBm)}/10}$. The theory developed in the text is consistent for low powers but we see that the first non-linear order approximation in (5.7) is not sufficient close to the critical point (lightblue).

The auto-consistent equation (5.10) exhibits a bifurcation at a critical input power $|\alpha_{\text{in}}|^2 = -\frac{1}{\sqrt{27}}\frac{\kappa}{K}$. When reaching this power, new solutions of equation (5.10) appear leading to an instability of the system. The reflection response of a JPA device can be seen in figure (5.3) where the critical point is marked with a black cross. Cuts of the 2D map are compared with the theory obtained by solving (5.10) and (5.8) with a good agreement below the critical point. For this device, internal losses were negligible compared to the coupling to the transmission line so all the information is contained in the phase of the outgoing signal.

5.3.1 *Different JPAs and different pumping schemes*

The denomination Josephson Parametric Amplifier encompasses a lot of different amplifiers. A JPA can be a lumped non-linear element connected to a transmission line [32, 36] or it can be embedded in a CPW or micro-strip resonator [33]. The non-linearity can be distributed over several elements to increase the dynamical range of the device [37]. The resonator is usually coupled to the rest of the circuitry by a geometric capacitance or impedance matched to the transmission line to enhance the gain bandwidth product of the amplifier [145]. Even for a given circuit design, several pumping schemes are available. The JPA can be pumped on resonance with a monochromatic micro-wave pump, with a bichromatic pump centered on its resonance frequency [35] or with a flux modulation at twice its frequency [34].

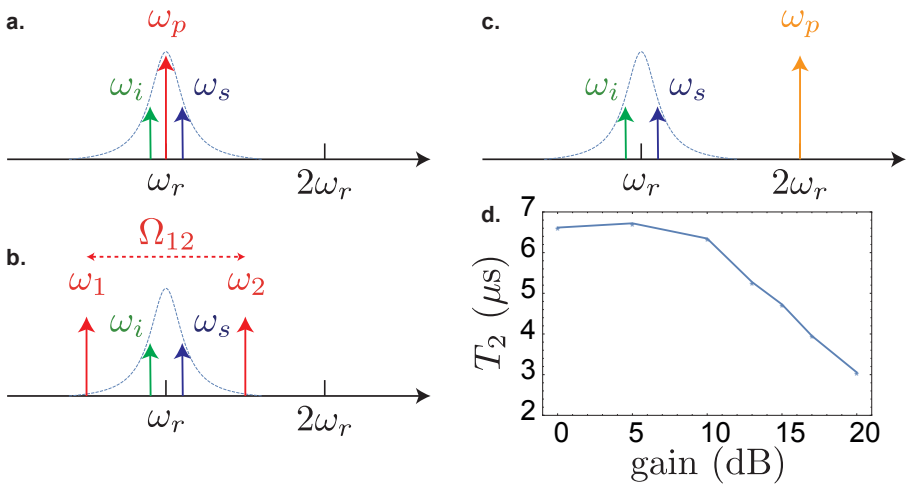

Figure 5.4: Frequency landscape for the differents pumping schemes of the JPA. The dashed lines represent the response function of the device close to ω_r. **a.** First pumping scheme: A monochromatic current pump (in red) is sent at the resonator frequency. **b.** Second pumping scheme: A bichromatic current pump (in red) is centered around the resonator frequency. **c.** Third pumping scheme: A monochromatic flux pump (in orange) is applied at twice the resonator frequency. **d.** Degradation of the coherence time of a 3D transmon followed by two isolators (40 dB of isolation) and a JPA pumped with a monochromatic current pump (pumping scheme **a**). In this case the frequency of the amplifier is matched with the frequency of the cavity of the 3D transmon. Increasing the pumping power will increase the amplifier gain but a fraction of the pump tone unavoidably populates the cavity leading to a reduction of the coherence time of the qubit by measurement induced dephasing.

Under different assumptions, all the three following pumping schemes lead to an effective Hamiltonian of the form of a perfect one-mode squeezer

$$\boxed{\hat{H} = \hbar\Omega\hat{a}^\dagger\hat{a} + \frac{\hbar\lambda}{2}a^{\dagger 2} + \frac{\hbar\lambda^*}{2}\hat{a}^2} \tag{5.11}$$

where Ω is the frequency of the amplifier in a rotating frame that depends on the pumping scheme and λ is the strength of the parametric pump. We are now going to detail the derivation of the Hamiltonian (5.11) for the three most common pumping schemes.

a) Single pump

The first pumping scheme is the current-pumped JPA [33] where a monochromatic pump near resonance with the oscillator is used. A_p denotes the pump amplitude and ω_p its angular frequency. The pumped Hamiltonian is

$$\hat{H} = \hbar\omega_r\hat{a}^\dagger\hat{a} + \frac{\hbar K}{2}\hat{a}^{\dagger 2}\hat{a}^2 + \hbar A_p(e^{-i\omega_p t}\hat{a}^\dagger + e^{i\omega_p t}\hat{a}). \tag{5.12}$$

In the displaced rotating frame of the pump $\hat{a} \to (\hat{a} + \alpha)e^{-i\omega_p t}$, one obtains

$$\frac{\hat{H}}{\hbar} = (\omega_r - \omega_p + 2K|\alpha|^2)\hat{a}^\dagger\hat{a} + \frac{K}{2}(\alpha^2\hat{a}^{\dagger 2} + \alpha^{*2}\hat{a}^2) + \frac{K}{2}\hat{a}^{\dagger 2}\hat{a}^2 + K(\alpha\hat{a}^{\dagger 2}\hat{a} + \alpha^*\hat{a}^\dagger\hat{a}^2) \tag{5.13}$$

under the condition $i\dot{\alpha} = A_p + (\Omega - K|\alpha|^2 - i\kappa/2)\alpha$ where $\Omega = \omega_r - \omega_p + 2K|\alpha|^2$, which is exactly the QLE (5.9) for $\sqrt{\kappa}a_{\text{in}} = A_p$. In the limit of small quantum fluctuations $\varphi_{\text{ZPF}} \ll 1$ and large pump $|\alpha| \gg 1$ the two last terms in (5.13) are negligible and one finds a squeezing Hamiltonian of the form (5.11) with a pumping amplitude $\lambda = K\alpha^2$.

The squeezing Hamiltonian (5.11) is obtained in a displaced rotating frame and there are tight constraints in order to fully neglect the cubic terms in (5.13). Another important drawback is that there are no spatial or spectral separation of the signal and the pump tone. The pump tone can then leak into the rest of the circuit and cause unwanted effect on other devices matched at the same frequency. In figure (5.4**d**) is an example of the degradation of coherence time of a transmon due to the leaking of a pump tone of a well-isolated amplifier matched at the frequency of the cavity hosting the qubit. A way to circumvent this last difficulty is to cancel the pump tone by destructive interferences but the amplitude and phase of the cancelation tone has to be recalibrated very often.

b) Bichromatic pump

A second way to obtain parametric amplification is by pumping the device with two symmetric tones around its resonant frequency. The pump amplitudes are denoted A_i and their angular frequencies are denoted ω_i. Similarly to (5.12), the Hamiltonian reads

$$\hat{H} = \hbar\omega_r \hat{a}^\dagger \hat{a} + \frac{\hbar K}{2}\hat{a}^{\dagger 2}\hat{a}^2 + \sum_{i=1}^{2} A_i(e^{-i\omega_i t}\hat{a}^\dagger + e^{i\omega_i t}\hat{a}). \tag{5.14}$$

In a displaced rotating frame rotating at $\Omega_{12} = (\omega_1 + \omega_2)/2$ such that $\hat{a} \to \hat{a}e^{-i\Omega_{12}t} + \alpha_1 e^{-i\omega_1 t} + \alpha_2 e^{-i\omega_2 t}$ and under the condition $\Delta_{12} \gg K|\alpha_1||\alpha_2|$, one obtains

$$\frac{\hat{H}}{\hbar} \underset{\text{RWA}}{\simeq} (\omega_r + 2K(|\alpha_1|^2 + |\alpha_2|^2) - \Omega_{12})\hat{a}^\dagger\hat{a} + K\alpha_1\alpha_2\hat{a}^{\dagger 2} + K\alpha_1^*\alpha_2^*\hat{a}^2 + \frac{K}{2}\hat{a}^{\dagger 2}\hat{a}^2 \tag{5.15}$$

under the assumption that α_1 and α_2 satisfy the coupled equations

$$\begin{cases} i\dot{\alpha_1} = A_1 + (\omega_r - \omega_1 + K|\alpha_1|^2 - i\kappa/2)\alpha_1 + K(2|\alpha_2|^2 + \alpha_1\alpha_2^* e^{-i\Delta_{12}t})\alpha_1 \\ i\dot{\alpha_2} = A_2 + (\omega_r - \omega_2 + K|\alpha_2|^2 - i\kappa/2)\alpha_2 + K(2|\alpha_1|^2 + \alpha_2\alpha_1^* e^{i\Delta_{12}t})\alpha_2 \end{cases}. \tag{5.16}$$

In the limit of small quantum fluctuation, the squeezing Hamiltonian (5.11) is recovered with $\Omega = \omega_r + 2K(|\alpha_1|^2 + |\alpha_2|^2) - \Omega_{12}$ and $\lambda = 2K\alpha_1\alpha_2$ by neglecting the last term in (5.15). We see that the cubic corrections in (5.15) are now safely neglected by the application of the RWA. Moreover the spectral separation of the signal and pump tones allows an efficient filtering of the pump tones without the need of a cancellation scheme.

c) Flux pumping

A third way to obtain parametric amplification with a JPA is by directly modulating the inductance of a SQUID, which behaves as a flux-dependent non-linear inductance. This slight modification of the amplifier allows for flux pumping and DC flux biasing

of the device in order to adjust its operating frequency as can be seen in figure (5.5 **b**). Let us start with the Hamiltonian (5.6). Replacing the junction by a SQUID modifies the Josephson energy such that

$$E_J \rightarrow E_J \cos(\varphi_{\text{ext}}) \tag{5.17}$$

where $\varphi_{\text{ext}} = \Phi_{\text{ext}} \frac{2e}{\hbar}$ is the reduced magnetic flux. We can decompose the magnetic flux in (5.17) into the sum of a static component and an oscillatory component at angular velocity ω_p $\varphi_{\text{ext}} = F + \delta f \cos(\omega_p t)$, with $\delta f \ll 1$. We then separate the different harmonics

$$\begin{aligned} E_J \cos(F + \delta f \cos(\omega_p t)) &\underset{\delta f \ll 1}{\simeq} E_J \cos(F) - E_J \delta f \sin(F) \cos(\omega_p t) \\ &\quad - \frac{E_J \delta f^2 \cos(F)}{4} \cos(2\omega_p t) + ... \end{aligned} \tag{5.18}$$

Let us derive the Hamiltonian of the system at first order in δf and fourth order in φ_{ZPF} with $\omega_p \simeq 2\omega_0$,

$$\begin{aligned} \hat{H} &\simeq \hbar\omega_0 \hat{a}^\dagger \hat{a} - E_J \delta f \sin(F) \cos(\omega_p t) \frac{\varphi_{\text{ZPF}}^2}{2} (\hat{a} + \hat{a}^\dagger)^2 \\ &\quad - E_J \frac{\varphi_{\text{ZPF}}^4}{4!} (\hat{a} + \hat{a}^\dagger)^4 \left(\cos(F) - \delta f \sin(F) \cos(\omega_p t)\right) + ... \\ &\underset{\text{RWA}}{\simeq} \hbar\omega_r \hat{a}^\dagger \hat{a} + E_J \delta f \frac{\varphi_{\text{ZPF}}^2}{2} \frac{\hat{a}^2 e^{i\omega_p t} + \hat{a}^{\dagger 2} e^{-i\omega_p t}}{2} - E_J \frac{\varphi_{\text{ZPF}}^4}{4} (\hat{a}^\dagger)^2 (\hat{a})^2 \\ &\quad + E_J \frac{\varphi_{\text{ZPF}}^4}{12} (\hat{a}^\dagger \hat{a}^3 e^{i\omega_p t} + \hat{a}^{\dagger 3} \hat{a} e^{-i\omega_p t}) \end{aligned} \tag{5.19}$$

In the limit of small quantum fluctuations, the two last φ^4 terms in (5.19) can be dropped. In the rotating frame $\hat{a} \rightarrow \hat{a} e^{-i\omega_p t/2}$ rotating at half the pump frequency, the Hamiltonian is of the form of (5.11) with $\Omega = \omega_r - \omega_p/2$ and $\lambda = E_J \delta f \varphi_{\text{ZPF}}^2 / 4\hbar$. A very interesting point here is that the strength of the drive is in φ_{ZPF}^2 so it does not depend on the Kerr non linearity of the resonator and in the small flux pump limit $\delta f \ll 1$, the leading correction are the same than for the bichromatic current pumped JPA. Also in this last scheme, there is no displacement transformation to obtain (5.19).

d) Summary

Pumping scheme	Frame $\hat{a} \rightarrow$	Ω	λ
Single	$\hat{a} e^{-i\omega_p t}$	$\omega_r - \omega_p + 2K\lvert\alpha\rvert^2$	$K\alpha^2$
Bichromatic	$\hat{a} e^{-i\Omega_{12} t} + \alpha_1 e^{-i\omega_1 t} + \alpha_2 e^{-i\omega_2 t}$	$\omega_r + 2K(\lvert\alpha_1\rvert^2 + \lvert\alpha_2\rvert^2) - \Omega_{12}$	$2K\alpha_1\alpha_2$
Flux	$\hat{a}$ (lab frame)	$\omega_r - \frac{\omega_p}{2}$	$\frac{E_J \delta f \varphi_{\text{ZPF}}^2}{4\hbar}$

Table 5.1: Comparison of the different pumping scheme of this section. In each case, we specify the transformation used to obtain the squeezing Hamiltonian (5.11) with the corresponding operating frequency of the amplifier in this frame as well as the strength of the parametric pump.

In this thesis the second pumping scheme of table 5.1 was used to avoid the need of a pump cancellation scheme and the addition on a on-chip flux pump.

5.3.2 *Amplification*

All the previous pumping schemes are ways to obtain a squeezing Hamiltonian (5.11)

$$\hat{H} = \hbar\Omega\hat{a}^\dagger\hat{a} + \frac{\hbar\lambda}{2}a^{\dagger 2} + \frac{\hbar\lambda^*}{2}\hat{a}^2 \tag{5.20}$$

The equation of motion of the intracavity field is given by the QLE (5.5) in the frame rotating at the frequency of the oscillator

$$\begin{pmatrix} \kappa/2 - i\tilde{\omega} & i\lambda \\ -i\lambda^* & \kappa/2 - i\tilde{\omega} \end{pmatrix} \begin{pmatrix} \hat{a}[\tilde{\omega}] \\ \hat{a}^\dagger[-\tilde{\omega}] \end{pmatrix} = \sqrt{\kappa} \begin{pmatrix} \hat{a}_{\text{in}}[\tilde{\omega}] \\ \hat{a}^\dagger_{\text{in}}[-\tilde{\omega}] \end{pmatrix} \tag{5.21}$$

where $\tilde{\omega} = \omega - \Omega$, $\hat{a}[\omega] = \int_{-\infty}^{+\infty} dt e^{i\omega t}\hat{a}(t)$ is the Fourier transformed signal mode and $\hat{a}^\dagger[\omega]$ is the corresponding idler mode.

By inverting the matrix in (5.21) and using the input-output relation (5.8), the amplified signal reads

$$\hat{a}_{\text{out}}[\tilde{\omega}] = g_{S,\omega}\hat{a}_{\text{in}}[\tilde{\omega}] + g_{I,\omega}\hat{a}^\dagger_{\text{in}}[-\tilde{\omega}] \tag{5.22}$$

where the signal and idler amplitude gains are defined as

$$\begin{cases} g_{S,\tilde{\omega}} = \dfrac{\kappa(\kappa/2 - i\tilde{\omega})}{(\kappa/2 - i\tilde{\omega})^2 - |\lambda|^2} - 1 \\ g_{I,\tilde{\omega}} = \dfrac{-i\kappa\lambda}{(\kappa/2 - i\tilde{\omega})^2 - |\lambda|^2} \end{cases}. \tag{5.23}$$

The power gain is defined as $G = |g_{S,\tilde{\omega}}|^2$. In the large gain limit, we can approximate $|\lambda|^2 = \frac{\kappa^2}{4}(1 + \delta x)$ with $\delta x \ll 1$. The expression of the gain reads

$$G[\tilde{\omega}] = \frac{(\kappa^2/2 + \omega^2)^2}{(\kappa^2/4)^2\delta x^2 + \kappa^2\tilde{\omega}^2 + \tilde{\omega}^4}. \tag{5.24}$$

Close to the resonance frequency $\omega \ll \kappa$, the gain curve is a Lorentzian function and the power gain reads

$$\boxed{G[\tilde{\omega}] = \frac{G_0}{1 + (2\tilde{\omega}/\gamma)^2}} \tag{5.25}$$

where $G_0 = 4/\ \delta x^2$ is the power gain of the amplifier and the bandwidth of the resonance γ given by

$$\boxed{\gamma = \kappa\delta x/2 = \kappa/\sqrt{G_0}.} \tag{5.26}$$

We notice that with this first order theory $\sqrt{G_0}\gamma$ is a constant. It is in fact a general feature of any parametric amplifier that increasing the gain by increasing the pump power comes with a reduction of the effective operating bandwidth[1]. An experimentally measured gain curve can be seen on Fig. 5.5. The power gain is $G_0 = 16$ dB over a bandwidth of 6.3 MHz leading to a gain-bandwidth product of $\sqrt{G_0}\gamma \simeq 39.8$ MHz.

When the pump strength reaches a critical value $|\lambda_{\text{crit}}| = \sqrt{\tilde{\omega}^2 + \kappa^2/4}$ the expression of the amplitude gain $g_{S,\omega}$ diverges. The amplification of zero-point fluctuations leads to

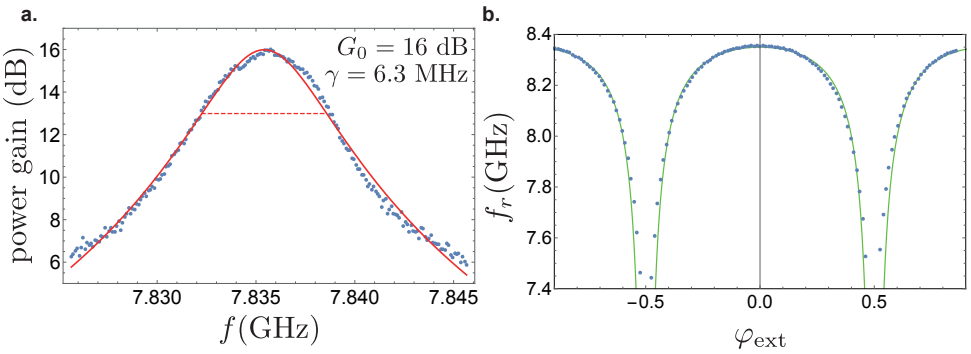

Figure 5.5: **a.** Power gain in reflection measured as a function of frequency. The dots correspond to gains measured with a Vector Network Analyzer and the red solid line is a Lorentzian function given by Eq. (5.25). We extract a gain $G_0 = 16$ dB over a bandwidth of 6.3 MHz from this fitting procedure. The gain-bandwidth product is $\sqrt{G_0}\gamma \simeq 39.8$ MHz so the amplifier has a bandwidth of 4 MHz when operated with a 20 dB power gain. **b.** Frequency of the resonator of the JPA as a function of the external magnetic flux applied. The theory given by Eq. (5.30) (green line) reproduces the experimental values (in blue) with a participation ratio $p \simeq 2$ %.

the generation of a large number of photons, this is known as parametric oscillation. In practice, the amplitude of the oscillation will be limited by additional extra non-linear terms that were not taken into account in the Hamiltonian (5.11).

An important point is that the Hamiltonian (5.11) corresponds to the case of a degenerate amplifier for which only one electromagnetic mode is involved. If the measurement bandwith of the detection setup includes both the signal at ω and the idler mode at $-\omega$, the device operates as a phase-sensitive amplifier [147]. On the contrary if the idler is filtered out, the amplifier is a phase preserving amplifier with power gain $|g_{S,\omega}|^2$. This technique was used to implement an heterodyne readout of the state of a qutrit in section 4.6.2.

It is also possible to use the same device as a non degenerate amplifier. For instance, pumping a $\lambda/2$-resonator JPA at a frequency close to $3\omega_r/2$ leas to amplification between two distinct modes. The signal mode is the first cavity mode whereas the idler is the second harmonic of the resonator.

5.3.3 *Frequency tunability*

The typical bandwidth of such amplifiers is of the order of a few MHz when operated at a gain of 20 dB. An essential requirement for such a practical amplifier is to be frequency tunable in order to match other frequencies of the setup. In our implementation, the frequency tunability is achieved by placing a SQUID in the middle of a $\lambda/2$ resonator. The inductance of the symmetric SQUID reads

$$L_J(\varphi_{\text{ext}}) = \frac{L_J(0)}{|\cos(\varphi_{\text{ext}})|} \tag{5.27}$$

1 It is possible to avoid this constraint using reservoir engineering [146] or impedance matching [145].

where $L_J(0)$ is half of the inductance of a single junction in the SQUID. The JPA is composed of two $\lambda/4$ resonators of characteristic impedance Z_0 linked by a SQUID. By symmetry, the electrical potential in the middle of the SQUID is 0 so the impedance of the device Z_{JPA} as seen from the transmission line is equal to the impedance of a $\lambda/4$ resonator terminated by a load $Z_L = iL_J(\varphi_{\text{ext}})\omega/2$ corresponding to half the impedance of the SQUID [148]

$$Z_{\text{JPA}} = Z_0 \frac{Z_L + iZ_0 \tan(\beta l)}{Z_0 + iZ_L \tan(\beta l)} \tag{5.28}$$

with $\beta = 2\pi/\lambda$ the angular wave number and l the effective length of the resonator that depends on the external flux. In the regime where the frequency of the resonator is only slightly affected by the SQUID, one can write

$$\omega(\varphi_{\text{ext}}) = \omega(0) + \underbrace{(\omega(\varphi_{\text{ext}}) - \omega(0))}_{\ll \omega(0)} \tag{5.29}$$

such that for a $\lambda/4$-resonator $\beta l \simeq \frac{\pi}{2} + \frac{\pi}{2}\frac{\omega(\varphi_{\text{ext}})-\omega(0)}{\omega(0)}$ and $\tan(\beta l) \simeq -\frac{2\omega(0)}{\pi(\omega(\varphi_{\text{ext}})-\omega(0))}$. The resonance frequencies are the poles of the input impedance (5.28)

$$\boxed{\omega_r(\varphi_{\text{ext}}) = \frac{\omega(0)}{1 + p/|\cos(\varphi_{\text{ext}})|},} \tag{5.30}$$

where $p = \omega(0)L_J(0)/Z_0\pi$ is the participation ratio of the SQUID to the inductance of the resonator. The measured flux dependence is shown in Fig. 5.5**b** from which a participation ratio of 2% was inferred with a *static bandwidth*[2] of the order of 600 MHz justifying *a posteriori* the approximation of Eq. (5.29).

5.4 JOSEPHSON PARAMETRIC CONVERTER

The Josephson Parametric converter (JPC) was first built at Yale in 2010 [38] as a non degenerate quantum limited microwave amplifier. The amplifier relies on a non linear element known as the Josephson ring modulator (JRM) built with 4 Josephson junctions in a Graetz bridge geometry which was later improved in our group in 2012 [39] by shunting the Josephson ring with linear inductances to increase its static bandwidth.

5.4.1 *Josephson ring modulator*

The Josephson ring modulator is analog of a Graetz bridge in which diodes are replaced by Josephson junctions. We will first describe the bridge and derive its Hamiltonian and then couple it to resonators to form a Josephson Parametric Converter. The ring is shunted by 4 linear inductances in order to increase the stability frequency range of the JRM and avoid phase-slip events. The Hamiltonian of the ring reads [40]

$$H = -E_J(\cos(\varphi_a) + \cos(\varphi_b) + \cos(\varphi_c) + \cos(\varphi_d)) + \frac{1}{2}E_L(\varphi_\alpha^2 + \varphi_\beta^2 + \varphi_\gamma^2 + \varphi_\delta^2) \tag{5.31}$$

2 Note that the *dynamic* bandwidth of the amplifier is the width of the gain curve in Fig. 5.5**a** whereas the *static bandwidth* is the range of frequencies accessible in Fig. 5.5**b** by changing the operating point of the amplifier.

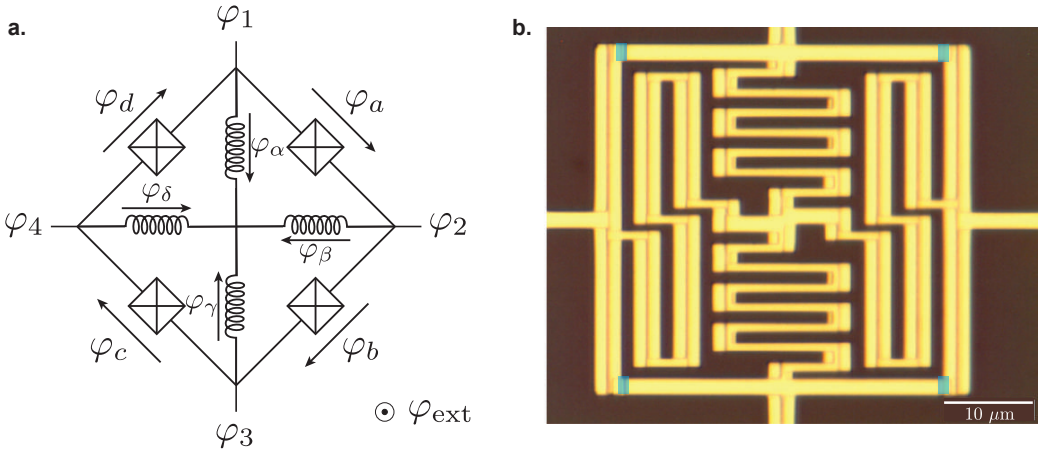

Figure 5.6: Josephson ring modulator. **a.** Circuit diagram of the Josephson ring modulator (JRM) consisting in a bridge of four identical junctions shunted by four linear inductors. **b.** Optical microscope image of a Josephson ring modulator [40] analog to the one used in the experiment. The Josephson junctions are marked by the blue rectangles.

where $E_L = \frac{\varphi_0^2}{L}$ is the magnetic energy associated to the shunt inductance and E_J is the Josephson energy of the junctions. By assuming that the shunting inductances participate symmetrically we can write

$$\begin{cases} \varphi_a = \varphi_2 - \varphi_1 + \varphi_{\text{ext}}/4 + 2\pi n_a \\ \varphi_b = \varphi_3 - \varphi_2 + \varphi_{\text{ext}}/4 + 2\pi n_b \\ \varphi_c = \varphi_4 - \varphi_3 + \varphi_{\text{ext}}/4 + 2\pi n_c \\ \varphi_d = \varphi_1 - \varphi_4 + \varphi_{\text{ext}}/4 + 2\pi n_d \end{cases}, \tag{5.32}$$

where $\varphi_{\text{ext}}/4$ is the reduced magnetic flux threading each sub-loop and (n_a, n_b, n_c, n_d) are the number of flux quanta threading the loops.

It is then convenient to introduce the normal modes of the ring

$$\begin{cases} \varphi_X = \varphi_3 - \varphi_1 \\ \varphi_Y = \varphi_4 - \varphi_2 \\ \varphi_Z = \dfrac{1}{2}(\varphi_2 + \varphi_4 - \varphi_1 - \varphi_3) \end{cases}. \tag{5.33}$$

The Hamiltonian (5.31) can be rewritten in these new variables as

$$\begin{aligned} H = &- 4E_J \cos(\varphi_X/2)\cos(\varphi_Y/2)\cos(\varphi_Z)\cos(\varphi_{\text{ext}}/4) \\ &- 4E_J \sin(\varphi_X/2)\sin(\varphi_Y/2)\sin(\varphi_Z)\sin(\varphi_{\text{ext}}/4) \\ &+ \frac{E_L}{4}(\varphi_X^2 + \varphi_Y^2 + 2\varphi_Z^2) \end{aligned} \tag{5.34}$$

For small applied voltage at the nodes, we can expand the Hamiltonian (5.34) at 3rd order in the normal modes

$$\begin{aligned} H = &-4E_J\cos(\varphi_{\text{ext}}/4) \\ &+\frac{1}{2}(\frac{E_L}{2}+E_J\cos(\varphi_{\text{ext}}/4))(\varphi_X^2+\varphi_Y^2)+\frac{1}{2}(E_L+4E_J\cos(\varphi_{\text{ext}}/4))\varphi_Z^2 \\ &-E_J\sin(\varphi_{\text{ext}}/4)\varphi_X\varphi_Y\varphi_Z. \end{aligned} \tag{5.35}$$

The last term is the three wave mixing term that we wanted to generate with the JRM that is used for several application including quantum limited amplification of microwave signals.

Note that a higher order expansion of (5.35) would reveal the following self-Kerr and cross-Kerr terms

$$H^{4^{\text{th}}\text{order}} = -\frac{E_J}{6}\left(\frac{\varphi_X^4+\varphi_Y^4}{16}+\varphi_Z^4\right)-\frac{E_J}{4}\left(\varphi_X^2\varphi_Z^2+\varphi_Y^2\varphi_Z^2+\varphi_X^2\varphi_Y^2/4\right). \tag{5.36}$$

Similarly to the JPA, the non linear element is inserted in microwave resonators that are addressable via a 180 hybrid coupler (see Fig 5.8(**a**) for the actual implementation). The JRM is connected to two resonators that will define 3 spatially separated electromagnetic modes that naturally couple to the modes X, Y and Z. The new modes of the whole circuit are denoted a, b and c and their quadratures are directly proportional to the quadratures of the normal modes X, Y and Z [40]. The three wave mixing Hamiltonian of the device can be re-expressed as

$$\boxed{H = \hbar\omega_a a^\dagger a+\hbar\omega_b b^\dagger b+\hbar\omega_c c^\dagger c+\hbar\chi(a+a^\dagger)(b+b^\dagger)(c+c^\dagger).} \tag{5.37}$$

The modes a, b and c interact via higher order non linear terms (5.36), that lead to unwanted effects limiting the ideal behavior of the JPC as a linear amplifier as described in the following section. It is the starting point of all the applications involving the JPC.

5.4.2 *Amplification mode*

The JPC is commonly used as an amplifier by applying a stiff classical pump p on the common mode at a frequency $\omega_p = \omega_a + \omega_b$, sum of the two non degenerate mode frequencies. The three wave mixing Hamiltonian then becomes

$$\frac{H}{\hbar} = \omega_a a^\dagger a+\omega_b b^\dagger b+\chi(p+p^*)(a+a^\dagger)(b+b^\dagger). \tag{5.38}$$

By applying the rotating wave approximation on the Eq. (5.38) with the frequency matching condition $\omega_p = \omega_a + \omega_b$ the rapidly oscillating term can be neglected so that the resulting Hamiltonian reads

$$\frac{H}{\hbar} = \omega_a a^\dagger a+\omega_b b^\dagger b+\chi(p^*ab+pa^\dagger b^\dagger). \tag{5.39}$$

The parametric down conversion term $pa^\dagger b^\dagger$ can be understood as the annihilation of one pump photon at ω_p and the creation of two photons at frequencies ω_a and ω_b. This

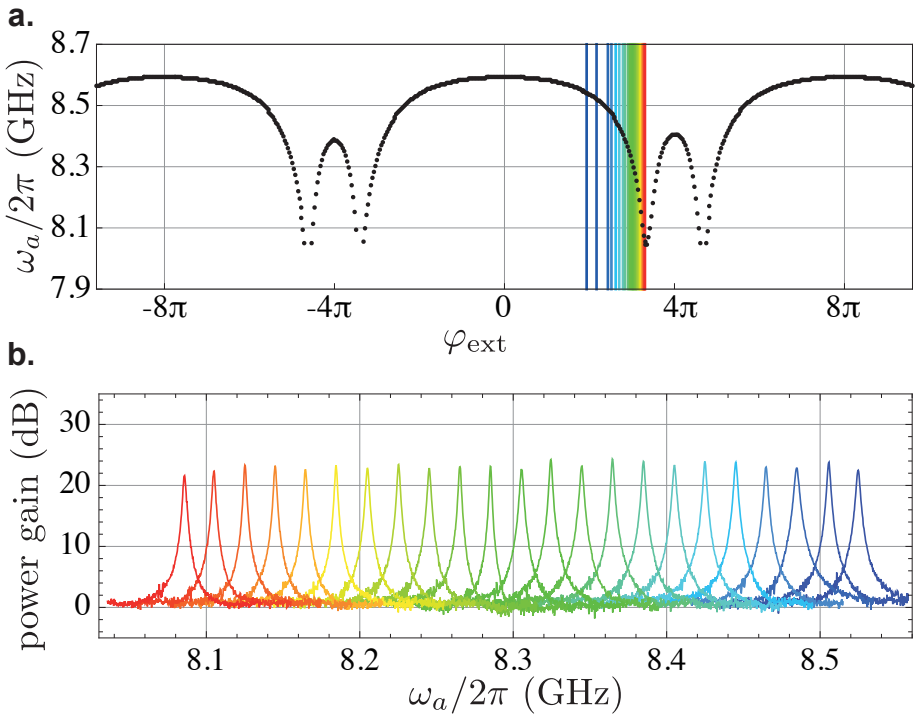

Figure 5.7: Figure from [39]. **a.** Measured frequency of the resonator mode at ω_a as a function of the external flux applied to the JPC without pump. **b.** Reflection gain on the mode a as a function of frequency for various external fluxes encoded by the color of lines in **a**.

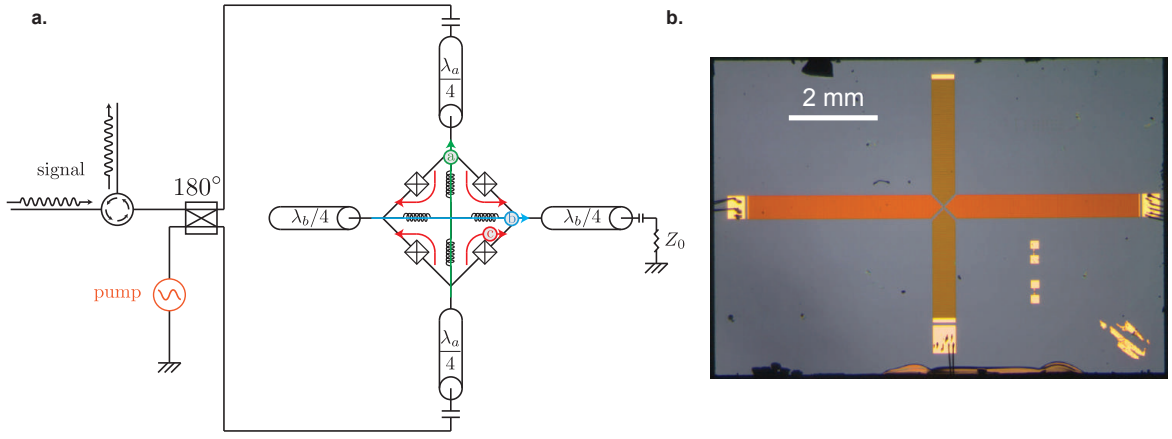

Figure 5.8: **a.** Schematic of a practical implementation of the JPC. A 180° hybrid coupler is used to excite the common mode with the pump tone and the mode a with the signal. **b.** Optical image of a Josephson parametric converter in the microstrip geometry. The Josephson ring modulator is placed at the center of two $\lambda/2$ resonators capacitively coupled to transmission lines.

gives rise to the phenomenon of amplification in the JPC. Let us write the QLE for modes a and b

$$\begin{cases} \dfrac{\partial \hat{a}}{\partial t} = \dfrac{i}{\hbar}[\hat{H}, \hat{a}] - \dfrac{\kappa_a}{2}\hat{a} + \sqrt{\kappa_a}\hat{a}_{\text{in}} \\ \dfrac{\partial \hat{b}}{\partial t} = \dfrac{i}{\hbar}[\hat{H}, \hat{b}] - \dfrac{\kappa_b}{2}\hat{b} + \sqrt{\kappa_b}\hat{b}_{\text{in}} \end{cases}, \tag{5.40}$$

with κ_a and κ_b the coupling rates of modes a and b to the transmission lines. By taking Eq. (5.40) to the Fourier domain and with the input-output relations

$$\begin{cases} \sqrt{\kappa_a}\hat{a}[\omega] = \hat{a}_{\text{in}}[\omega] + \hat{a}_{\text{out}}[\omega] \\ \sqrt{\kappa_b}\hat{b}[\omega'] = \hat{b}_{\text{in}}[\omega'] + \hat{b}_{\text{out}}[\omega'] \end{cases}, \tag{5.41}$$

one obtains the scattering relation [135]

$$\begin{pmatrix} \hat{a}_{\text{out}}[\omega] \\ \hat{b}^{\dagger}_{\text{out}}[\omega'] \end{pmatrix} = \begin{pmatrix} r_{aa} & s_{ab} \\ s_{ba} & r_{bb} \end{pmatrix} \begin{pmatrix} \hat{a}_{\text{in}}[\omega] \\ \hat{b}^{\dagger}_{\text{in}}[\omega'] \end{pmatrix} \tag{5.42}$$

where

$$\begin{cases} r_{aa} = \dfrac{(1-\delta_b)(1-\delta_a) + |\rho|^2}{(1-\delta_b)(1+\delta_a) - |\rho|^2} \\ r_{bb} = \dfrac{(1+\delta_b)(1+\delta_a) + |\rho|^2}{(1-\delta_b)(1+\delta_a) - |\rho|^2} \\ s_{ab} = \dfrac{2i\rho}{(1-\delta b)(1+\delta_a) - |\rho|^2} \\ s_{ba} = \dfrac{-2i\rho^*}{(1-\delta b)(1+\delta_a) - |\rho|^2} \end{cases}. \tag{5.43}$$

with $\rho = 2\chi p/\sqrt{\kappa_a \kappa_b}$, $\delta a = 2i(\omega - \omega_a)/\kappa_a$ and $\delta b = 2i(\omega' - \omega_b)/\kappa_b$. We defined the cooperativity as $C = |\rho|^2$. The gain of the amplifier is defined by $G = |r_{aa}|^2 = |r_{bb}|^2$.

In the large gain limit, the gain curve is given by a Lorentzian function close to the frequency of the amplifier. For a detuning $\Delta\omega$ around the central frequency of the amplifier, the gain reads

$$\boxed{G[\Delta\omega] = \frac{G_0}{1 + (2\Delta\omega/\gamma)^2}} \tag{5.44}$$

where G_0 is the maximum gain and the bandwidth γ of the resonance reads

$$\boxed{\gamma = \frac{2}{\sqrt{G_0}(1/\kappa_a + 1/\kappa_b)}.} \tag{5.45}$$

Measured gain curves are represented on Fig. 5.7(**b**). We achieved typical values of $G_0 = 20$ dB for the power gain over dynamical bandwidths of $\gamma = 3$ MHz.

When the pump is driven above the critical value $C = 1$, the parametric gain overcomes the damping rate of the electromagnetic modes and the oscillator enters the self-oscillation regime [149] similarly to the bifurcation physics of the JPA.

5.4.3 *Flux tunability*

Similarly to the JPA, the operating frequency of the JPC can be tunned by application of an external magnetic flux because of the φ_{ext} dependence of Eq. (5.35). This tunability enable the experimentalist to match the frequency of the system under study. The frequencies of modes a and b are adjustable by varying the external applied flux [39]

$$\boxed{\omega_{a,b}(\varphi_{\text{ext}}) = \omega_{a,b}^{0} \frac{\pi^2 L_{a,b}/2}{\pi^2 L_{a,b}/2 + L_{a,b}(\varphi_{\text{ext}})}} \tag{5.46}$$

where $\omega_{a,b}^{0}$ is the bare frequency of the $\lambda/2$ resonator of mode a (resp. b) without the JRM, $L_{a,b}$ is its equivalent lumped inductance and $L_{a,b}(\varphi_{\text{ext}})$ is the JRM inductance. As long as $E_L/4 + E_J \cos(\varphi_{\text{ext}}) > 0$ the JRM inductance reads

$$L_{a,b}(\varphi_{\text{ext}}) = \varphi_0^2 \left(\frac{E_L}{2} + E_J \cos(\varphi_{\text{ext}}/4) \right)^{-1}. \tag{5.47}$$

The flux dependence of mode a can be observed in Fig. 5.7(**a**). The 'stable configuration' of the ring $E_L/4 + E_J \cos(\varphi_{\text{ext}}) > 0$ corresponds to the wide arches. For small shunting inductances $4 < E_L/E_J$, the stability condition is always met and the narrow arches disappear. The inductance of the ring is then always given by Eq. (5.47).

If we want to work on one of the wide arches and by noticing that a non zero flux bias is required to obtain amplification[3], we can estimate the overall flux tunability of our amplifiers to be of the order of ~ 300 MHz.

5.5 TRAVELLING WAVE PARAMETRIC AMPLIFIER

The last amplifier that we use in our lab is the Josephson traveling wave parametric amplifier (JTWPA) [150, 151, 152, 136] provided by the Lincoln laboratory (MIT). In the section, we describe only briefly its principle of operation since the measurements that I performed with this amplifier are not reported in the present manuscript.

5.5.1 *Phase matching condition*

We saw from Eq. (5.26) and Eq. (5.45) that the gain bandwidth product of our amplifiers are limited by the linewidth of the resonant mode that hosts the non-linearity. In order to get rid of this constraint, one can replace the stationary resonant mode stored in the cavity by a free propagating mode of a transmission line. However, the participation ratio of the non linearity is diluted and the gain of the amplifier vanishes. A way to solve this issue is to create a very long non linear transmission where the non linearity is distributed all over the line. The signal and a large pump tone are sent in the transmission line and a four wave mixing process converts pairs of pump photons into a signal photon and an idler photon. This four-wave mixing process has an hamiltonian of the form $a_P a_P a_S^\dagger a_I^\dagger$ and this process is resonant if and only if the pump and the signal and idler mode are *in phase* all along the line. Obtaining this condition is challenging

3 Because of the $\sin(\varphi_{\text{ext}}/4)$ dependence of the Hamiltonian (5.35).

because the presence of a strong co-propagating pump modifies the phase velocities through self and cross Kerr effects hence generating a *phase mismatch* and preventing an exponential gain during the propagation. However, if this condition is satisfied, the non linear transmission line implements the exact microwave analog of the celebrated optic parametric amplifier [153].

The JTWPA is made of approximately two thousand of periodically repeated sections creating a lumped-element transmission line with a Josephson junction as the inductive element. In [136], every three unit cells of 16 μm, a lumped resonator is inserted in the transmission line to ensure the phase-matching condition in agreement with the proposition of O'Brien *et al.* [152]. Several other attempts were carried out to fulfill the phase-matching condition such as periodic loading of TWPAs based on weak nonlinear kinetic inductance materials [150, 154] but they require a significantly higher pump power to achieve comparable gains combined with a longer propagation length. They are also much more sensitive to backward parametric amplification because the phase-matching direction is satisfied for both directions.

In practice, building such an amplifier is very challenging because of the very large number of repeated sections and any impedance mismatch[4] along the line or any inhomogeneity in the frequency of the resonators creates standing waves in the system that leads to ripples in the transmission signal as a function of frequency and thus a frequency-dependent gain (see Fig. 5.9 **b** and **c**).

5.5.2 *Amplification performance*

Getting rid of the gain-bandwidth constraint leads to remarkable performance as depicted in the measurement of Greg Calusine in Fig. 5.9. We obtain a 20 dB gain over more than 3 GHz in the $4-7$ GHz frequency range (Fig. 5.9 **c**) corresponding to a gain bandwidth product beyond 30 GHz that outperforms our other quantum limited amplifiers by more than two orders of magnitude. The JTWPA acts as a phase-preserving parametric amplifier because of the large spectral separation of the signal and idler modes. By probing the unpumped device with a low power tone, the above-mentioned ripples are observed as well as a large dip corresponding to a *stop-band* created by the resonators inserted along the line. The pump tone should be sent in the vicinity of the stop-band so that the phase-matching condition is met (red arrow on Fig. 5.9 **b**) and the pump power is adjusted to obtain the desired gain at the frequency of interest. This stop-band in the dispersion relation prevents amplification on a 200 MHz window that can easily be avoided when designing our experiments. Finally, the amplifier operates close to the quantum limit as seen from the SNR improvement of the detection chain (Fig. 5.9 **d**) and total quantum efficiencies as high as 0.49% were reported in [136] for qubit readout experiments.

4 A special care must be taken to ensure a continuous impedance matching where the lumped filters are inserted by locally adjusting the parameters of the lumped element of the transmission line.

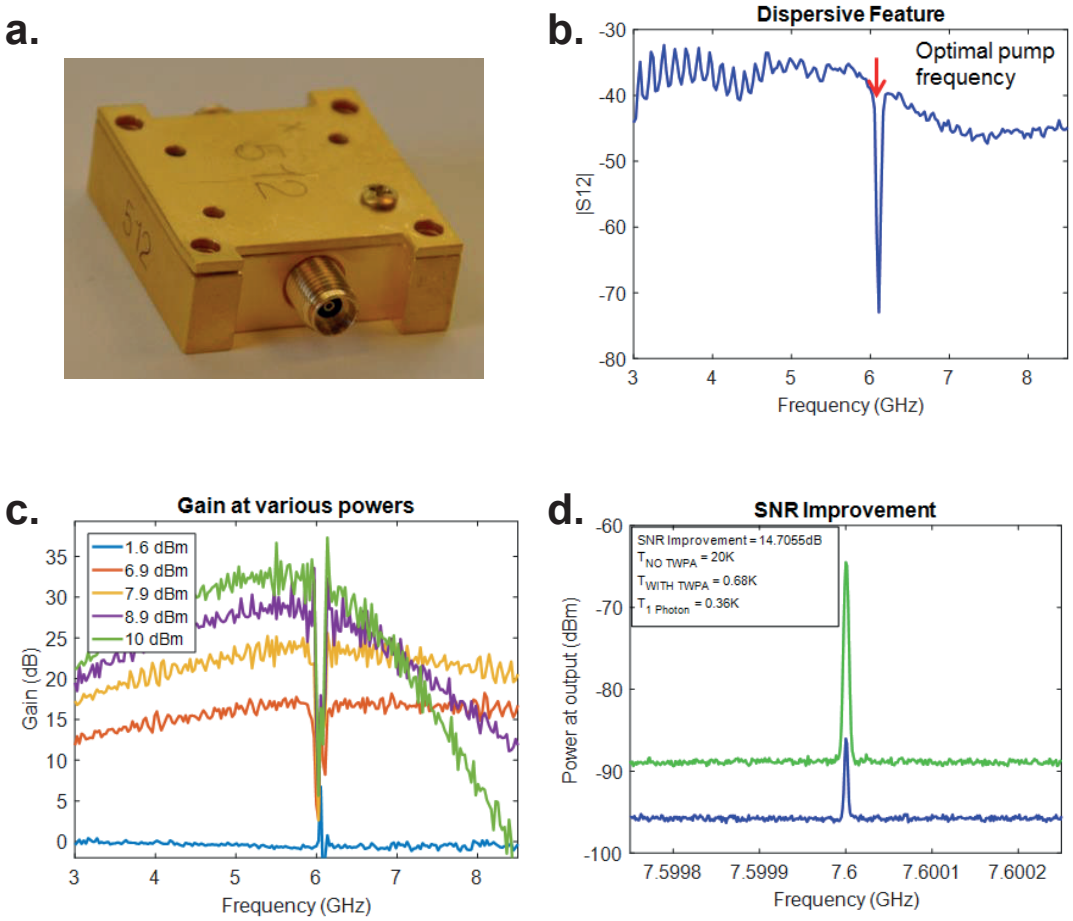

Figure 5.9: Image and measurements performed by Greg Calusine at Lincoln laboratory at MIT [141]. **a.** JTWPA device package. In an actual experiment, the pump is combined with the signal by a directional coupler and routed to the amplifier. The experiments must be isolated from the JTWPA using commercial cryogenic circulators to prevent injection of residual backward amplified noise in the experiment. The device is made of a symmetric lumped-element transmission line so that any of the two ports can be used as the input. A careful handling of the amplifier is appropriate because of the high sensitivity of the device to electrostatic discharge. **b.** Measured transmission coefficient S_{21} through the JTWPA at low power and without any pump. We observe a broadband transmission with some ripples probably due to standing waves arising from imperfect impedance matching along the line or inhomogeneity in the frequency of the filters. A clear dip in the transmission signal is observed around 6.1 GHz corresponding to the so-called *resonant phase-matching* stop band [136]. The optimal pump frequency is indicated by a red arrow. **c.** Power gains for various pump powers. We observe a 20 dB of gain over a dynamical bandwidth of more than 3 GHz leading to a gain bandwidth product beyond 30 GHz. **d.** Noise spectral density at the output of the JTWPA when the pump is on (green) or off (blue). We observe a large SNR enhancement bringing the noise temperature of the detection chain from 20 K to 0.68 K.

5.6 FIGURES OF MERIT OF AMPLIFIERS

In the above sections, we described the amplifiers available in our lab. We saw that phase preserving amplifiers are suitable for heterodyne measurement of a quantum signal whereas phase sensitive amplification is the best choice to perform an homodyne measurement. Several other criteria are important to select the best practical amplifiers for one given experiment. In this section, we enlighten the relevant figures of merit of the amplifiers presented in this chapter and we explain our amplification constraints to carry out the quantum trajectories experiments described in section 6.2.

5.6.1 *Amplifying setup*

Our detection setup is composed of a succession of *low noise amplifiers* amplifiers as depicted in Fig. 5.10 **a** that are designed to amplify *low level signals* with minimal *additive noise*. However, the noise is amplified with the same gain as the signal in addition to any *additive noise*. Therefore the amplifier cannot increase the *signal to noise ratio* (SNR) as the signal level and the noise level rise with the same gain. In the case of narrow band amplifiers, the amplifier is able to filter signals that are out of band but it cannot improve the SNR due to the in-band noise.

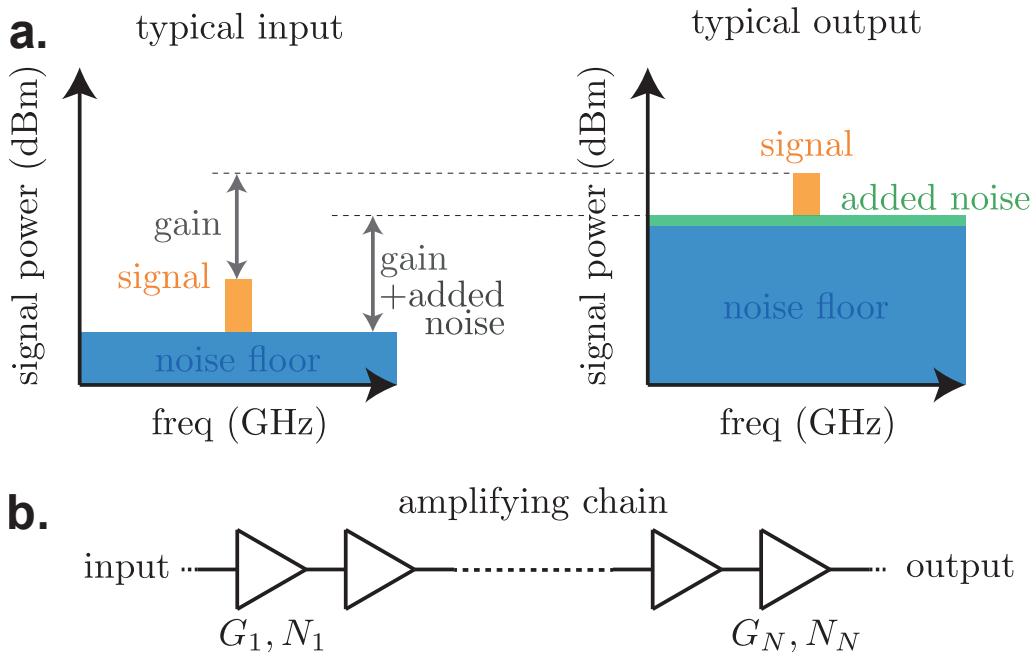

Figure 5.10: **a.** Typical input and output signal of a low noise amplifier. The signal and the noise floor are amplified by the same gain leading to a similar SNR at the input and at the ouput. The degradation of the SNR is due to additive noise referred to the input of the amplifier. **b.** Amplifying chain composed of N low noise amplifiers in series that take a low level signal at the input to a detectable voltage at the end of the chain. Each amplifier has a gain G_i and a noise level N_i. In the large G_1 gain limit, the noise figure of the first amplifier dominates the noise figure of the entire amplifying chain.

It may seem pointless to amplify a signal if the SNR remains unchanged. To understand the relevance of amplification, we need to think about losses. In the case of a chain of amplifiers in series, a loss at the input of one of the amplifiers will not significantly degrade the SNR of the signal if the noise level is already well above the thermal noise level of the lossy channel. Following [40], let us consider the amplifying chain of Fig. 5.10 **b** composed of n amplifiers. Each amplifier has a gain G_i and an input noise level N_i. The total gain of the chain is $G = G_1 \times G_2 \times ... \times G_n$ and the total noise of the chain at the output is

$$N_{\text{output}} = (G_1 G_2 ... G_n) N_1 + (G_2 G_3 ... G_n) N_2 + (G_3 G_4 ... G_n) N_3 + ... \tag{5.48}$$

The total noise of the chain referred to its input reads

$$N = \frac{N_{\text{output}}}{G} = N_1 + \frac{N_2}{G_1} + \frac{N_3}{G_1 G_2} + ... \tag{5.49}$$

This measurement imperfection is best characterized by the total quantum efficiency of the detection setup. In the case of phase preserving amplifiers, the quantum efficiency is given by $\eta_i = \frac{1}{N_i + 1/2}$ where the added noise N_i is expressed in number of photons. As explained in section 5.2.1, the minimal added noise for a phase-preserving amplifier is $1/2$ photon and corresponds to unit quantum efficiency. In the large gain limit $G_i \gg 1$, the inverse detection efficiency of the chain is

$$\boxed{\eta^{-1} = \eta_1^{-1} + \frac{\eta_2^{-1}}{G_1} + \frac{\eta_3^{-1}}{G_1 G_2} + ...} \tag{5.50}$$

If the first low noise amplifier has a sufficiently large gain $G_1 \gg \eta_1/\eta_2, \eta_1/\eta_3 G_2, ...$, the noise figure of the first amplifier dominates the noise figure of the entire amplifying chain.

The most widespread commercial low noise amplifier able to operate at cryogenic temperature of about 4 K are High Electron Mobility Transistor (HEMT) amplifiers. They are able to reach high gain values around 40 dB on a bandwidth of several GHz but they are limited by their input noise of $2.5 - 4$ K for Caltech HEMT amplifiers [155] and $2 - 2.5$ K for Low Noise Factory (LNF) HEMT amplifiers [156] at 5 GHz. The gain conversion between a noise temperature T and a number of photons N is given by the Bose-Einstein statistics

$$N = \frac{1}{e^{\hbar\omega/k_B T} - 1} = \frac{1}{2} \coth\left(\frac{\hbar\omega}{2k_B T}\right) - \frac{1}{2}. \tag{5.51}$$

Commercial amplifiers add of the order of 8 photons to the input signal before amplification at 5 GHz. If we take into account the losses between a qubit and an amplifying chain we find that the total added noise is equivalent to 20 photons at 5 GHz. Our experiments require high detection efficiencies that are incompatible with using HEMT amplifiers as the first detector of the chain.

5.6.2 *Gain*

A sufficient power gain of the near quantum limited amplifier that is the closest to the system of interest is needed so that a significant part of the noise that we measure is

due to zero-point fluctuations. Operating a quantum limited amplifier with a 20 dB power gain as the first amplifier of the chain followed by a HEMT brings the noise temperature of the HEMT to about 0.08 photons at 5 GHz referred to the input of the chain. Roughly speaking, it means that about 16% of the measured noise is technical noise coming from the HEMT amplifier and the other 84% comes from zero-point fluctuations[5]. In section 6.2, we measure quantum trajectories with a JPA operated with a gain of 22 dB and a JPC with a gain of 17 dB to make sure that the efficiency of the detection chain is mainly limited by the efficiency of the first quantum limited amplifier and not by the noise temperature of the following HEMT. A gain of 22 dB set an upper bound of 94% on the quantum efficiency of detection of the dispersive signal at 7.8 GHz while a gain of 17 dB set an upper bound of 70% on the quantum efficiency of detection of fluorescence at 5.3 GHz.

5.6.3 *Quantum efficiencies*

The signal-to-noise ratio (SNR) of the measurement is limited by unavoidable losses in the cables, insertion losses at the input of the amplifier in addition to the above-mentioned noise temperature of the HEMT. The losses in the lines and microwave components (diplexer and circulators) before the signal reaches the amplifier are estimated to be at least of the order of -1.5 dB which leads to an efficiency $\eta_{\text{cables}} \sim 0.7$. Since the first amplifier is not perfectly quantum limited, the inefficiency of the quantum amplifier itself is routinely modeled as a beam splitter with a transmission $\eta_{\text{amplifier}}$ followed by a lossless device. The beam splitter mixes the input signal with an extra channel, which unavoidably comes with an additional noise. Intrinsic quantum efficiencies of JPA and JPC can reach 1 in principle but they are often reported to have a finite value greater than 80% [40]. For the fluorescence signal we must introduce an additional collection efficiency $\eta_{\text{coll}} = \frac{\kappa_{\text{out}}}{\kappa_{\text{tot}}} \simeq 87\%$ that contains the probability that a qubit emits a photon into the output line during a relaxation event [157]. In practice our total quantum efficiencies are the product of all the above mentioned efficiencies and they were limited to 34% for the JPA and 14% for the JPC[6].

5.6.4 *Dynamical bandwidth*

In order to measure the real time dynamics of a quantum system continuously, the dynamical bandwidth of the amplifier has to be larger than the typical rates and frequency of the evolution of interest. However, amplitude gain of the amplifier is inversely proportional to the bandwidth of the amplifier (see Eq. (5.26)). The gain-bandwidth product of the device being constant, there is a tradeoff between reactivity and gain for our amplifiers. In practice we decided to operate both amplifiers with a bandwidth of 4.25 MHz that led to the above-mentioned gains to reach a sampling time of $dt = 100$ ns separating two successive independent measurements.

5 We assume in this simplified calculation that there is no extra added noise by the first amplifier of the chain.

6 We also showed by numerical simulation in section 6.4 that the quantum efficiency of the detection setup only qualitatively changes the statistics of quantum trajectories for efficiencies up to 75%.

5.6.5 *Static bandwidth*

The frequency tunability of the amplifiers allows to shift the operating frequency on a range called the *static bandwidth*. It was of the order of 300 MHz for the JPC and 500 MHz for the JPA. This figure characterizes our ability to match the center frequency of each amplifier with either the frequency of the qubit or cavity. In practice it took us several tries to get the correct frequency agreement with decent quantum efficiencies because of fabrication uncertainties and aging of the junctions that shift the frequencies from one cool-down to another.

5.6.6 *Dynamical range*

The 1 dB-*compression point* is defined by the amount of input power beyond which the power gain is reduced by 1 dB. The theories described above rely on the first order expansion of the cosine of the inductive part of the Hamiltonian. When the number of photons inside the amplifier increases this approximation breaks down and the power gain starts to deteriorate[7]. Higher order non linearities are known to limit not only the gain of the amplifiers but the quantum efficiencies and to introduce non gaussian signatures in the output field [144]. 1 dB-compression points of the order of -120 dBm are routinely reported for JPAs and JPCs. In our experiments, we operated within the single photon limit so the compression of the amplifier gain is negligible for both measurements and this figure of merit is not important.

5.6.7 *Comparison between two detection chains and a JTWPA*

In the final year of this thesis, we received a JTWPA from Lincoln Labs [141], which has incredible performances in term of gain-bandwidth product and a very high 1 dB-compression point[8] of -95 dBm when operated with a gain greater than 15 dB. This amplifier could have been used as a quantum limited amplifiers for both measurement channels and total quantum efficiencies has high as 49% are reported for qubit readout [136]. However, using a phase preserving amplifier to perform an homodyne detection leads to an effective reduction of the quantum efficiency of the chain. In current state of the art experiments, the JTWPA is placed after JPAs or JPCs pre-amplifiers and immediately followed by a HEMT amplifier [49] to obtain a maximal quantum efficiency.

7 Note that the 1 dB-compression point of a JPA can be increased by replacing the SQUID with an array of M SQUIDS. It changes the inductive energy $-E_J \cos(\varphi) \rightarrow -ME_J \cos(\varphi/M)$ so the non-linearity is 'distributed' over several junctions [158].

8 JTWPA are designed for multiplexed readout of many qubits. A broadband gain combined with a high 1 dB-compression point is required for this kind of application.

5.7 CONCLUSION

This chapter was dedicated to the operation principle of quantum limited amplifiers. We explained

- the general distinction between phase preserving and phase sensitive amplification.
- the choice of design and operating principle of the Josephson parametric amplifier (JPA) with a detailed discussion on the different pumping schemes.
- the Josephson ring modulator (JRM) and its use in the Josephson parametric converter (JPC).
- the figures of merit of the different amplifiers and their optimization for our experiments.

The field of superconducting amplifiers in the microwave domain is still a very active field of research. Recent works are pushing further the limitations mentioned in this chapter. *Roy et al.* went beyond the usual gain-bandwidth product by correctly engineering the input impedance of a JPA [145]. Quantum efficiencies as high as 80% were reported [159] by placing an artificial atom directly inside a parametric amplifier[9]. The Josephson junctions can be replaced by a pure three-wave mixing Josephson dipole element [160] to reduce the non-linearity of the amplifier. There has been interest is developing quantum limited nonreciprocal devices [161, 162, 163, 146, 164, 165]. The long term goal is to replace the lossy commercial isolators between the system and the amplifier by a on-chip nonmagnetic nonreciprocal device compatible with superconducting technology.

9 The amplification chain following the device was composed of a JPA, a JTWPA, a HEMT and room temperature amplifiers.

Part II

MEASUREMENT BACK-ACTION

6

QUANTUM TRAJECTORIES

One of the first non-classical aspects we learn about quantum mechanics is that measuring a system affects its state. This measurement back-action can lead to great confusion if one does not recall precisely what is a quantum state. For instance, why would the state of a system S depend on the fact that an observer recorded the measurement outcome or not? A quantum state is nothing but an efficient way of encoding anything one can predict about the statistics of a future measurement on the system. OK but statistics on what ensemble? The prediction in fact concerns statistics on realizations of the experiment with common assumptions. When we say that the measurement affects the state of a quantum system, it means that if we do the statistics on realizations where that measurement lead to a given outcome, it may differ from the statistics on realizations where we do not condition on the measurement outcome at all. In a given realization of an experiment, several observers may have different quantum states. There is no conflict in their predictions as they do not concern identical selections of experimental realizations. Simply, the observers that extract more information will be able to predict better the outcome of a later measurement for a given realization. Therefore, the measurement back-action boils down to calculating conditional probabilities on quantum systems measurements. The way a quantum measurement modifies a quantum state is thus specific to the nature of the measurement and to the outcome that the observer records.

This chapter is dedicated to the *quantum back-action* of continuous measurements on a spin-1/2 with two kinds of detectors by several observers. We were able to reconstruct the modified quantum state of the system as a function of time from the experimental records, from the point of view of three observers. This path in the Hilbert space is called a quantum trajectory. The continuous reconstruction of the state of the system is described by the formalism hereinafter referred to as repeated Kraus operations or quantum *Stochastic Master Equation* (SME) in the continuous time limit. The concept of quantum trajectories dates back to the 1990's, when they were introduced [166, 42, 167] as a mathematical trick to reduce the complexity of Monte Carlo simulation of Lindblad equation[1]. In the case of weak measurements of a quantum system, the state diffuses in the Hilbert space under the stochastic measurement backaction. This diffusion was first predicted in 1992 as a mathematical possibility by Gisin and Percival [41] and understood a year later as corresponding to a physical measurement backaction by Wiseman and Milburn [168]. Excellent reviews on the subject can be found in [42, 44, 45, 46].

Diffusive quantum trajectories were observed in two physical systems until now. Using a series of propagating Rydberg atoms, it was possible to measure weakly and repeatedly the state of a microwave cavity and reconstruct its quantum trajectories [43]. This

1 The idea was to replace the open dynamics of an $N \times N$ density matrix by a collection of pure stochastic wave functions of dimension N.

pioneer experiment soon found its equivalent in the field of superconducting circuits. Indeed, owing to the development of high-efficiency quantum limited detectors in the microwave domain over the last decade, it became possible to realize weak continuous measurement of superconducting qubits with observable measurement backaction. Before the present work, several experimental reconstructions of quantum trajectories were performed using continuous homodyne [27, 28, 29] or heterodyne [26] detection of a dephasing channel, homodyne [25] or heterodyne [23] detection of fluorescence. More exotic experiments were carried out such as the observation of quantum trajectories of two qubits [47, 48, 169] or the simultaenous detection of two incompatible dephasing channels [49, 170].

We will first explain the effect of a weak measurement on the state of the system by tracking its evolution conditioned on the measurement outcome by using the generalized measurement theory explained in chapter 3. Second, we will describe a sequence of such measurements forming a diffusive *quantum trajectory* and prove that they provide a faithful record of the state of the system. Then, we will describe the statistics of the trajectories and observe a continuous transition from the *Zeno regime* to the usual Rabi oscillations. Similarly to other diffusion phenomena, the probability to find a quantum trajectory at a given time and position inside the Bloch sphere is ruled by the *Fokker-Planck* equation. The diffusion tensor reveals that the trajectory diffuses in 3 dimensions and the magnitude of the diffusion is lower bounded by a *Heisenberg-like inequality*.

6.1 QUANTUM BACK-ACTION OF MEASUREMENT

6.1.1 *Kraus operators formulation*

The Copenhagen interpretation of quantum mechanics usually arouses every student curiosity because of its measurement postulates that imply an instantaneous collapse of the density matrix whenever a *Von Neumann measurement* occurs. We introduced the concept of generalized measurements in chapter 3 wherein the system first interacts with a probe that finally undergoes a Von Neumann measurement resulting in a *partial collapse* of the density matrix of the system. While keeping the same postulates[2], this paradigm allows us to 'zoom' in on the measurement process and observe the dynamics of the collapse of the density matrix. Let us assume that the state of the system under study is described by a density matrix ρ. Immediately, after the measurement of an outcome μ, the conditional state of the system is given by Eq. (3.5)

$$\rho_\mu = \frac{M_\mu \rho M_\mu^\dagger}{\mathrm{Tr}(M_\mu \rho M_\mu^\dagger)} \tag{6.1}$$

where $\{M_\mu\}$ is a set of Kraus operators. In the continuous measurement limit, we saw that one of these operators can be singled out as being the 'no-click' Kraus operator

$$M_0 = \mathbb{1} - \frac{i}{\hbar} H dt - J dt \tag{6.2}$$

2 Our approach does not solve the philosophical questions associated to the measurement postulates but it allows us to understand some of the consequences of this theory.

while the others are at best of order $\sqrt{dt}$ i.e.

$$M_\mu = \sqrt{dt} L_\mu, \tag{6.3}$$

where the $\{L_\mu\}$ are the *jump operators* of order unity and $J = \frac{1}{2}\sum_{\mu\neq 0} L_\mu^\dagger L_\mu$. To clarify the discussion, let us take the example of a spin-1/2 spontaneously emitting photons collected by a photocounter. We work in the rotating frame oscillating at the frequency of the atom so that $H = 0$ in this frame. There is only one jump operator $L = \sqrt{\Gamma_1}\sigma_-$ where Γ_1 is the inverse lifetime of the atom. If no photons are detected, the state of the system evolves according to Eq. (6.1) under the 'no-click' operator

$$M_0 = \mathbb{1} - \frac{\Gamma_1}{2}\sigma_+\sigma_- dt \tag{6.4}$$

and this possibility happens with probability $p_0 = \mathrm{Tr}(M_0 \rho M_0^\dagger) = 1 - \frac{dt\Gamma_1}{2}(1+z) + O(dt^2)$. When one photon is detected, the system evolves under the 'click operator'

$$M_1 = \sqrt{\Gamma_1 dt}\sigma_- \tag{6.5}$$

with an associated probability $p_1 = \mathrm{Tr}(M_1 \rho M_1^\dagger) = \frac{\Gamma_1 dt}{2}(1+z)$. At order dt, the complete evolution of the system can be recasted with a unique operator M as follows

$$\begin{cases} \rho_{t+dt} = \dfrac{M\rho_t M^\dagger}{\mathrm{Tr}(M\rho_t M^\dagger)} \\ \text{with } M = \mathbb{1} - \dfrac{\Gamma_1}{2}\sigma_+\sigma_- dt + N\sqrt{dt} \end{cases} \tag{6.6}$$

where $N = 0$ if no click ocured and $N = 1$ if a photon was detected during dt, N is a discrete stochastic variable (a Poisson process) sampled with probability p_0 and $p_1 = 1 - p_0$. If the photocounter has a finite efficiency $0 \leq \eta \leq 1$, the relation of evolution Eq. (6.6) becomes [44, 171]

$$\begin{cases} \rho_{t+dt} = \dfrac{M\rho_t M^\dagger + (1-\eta)\Gamma_1 dt \sigma_-\rho_t\sigma_+}{\mathrm{Tr}\left(M\rho_t M^\dagger + (1-\eta)\Gamma_1 dt \sigma_-\rho_t\sigma_+\right)} \\ \text{with } M = \mathbb{1} - \dfrac{\Gamma_1}{2}\sigma_+\sigma_- dt + \sqrt{\eta}N\sqrt{dt} \end{cases} \tag{6.7}$$

where the new term $\Gamma_1\sigma_-\rho_t\sigma_+$ corresponds to the Kraus evolution resulting from an unread measurement performed by the environment. This unread measurement happens with a probability $1-\eta$ to account for imperfect detection of the photocounter.

The Eq. (6.7) gives the conditional evolution of the density matrix depending on the output of the detector and we showed that the Kraus formulation encompasses at the same time the decoherence resulting from the unread part of the measurement and the innovation of the density matrix due to the stochastic output N of the measurement. Let us apply this formalism to our experiments with either the homodyne detection of the cavity field or the heterodyne detection of fluorescence and compare the integrated measurement records with a subsequent and independent tomography of the partially collapsed system.

6.1.2 *Dispersive interaction*

In the case of the continuous dispersive measurement, the jump operator is of the form $L_w = \sqrt{\frac{\eta_d \Gamma_d}{2}}\sigma_z$ and the evolution of the state is given by the Kraus map

$$\begin{cases} \rho_{t+dt} = \dfrac{\mathbf{K}(\rho_t)}{\mathrm{Tr}(\mathbf{K}(\rho_t))} \\ \text{where } K(\rho_t) = M\rho M^\dagger + (1-\eta_d)\dfrac{\Gamma_d}{2}\sigma_z\rho\sigma_z dt \\ \text{and } M = \mathbb{1} - \left(\dfrac{i}{\hbar}H + \dfrac{\Gamma_d}{4}\right)dt + \sqrt{\dfrac{\eta_d\Gamma_d}{2}}\sigma_z w(t)dt \\ \text{with the record } w(t)dt = \sqrt{2\eta_d\Gamma_d}z_t dt + dW_w(t) \end{cases} . \tag{6.8}$$

The expression of the measurement records comes from Eq. (3.23) and $z_t = \mathrm{Tr}(\sigma_z\rho_t)$ is the z component of the Bloch vector. Note that we neglected any energy relaxation of the qubit and the pure dephasing of the artificial atom so Eq. (6.8) is valid for times much smaller than $T_1 \simeq 15$ μs and $T_\varphi = 17.9$ μs. In the case of an undriven system, the projections of Eq. (6.8) along the Bloch coordinates in the rotating frame of the qubit read

$$\begin{cases} dx_t = -\Gamma_d x_t dt - \sqrt{2\eta_d\Gamma_d}x_t z_t dW_w(t) \\ dy_t = -\Gamma_d y_t dt - \sqrt{2\eta_d\Gamma_d}y_t z_t dW_w(t) \\ dz_t = \sqrt{2\eta_d\Gamma_d}(1-z_t^2)dW_w(t) \end{cases} . \tag{6.9}$$

In the actual experiments (Fig. 6.1), we integrate the record $w(t)dt$ of Eq. (6.8) during a time $T = 1$ μs $\ll T_1$ and we compare it with an independent tomography (see Fig. 6.1 **a**) similarly to Murch *et al.* [27]. Owing to the stochastic nature of Eq. (6.9), integration and differentiation require the so-called Ito's formula.

For a stochastic variable[3] H_t of the form

$$dH_t = A_t dt + B_t dW_t \tag{6.10}$$

where dW_t is a *Brownian motion*. The differential of a function $f(H_t, t)$ that depends on the stochastic variable H_t is modified according to Ito's formula

$$d(f(H_t,t)) = \frac{\partial f}{\partial t}(H_t,t)dt + \frac{\partial f}{\partial h}(H_t,t)dH_t + \frac{1}{2}\frac{\partial^2 f}{\partial h^2}(H_t,t)B_t^2 dt \tag{6.11}$$

From Eq. (6.11) we obtain

$$d(\mathrm{arctanh}(z_t)) = \frac{dz_t}{1-z_t^2} + 2z_t\eta_d\Gamma_d dt = \sqrt{2\eta_d\Gamma_d}w(t)dt \tag{6.12}$$

that can be integrated between 0 and T to obtain the evolution of the z component of the qubit under measurement as a function of the integrated measurement record

$$\mathrm{arctanh}(z_T) = \mathrm{arctanh}(z_0) + \sqrt{2\eta_d\Gamma_d}\int_0^T w(t)dt. \tag{6.13}$$

3 In our experiments, dH_t plays the role of the increments of the Bloch coordinates (dx_t, dy_t, dz_t).

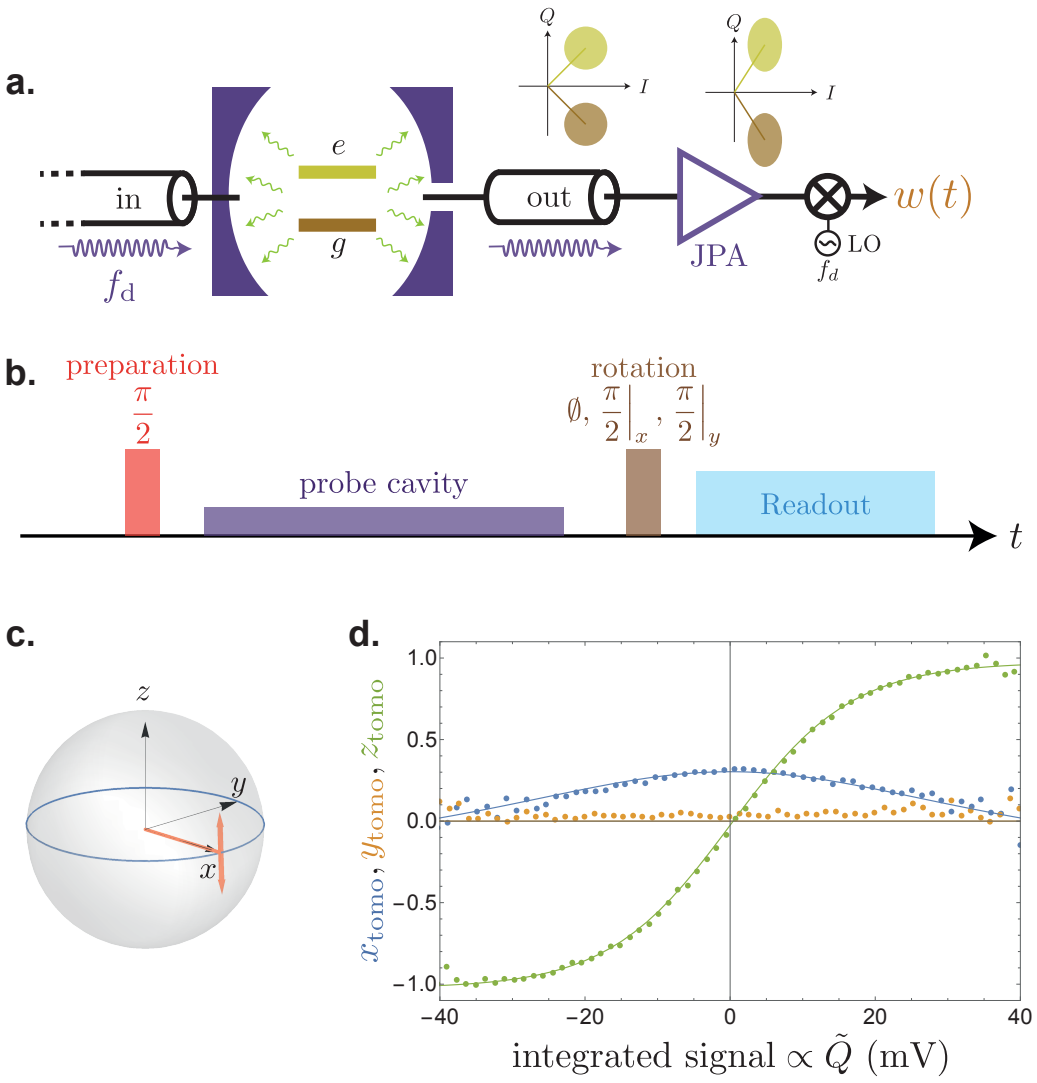

Figure 6.1: **a.** Similarly to section 3.2. We amplify and detect the imaginary quadrature $\text{Im}[a_{\text{out}}]$ of the cavity field leading to the measurement record $w(t)$. The signal in the IQ plane is squeezed along the Q quadrature before mixing with the local oscillator. The measurement records encode the σ_z component of the qubit state according to Eq. (6.8). **b.** Pulse sequence. We initialize the qubit in $\langle\sigma_x\rangle = 1$ with a $\pi/2$ pulse. We integrate the measurement records $w(t)$ during $T = 1$ μs, $\tilde{Q} = \int_0^T w(t)dt$. We then perform a strong tomography of σ_x, σ_y or σ_z at the end of the experiment. **c** Back-action of the measurement on a qubit superposition state. The state of the system is thrust toward $|g\rangle$ (south pole) or $|e\rangle$ (north pole) depending on the sign and magnitude of the integrated record $\tilde{Q}$. **d.** We gather the experimental realizations yielding the same integrated measurement record $\tilde{Q}$ within ± 1 mV and we average the tomography results over 5×10^6 realizations. The signal measured at the output of the refrigerator $\tilde{Q}$ is amplified with a constant (cables attenuation, LO power, ...) that was calibrated by measuring the output noise of the detection setup (see section 6.2.3.1). The correlation between the integrated records and the tomography behaves according to Eq. (6.15) (solid lines) with a quantum efficiency $\eta_d = 25\%$ and measurement induced dephasing rate $\Gamma_d = 0.95$ μs in agreement with independent calibrations. Note that the value of η_d is smaller than the one used to unravel quantum trajectories in section 6.2 because the JPA was operated at a different operating point.

Moreover we can infer the z component of the qubit because Sarlette and Rouchon showed [172] that the dynamics of the density matrix is confined to an ellipsoid for this detection. The equation of the ellipsoid reads

$$x_t^2 + y_t^2 + b_t(z_t^2 - 1) = 0 \tag{6.14}$$

where $\gamma = (1-\eta_d)\Gamma_d$ and $b_t = b_0 e^{-\gamma t}$ with b_0 determined by the initial conditions. The confinement of the dynamics to this manifold can be shown by direct calculation from Eq. (6.11) and a physical explanation is given in section 6.4.

From Eq. (6.13) and Eq. (6.14), we obtain that for a qubit initialized in the pure state $|+\rangle = (|g\rangle + |e\rangle)/\sqrt{2}$ [27],

$$\boxed{\begin{cases} x_T = \sqrt{1 - z_T^2}\, e^{-\gamma T} \\ y_T = 0 \\ z_T = \tanh\left(\sqrt{2\eta_d \Gamma_d}\tilde{Q}\right) \end{cases}} \tag{6.15}$$

where $\tilde{Q} = \int_0^T w(t)dt$ is the integrated measurement record.

We perform such an experiment in Fig. 6.1 **a-b**, we recall the detection setup and the pulse sequence for this measurement. The back-action of the weak measurement takes the state of the qubit away from the equator and brings it toward one of the pointer states of the measurement $|g\rangle$ or $|e\rangle$ depending on the integrated signal (Fig. 6.1 **c**). We can check the prediction of Eq. (6.15) to demonstrate that the Kraus operator formalism (6.8) accurately describes the update of the quantum state conditioned on the measurement record. This measurement provides a calibration of the quantum efficiency of the detection setup $\eta_d = 25\%$ in agreement with the method of section 3.2.

We demonstrated that we are able to observe the partial collapse of the wave function under the *weak measurement* of an observable. When the integrated signal is close to zero, no information was extracted on the state of the system. The density matrix stays close to the equator. When the integrated signal is extremal, the qubit state collapses in $|g\rangle$ or $|e\rangle$. Increasing the measurement rate $\eta_d\Gamma_d \to +\infty$, the hyperbolic tangent of Eq. (6.15) can be replaced by a step function. We then recover the case of a *Von Neumann measurement*.

6.1.3 *Measurement along the orthogonal quadrature*

By changing the phase of the pump of the JPA, we can tune the squeezed quadrature of the amplifier. The information on the qubit state is encoded in the phase of the outgoing signal that only contributes to the imaginary part of a_{out}. This former quadrature is thus always chosen to readout a qubit. Conversely, the real part of the field does not depend on the state of the qubit. It is thus discarded when performing a tomography. In this section, we demonstrate that the fluctuations of the real quadrature of the signal carry the information about the back-action of the measurement induced dephasing [27].

The jump operator of the problem is $L_{w'} = iL_w = i\sqrt{\frac{\eta_d\Gamma_d}{2}}\sigma_z$. The projected dynamics reads

$$\begin{cases} dx_t = -\Gamma_d x_t dt + \sqrt{2\eta_d\Gamma_d}y_t dW_w(t) \\ dy_t = -\Gamma_d y_t dt + \sqrt{2\eta_d\Gamma_d}x_t dW_w(t) \\ dz_t = 0 \end{cases} \tag{6.16}$$

with the measurement record

$$w'(t)dt = dW_{w'}(t). \tag{6.17}$$

Note that in this case, the total output signal of the detection setup corresponds to an offset signal $\kappa\sqrt{\frac{n\kappa}{\kappa^2+\chi^2}}$ (projection along the Q axis of the mean of the distributions in Fig. 6.2 **a**) with n the average number of photons stored inside the cavity plus the measurement record (6.17) that contains noise alone. This case is very interesting because the measurement record (6.17) does not depend on ρ but still induces a back-action on the qubit state. The integrated record allows us to track the evolution of the qubit state according to Eq. (6.16). This measurement leads to a diffusive behavior of the qubit state along the equator of the Bloch sphere (Fig. 6.2 **c**). It can even be corrected by feedback if one wants to stabilize a given state [28].

Similarly to the previous case, the state of the qubit is confined to a deterministic circle [172] at a constant z altitude in the Bloch sphere. Besides,

$$x_t^2 + y_t^2 = e^{-\gamma t}, \tag{6.18}$$

where $\gamma = (1-\eta)\Gamma_d$ is the measurement induced dephasing rate corresponding to the unmonitored part of the cavity field. A physical explanation of this property is given in section 6.4. Let us use Ito rule (6.11) and differentiate

$$\begin{cases} d(\arccos(\tilde{x}_t)) = \dfrac{\eta_d\Gamma_d\tilde{x}_t dt}{\sqrt{1-\tilde{x}_t^2}}\left(1 - \dfrac{\tilde{y}_t^2}{1-\tilde{x}_t^2}\right) - \dfrac{\sqrt{2\Gamma_m}\tilde{y}_t dW_{w'}(t)}{\sqrt{1-\tilde{x}_t^2}} \\ d(\arcsin(\tilde{y}_t)) = -\dfrac{\eta_d\Gamma_d\tilde{y}_t dt}{\sqrt{1-\tilde{y}_t^2}}\left(1 - \dfrac{\tilde{x}_t^2}{1-\tilde{y}_t^2}\right) - \dfrac{\sqrt{2\Gamma_m}\tilde{x}_t dW_{w'}(t)}{\sqrt{1-\tilde{y}_t^2}} \end{cases} \tag{6.19}$$

where $\tilde{x}_t = e^{\gamma t}x_t$ and $\tilde{y}_t = e^{\gamma_t}y_t$. Using Eq. (6.18), the expression boils down to

$$\begin{cases} d(\arccos(e^{\gamma t}x_t)) = -\sqrt{2\eta_d\Gamma_d}dW_{w'}(t) \\ d(\arcsin(e^{\gamma t}y_t)) = \sqrt{2\eta_d\Gamma_d}dW_{w'}(t) \end{cases}. \tag{6.20}$$

We obtain the evolution of the Bloch coordinate between 0 and T as a function of the integrated measurement record, for a qubit starting in $(|g\rangle + |e\rangle)/\sqrt{2}$

$$\boxed{\begin{cases} x_T = \cos\left(\sqrt{2\eta_d\Gamma_d}\tilde{I}\right)e^{-\gamma T} \\ y_T = \sin\left(\sqrt{2\eta_d\Gamma_d}\tilde{I}\right)e^{-\gamma T} \end{cases}} \tag{6.21}$$

where $\tilde{I} = \int_0^T w'(t)dt$ is the integrated measurement record.

Histograms of the integrated measurement (Fig. 6.2) records reveal a clear correlation with the final tomography according to Eq. (6.21). We find a corresponding quantum efficiency of $\eta_d = 24\%$ with the same operating point as in Fig. 6.1.

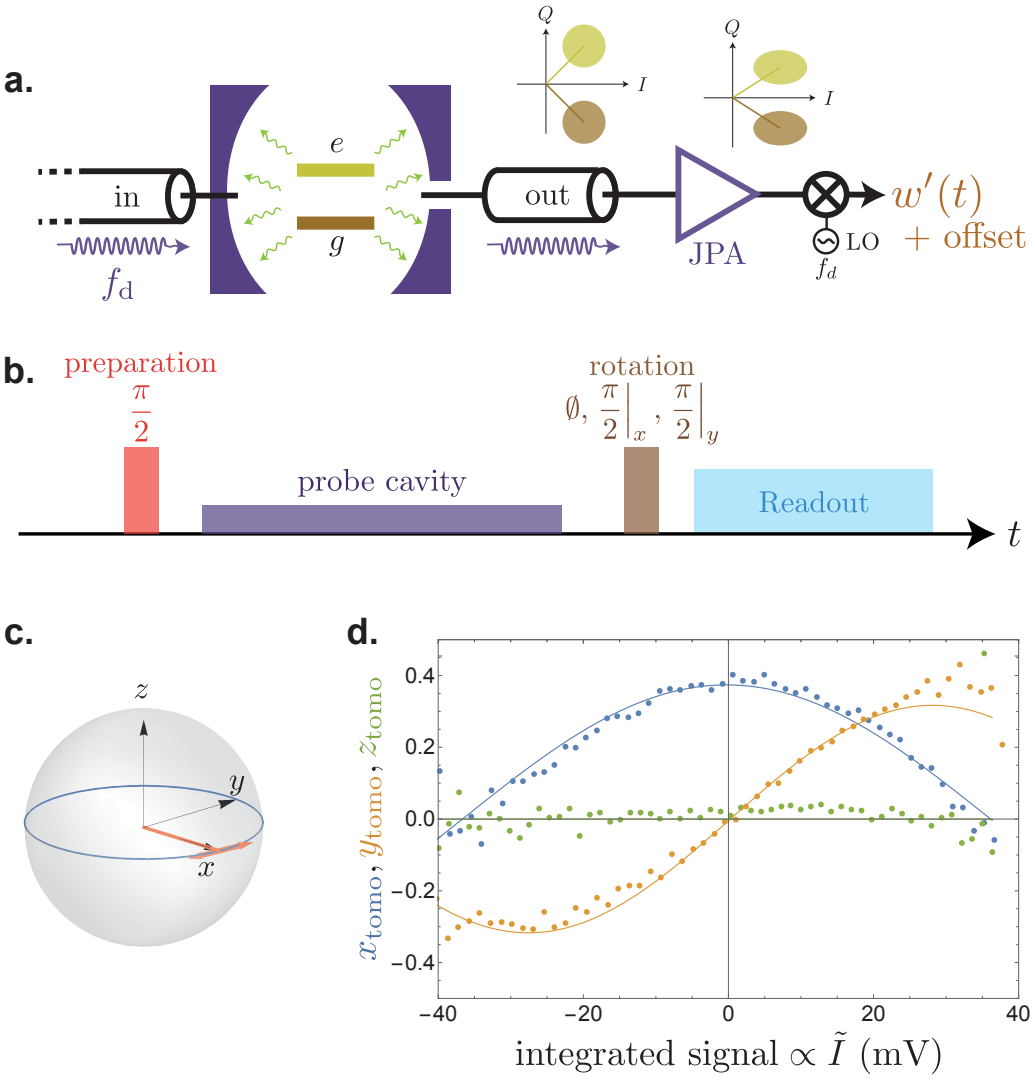

Figure 6.2: **a.** We amplify and detect the quadrature $\mathrm{Re}[a_{\mathrm{out}}]$ of the cavity field leading to the measurement record $w'(t)$. The signal in the IQ plane is squeezed along the I quadrature before mixing with the local oscillator. The measurement records do not depend on the qubit state according to Eq. (6.17) but its noise contains the information on the dephasing of the qubit. Note that we do not take into consideration the offset signal $\kappa\sqrt{\frac{n\kappa}{\kappa^2+\chi^2}}$ in the IQ plane so that $w'(t)$ has a zero average. **b.** Pulse sequence. We initialize the qubit in $\langle\sigma_x\rangle = 1$ with a $\pi/2$ pulse. We integrate the measurement records $w'(t)$ during $T = 1$ μs, $\tilde{I} = \int_0^T w'(t)dt$. We perform a strong tomography of σ_x, σ_y or σ_z at the end of the experiment. **c** Back-action of the measurement on a qubit superposition state. The state of the system picks up a random phase that depends on the measurement record. **d.** We gather the experimental realizations yielding the same integrated measurement record $\tilde{I}$ and we average the tomography results over 5×10^6 realizations. The signal measured at the output of the refrigerator $\tilde{I}$ is amplified by a constant that was calibrated by measuring the output noise of the detection setup (see section 6.2.3.1). The correlation between the integrated records and the tomography behaves according to Eq. (6.21) (solid lines) with a quantum efficiency $\eta_d = 24\%$ and measurement induced dephasing rate $\Gamma_d = 0.95$ μs in agreement with independent calibrations.

6.1.4 *Fluorescence signal*

One can also investigate the back-action of the fluorescence measurement. Following [85], we obtain integrable quantities for the monitoring of energy relaxation. In this case, the evolution of the density matrix is related to *integrated weighted signal* and not to the raw integrated signals. The problem is described by two jump operators $L_u = \sqrt{\Gamma_1/2}\sigma_-$ and $L_v = iL_u$. Similarly to Eq. (6.8), we can write the incremental evolution of the density matrix as a function of Kraus operators

$$\begin{cases} \rho_{t+dt} = \dfrac{\mathbf{K}(\rho_t)}{\mathrm{Tr}(\mathbf{K}(\rho_t))} \\ \text{where } K(\rho_t) = M\rho M^\dagger + (1-\eta_f)\Gamma_1(\sigma_-\rho\sigma_+)dt \\ \text{and } M = \mathbb{1} - (\dfrac{i}{\hbar}H + \dfrac{\Gamma_1}{2}\sigma_+\sigma_-)dt + \sqrt{\dfrac{\eta_f\Gamma_1}{2}}\sigma_-(u(t)+iv(t))dt \end{cases}. \tag{6.22}$$

with the records

$$\begin{cases} u(t)dt = \sqrt{\dfrac{\eta_f\Gamma_1}{2}}x_t dt + dW_u(t) \\ v(t)dt = \sqrt{\dfrac{\eta_f\Gamma_1}{2}}y_t dt + dW_v(t) \end{cases}. \tag{6.23}$$

In the case $H = 0$, projecting Eq. (6.22) along the Bloch coordinates yields

$$\begin{cases} dx_t = -\dfrac{\Gamma_1}{2}x_t dt + \sqrt{\dfrac{\eta_f\Gamma_1}{2}}\left((1+z_t-x_t^2)dW_u(t) - x_t y_t dW_v(t)\right) \\ dy_t = -\dfrac{\Gamma_1}{2}y_t dt + \sqrt{\dfrac{\eta_f\Gamma_1}{2}}\left((1+z_t-y_t^2)dW_v(t) - x_t y_t dW_u(t)\right) \\ dz_t = -\Gamma_1(1+z_t)dt - \sqrt{\dfrac{\eta_f\Gamma_1}{2}}(1+z)(xdW_u(t) + ydW_v(t)) \end{cases} \tag{6.24}$$

Remarkably, the dynamics of the quantum state predicted by Eq. (6.24) is restricted to the surface of a deterministic *spheroid* going through the south pole of the Bloch sphere [23, 172]

$$c_t(x_t^2 + y_t^2) + c_t^2\left(z_t + 1 - \frac{1}{c_t}\right)^2 = 1 \tag{6.25}$$

where $c_t = \eta_f + (c(0) - \eta)e^{\Gamma_1 t}$ and $c(0)$ is determined by the initial condition. We worked in the presence of a parasitic pure dephasing of rate $\Gamma_\varphi \simeq (27\ \mu\mathrm{s})^{-1}$ that leads to an additional decoherence dynamics $dx_t = -\Gamma_\varphi x_t dt$ and $dy_t = \Gamma_\varphi y_t dt$. Using Ito rule

$$\begin{cases} d\left(\dfrac{x_t}{1+z_t}\right) = \left(\dfrac{\Gamma_1}{2} - \Gamma_\varphi\right)\dfrac{x_t}{1+z_t} + \dfrac{\eta_f\Gamma_1}{2}x_t + \sqrt{\dfrac{\eta_f\Gamma_1}{2}}dW_u \\ \qquad\qquad = \left(\dfrac{\Gamma_1}{2} - \Gamma_\varphi\right)\dfrac{x_t}{1+z_t} + \sqrt{\dfrac{\eta_f\Gamma_1}{2}}u(t)dt \end{cases}. \tag{6.26}$$

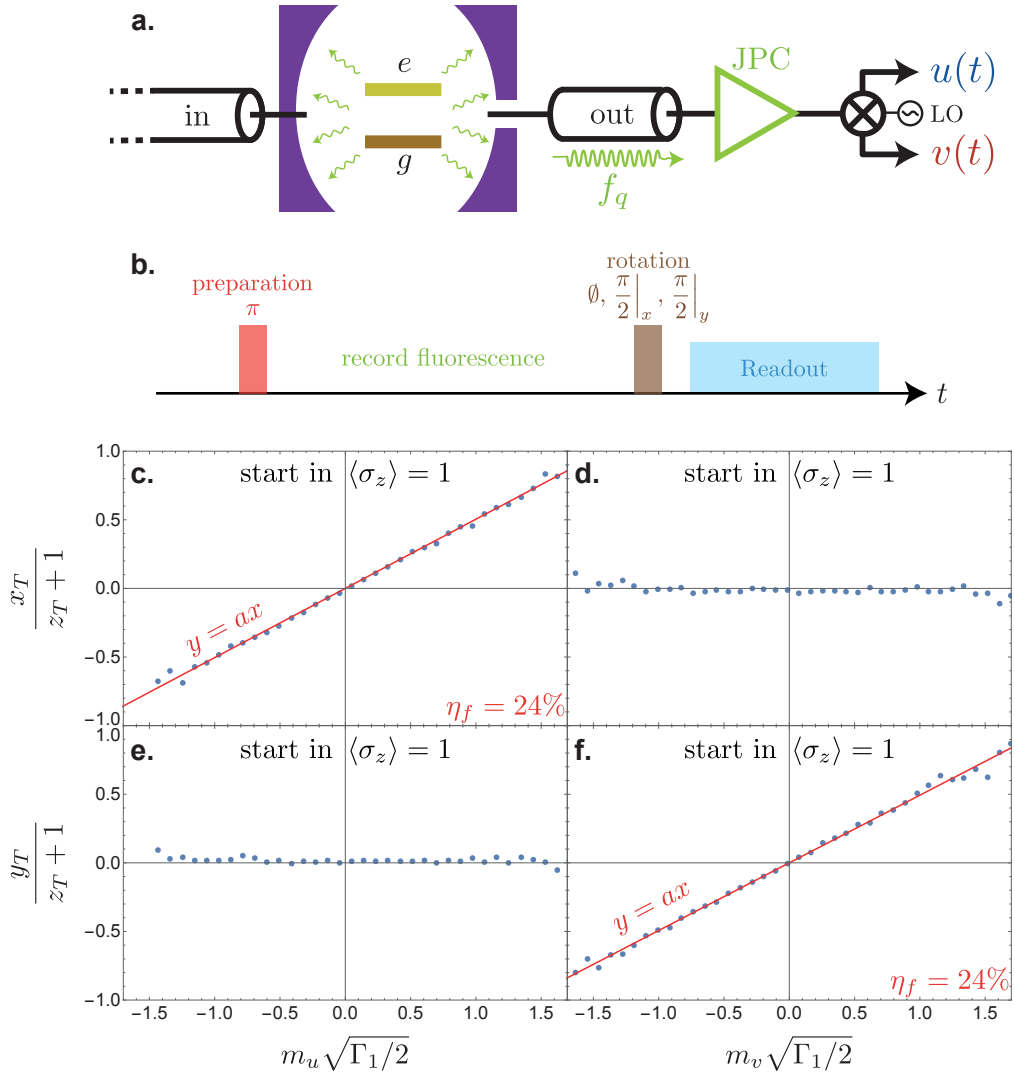

Figure 6.3: **a.** We detect the complex amplitude of the fluorescence emitted by the qubit leading to two measurement records $u(t)$ and $v(t)$. The signal is amplified by a near quantum limited amplifier (JPC) to ensure a significant detection efficiency. **b.** Pulse sequence for the measurement. We initialize the qubit in $|e\rangle$ and we integrate the measurement records $(u(t), v(t))$ during $T = 10$ μs to construct the integrated weighted signals $m_u = \int_0^T e^{-(\Gamma_1/2-\Gamma_\varphi)t} u(t)dt$ and $m_v = \int_0^T e^{-(\Gamma_1/2-\Gamma_\varphi)t} v(t)dt$. We then perform a strong tomography of σ_x, σ_y or σ_z. **c-f.** We bin together all the experiments that yield the same m_u or m_v and we average the tomography results on each subset to reconstruct the ratios $\frac{x}{z+1}$ and $\frac{y}{z+1}$. The figure contains 9.5×10^5 measurements. We observe a linear correlation between m_u (resp. m_v) and $\frac{x_T}{z_T+1}$ (resp. $\frac{y_T}{z_T+1}$) and no correlations between m_u (resp. m_v) and $\frac{y_T}{z_T+1}$ (resp. $\frac{x_T}{z_T+1}$) in agreement with Eq. (6.27). We extract the value of the quantum efficiency $\eta_f = 24\%$ from this measurement. Note that this value is higher than the one used in the trajectories of section 6.2 because the gain of the JPC was higher in this measurement.

The quantity $y_t/1+z_t$ can also be differentiated. We obtain the following result for a qubit starting in $\langle\sigma_z\rangle = 1$

$$\boxed{\begin{cases} e^{-(\frac{\Gamma_1}{2}-\Gamma_\varphi)T}\dfrac{x(T)}{z(T)+1} = \sqrt{\dfrac{\eta_f\Gamma_1}{2}}m_u \\ e^{-(\frac{\Gamma_1}{2}-\Gamma_\varphi)T}\dfrac{y(T)}{z(T)+1} = \sqrt{\dfrac{\eta_f\Gamma_1}{2}}m_v \end{cases}} \tag{6.27}$$

where $m_u = \int_0^T e^{-(\Gamma_1/2-\Gamma_\varphi)t}u(t)dt$ and $m_v = \int_0^T e^{-(\Gamma_1/2-\Gamma_\varphi)t}v(t)dt$ are the integrated weighted signals.

The predicted Bloch coordinates $x_t = \mathrm{Tr}[\sigma_x\rho_t]$, $y_t = \mathrm{Tr}[\sigma_y\rho_t]$ and $z_t = \mathrm{Tr}[\sigma_z\rho_t]$ are not independently measurable in a single realization of an experiment. Let us select a set of trajectories sharing a given m_u. Every trajectory k as the same $\frac{x^k}{1+z^k}$ ratio which is also equal to $\frac{\bar{x}}{1+\bar{z}}$ where $\bar{\cdot}$ denotes the average of the set of trajectory of equal m_u. We can thus repeat the experiment and carry alternatively a strong measurement of either σ_x, σ_y or σ_z and compute the $\frac{\bar{x}}{1+\bar{z}}$ ratio of all trajectories that led to the same m_u. In Fig. 6.3, we record the fluorescence signal of a qubit initialized in $\langle\sigma_x\rangle = 1$ for $T = 10$ μs. We sort the trajectories according to the values of m_u and m_v calculated by integration of the measurement records. We observe a linear correlation between m_u and $\frac{x}{z+1}$ and between m_v and $\frac{y}{z+1}$ validating the Kraus operator formalism to predict the evolution of a relaxing qubit undergoing an heterodyne measurement. The measurement is a calibration of the quantum efficiency of detection, here $\eta_f = 24\%$.

6.2 QUANTUM TRAJECTORIES

6.2.1 *Repeated Kraus map and Markov chain*

In the previous section, we saw measurement 'in action' and we demonstrated that the Kraus formalism of equations (6.7,6.8,6.22) faithfully predicts the update of the density matrix conditioned to the information written in an observer's memory during a single measurement of duration T. Let us extend this formalism to an arbitrary set of jump operators $\{L_\mu\}$ associated to the detection efficiencies $\{\eta_\mu\}$ characterizing every decoherence channel of the system.

The incremental evolution of a quantum state ρ of a monitored open quantum system reads

$$\boxed{\begin{cases} \rho_{t+dt} = \dfrac{\mathbf{K}_{y(t)}(\rho_t)}{\mathrm{Tr}(\mathbf{K}_{y(t)}(\rho_t))} \\ \text{with } \mathbf{K}_{y(t)}(\rho_t) = M_{y(t)}\rho_t M_{y(t)}^\dagger + \displaystyle\sum_{\mu\neq 0}(1-\eta_\mu)dtL_\mu\rho_t L_\mu^\dagger \\ \text{and } M_{y(t)} = \mathbb{1} - \left(\dfrac{i}{\hbar}H + \displaystyle\sum_{\mu\neq 0}L_\mu^\dagger L_\mu/2\right)dt + \displaystyle\sum_{\mu\neq 0}\sqrt{\eta_\mu}L_\mu y_\mu(t)dt \end{cases}} \tag{6.28}$$

The associated measurement records read

$$\boxed{y_\mu(t)dt = \sqrt{\eta_\mu}\mathrm{Tr}(L_\mu\rho + \rho L_\mu^\dagger)dt + dW_\mu(t).} \tag{6.29}$$

and $y(t) = (y_\mu(t))_\mu$ is the vector of the measurement records at time t. The super-operator $\mathbf{K}$ is called a *partial*[4] Kraus map. We recall the properties of the Wiener processes $\{W_\mu\}$ in Ito formalism

$$\begin{cases} \mathbb{E}[dW_\mu(t)] = 0 \\ dW_\mu(t)^2 = dt \end{cases}. \tag{6.30}$$

Repeating a series of such measurements[5] yields a succession of outcomes $y(0), y(dt), y(2dt), ...$ and at each time step the density matrix is updated in agreement with

$$\boxed{\rho_{ndt} \to \rho_{ndt+dt} = \rho_{(n+1)dt} = \frac{\mathbf{K}_{y(ndt)}(\rho_{ndt})}{\mathrm{Tr}(\mathbf{K}_{y(ndt)}(\rho_{ndt}))}} \tag{6.31}$$

Under Markov assumption, the successive evolutions (6.31) are independent and stochastic specifying a *Markov chain*[6] on the density matrix called *quantum trajectory*. A *quantum trajectory* is the time evolution of the density matrix of a system monitored by an observer[7] conditioned on the realization of the measurement records.

6.2.2 *The stochastic master equation*

At first order in dt, the partial Kraus map of Eq. (6.28) reads

$$\begin{aligned} \mathbf{K}_{y(t)}(\rho_t) = \rho_t - \frac{i}{\hbar}[H, \rho_t]dt + \sum_\mu dt(L_\mu \rho_t L_\mu^\dagger - \frac{L_\mu^\dagger L_\mu}{2}\rho_t - \rho_t \frac{L_\mu^\dagger L_\mu}{2}) \\ + \sum_\mu \sqrt{\eta_\mu}(L_\mu \rho_t + \rho_t L_\mu^\dagger) y_\mu(t) dt. \end{aligned} \tag{6.32}$$

And since $\mathrm{Tr}(\mathbf{K}_{y(t)}(\rho_t)) = 1 + \sum_\mu \sqrt{\eta_\mu}\mathrm{Tr}(L_\mu\rho_t + \rho_t L_\mu^\dagger) y_\mu(t)dt$. The normalisation factor can be approximated at order dt by

$$\frac{1}{\mathrm{Tr}(\mathbf{K}_{y(t)}(\rho_t))} = 1 - \sum_\mu \sqrt{\eta_\mu}\mathrm{Tr}(L_\mu\rho_t + \rho_t L_\mu^\dagger) y_\mu(t)dt + \sum_\mu \eta_\mu \mathrm{Tr}(L_\mu\rho_t + \rho_t L_\mu^\dagger)^2 dt. \tag{6.33}$$

By combining Eq. (7.8) and Eq. (7.9), we obtain the so-called *stochastic master equation* (SME)

$$\boxed{d\rho_t = -\frac{i}{\hbar}[H, \rho_t]dt + \sum_{i=1}^m \mathcal{D}_i(\rho_t)dt + \sum_{i=1}^m \sqrt{\eta_i}\mathcal{M}_i(\rho_t)dW_i(t)} \tag{6.34}$$

where the Lindblad super-operator is $\mathcal{D}_i(\rho_t) = L_i\rho_t L_i^\dagger - \frac{1}{2}\rho_t L_i^\dagger L_i - \frac{1}{2}L_i^\dagger L_i \rho_t$, the innovation super-operator is $\mathcal{M}_i(\rho_t) = L_i\rho_t + \rho_t L_i^\dagger - \mathrm{Tr}(L_i\rho_t + \rho_t L_i^\dagger)\rho_t$ and the measurement records are given by Eq. (6.29).

4 A *partial* Kraus map is not trace preserving in general $\mathrm{Tr}(\mathbf{K}(\rho)) \leq \mathrm{Tr}(\rho)$ contrary to a Kraus map.

5 This formalism can be extended to an arbitrary sequence of measurements of unequal duration $T_1, T_2, T_3, ...$

6 See for instance [108, 173] for an introduction on the subject.

7 The quantum trajectory is observer-dependent. The dynamics of the system is defined by its Hamiltonian, the set of jump operators $\{L_\mu\}$ and the initial condition. A class of observer is specified by the set of measurement efficiencies $\{\eta_\mu\}$ associated to each information channel.

The contributions of the terms in Eq. (6.34) are well-separated. The first two terms correspond to the Hamiltonian evolution and the dissipation of Lindblad equation. The third term is called the *innovation*. It originates from the measurement back-action associated to the different jump operators. This last term averages out to zero because of the properties of the Wiener processes (see Eq. (6.30)). The solution of Lindblad equation is thus recovered by averaging a large number of quantum trajectories.

The SME is a continuous stochastic partial differential equation used to describe random walkers. It is equivalent to the Kraus formulation (6.28) when dt is much smaller than any other time-scale of the system. We will use this equation in section 6.4 to derive a Fokker-Planck equation for our system.

6.2.3 *From measurement records to quantum trajectories*

We follow a systematic procedure to *unravel* the quantum trajectories from the raw measurement records.

6.2.3.1 *Correlation of the output signals*

The JPA and JPC are used as pre-amplifier with a bandwidth of 4.25 MHz $\gg \Gamma_1$ (measured by a Vector Network Analyzer sent on the reflection probe of the cavity as in chapter 5) and the signal is integrated over time steps of duration $dt = 100$ ns. The filtering of the signal is incompatible with our white Gaussian noise description (6.30) of the stochastic part of the signal. We propose here a method to 'unfilter' the records. The filtering effect can be modeled as a first order low-pass temporal filter with a time constant τ_{JPA} or τ_{JPC} and a gain β_{JPA} or β_{JPC} that depends on the amplifier. At room temperature, we acquire $(\tilde{u}(t), \tilde{v}(t), \tilde{w}(t))$ such that

$$\begin{cases} \tilde{u}(t) = \beta_{\mathrm{JPC}}(1 - e^{-dt/\tau_{\mathrm{JPC}}})u(t) + e^{-dt/\tau_{\mathrm{JPC}}}\tilde{u}(t - dt) \\ \tilde{v}(t) = \beta_{\mathrm{JPC}}(1 - e^{-dt/\tau_{\mathrm{JPC}}})v(t) + e^{-dt/\tau_{\mathrm{JPC}}}\tilde{v}(t - dt) \\ \tilde{w}(t) = \beta_{\mathrm{JPA}}(1 - e^{-dt/\tau_{\mathrm{JPA}}})w(t) + e^{-dt/\tau_{\mathrm{JPA}}}\tilde{w}(t - dt) \end{cases} \tag{6.35}$$

where $(u(t), v(t), w(t))$ are the normalized records with an infinite bandwidth discussed up to now in this thesis.

The value of the aforementioned parameters were experimentally determined. The prefactors β are obtained by rescaling the variance of the measurement records to dt according to Eq. (6.30). The correlation times of the filters are chosen to cancel out the first order correlations of the measurement records $\mathbb{E}[u(t)u(t + dt)] = \mathbb{E}[v(t)v(t + dt)] = \mathbb{E}[w(t)w(t + dt)] = 0$. The corresponding time constants are found to be $\tau_{\mathrm{JPA}} = \tau_{\mathrm{JPC}} = 78$ ns (see Fig. 6.4). We independently checked that this condition maximizes the amount of information gathered on the quantum system via the measurement records i.e. this value of time constants gives the highest detection efficiencies. The equality between the two time constants is due to the equality of the bandwidths of the amplifiers that occurs owing to a careful choice of power gains for each amplifier. The time step dt used in the trajectories cannot thus be chosen arbitrarily small because of the finite bandwidth of the amplifiers or arbitrarily large because the reconstruction with Eq. (6.28) is only valid for dt much smaller than any time scale involved in the

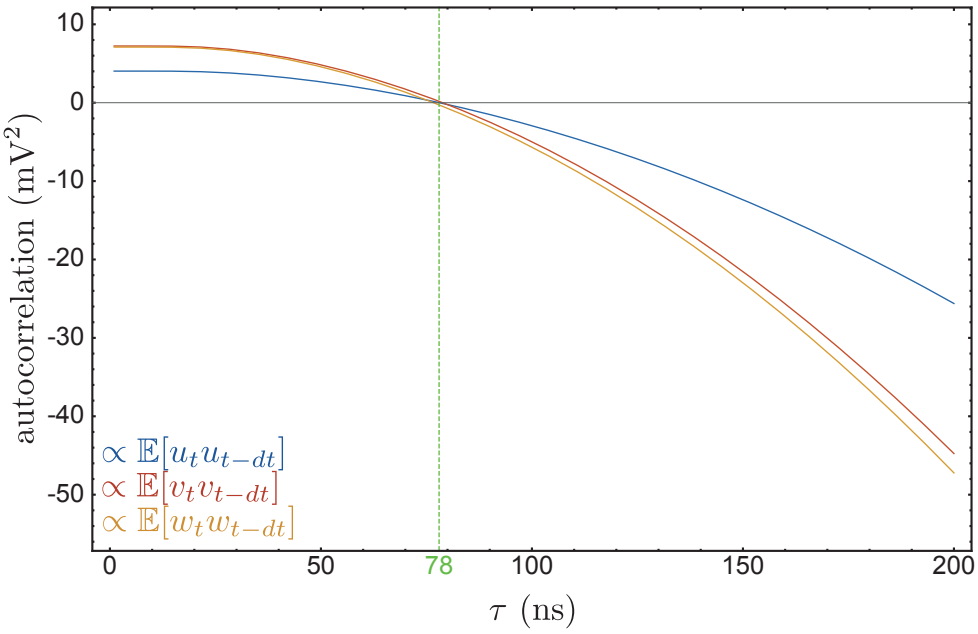

Figure 6.4: Non normalized experimental correlations between two consecutive unfiltered measurement records before normalizing their variance to dt as a function of the time scale τ of Eq. (6.35). The parameters $\tau_{\mathrm{JPA}} = \tau_{\mathrm{JPC}} = 78$ ns (green dashed line) were found to cancel the autocorrelation of the signals induced by the finite bandwidth of the amplifiers.

experiment. Our choice $dt = 100$ ns was the smallest achievable time step compatible with the bandwidth of the amplifiers. The unfiltered and rescaled measurement records are used to reconstruct all the trajectories presented in this thesis.

6.2.3.2 *Unravelling the trajectory*

We model our system with four jump operators $L_u = \sqrt{\frac{\Gamma_1}{2}}\sigma_-$, $L_v = iL_u$, $L_w = \sqrt{\frac{\eta_d \Gamma_d}{2}}\sigma_z$ and $L_\varphi = \sqrt{\frac{\Gamma_\varphi}{2}}\sigma_z$. The fourth jump operator takes into account the unread ($\eta_\varphi = 0$) pure dephasing[8] of the qubit so that the total decoherence rate of the system is $\Gamma_2 = \frac{\Gamma_1}{2} + \Gamma_\varphi + \Gamma_d$. The measurement record-dependent evolution reads

$$\begin{cases} \rho_{t+dt} = \dfrac{\mathbf{K}_{y(t)}(\rho_t)}{\mathrm{Tr}(\mathbf{K}_{y(t)}(\rho_t))} \\ \text{with } \mathbf{K}_{y(t)}(\rho_t) = M_{y(t)}\rho_t M_{y(t)}^\dagger + (1-\eta_f)dt\Gamma_1\sigma_-\rho\sigma_+ + (1-\eta_d)dt\dfrac{\Gamma_d}{2}\sigma_z\rho\sigma_z \\ \text{and } M_{y(t)} = \mathbb{1} - \left(i\dfrac{H}{\hbar} + \dfrac{\Gamma_1}{2}\sigma_+\sigma_- + \dfrac{\Gamma_d + \Gamma_\varphi}{4}\right)dt + \sqrt{\dfrac{\eta_f\Gamma_1}{2}}\sigma_-(u(t) + iv(t))dt + \sqrt{\dfrac{\eta_d\Gamma_d}{2}}\sigma_z w(t)dt \end{cases} . \tag{6.36}$$

The system is driven by an Hamiltonian of the form $H = -\frac{\hbar\Omega}{2}\sigma_y$ where Ω is the Rabi frequency. All the parameters that enter Eq. (6.36) are determined by independent

8 Γ_φ is the residual dephasing rate of the qubit when the cavity is not populated.

measurements and we check that the average evolution[9] is faithfully described by the Lindblad equation with the corresponding parameters.

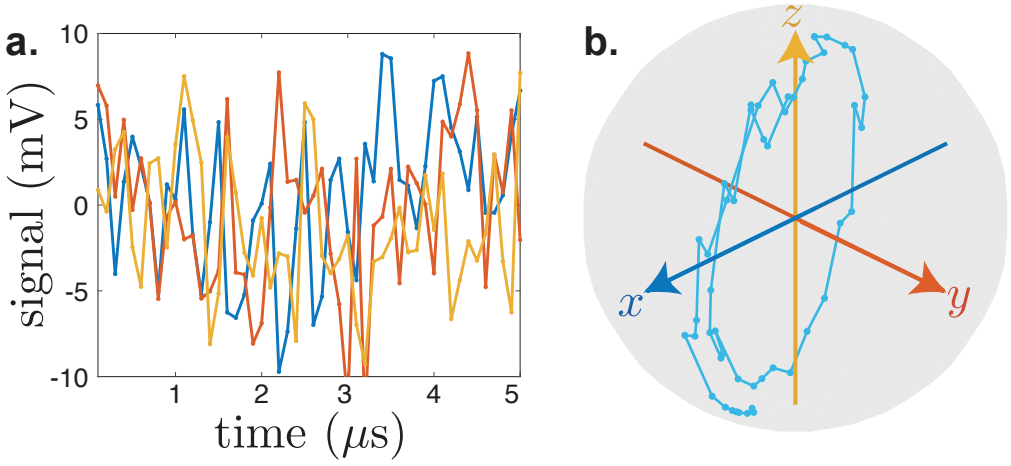

Figure 6.5: A typical 5 μs-long tracking of a quantum state. **a.** Raw (not normalized) measurement records $\tilde{u}(t)$ (blue), $\tilde{v}(t)$ (red) and $\tilde{w}(t)$ (yellow) as a function of time for one realization of the experiment. These records feed Eq. (6.36) with the parameters $\Gamma_1 = (15\ \mu\text{s})^{-1}$, $\Gamma_d = (0.9\ \mu\text{s})^{-1}$, $\Gamma_\varphi = (17.9\ \mu\text{s})^{-1}$, $\Omega/2\pi = 5.2\ \mu$s and $(\eta_f, \eta_d) = (14\%, 34\%)$. The records are very noisy but Eq. (6.36) acts as a filter that leads to the trajectory represented in the Bloch sphere in **b**.

In Fig. 6.5, we give Bloch sphere representation of a 5 μs-long quantum trajectory. The measurement records are dominated by noise but Eq. (6.36) acts as a Bayesian filter leading to a diffusive trajectory. The trajectory is oscillating around the y axis because of the drive described by the Hamiltonian.

6.2.4 *Validation by an independent tomography*

Quantum trajectories are physically meaningful if and only if they can be used to predict the distribution of outcomes of any future measurement performed of the system. The validity of the reconstructed trajectories can be tested by *post-selecting* an ensemble of realizations of the experiment for which the trajectory predicts a given value $x(T) = x_{\text{traj}}$ at a time T. If the trajectories are valid, then a strong measurement of σ_x at time T should give x_{traj} on average on this post-selected ensemble of realizations. In practice, we compare the prediction of the quantum trajectories with a strong measurement by selecting all the trajectories of a large ensemble that ends up in some slice of the Bloch sphere (see Fig. 6.6). An example of 4 trajectories ending up with $0.74 < x_{\text{traj}} < 0.76$ are depicted on Fig. 6.6 **d**. Here, the average over the strong σ_x measurement yields a value $\simeq 0.75$.

9 We recall that the raw average of the measurement records is a full quantum tomography of the system (see section 3.4).

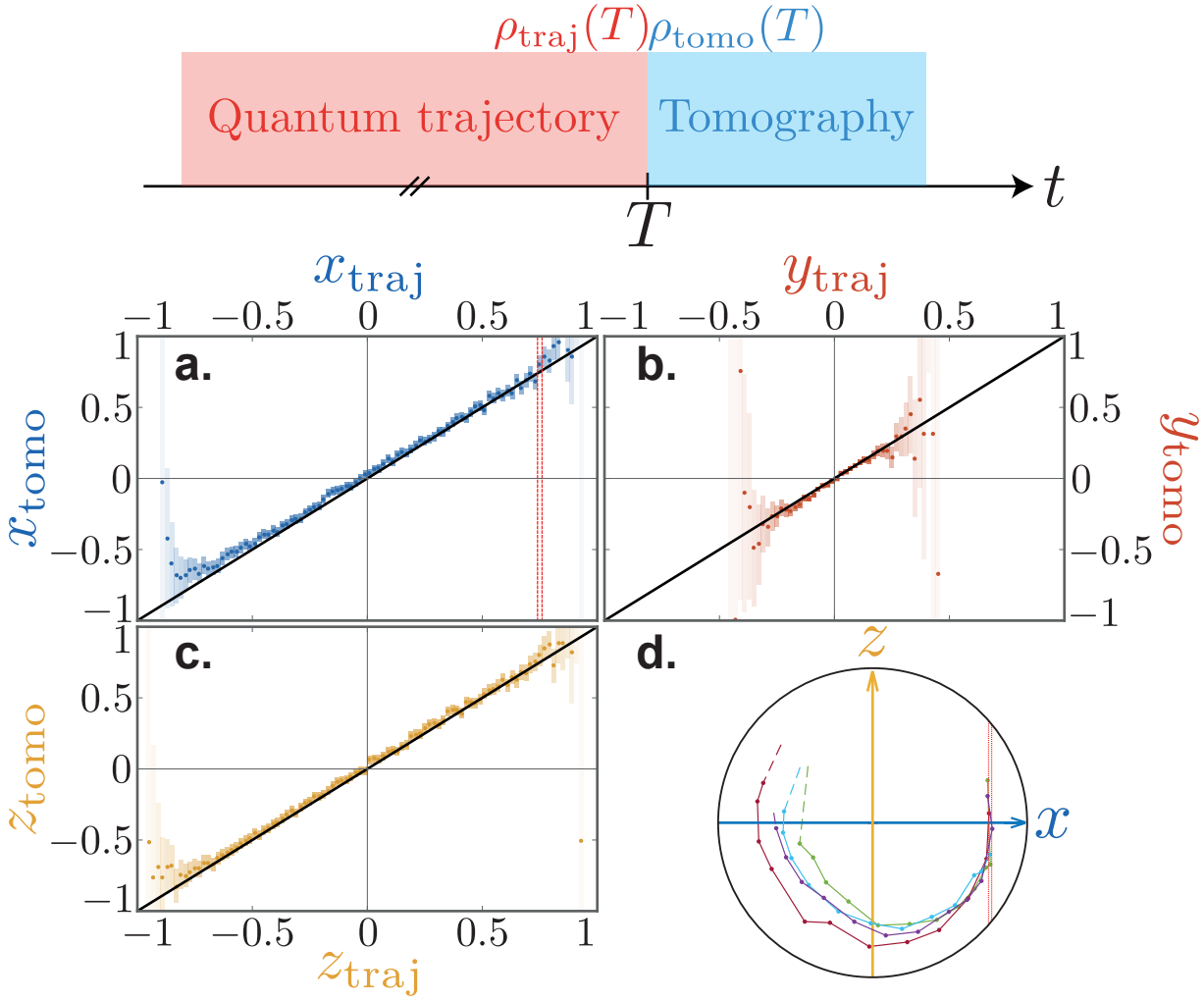

Figure 6.6: Tomographic validation of the quantum trajectories. **a. b. c.** Correlations between the coordinates $(x_{\text{traj}}, y_{\text{traj}}, z_{\text{traj}})$ of the trajectories after 19.8 μs of evolution and an independent tomography. The quantum trajectories were reconstructed from Eq. (6.36) with the parameters $\Gamma_1 = (15\ \mu\text{s})^{-1}$, $\Gamma_d = (5\ \mu\text{s})^{-1}$, $\Gamma_\varphi = (17.9\ \mu\text{s})^{-1}$, $\Omega/2\pi = (5\ \mu\text{s})^{-1}$ and $(\eta_f, \eta_d) = (14\%, 34\%)$. Each panel represents the average value of the tomography results for the subset of trajectories ending up less than 0.01 away from a given value of x_{traj} (**a**), y_{traj} (**b**) or z_{traj} (**c**). The error bars are given by the standard deviation of the tomography results divided by the square root of the number of trajectories in the subset out of a total number of 1.5 million trajectories per panel. The agreement between the tomography and the coordinates of the trajectories demonstrates the validity of the quantum trajectories. **d.** Bloch sphere representation of 4 quantum trajectories that end up with $0.74 < x_{\text{traj}} < 0.76$ (red dashed line) after 19.8 μs corresponding to one bin of the histogram in **a**.

We have checked for any value of x_{traj} (Fig. 6.6 **a**), y_{traj} (Fig. 6.6 **b**) and z_{traj} (Fig. 6.6 **c**), and for 30 representative values of measurement strength and drive that the trajectories predict accurately the tomography results. However, in the presence of a large drive $\Omega \sim 1/dt$ or a large measurement rate $\Gamma_d \sim 1/dt$, the unravelling (6.36) is no longer valid and large deviations are observed between the reconstructed trajectories and the independent tomography.

6.2.5 *Parameter estimation*

In this section, we show that the parameters of the filter (6.36) can be inferred in a self-consistant manner from the measurement records themselves. It was already demonstrated in our group by Six et al with a *maximum likelihood estimation* in the framework of *hidden Markov problems* [174]. We propose instead a new empirical method that rely on the validation of the trajectories by an independent tomography. We apply the stochastic filter (6.36) for various values of the parameter that we want to estimate. Only the correct value provides valid quantum trajectories in agreement with a subsequent tomography. The time constants entering Eq. (6.36) can be estimated by comparing the average evolution of the system with the solution of the Lindblad equation or by Rabi and Ramsey calibrations, which is not the case for the quantum efficiencies η_f and η_d. We thus apply this method to estime them precisely.

In Fig. 6.7, the trajectories are reconstructed for several values of η_f and η_d and their coordinates (x_{traj},y_{traj},z_{traj}) are statistically compared to an independent tomography (similarly to Fig. 6.6). The results of the trajectories and the tomography are in agreement only for the correct values of the efficiencies. In practice, there exists a correlation between the coordinates of the trajectory and the measurement records in the other cases that is approximately linear with a slope different from 1. We extract the slope of the correlation histograms by linear regression for the different values of the efficiencies. We find that the agreement is verified for efficiencies $\eta_f = 0.14$ and $\eta_d = 0.34$ within a confidence interval of ± 0.01 for any values of the amplitude drive and measurement induced dephasing rate.

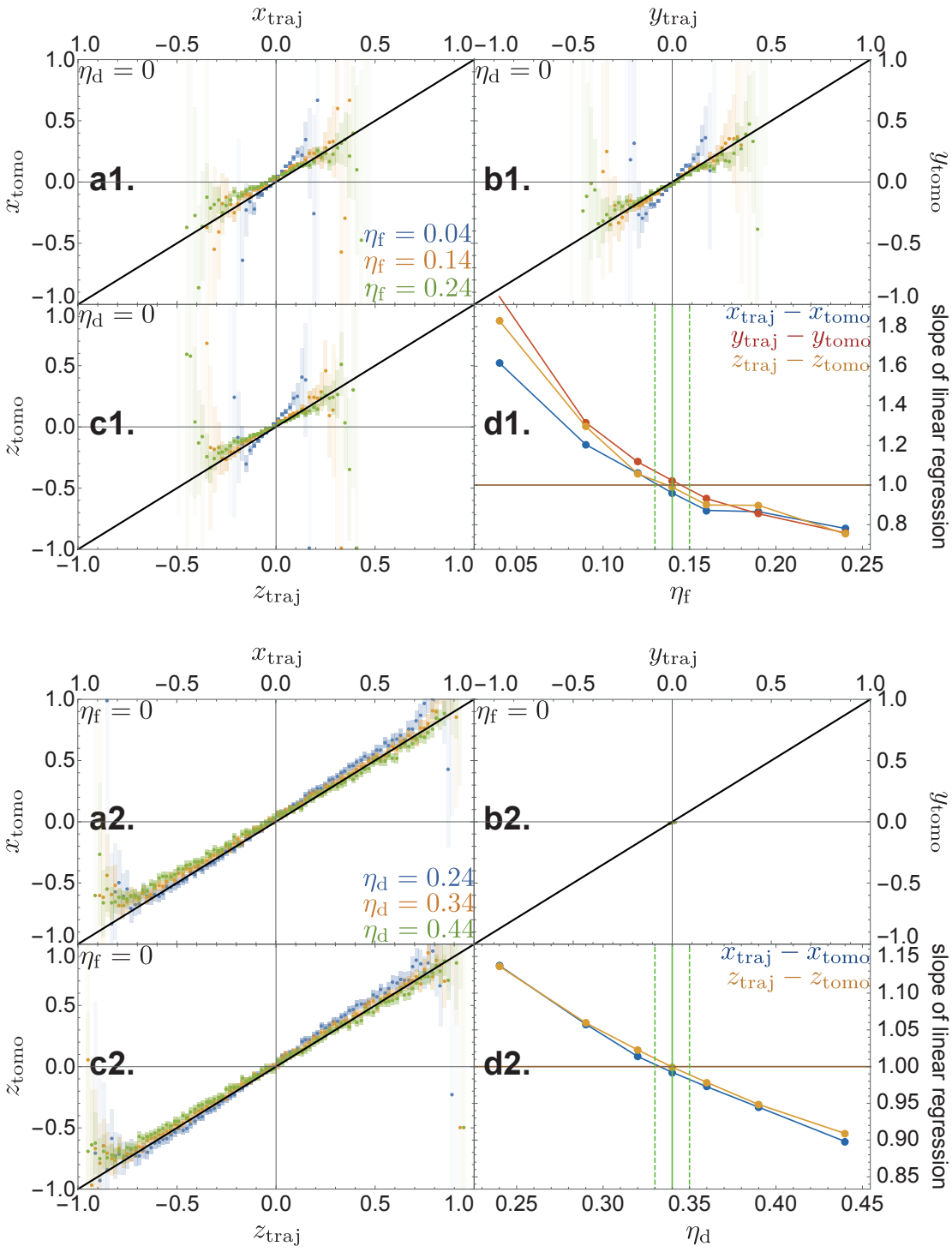

Figure 6.7: Correlations between the coordinates $(x_{\rm traj},y_{\rm traj},z_{\rm traj})$ of the trajectories after 19.8 μs of evolution and an independent tomography on the dataset corresponding to $\Gamma_1 = (15\ \mu{\rm s})^{-1}$, $\Gamma_d = (5\ \mu{\rm s})^{-1}$, $\Gamma_\varphi = (17.9\ \mu{\rm s})^{-1}$ and $\Omega/2\pi = (2.0\ \mu{\rm s})^{-1}$. In Fig. **a1**,**b1**,**c1** the sole output of the fluorescence records is used to reconstruct the trajectories ($\eta_d = 0$) and η_f takes 3 different values in Eq. (6.36). Incorrect values of η_f lead to a deviation from a slope one line (in black). Similarly η_f is set to 0 in **a2**,**b2**,**c2** and three values of η_d are tested. Note that because of the structure of the dispersive measurement back-action, all the dynamics of the qubit is confined in the $x-z$ plane with this sole detection thus $y_{\rm traj} = 0$ at all times in agreement with Fig. 6.1. In Fig. **d1** and **d2** the slopes of the correlation histograms are extracted by linear regression for the different values of η_f and η_d used each time in Eq. (6.36). The values $\eta_f = 0.14$ and $\eta_d = 0.34$ (green solid lines) are found by this method with a precision ± 0.01 (green dashed lines).

6.3 TRAJECTORIES STATISTICS

A quantum trajectory is a stochastic process corresponding to a random walk in the Bloch sphere. The inherent back-action of a quantum measurement is thus better discussed by representing distributions of states at a given time [27, 175, 176, 23, 24, 49] or distributions of trajectories for a given duration [175, 177, 25, 169, 178]. Before representing the statistics of our trajectories, we observe the impact of the values of the Rabi frequency and measurement induced dephasing rate on the average trajectory. Then, we compare the statistics obtained by different observers in two characteristic regimes. Finally, we advertise an online animated viewer created for this thesis to observe the trajectories in all regimes from the viewpoints of the different observers.

6.3.1 *Different regimes*

By varying the drive amplitudes at the cavity and qubit transition frequencies, we are able to reach a variety of regimes corresponding to different values of Ω/Γ_1 and Γ_d/Γ_1. The timescales Γ_1^{-1} and Γ_φ^{-1} are fixed because they characterize the lifetimes of the energy and coherences of the undriven qubit. The measurement induced dephasing rate Γ_d can be tuned arbitrarily[10] as it is proportional to the drive power at f_c. The Rabi frequency Ω is arbitrarily tunable as well as it is proportional to the drive amplitude at f_q.

As we showed in section 3.4, the raw average of the measurement records is a full quantum tomography of the qubit in time. In this section, we reveal the impact of the configuration of parameters on the average trajectory. Let us exemplify the variety of obtainable regimes with two configurations of the input drive: one in the regime of *underdamped Rabi oscillations* (Fig. 6.8 **a**) and another one in the regime of strong dispersive measurement rate, the so-called Zeno regime [30, 31] (over-damped oscillations of Fig. 6.8 **b**). In both cases, the qubit is initialized in the ground state and a Rabi rotation around σ_y is applied. The effect of decoherence under a strong Rabi drive corresponds to an average *loss of purity* $\mathrm{Tr}(\rho^2) = \frac{1}{2}(\mathbb{1} + x^2 + y^2 + z^2)$ that can be seen as a decreasing distance of the mean trajectory from the center of the Bloch sphere when time increases. In the long time limit, the state converges towards the center of the Bloch sphere, which is the *maximally mixed* state or *most entropic* state of the sphere. In Fig. 6.8 **a**, the qubit state evolves with underdamped oscillations because the decoherence rates are much smaller than the Rabi frequency $\Gamma_1, \Gamma_d \ll \frac{\Omega}{2\pi}$. In contrast, in Fig. 6.8 **a** the qubit state endures over-damped oscillations because $\Gamma_1,\ \frac{\Omega}{2\pi} \ll \Gamma_d$. The circular motion is blocked by the presence of a large dephasing channel and the average trajectory quickly reaches its steady state.

10 For high values of $\Gamma_d \sim dt^{-1}$, Eq. (6.36) is not valid. When reaching a critical number of photons (around 100 photons in our system), the transmon is driven into highly excited states and it is no longer a qubit. This is the high power readout regime (see introduction of chapter 3).

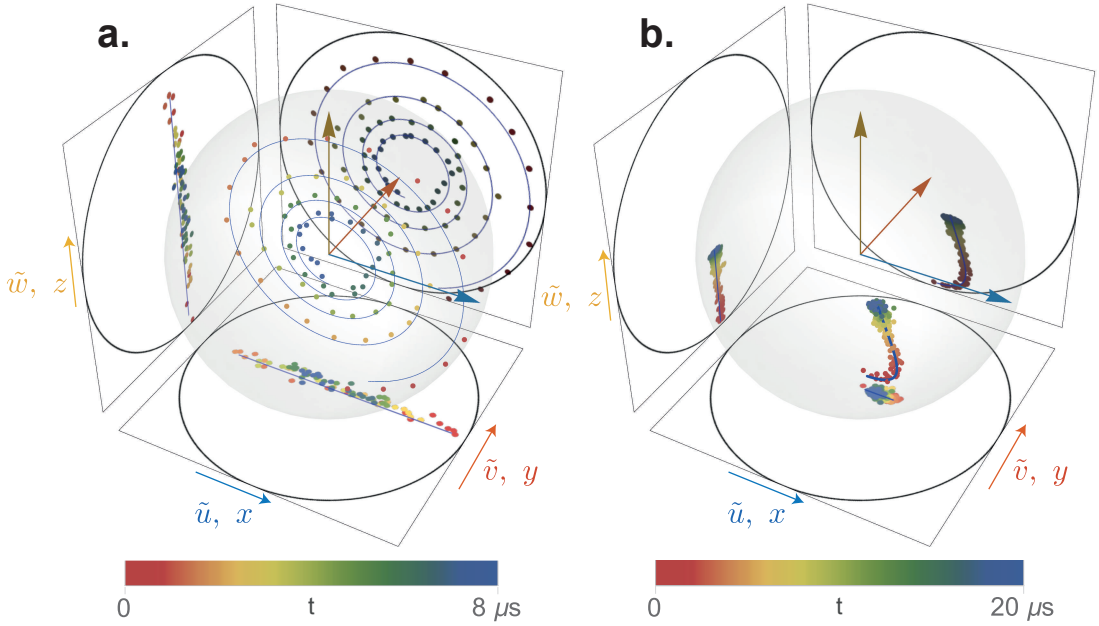

Figure 6.8: Direct averaging of the three measurement records in the under-damped Rabi oscillation regime and in the over-damped Zeno regime. **a.** Dots: Rescaled average of the measurement records $\tilde{u}(t) = \bar{u}(t)/\sqrt{\eta_f \Gamma_1/2}$, $\tilde{v}(t) = \bar{v}(t)/\sqrt{\eta_f \Gamma_1/2}$ and $\tilde{w}(t) = \bar{w}(t)/\sqrt{2\eta_d \Gamma_d}$ for 1.5×10^6 realizations of an experiment where the qubit starts in $|g\rangle$ at time 0 and is driven so that it rotates at a Rabi frequency $\Omega/2\pi = (2\ \mu\text{s})^{-1}$ around σ_y and endures a measurement induced dephasing rate $\Gamma_d = (5\ \mu\text{s})^{-1}$. Lines: Calculated coordinates of the Bloch vector $x(t)$, $y(t)$ and $z(t)$ from the master equation (6.36) with $\eta_{d,f} = 0$). **b.** Same figure in the Zeno regime with a drive such that $\Omega/2\pi = (16\ \mu\text{s})^{-1}$ and $\Gamma_d = (0.9\ \mu\text{s})^{-1}$.

6.3.2 *Zeno dynamics - Interplay between detectors*

We first focus on the Zeno regime of Fig. 6.8 **b** because the *competition* between the back-action of fluorescence measurement and dispersive measurement can be better observed when decoherence dominates the dynamics. We reconstruct an ensemble of 1.5 million experiments and obtain the statistics of the trajectories. In Fig. 6.9, we show the distributions of qubit states in color at a long time $\tau = 6.5$ μs after which the distribution is close to its steady state while the qubit is both Rabi driven and dispersively measured at a strong measurement rate. The average over this set of trajectories gives the average trajectory (black solid line). The finite *spread* of the distribution around the average trajectory is only due to the measurement back-action corresponding to the stochastic term in Eq. (6.34). The trajectories are determined using three sets of measurement records: dispersive only $\{w(t)\}$ (Fig. **a b c**), fluorescence only $\{u(t), v(t)\}$ (Fig. **d e f**) or both (Fig. **g h i**). These three cases correspond to three different *observers* that access different quantum states based on their records during the same realization of the experiment. The uniqueness of perception of the three observers has its roots in the records stored in the *observer's memory* and it leads to the distinct statistics of Fig. 6.9. In practice, we retrieve the information from both detectors for every experiment and we discard a part of this information in hindsight by setting $\eta_f = 0$ or $\eta_d = 0$ in Eq. (6.36) to reconstruct the trajectories, which is exactly equivalent to removing the unread detector.

The Zeno effect leads to the damping of the Rabi oscillations and the average trajectory (solid line) quickly reaches its steady state. The average trajectory is the same for every observer because it is predicted to be independent of the measurement records (average of Eq. (6.34)). Interestingly, while the average trajectory stays in the $x - z$ plane with $\langle \sigma_y \rangle = 0$ (similarly to Fig. 6.8 **b**), the back-action of the fluorescence measurement leads to a nonzero spread (back-action) in the y direction of the Bloch sphere (Fig. 6.9 **d**). This is in stark constrast with the dispersive measurement alone that does not provide any back-action towards the y direction of the Bloch sphere(Fig. 6.9 **a**) so that the qubit states keeps a zero σ_y component during its evolution. In the case of fluorescence, in the long time, the combined action of Rabi drive and fluorescence measurement back-action leads to a uniform spread of the qubit state close to the most entropic state $\mathbb{1}/2$ at the center of the sphere (Fig. 6.9 **d e f**). The qubit states span a small Bloch sphere composed of very *unpure states* revealing only a small amount of information on the state of the system because of the large measurement induced dephasing rate created by the strong dispersive measurement.

When the dispersive measurement is recorded (Fig. 6.9 **a b c**), a trajectory corresponding to a single realization of the experiment experiences a series of stochastic jumps between two areas of the Bloch sphere that are close to the two eigenstates of the σ_z measurement operator. In the distribution of states, this leads to two areas with high probability of occupation near the poles of the Bloch sphere. The dispersive measurement records can thus reveal that the state of the qubit was either close to $|g\rangle$ or $|e\rangle$ revealing almost one bit of information on the qubit. These two areas can be interpreted as zones frozen by the *Zeno effect*. The rest of the Bloch sphere is still

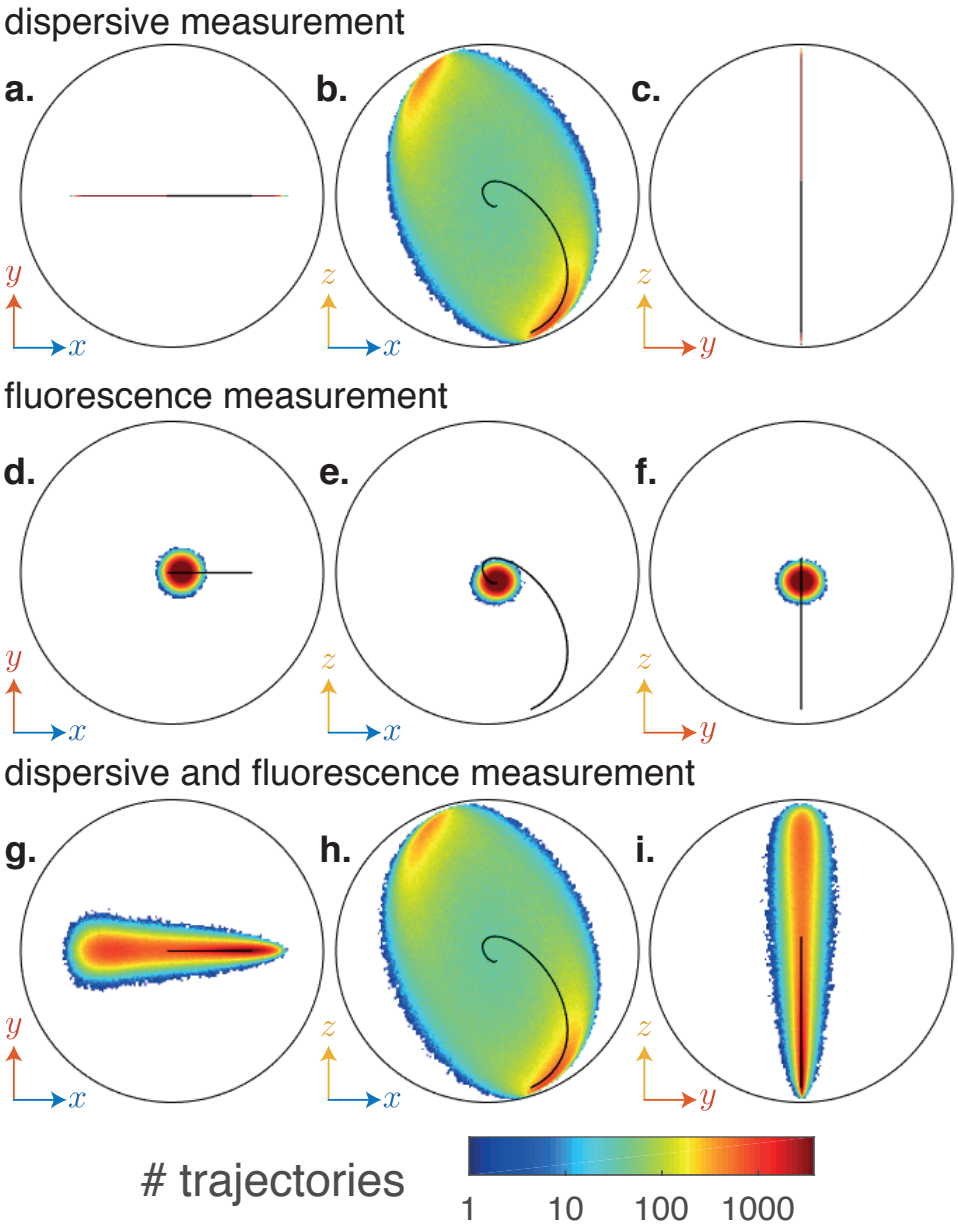

Figure 6.9: Impact of the type of detector on the distribution of quantum states in the Zeno regime. **a**,**b**,**c** Marginal distribution in the $x-y$ (**a**), $x-z$ (**b**) and $y-z$ (**c**) planes of the Bloch sphere of the qubit states ρ_τ corresponding to 1.5 millions of measurement records at the cavity frequency only $\{w(t)\}$ from time t between 0 and $\tau = 6.5$ μs. The information about $\{u(t), v(t)\}$ is here discarded (by setting $\eta_f = 0$). All panels in the figure correspond to the Zeno regime with $\Omega/2\pi = (5.2\ \mu\text{s})^{-1}$ and $\Gamma_d = (0.9\ \mu\text{s})^{-1}$. The boundary of the Bloch sphere is represented as a black circle and the average quantum trajectory as a solid line. **d**,**e**,**f** Case where the states are conditioned on fluorescence records $\{u(t), v(t)\}$ instead while discarding the information on $\{w(t)\}$ ($\eta_d = 0$). **g**,**h**,**i** Case where the states are conditioned on both fluorescence and dispersive measurement records $\{u(t), v(t), w(t)\}$.

occupied with a lower probability because of the finite time it takes for the jump to occur from one pole to the next under strong dispersive measurement rate [179].

It is crucial to understand that the records reveal the *information leaking* in the two decoherence channels of the qubit[11]. In this sense, we take the place of the environment and reveal the knowledge that only the bath acquires in most experiments.

As expected, the quantum states that are conditioned on all measurement records $\{u(t), v(t), w(t)\}$ are less entropic than with a single measurement. This can be seen in Figs. 6.9 **g-i** where the spread of the distributions is larger than for the cases of single measurements. A clear asymmetry appears in the spread of the marginal distribution in the $x-y$ plane of Fig. 6.9 **g** between positive and negative values of x. The non zero spread in this plane is solely due to back-action of the fluorescence as seen from Fig. 6.9 **a** and **d**. This asymmetry originates from the fact that the fluorescence measurement is linked to the jump operator σ_- for which $|g\rangle$ is the single pointer state. Indeed the measurement back-action is null when the qubit state is close to $|g\rangle$ while it is strongest when the qubit state is close to $|e\rangle$. Since the Rabi drive correlates the ground state to positive x (red zone shifted to the right of the south pole in Fig. 6.9 **g**) and the excited state to negative x, the spread in y is smaller for positive x than for negative x. This asymmetry highlights the profound difference between measuring both quadratures of fluorescence and measuring σ_x and σ_y simultaneously [49]. While both methods lead to the same result on average, their back-action differs. The latter corresponds to quantum non-demolition measurements, while fluorescence does not. In the end, the asymmetry in the distributions of Figs. 6.9 **g** and **i** results from the incompatibility between a dispersive measurement with no back-action on $|e\rangle$ and a fluorescence measurement with maximal back-action on $|e\rangle$ as will be explained in section 6.4.

6.3.3 *Rabi oscillations*

By decreasing the decoherence rates to values much lower than the Rabi rate Ω, we enter the *Rabi oscillations regime* corresponding to Fig. 6.8 **a**. Rabi oscillation in the presence of weak decoherence is very well-documented as it is predicted from Lindblad equation. We aim here at revealing the information acquired by the environment through decoherence during the evolution.

In Fig. 6.10, we show projections of probability distribution in $x-y$ (Fig. **a**), $x-z$ (Fig. **b**) and $y-z$ (Fig. **c**) planes associated to the complete measurement record $\{u(t), v(t), w(t)\}$. The first interesting feature is that the maximum of the distribution is distinct from the mean path of the average trajectory (black solid line) as can be seen from Fig. 6.10 **b**. In the long time limit, we observe that the combination of weak measurement with the Rabi rotation *spreads uniformly* the distribution over all the $x-z$ plane which is similar to what is obtained by simultaneously measuring σ_x and σ_z in an effectively undriven qubit [49]. Even though the distribution of states is stationary, the individual trajectory *diffuses indefinitely* inside the Bloch sphere [180].

11 There are only two decoherence mechanisms for this qubit because the excitation channel is negligible as it is associated to a very long time-scale $\Gamma_\uparrow^{-1} = 0.75$ ms.

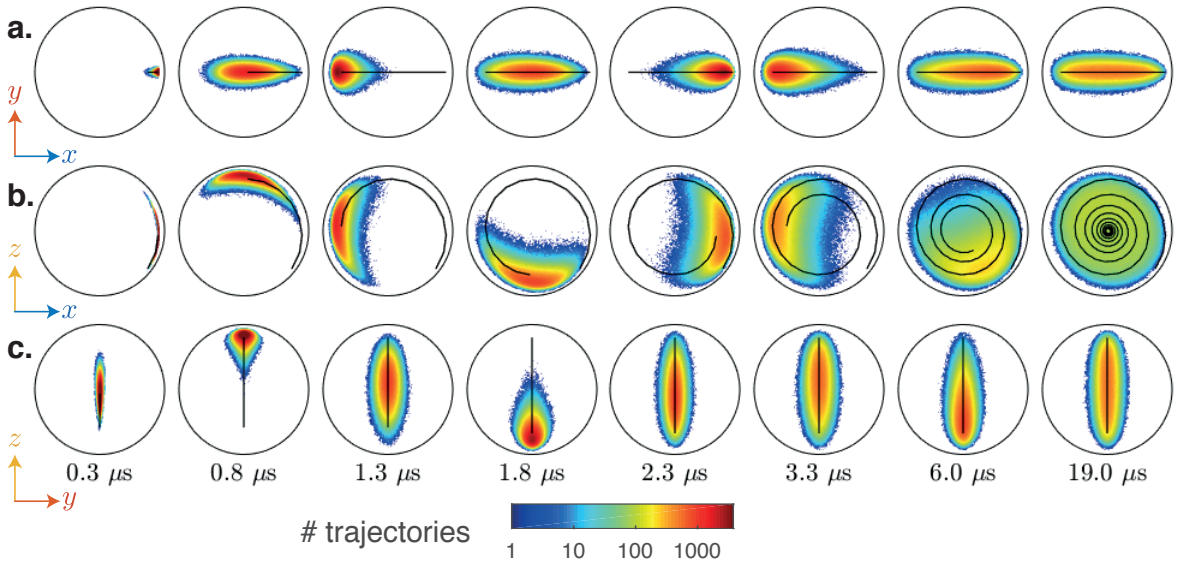

Figure 6.10: Evolution of the distribution of quantum states. **a**,**b**,**c** Colored dots: Each frame represents the marginal distribution, in the $x-y$ (Fig. **a**), $x-z$ (Fig. **b**) and $y-z$ (Fig. **c**) planes of the Bloch sphere, of the states of the qubit at a given time τ for 1.5 million realizations of the experiment, in the same experimental conditions as Fig. 6.8 **a**. Each state (x, y, z) is reconstructed from the complete measurement records $\{u(t), v(t), w(t)\}$ from time t between 0 to τ using Eq. (6.36). Time τ is increasing from 0.3 μs to 19 μs from left to right as indicated at the bottom of the figure. For each figure, the surrounding black circles represent the pure states of the plane (e.g. $z = 0$ for **a**). Solid lines: average projection of all 1.5 millions of quantum trajectories $\{x(t), y(t), z(t)\}$ for 0.2 μs $< t < \tau$.

6.3.4 *Exploration of several regimes*

The two regimes presented in the previous discussion are just two examples of many possible ones. In fact we carried out similar experiments for 30 different regimes (see Fig. 6.12) with $(30\ \mu s)^{-1} \leq \Gamma_d \leq (0.3\ \mu s)^{-1}$ and $0 \leq \frac{\Omega}{2\pi} \leq 2\ \mu s$. All the experimental results can be visualized in a small animated application available online[12]. A typical visual of the application is shown in Fig. 6.11. The values of Γ_d and Ω can be changed in the application thanks to sliders. The measurement can be chosen to take into account the measurement records of the dispersive measurement only, the fluorescence measurement only or both. All the movies are also available for download from an online repository[13].

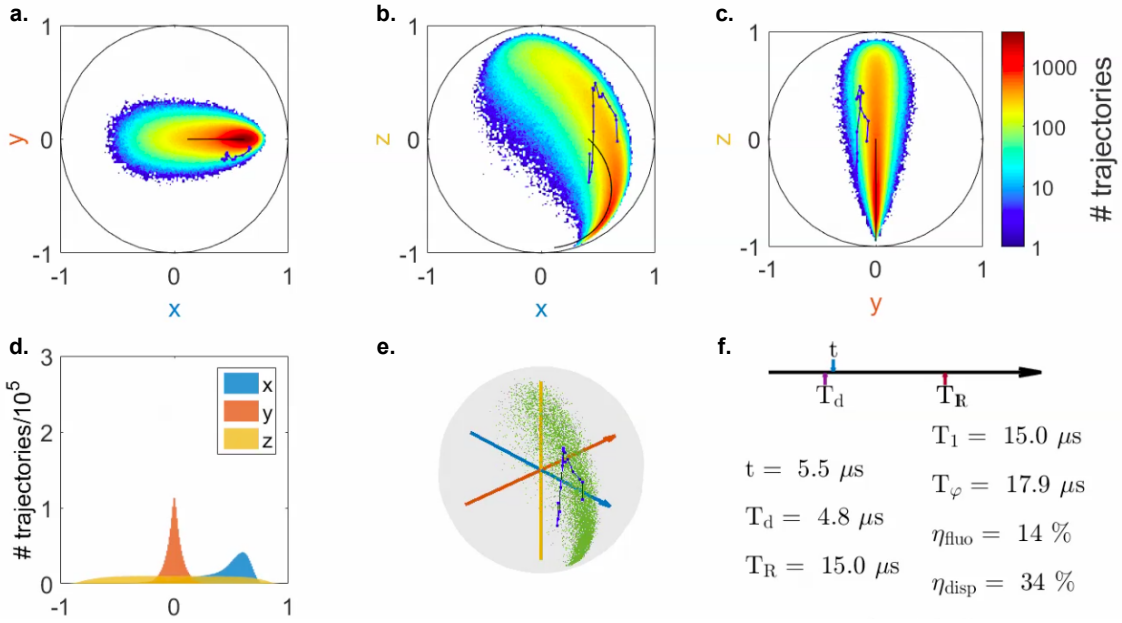

Figure 6.11: Typical visual of the application available online. Projections of 1.5 million measured trajectories in the $x-y$ (Fig. **a**), $x-z$ (Fig. **b**) and $y-z$ (Fig. **c**) planes. The solid black line is the average trajectory, the blue doted line is a randomly chosen trajectory and the color plot is the probability distribution of the trajectories. **d.** Histograms of the x, y and z component of the trajectories. **e.** Bloch sphere representation of the probability distribution (green dots) and of the particular trajectory (blue) represented in a, b and c. **f.** parameters of the experiment.

In Fig. 6.12, we show the $x-z$ distribution of trajectories reconstructed from the complete record $\{u(t), v(t), w(t)\}$ in all 30 reachable configurations. The movie associated to any of these configurations can be accessed by clicking on the corresponding figure. Note how the ensemble of trajectories can go from uniform for weak measurement in the presence of a strong Rabi rate $\Omega/2\pi \gg \Gamma_1, \Gamma_d$ to localized at the poles for a strong measurement rate in the presence of a weak or zero oscillation rate $\Gamma_d \gg \Gamma_1, \Omega/2\pi$ (lower left corner).

12 http://www.physinfo.fr/publications/Ficheux1710.html
13 https://figshare.com/articles/Supplementary_Videos_for_Dynamics_of_a_qubit_while_ simultaneously_monitoring_its_relaxation_and_dephasing_/6127958/1

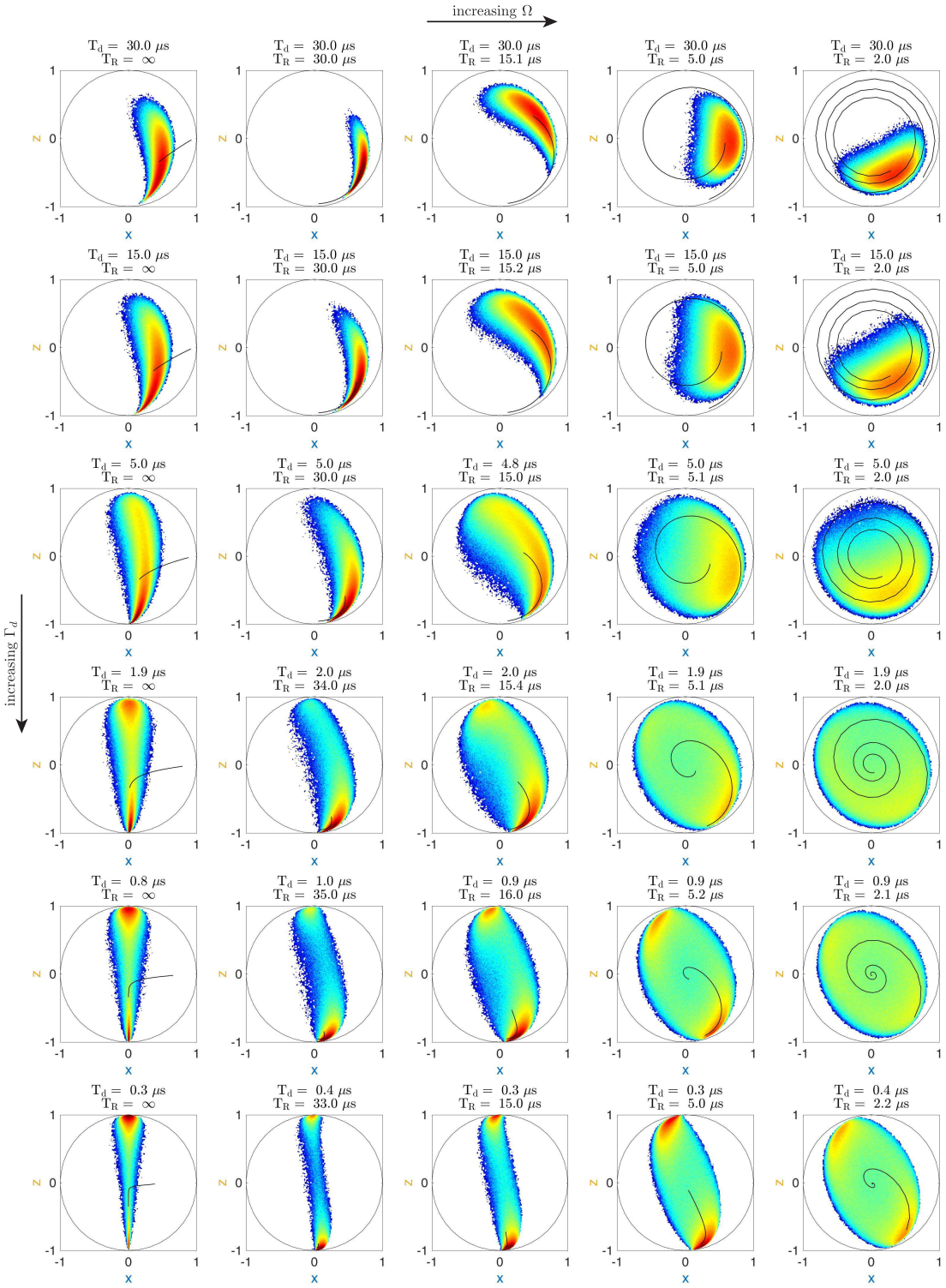

Figure 6.12: Distributions of the $x - z$ Bloch coordinates for 1.5 million measured trajectories shown 6 μs after the beginning of the measurement sequence. Each panel represents a particular choice of Rabi frequency Ω and dispersive measurement rate Γ_d. The representation is identical to that of Fig. 6.9 and both fluorescence and dispersive measurement records are taken into account. The movie of any of these 30 configurations can be accessed by clicking on the figure.

6.4 DIFFUSION OF QUANTUM TRAJECTORIES

6.4.1 *Introduction*

We saw in the previous sections that our quantum trajectories *diffuse* similarly to the *Brownian motion* [51] of a *particle* inside a colloid. Starting from a known initial condition, the evolution of the probability to find such a *particle* at a given position and time is ruled by the so-called *Fokker-Planck* equation (referred to as FP equation) proposed by Adriaan Fokker in 1913 and Max Planck in 1917. The FP equation is a partial differential equation that found application in all domains of science where *fluctuations* are important including physics, chemistry and biology [181].

Following a private discussion with Alain Sarlette and Pierre Rouchon, we introduce in this section a *Fokker-Planck equation* for the quantum state of a qubit undergoing weak measurements. By doing so, we switch to a 'macroscopic viewpoint' to describe the evolution of the ensemble of trajectories between t and $t + dt$. We are thus losing the 'microscopic viewpoint' of individual trajectories. In particular, the FP equation does not describe the time-correlations in individual trajectories.

In analogy with *Brownian motion*, measurement back-action plays the role of the *Langevin's force*. The Wiener process is the quantum analog of the noise term resulting from thermal collisions with molecules of the solvent. Drives and dissipation enter a *convection* term[14] analogous to the one resulting from *advection flows* and *transport phenomena* in hydrodynamics [182].

First, we derive the Fokker-Plank equation for a monitored qubit and validate it by comparing the trajectory statistics with random walk simulations. We use these simulations to explore high detection efficiency regimes that were not achievable in our experiment. The Fokker-Planck equation can be re-expressed with a *convection* and a *diffusion* term. We gain insight into the physics of diffusion by analyzing these terms. We study the dimensionality of the diffusion and we prove that our experiment is the first qubit experiment with a non zero determinant for the diffusion tensor revealing a genuine 3D diffusion. Finally, we show that an *Heisenberg-like* lower bound on the magnitude of the diffusion of pure states results from the *incompatibility* of the two measurements[15].

6.4.2 *Fokker-Planck equation*

For our system, the *stochastic master equation* (6.34) can be written in terms of Bloch coordinates as

$$\begin{pmatrix} dx_t \\ dy_t \\ dz_t \end{pmatrix} = A(x_t, y_t, z_t)dt + B(x_t, y_t, z_t). \begin{pmatrix} dW_u(t) \\ dW_v(t) \\ dW_w(t) \end{pmatrix} \tag{6.37}$$

14 Using this analogy, we talk about *convection* and *advection* for a qubit even if there is no medium in which the qubit state propagates.

15 We thank Irfan Siddiqi for pointing out this interesting question.

with the following vector and matrix

$$
\begin{aligned}
A(x_t, y_t, z_t) &= \begin{pmatrix} -(\frac{\Gamma_1}{2} + \Gamma_d + \Gamma_\varphi)x_t - \Omega z_t \\ -(\frac{\Gamma_1}{2} + \Gamma_d + \Gamma_\varphi)y_t \\ -\Gamma_1(1+z_t) + \Omega x_t \end{pmatrix}, \\
B(x_t, y_t, z_t) &= \begin{pmatrix} \sqrt{\frac{\eta_f\Gamma_1}{2}}(1 - x_t^2 + z_t) & -\sqrt{\frac{\eta_f\Gamma_1}{2}}x_t y_t & -\sqrt{2\eta_d\Gamma_d}x_t z_t \\ -\sqrt{\frac{\eta_f\Gamma_1}{2}}x_t y_t & \sqrt{\frac{\eta_f\Gamma_1}{2}}(1 - y_t^2 + z_t) & -\sqrt{2\eta_d\Gamma_d}y_t z_t \\ -\sqrt{\frac{\eta_f\Gamma_1}{2}}(1+z_t)x_t & -\sqrt{\frac{\eta_f\Gamma_1}{2}}(1+z_t)y_t & \sqrt{2\eta_d\Gamma_d}(1 - z_t^2) \end{pmatrix}.
\end{aligned}
\tag{6.38}
$$

Let us introduce $p(x, y, z, t)$ the probability to find a quantum trajectory at position (x, y, z) at time t. Following [183], p is ruled by a *Fokker-Planck* partial differential equation of the form

$$
\boxed{\frac{\partial p}{\partial t} = -\sum_{\chi \in \{x,y,z\}} \frac{\partial (pA_\chi)}{\partial \chi} + \sum_{\chi,\chi' \in \{x,y,z\}} \frac{\partial^2}{\partial \chi \partial \chi'}(pD_{\chi,\chi'})}
\tag{6.39}
$$

where the *diffusion tensor* is defined as $D = BB^\dagger/2$. The partial differential equation (6.39) can also be written as a *convection-diffusion equation*

$$
\boxed{\frac{\partial p}{\partial t} = -\nabla.(pC) + \nabla.(D\nabla p)}
\tag{6.40}
$$

with $\nabla = \begin{pmatrix} \frac{\partial}{\partial x} \\ \frac{\partial}{\partial y} \\ \frac{\partial}{\partial z} \end{pmatrix}$ and where the convection velocity is defined by

$$
C(x, y, z) = A(x, y, z) - \frac{1}{2}\begin{pmatrix} \sum_\chi \frac{\partial D_{x,\chi}}{\partial \chi} \\ \sum_\chi \frac{\partial D_{y,\chi}}{\partial \chi} \\ \sum_\chi \frac{\partial D_{z,\chi}}{\partial \chi} \end{pmatrix}.
\tag{6.41}
$$

In practice, the FP equation (6.39) is hard to solve[16]. We propose instead to perform random-walk simulation of a particle experiencing a convection velocity $C(x_t, y_t, z_t)$ and a diffusion tensor $D(x_t, y_t, z_t)$ calculated from the expression of A and B given by Eq. (6.38). The Fokker-Planck equation (6.39) is associated to the initial condition $p(x, y, z, 0) = \delta(x)\delta(y)\delta(1+z)$ corresponding to a qubit initialized in the ground state at time $t = 0$ in the experiment. For the simulation, we impose the boundary condition $x^2 + y^2 + z^2 \leq 1$ implying a zero probability flow outside the boundary of the Bloch sphere. In figure 6.13, we observe a good agreement between the experimental statistics of 1.5 million trajectory and the simulated probabiliy density $p(x, y, z, t)$. We verified that the simulation reproduced the experimental observation at all times and for each of the 30 configurations of Fig. 6.12 validating the Fokker-Planck equation (6.39) to describe the evolution of the trajectory statistics.

16 It might be possible to estimate the stationary solution $\bar{p}$ from the stationary convection-diffusion equation $-\nabla.(\bar{p}C) + \nabla.(D\nabla\bar{p}) = 0$.

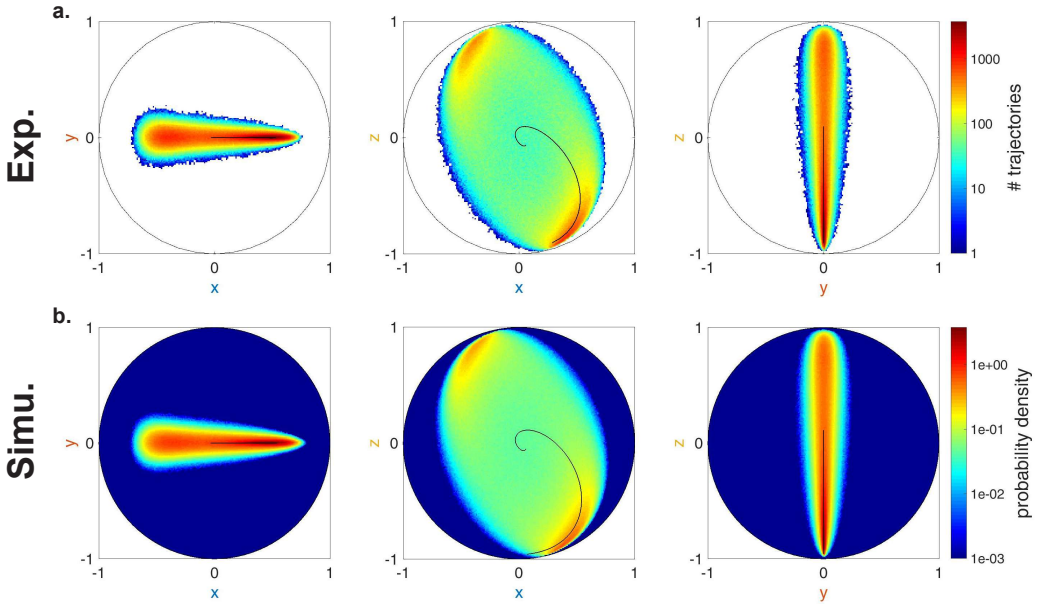

Figure 6.13: Comparison between the statistics of the projection of qubit trajectories in the $x-y$, $x-z$ and $y-z$ planes of the Bloch sphere for the complete measurement records $\{u(t), v(t), w(t)\}$ (Fig. **a**) with the projection of the simulated probability density to find a particle experiencing a Brownian motion with a convection velocity $C(x, y, z)$ and a diffusion tensor $D(x, y, z)$ (Fig. **b**). The experimental parameters $\Gamma_1 = (15\ \mu\text{s})^{-1}$, $\Gamma_\varphi = (17.9\ \mu\text{s})^{-1}$, $\Gamma_d = (0.9\ \mu\text{s})^{-1}$ and $\Omega/2\pi = (5.2\ \mu\text{s})^{-1}$ enter Eq. (6.38) to compute the convection velocity field C (Eq. (6.41)) and the diffusion tensor field $D = BB^\dagger/2$ used in the simulation.

6.4.3 *Impact of the efficiencies on the statistics*

We demonstrated the accuracy of FP equation to describe the dynamics of the probability distribution of the quantum trajectory of a qubit. Assuming that it is still valid for parameters that are not accessible in the experiment, we can simulate the trajectory statistics to explore unattainable regimes of parameters. As explained in section 5.6, increasing the detection efficiencies η_d and η_f is a difficult technical challenge[17]. However, in the FP equation (6.39), the efficiencies only play a role in the diffusion term, which can be computed at will.

In Fig. 6.14, we show the simulated probability densities in the condition of Fig. 6.13 for increasing efficiencies up to 100%. As the efficiency increases, the shape of the distribution resulting from the diffusion (measurement back-action) appears more clearly and the random walkers (trajectories) span a larger area of the Bloch sphere with a higher density closer to the surface of the sphere (higher purity states). Interestingly though, the characteristic shapes that are linked to the incompatibility between our various detectors explained in section 6.3.2 are already qualitatively captured at our experimental level of efficiency and only change quantitatively as the efficiencies rise.

17 We recall that the inefficiency of the detection setup originates from unavoidable losses of microwave components between the system and the quantum limited amplifier, the finite noise temperature of the following amplifier, losses to spurious other modes such as the input line. See chapter 5.

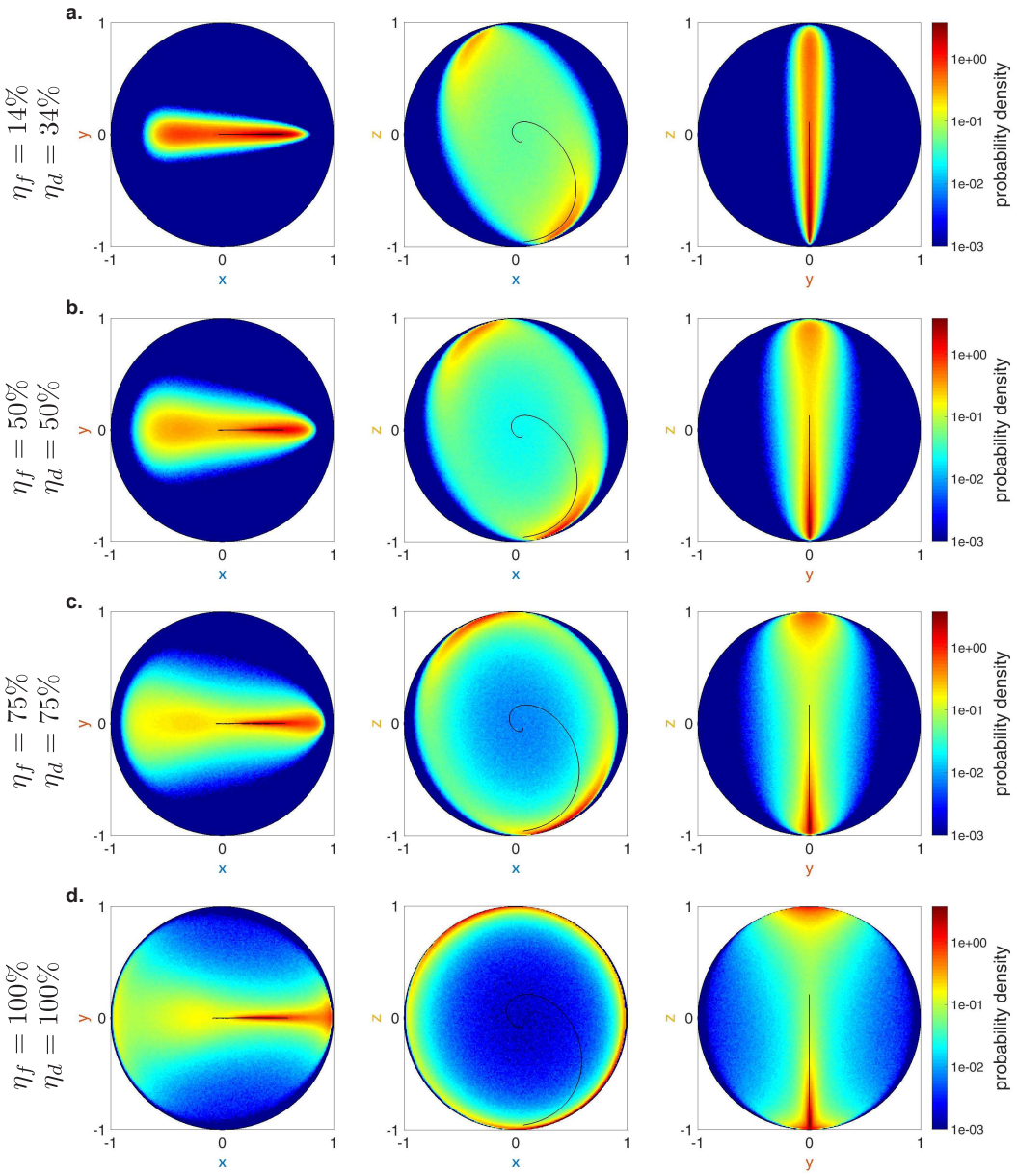

Figure 6.14: Projections of the simulated probability density on three planes of the Bloch sphere in the configuration of Fig. 6.9. Fig. **a** is a simulation with the efficiencies $\eta_f = 0.14$ and $\eta_d = 0.34$ as in the experiment. We increase jointly the efficiencies $\eta_{f,d} = 0.5$ (Fig. **b**), $\eta_{f,d} = 0.75$ (Fig. **c**), and $\eta_{f,d} = 1$ (Fig. **d**). A clear broadening of the distribution of states occurs for simulated higher detector efficiencies. The shape of the distribution remains qualitatively the same except for unit efficiencies, which is out of experimental reach.

At unit efficiency, the quantum states is confined to a pure wavefunction diffusion on the surface of the Bloch sphere. The characteristic shape of the projected distribution changes in the last row of Fig. 6.14 but this situation is unreachable in practice[18].

6.4.4 *Convection velocity*

We can gain insight into the transport phenomena of qubit states by analyzing the convection velocity C. Using Eq. (6.41), the convection velocity reads

$$C(x_t, y_t, z_t) = \begin{pmatrix} -\Gamma_2 x_t - \Omega z_t \\ -\Gamma_2 y_t \\ -\Gamma_1(1+z_t) + \Omega x_t \end{pmatrix} + \frac{\eta_d \Gamma_d}{2} \begin{pmatrix} x_t(1-6z_t^2) \\ y_t(1-6z_t^2) \\ 6z_t(1-z_t^2) \end{pmatrix} + \eta_f \Gamma_1 \begin{pmatrix} x_t(1+z_t-\frac{3}{4}(x_t^2+y_t^2)) \\ y_t(1+z_t-\frac{3}{4}(x_t^2+y_t^2)) \\ \frac{1}{4}(1+z_t)(1+z_t-3(x_t^2+y_t^2)) \end{pmatrix} \tag{6.42}$$

where the inverse coherence time is $\Gamma_2 = \frac{\Gamma_1}{2} + \Gamma_d + \Gamma_\varphi$.

The first term of Eq. (6.42) corresponds to the *advection* of the probability flow by the circular motion induced by the Rabi torque and by the damping caused by decoherence. This *advection* term alone brings the qubit state along the average trajectory depicted in Fig. 6.13. The two other contributions emanate from the diffusive back-action of the measurements translated into the finite spread of the probability distribution. The convection of the probability flow takes place both by *advection* and by *diffusion*[19].

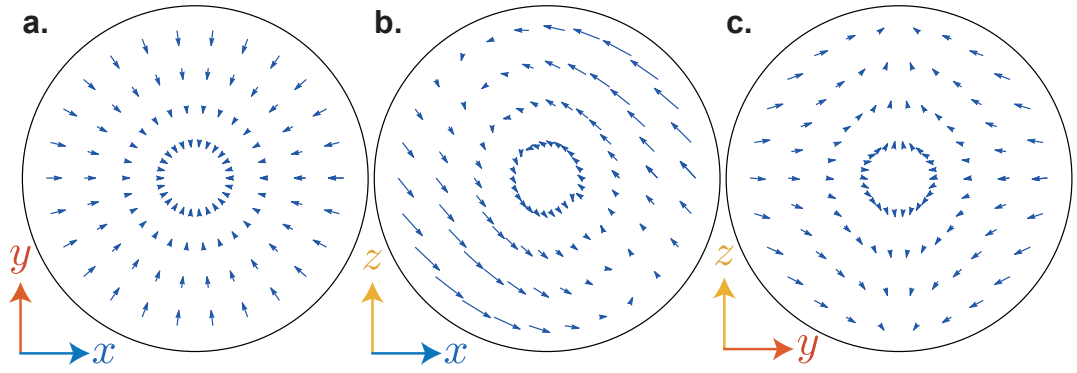

Figure 6.15: Cuts of the convection velocity field (6.42) in the $x-y$ (Fig. **a**), $x-z$ (Fig. **b**) and $y-z$ (Fig. **c**) planes. The blue arrows correspond to $C(x_t, y_t, z_t)dt$ with the parameters of Fig. 6.13 $\Gamma_1 = (15\ \mu\text{s})^{-1}$, $\Gamma_\varphi = (17.9\ \mu\text{s})^{-1}$, $\Gamma_d = (0.9\ \mu\text{s})^{-1}$, $\Omega/2\pi = (5.2\ \mu\text{s})^{-1}$ and $dt = 100$ ns. The solid black circle represents the pure state of the plane that is also the rigid boundary condition for the FP equation.

In Fig. 6.15, we show cuts of the convection velocity field. In the plane $\langle\sigma_z\rangle = 0$ (Fig. **a**), the convection brings the qubit along the z-axis. Away from this plane, the convection tends to bring quantum states to negative (resp. positive) x for $\langle\sigma_z\rangle > 0$ (resp. $\langle\sigma_z\rangle < 0$) planes (not represented on Fig. 6.15). Interestingly, a cut of the $x-z$

18 At the time of writing this thesis, the highest total detection efficiency reported in the microwave domain is 80% for a single dispersive channel [159].

19 This situation is reminiscent of convective heat transfer. For instance in fluid dynamics, the apparition of Rayleigh–Bénard convection originates jointly from the diffusion of heat from the fluids to the plates and advection of heat in the fluid under the action of buoyancy and gravity.

plane (Fig. **b**) reveals two regions where the convection tends to vanish corresponding to the two maxima of the probability distribution of Fig. 6.13. The convection velocity in the $x-z$ plane is independent of the $\langle\sigma_y\rangle$ value. Finally, Fig. **c** reveals that the convection flow pushes the probability density toward the pointer states of the σ_z measurement (the poles) owing to its large measurement rate.

6.4.5 *Diffusion tensor*

In the Zeno regime, we showed that the general shape of the probability distribution can be understood from an analysis of the convection velocity field. However, the *diffusion tensor* alone induces the non-deterministic behavior of the system. The diffusion does not depend on the applied drives, nor on unmonitored channels and thus exclusively characterizes the measurement process. We can compute $D = BB^\dagger/2$ from Eq. (6.38). The diffusion can be decomposed into independent contributions[20] corresponding to the Wiener processes W_u, W_v and W_w

$$D(x,y,z) = \frac{1}{2}B(x,y,z)B(x,y,z)^\dagger = D_u(x,y,z) + D_v(x,y,z) + D_w(x,y,z) \quad (6.43)$$

where the independent contributions read

$$D_u(x,y,z) = \frac{\eta_f\Gamma_1}{2}\begin{pmatrix} (1+z-x^2)^2 & -(1+z-x^2)xy & -(1+z)x(1+z-x^2) \\ -(1+z-x^2)xy & x^2y^2 & x^2y(1+z) \\ -x(1+z)(1+z-x^2) & x^2y(1+z) & x^2(1+z)^2 \end{pmatrix}$$

$$D_v(x,y,z) = \frac{\eta_f\Gamma_1}{2}\begin{pmatrix} x^2y^2 & -(1+z-y^2)xy & xy^2(1+z) \\ -(1+z-y^2)xy & (1+z-y^2)^2 & -(1+z)y(1+z-y^2) \\ xy^2(1+z) & -(1+z)y(1+z-y^2) & y^2(1+z)^2 \end{pmatrix}$$

$$D_w(x,y,z) = 2\eta_d\Gamma_d\begin{pmatrix} x^2z^2 & xyz^2 & -(1-z^2)xz \\ xyz^2 & y^2z^2 & -(1-z^2)yz \\ -(1-z^2)xz & -(1-z^2)yz & (1-z^2)^2 \end{pmatrix}$$

In contrast to the convection velocity, the diffusion is given by a *tensor field*, which cannot be easily represented inside the Bloch sphere. We further improve our understanding of the diffusion by looking at two invariant quantities of the tensor, its *determinant* and *trace*.

6.4.6 *Dimensionality of the diffusion*

The *determinant* of the diffusion tensor tells whether, the diffusion occurs in all directions or if it is singular and restricted a subspace of the Bloch sphere. If the random walk is confined in one direction (resp. two directions), the diffusion tensor will have two zero eigenvalues (resp. one zero eigenvalue) and a zero determinant. In this case, the quantum state can still diffuse in the complete Bloch ball if the vector fields of the stochastic Eq. (6.34) satisfy Hörmander's condition [184]. Let us give a brief analysis to understand the dimensionality of diffusion in experimentally relevant situations.

20 The independence between the contributions to the diffusion tensor is a property of the *stochastic master equation* (6.34). For a set of jump operators $\{L_\mu\}$ acting on a qubit, the diffusion tensor reads $D_{i,j} = \frac{1}{2}\sum_k \mathrm{Tr}(\mathcal{M}_k(\rho)\sigma_i)\mathrm{Tr}(\mathcal{M}_k(\rho)\sigma_j)$ where $\mathcal{M}_k(\rho) = L_k\rho + \rho L_k^\dagger - \mathrm{Tr}(L_k\rho + \rho L_k^\dagger)\rho$.

In the case of a dispersive measurement alone, the only contribution to the diffusion tensor (6.43) is D_w, which has two zero eigenvalues. The diffusion is thus *1-dimensional*. This is in agreement with the result of Sarlette and Rouchon [172] who showed that at every time-step, the diffusion develops on an *ellipse* that shrinks toward the z axis of the Bloch sphere according to Eq. (6.14). A similar result can be obtained when measuring the orthogonal quadrature of the cavity field. The diffusion occurs on a deterministic *circle* given by Eq. (6.18).

For an exclusive fluorescence measurement, the two contributions to the diffusion tensor (6.43) correspond to the Wiener processes W_u and W_v. The diffusion tensor $D = D_u + D_v$ has one zero eigenvalue revealing a *2-dimensional* diffusion. The random walk takes place on the surface of a *spheroid* [23, 172] given by Eq. (6.25) that goes through the south pole of the Bloch sphere.

Recently, Hacohen-Gourgy et al. [49] were able to measure simultaneously two non-commuting observable of a qubit in a rotating frame namely the observables σ_x and σ_y. They observed an *isotropic* and *persistent* diffusion in $x-y$ plane when the strengths of the two measurement are balanced. In their case, the diffusion tensor has one zero eigenvalue revealing that they observed a *2-dimensional* diffusion phenomenon in a plane.

By taking into account the outcomes of the two detectors in our experiment, the three Wiener processes contribute to the diffusion (see Eq. (6.43)). The determinant reads

$$\boxed{\mathrm{Det}[D(x,y,z)] = \frac{\eta_d \Gamma_d \eta_f \Gamma_1}{8}(1+z)^4\left(1-x^2-y^2-z^2\right)^2.} \tag{6.44}$$

The determinant annihilates on the surface of the Bloch sphere as it is not possible to diffuse in the direction orthogonal to the boundary. In the bulk of the Bloch ball, the determinant (6.44) takes finite values when the two channels are monitored $\eta_d\eta_f \neq 0$. Our experiment is thus the first qubit experiment with a non zero determinant for the diffusion tensor revealing a genuine *3D diffusion* in the volume of the Bloch ball.

6.4.7 *Diffusivity*

Instead of considering the diffusion along particular coordinates, we consider the 'overall' diffusion. We express the *average diffusivity* as follows

$$\boxed{d(x,y,z) = \mathrm{Tr}[D(x,y,z)].} \tag{6.45}$$

The diffusivity is a scalar field that represents the magnitude of the *back-action* at any point of the Bloch sphere regardless of the direction of the diffusion. This scalar field is invariant under rotation around z. In Fig. 6.16, we represent cuts of the diffusivity in the $x-z$ plane. We separate the different contributions coming from the monitoring of the cavity field (Fig. **a**), the monitoring of fluorescence (Fig. **b**) and the simultaneous monitoring of both (Fig. **c**).

Whenever measuring continuously an observable (such as σ_z) or an operator (such as σ_-), the quantum back-action stochastically kicks the quantum state to update it based on the result of the measurement. However, the *back-action* vanishes when reaching the

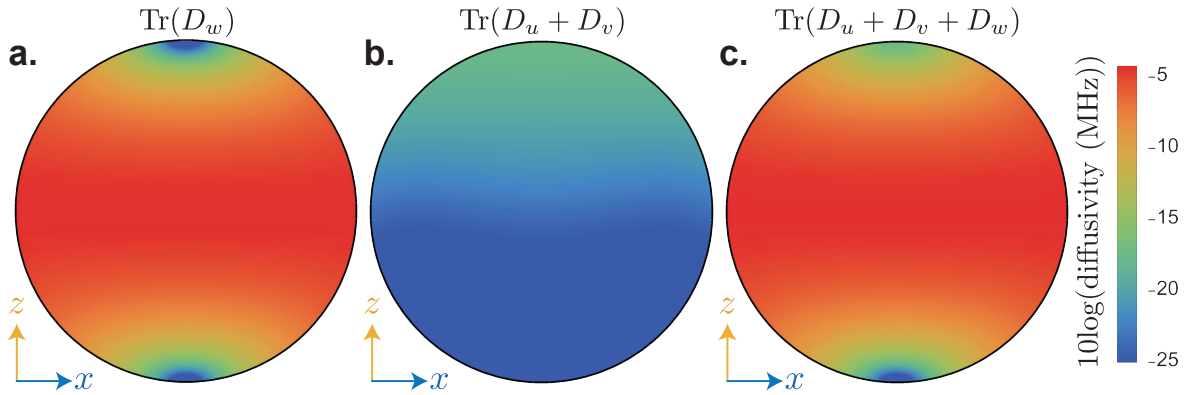

Figure 6.16: Magnitude of the average diffusivity given by Eq. (6.45) in a $\langle\sigma_y\rangle = 0$ slice of the Bloch sphere for dispersive measurement (Fig. **a**), fluorescence measurement (Fig. **b**) and both (Fig. **c**). In Fig. **a**, the diffusion is symmetric under $z \to -z$. We use the parameters of Fig. 6.13, $\Gamma_1 = (15\ \mu\mathrm{s})^{-1}$, $\Gamma_d = (0.9\ \mu\mathrm{s})^{-1}$ and $(\eta_f, \eta_d) = (0.14, 0.34)$. Diffusion vanishes when the quantum state approaches one of the pointer states of the σ_z measurement (poles of the sphere). Monitoring energy relaxation (Fig. **b**) leads to a maximal diffusivity at the north pole of the Bloch sphere where the quantum state experiences the strongest measurement back-action and minimal diffusivity in the ground state. The average magnitude of the diffusion induced by this last measurement is much smaller than the one of Fig. **a** because of the measurement rate asymmetry $\frac{\eta_f \Gamma_1}{\eta_d \Gamma_d} \simeq 0.025$. The resulting total diffusivity (Fig. **c**) only vanishes at the south pole of the Bloch sphere.

so-called *pointer states* of the measurement. In the case of a σ_z measurement, the pointer states are given by the poles of the Bloch sphere (Fig. 6.16 **a**). In between, the magnitude of the coefficient diffusion is maximal near the equator so the qubit state 'must' jump quickly from one region to the other in quantum trajectories. When monitoring σ_-, the south pole $|g\rangle$ of the Bloch sphere is the only pointer state (Fig. 6.16 **b**). When the qubit state is close to the excited state $|e\rangle$, the energy relaxation probability is maximal and the back-action of the associated measurement chases the state away from the north pole. Hence, the total diffusivity (Fig. 6.16 **c**) only goes to zero in the ground state $|g\rangle$. In the excited state, the diffusion is *persistent* even if the contribution of the dispersive measurement vanishes.

6.4.8 *An Heisenberg-like inequality for pure states*

We used throughout this thesis the concept of *incompatible measurement* to describe the quantum back-action of energy relaxation and dispersive measurement. We may wonder if there is an *Heisenberg-like* inequality for our system. The usual *Heisenberg-Roberston* uncertainty relation [185] states that the accuracy with which two Von Neumann measurements can be performed is limited by the restriction that the product of the uncertainties in the two measurements is at least of the order of the commutator of the associated observables[21].

21 In the case of the two conjugate variable X and P describing the free propagation of a particle, we recover the historical *Heisenberg inequality* $\sigma_X \sigma_P \geq \hbar/2$.

In the continuous measurement framework, the signature of the incompatibility of the measurement is encoded in a lower bound of the diffusion coefficients [186]. We show that the *Heisenberg inequality* finds its correspondence in a *lower bound* on the total diffusivity of pure states. From Eq. (6.37) we notice that $\mathrm{Tr}[BB^\dagger]dt = 2\mathrm{Tr}[d\rho d\rho]$. We link the diffusivity to the incremental evolution of the density matrix[22]

$$d(x,y,z) = \frac{1}{dt}\mathrm{Tr}[d\rho d\rho]. \tag{6.46}$$

For pure states, the quantity $\mathrm{Tr}[d\rho d\rho]$ is known to be related to the sum of the variances of the measurements [49]. On the surface of the Bloch sphere, we obtain

$$d(x,y,z) = \eta_f\Gamma_1 \langle(\Delta\sigma_+)(\Delta\sigma_-)\rangle + \eta_d\Gamma_d \langle\Delta{\sigma_z}^2\rangle \tag{6.47}$$

where $\Delta A = A - \langle A\rangle$. A complication arises from the fact that the monitored operator $\sigma_- = (\sigma_x - i\sigma_y)/2$ is not hermitian nor skew-hermitian hence the apparition of $\sigma_+ = \sigma_-^\dagger$. However, we can develop

$$\langle(\Delta\sigma_+)(\Delta\sigma_-)\rangle = \frac{1}{4}\left(\langle\Delta{\sigma_x}^2\rangle + \langle\Delta{\sigma_y}^2\rangle - i\langle[\sigma_x,\sigma_y]\rangle\right). \tag{6.48}$$

The two first terms are the variances associated to the measurement of the x and y coordinates of the qubit, the last term shows how the hermitian and skew-hermitian parts interference of the jump operator associated to the energy relaxation channel. In the end, we obtain

$$d(x,y,z) = \frac{\eta_f\Gamma_1}{4}\langle\Delta{\sigma_x}^2\rangle + \frac{\eta_f\Gamma_1}{4}\langle\Delta{\sigma_y}^2\rangle + \eta_d\Gamma_d\langle\Delta{\sigma_z}^2\rangle - \frac{\eta_f\Gamma_1}{4}i\langle[\sigma_x,\sigma_y]\rangle. \tag{6.49}$$

The diffusivity is thus related to the sum of the variances associated to the measurement of every Pauli observable (plus the previously mentioned correction), and not to their product like in the Heisenberg inequality. In the general case, for a pure state $\rho = |\psi\rangle\langle\psi|$ and an arbitrary set of jump operators $\{L_k\}$, the diffusivity is linked to jump operators by the relation

$$\mathrm{Tr}[d\rho d\rho] = 2\sum_k \eta_k \langle\psi|(\Delta L_k^\dagger)(\Delta L_k)|\psi\rangle\, dt. \tag{6.50}$$

Our task is thus to find a lower bound on $\langle\psi|(\Delta L_k^\dagger)(\Delta L_k)|\psi\rangle = ||(\Delta L_k)|\psi\rangle||^2$. Such a lower bound is not unique. For incompatible observable, there always exists a non zero lower bound on the sum of incompatible *observable* [187]. This statement does not hold in general for *operators*. We can however give a lower bound on Eq. (6.50) using the geometrical inequality

$$|\langle\psi|L^\dagger|\psi^\perp\rangle|^2 \leq ||L|\psi\rangle||^2 \tag{6.51}$$

valid for $|\psi^\perp\rangle$ orthogonal to $|\psi\rangle$. In the end we obtain the following lower bound on the diffusivity

$$\boxed{d(x,y,z) \geq (1+z)\left(\frac{\eta_f\Gamma_1}{2}(1+z) + \eta_d\Gamma_d(1-z)\right).} \tag{6.52}$$

22 This identity is not specific to our system. It holds for any monitored open quantum system ruled by the *stochastic master equation* (6.34).

In the excited state the diffusion never vanishes as it is lower bounded by the magnitude of the back-action of energy relaxation $2\eta_f\Gamma_1$ (see Fig. 6.16). In the ground state, the lower bound vanishes as the back-action goes to zero. However, this is a special case for which the lower bound (6.52) is always saturated. The fact that the Heisenberg inequality transforms into a lower bound on the diffusion is a signature of the enhancement of the diffusion due to the different measurements. Equilibrium points (pointer states) correspond to where the diffusivity vanishes (see Fig. 6.16 or [49]). We talk about a *persistant diffusion* around these points. The contributions of the measurements are independent in Eq. (6.52). In the spirit of the Heisenberg inequality we 'mix' the two contributions by application of the Cauchy-Schwarz inequality to Eq. (6.47)

$$d(x,y,z) \geq \sqrt{\eta_f\Gamma_1\eta_d\Gamma_d}\,|\langle\psi|\Delta\sigma_+\Delta\sigma_z|\psi\rangle|^2 = \frac{\sqrt{\eta_f\Gamma_1\eta_d\Gamma_d}}{4}(1+z)^2(x^2+y^2) \quad (6.53)$$

this last bound is similar to the one of [49] but it is weaker than Eq. (6.52) and it vanishes in the excited state.

6.5 CONCLUSION

In this chapter we discussed

- the general framework for measurement back-action with the example of weak measurement of the dispersive and energy relaxation channels.
- the formalism of quantum trajectories leading to a stochastic diffusion in the Bloch sphere.
- the shape of the trajectory statistics that contains the knowledge of different observers about a same quantum system.
- the Fokker-Planck equation revealing a 3-dimensional diffusion, which is characteristic of our incompatible measurements.
- an Heisenberg like inequality for continuous measurements of arbitrary operators.

Quantum trajectories have a bright future with numerous applications including real-time adaptative measurement [188], quantum parameter estimation with a neural network [189], the determination of the arrow of time from the irreversibility of quantum measurement [190], the observation of spikes in quantum trajectories [191, 192], investigation of chaos [193], the determination of quantum caustics [175, 25, 177] and applications in single-shot quantum thermodynamics [194, 195, 196].

7

POST-SELECTED QUANTUM TRAJECTORIES

Our everyday experience teaches us that the future is different from the past so we can intuitively determine the direction of an *arrow of time* pointing towards the future. *Time asymmetry* arises in classical physics for *irreversible* evolution of either a dissipative system or an out-of-equilibrium closed system with an internal dynamics. In the latter case, the *irreversibility* of the evolution is formalized by the second law of thermodynamics, which proclaims that the entropy of an isolated system can never decrease over time. In the absence of irreversibility, watching a 'movie' backwards shows an evolution consistent with the laws of physics.

In quantum mechanics, the Schrödinger equation for isolated system is time symmetric as is its classical counterpart. In the 50s, von Neumann and Bohm [52, 53] suggested that the irreversible collapse of a wave packet of the state of a system under the influence of measurement introduces a fundamental *time asymmetry* at the microscopic level. The *measurement back-action* was thus thought of as a time asymmetric element in quantum theory. Nevertheless, the symmetry of the rules of quantum mechanics is fully restored when specifying both the initial state and the final state of a closed system. The equivalent role of *preparation* or *pre-selection* and *post-selection* was enlightened by Aharonov et al. in a seminal paper [54] and gave rise to the two-state vector formalism [197]. Aharonov et al. introduced a *retrodiction* estimation of a quantum state which was revisited in the case of open systems with the introduction of an *effect matrix* [55, 56, 57, 58]. While the density matrix is the quantum state of the system conditioned on the *past* measurement records, the *effect matrix* is the quantum state conditioned on the information available in the *future*. Taking into account the *forward* and *backward* estimation of the quantum state at the same time provides a so-called *past quantum state* that encapsulates all the information available from past and future measurements.

In 1987, Aharonov noticed [59] that in the presence of both *preparation* and *post-selection*, the measured expectation values of the signal can spread outside of the normal eigenvalue range. This anomalous values were called *weak values* [60]. Thus, on a carefully selected sub-ensemble of realizations of the experiment, the result of a weak measurement of a component of a qubit can in principle reach arbitrarily larges values[1]. In this chapter, we present the results of an experiment illustrating this fact. By combining preparation and post-selection, the Bloch vector resulting from the direct quantum tomography method exposed in chapter 3 exceeds the boundary of the unit sphere [61, 62, 63, 64].

Weak values were observed for the first time in 1991 [198] and have been shown to lead to a violation of Leggett-Garg inequality [61, 199, 200, 201] and thus to rule out macro-

1 In practice, the magnitude of the *weak value* is limited by the decoherence between preparation and post-selection.

realistic physical theories[2]. Weak values are claimed to provide interesting features such as noiseless amplification [202, 203, 60], a direct measurement of a wavefunction [204] or even to solve quantum 'paradoxes' [205]. These anomalous values seem to originate from a statistical effect arising from measurement back-action with preparation and post-selection but this topic is the subject of considerable debates [206, 60, 207, 208, 209, 210]. However there is no question that post-selecting realizations is well defined and that one needs the tools to predict the average outcome under post-selection. This chapter intends to put the formalism to the test and understand its limitations.

Similarly to classical estimation theory, predictions on the outcome of a measurement at time t can be made by *filtering* given observations before and up to t, by *retrodiction* given the observations after t or by *smoothing* given observations before and after t. The *smoothed* estimate conditioned on the complete measurement record is obtained by *filtering* and *retro-filtering* techniques [211, 57]. Using all the information extracted from the past and future measurements relative to the time at which an observable is estimated leads to an *acausal smoothed estimation* of the probability of outcomes associated to this measurement [212].

First, let us introduce the *past quantum state* composed of the density matrix and the *effect matrix* to describe pre-selected and post-selected trajectories [55, 56, 57, 58]. Similarly to the density matrix, the effect matrix evolves according to a stochastic differential equation in the continuous times limit. This formalism is then related to the *weak values* envisioned by Aharonov. Finally its operational meaning is investigated by confrontation with our experimental results.

7.1 PAST QUANTUM STATE

7.1.1 *Prediction and retrodiction*

This derivation is based on the work of Gammelmark et al. [58]. We introduce in this section the *effect matrix* and the associated *past quantum state*. A quantum trajectory is defined as iterated Kraus maps given by Eq. (6.31)

$$\boxed{\rho_{t_{n+1}} = \frac{\mathbf{K}_{y(t_n)}(\rho_{t_n})}{\mathrm{Tr}[\mathbf{K}_{y(t_n)}(\rho_{t_n})]} = \frac{\mathbf{K}_{y(t_n)} \circ ... \circ \mathbf{K}_{y(t_0)}(\rho_0)}{\mathrm{Tr}[\mathbf{K}_{y(t_n)} \circ ... \circ \mathbf{K}_{y(t_0)}(\rho_0)]}} \tag{7.1}$$

where we define the discrete times $t_n = ndt$ between each time step of the trajectory for $0 \leq n \leq N$ and $\{y_{t_n}\}$ are the vectors of the measurement records at each time. For a system with a set of jump operators $\{L_\mu\}$, the partial Kraus map giving the incremental evolution during dt is given by Eq. (6.28)

$$\begin{cases} \mathbf{K}_{y(t)}(\rho_t) = M_{y(t)}\rho_t M_{y(t)}^\dagger + \sum_{\mu\neq 0}(1-\eta_\mu)dtL_\mu\rho_t L_\mu^\dagger \\ \text{with } M_{y(t)} = \mathbb{1} - \left(\frac{i}{\hbar}H + \sum_{\mu\neq 0} L_\mu^\dagger L_\mu/2\right)dt + \sum_{\mu\neq 0}\sqrt{\eta_\mu}L_\mu y_\mu(t)dt \end{cases} \tag{7.2}$$

2 under the assumption that the detector does not disturb the system in a classical sense.

as a function of the measurement record $y_\mu(t)dt = \sqrt{\eta_\mu}\mathrm{Tr}(L_\mu\rho_t + \rho_t L_\mu^\dagger)dt + dW_\mu(t)$.

We want to perform a generalized measurement[3] between $t_{n-1} = t_n - dt$ and t_n that replaces the Kraus map evolution of Eq. (7.1) during this time step. The measurement is associated to a set of measurement operators $\{\Omega_m\}$ (see chapter 3). The probability to measure m between t_{n-1} and t_n conditioned on the *past* measurement records is given by

$$\mathbb{P}[m|\rho_0, y(t_0), ..., y(t_{n-2})] = \mathrm{Tr}[\Omega_m \rho_{t_{n-1}} \Omega_m^\dagger]. \tag{7.3}$$

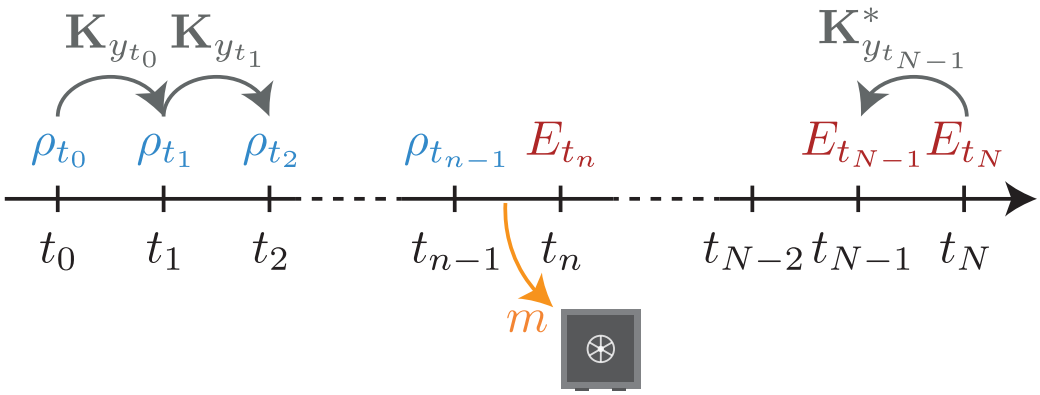

Figure 7.1: The *forward* estimation of the state of the system is obtained by iteration of the Kraus map (7.2) yielding the usual density matrix. Reciprocally, the state of the system conditioned on the *future* measurement records is captured by the *effect matrix* that propagates backward in time according to Eq. (7.6). We perform a generalized measurement between t_{n-1} and t_n leading to a record m stored in a safe. The probability to find m is best estimated conditioning on the complete sequence of measurement records with $p(m|y) \propto \mathrm{Tr}[\Omega_m \rho_{t_{n-1}} \Omega_m^\dagger E_{t_n}]$ according to Eq. (7.4).

Imagine that the record m is stored 'in a safe' for later inspection (see Fig. 7.1). At the end of the experiment we want to estimate *a posteriori* the value observed when the safe is opened knowing the *complete* measurement record of the experiment. The probability to find the record m conditioned on the complete record reads

$$\mathbb{P}[m|\rho_0, y(t_0), ..., y(t_T)] = \frac{\mathrm{Tr}[\mathbf{K}_{y(t_{N-1})} \circ ... \circ \mathbf{K}_{y(t_n)}(\Omega_m \rho_{t_{n-1}} \Omega_m^\dagger)]}{\sum_k \mathrm{Tr}[\mathbf{K}_{y(t_{N-1})} \circ ... \circ \mathbf{K}_{y(t_n)}(\Omega_k \rho_{t_{n-1}} \Omega_k^\dagger)]}. \tag{7.4}$$

This expression can be recast as

$$\mathbb{P}[m|\rho_0, y(t_0), ..., y(t_T)] = \frac{\mathrm{Tr}[\Omega_m \rho_{t_{n-1}} \Omega_m^\dagger E_{t_n}]}{\sum_k \mathrm{Tr}[\Omega_k \rho_{t_{n-1}} \Omega_k^\dagger E_{t_n}]} \tag{7.5}$$

where we introduced the *effect matrix*

$$\boxed{E_{t_n} = \frac{\mathbf{K}^*_{y(t_n)} \circ ... \circ \mathbf{K}^*_{y(t_{N-1})}(\mathbb{1})}{\mathrm{Tr}[\mathbf{K}^*_{y(t_n)} \circ ... \circ \mathbf{K}^*_{y(t_{N-1})}(\mathbb{1})]}.} \tag{7.6}$$

3 We allow the measurement apparatus during this particular time step to differe from the other measurements along the trajectory.

The adjoint[4] of the Kraus map is $\mathbf{K}^*_{y(t)}(E) = M^\dagger_{y(t)} E M_{y(t)} + \sum_\mu (1-\eta_\mu) dt L^\dagger_\mu E L_\mu$. The *effect matrix* is an estimation of the state of the qubit conditioned on the information available from the 'future'[5] measurement records of the trajectory. This hermitian matrix evolves *backward* in time by application of the conjugated Kraus maps according to the *retrodiction* formula

$$E_{t_n} = \frac{\mathbf{K}^*_{y(t_n)}(E_{t_{n+1}})}{\mathrm{Tr}[\mathbf{K}^*_{y(t_n)}(E_{t_{n+1}})]}. \tag{7.7}$$

The time symmetry of the formalism is restored by specifying the *final state* of the evolution E_{t_N} along with the initial condition ρ_{t_0}. Note that in the absence of *post-selection* after time t_N, $E_{t_N} = \frac{\mathbb{1}}{2}$. In contrast, in the absence of *preparation*, ρ_{t_0} is in its equilibrium thermal state.

The pair of matrices $\Xi_{t_n} = (\rho_{t_{n-1}}, E_{t_n})$ is called the *past quantum state* in the formalism of Gammelmark et al. [58]. It contains all the available information to make a predictions about the outcome of a measurement occurring between t_{n-1} and t_n thanks to Eq. (7.5). The introduction of an initial (preparation) and final (post-selection) selection procedures makes our formalism perfectly time symmetric in the absence of dissipation.

7.1.2 *Continuous time dynamics*

In the continuous time limit, the Kraus map defined by Eq. (7.2) reads

$$\begin{aligned}\mathbf{K}^*_{y(t)}(E_{t+dt}) = E_{t+dt} + \frac{i}{\hbar}[H, E_{t+dt}]dt + \sum_\mu dt(L^\dagger_\mu E_{t+dt} L_\mu - \frac{L^\dagger_\mu L_\mu}{2} E_{t+dt} - E_{t+dt}\frac{L^\dagger_\mu L_\mu}{2}) \\ + \sum_\mu \sqrt{\eta_\mu}(L^\dagger_\mu E_{t+dt} + E_{t+dt} L_\mu) y_\mu(t) dt.\end{aligned} \tag{7.8}$$

And since $\mathrm{Tr}(\mathbf{K}^*_{y(t)}(E_{t+dt})) = 1 + \sum_\mu \sqrt{\eta_\mu}\mathrm{Tr}(L^\dagger_\mu E_{t+dt} + E_{t+dt} L_\mu) y_\mu(t) dt$. The normalisation factor can be approximated at order dt by

$$\begin{aligned}\frac{1}{\mathrm{Tr}(\mathbf{K}^*_{y(t)}(E_{t+dt}))} = 1 - \sum_\mu \sqrt{\eta_\mu}\mathrm{Tr}(L^\dagger_\mu E_{t+dt} + E_{t+dt} L_\mu) y_\mu(t) dt \\ + \sum_\mu \eta_\mu \mathrm{Tr}(L^\dagger_\mu E_{t+dt} + E_{t+dt} L_\mu)^2 dt.\end{aligned} \tag{7.9}$$

At first order in dt, the evolution of the effect matrix is ruled by a *stochastic master equation*[6]

$$\boxed{dE_t = -\frac{i}{\hbar}[H, E_t]dt - \sum_{i=1}^m \mathcal{D}^*_i(E_t)dt - \sum_{i=1}^m \sqrt{\eta_i}\mathcal{M}_i(E_t)\left(y_\mu(t)dt - \mathrm{Tr}(L^\dagger_\mu E_t - E_t L_\mu)dt\right)}$$

4 The adjoint of $\mathbf{K}$ is defined by $\mathrm{Tr}[A\mathbf{K}(B)] = \mathrm{Tr}[\mathbf{K}^*(A)B]$ for any hermitian operators A, B.

5 The notion of future and past is referred to the time t_n, at which the record of the generalized measurement is stored in the safe.

6 In [58] they use the backward time definition for the following equation (7.10). We use the forward time $t > 0$ instead.

(7.10)

where the adjoint of Lindblad operator reads $D_i^*(E_t) = L_i^\dagger E_t L_i - (L_i^\dagger L_i E_t - E_t L_i^\dagger L_i)/2$, the innovation super-operator is $\mathcal{M}_i(E_t) = L_i^\dagger E_t + E_t L_i - \mathrm{Tr}(L_i^\dagger E_t + E_t L_i) E_t$.

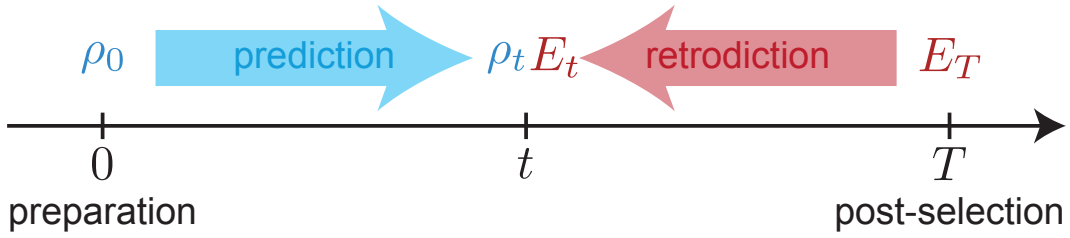

Figure 7.2: The state of the system can be *predicted* conditioned on *past* measurement records using the density matrix ρ_t provided by the *stochastic master equation* (see Eq. (6.34) in chapter 6). Conversely the state of the system can be *rectrodicted*, *a posteriori*, conditioned on the *future* measurement records by unravelling the effect matrix E_t with Eq. (7.10). The past quantum state (ρ_t, E_t) uses the complete measurement records to give an estimate of the distribution of any measurement performed on the system at time t according to Eq. (7.12).

In the case of unread measurements ($\eta_i = 0$), we obtain the equivalent of the Lindblad equation for the effect matrix with an adjoint Lindblad super-operator

$$dE_t = -\frac{i}{\hbar}[H, E_t]dt - \sum_{i=1}^{m} \mathcal{D}_i^*(E_t)dt. \tag{7.11}$$

When pre and post-selecting the evolution, we average a selected ensemble of realizations of the experiments. The recorded signal is thus impacted. On a large number of realizations, the experimentalist acquires a mean *smoothed* measurement record $\bar{y}_\mu^S(t)$ associated to a jump operator L_μ with an efficiency η_μ instead of the mean of the usual record $\bar{y_\mu}(t)$. The mean *smoothed* measurement records in presence of preparation and post-selection reads [55, 58, 85]

$$\boxed{\bar{y}_\mu^S(t)dt = \frac{\mathrm{Tr}[E_t\sqrt{\eta_\mu}(L_\mu\rho_t + \rho_t L_\mu^\dagger)]}{\mathrm{Tr}[E_t\rho_t]}dt = 2\mathrm{Re}[\frac{\mathrm{Tr}[\sqrt{\eta_\mu}\rho_t E_t L_\mu]}{\mathrm{Tr}[\rho_t E_t]}] = 2\sqrt{\eta_\nu}\mathrm{Re}[\langle L_\nu\rangle_w]} \tag{7.12}$$

where $\langle . \rangle_w$ denotes the expectation value conditioned on the full measurement record. The quantity $\frac{\rho_t E_t}{\mathrm{Tr}[\rho_t E_t]}$ plays the analog of a density matrix even if it does not define a quantum state[7]. Note that it is possible to defined a *quantum smoothed state* using the complete measurement record [213] but we will not need it in the rest of the manuscript.

7 The matrix $\frac{\rho_t E_t}{\mathrm{Tr}[\rho_t E_t]}$ is not a density operator because it is not Hermitian or (even if symmetrized) positive semi-definite.

An important feature of the formalism is that Eq. (7.12) is proportional to the real part of the *weak value* of the jump operator. The *generalized weak value* of an operator A is defined as follows[8] [55]

$$\boxed{\langle A \rangle_w = \frac{\mathrm{Tr}[A\rho_t E_t]}{\mathrm{Tr}[\rho_t E_t]}.} \tag{7.13}$$

The magnitude of the *weak value* given by Eq. (7.13) can in principle diverge as the denominator can be very small and even reaches zero when the past (density matrix) and future (effect matrix) quantum states are orthogonal. The conditioned measured averages can lie outside of the unconditioned range. However as we will see, both the density matrix and the effect matrix evolve into a statistical mixture between pre and post selection owing to decoherence preventing a perfect orthogonality of the two states. Therefore, decoherence sets an upper bound on the measured weak value.

This formalism is an extension of chapter 6. Indeed, we can recover the usual case without post-selection by setting $E = \mathbb{1}/2$ in Eq. (7.13) but we can also use exclusively the backward estimate by setting $\rho = \mathbb{1}/2$. Now that we introduced the *past quantum state* that uses the whole measurement records, let us confront it with experimental results with preparation and post-selection.

7.2 PRE AND POST-SELECTED TRAJECTORIES

7.2.1 *Time symmetric Rabi evolution*

In the experiment, our qubit is driven with an Hamiltonian $H = -\frac{\hbar\Omega}{2}\sigma_y$. The average evolution of the density matrix is given by the Lindblad equation (see section 3.4)

$$\frac{d\rho_t}{dt} = i[\frac{\Omega}{2}\sigma_y, \rho_t] + \frac{\Gamma_\mathrm{d} + \Gamma_\varphi}{2}\mathcal{D}[\sigma_z](\rho_t) + \Gamma_1\mathcal{D}[\sigma_-](\rho_t) \tag{7.14}$$

where Γ_1 is the inverse lifetime of the qubit, Γ_d is the measurement induced dephasing rate and Γ_φ is the pure dephasing rate. The Lindblad super-operator is $\mathcal{D}[L](\rho) = L\rho L^\dagger - \frac{1}{2}(\rho L^\dagger L + L^\dagger L\rho)$. The qubit is prepared at time $t = 0$ in a state ρ_0 that gives the initial condition of Eq. (7.14). Note that we neglected qubit excitation in Eq. (7.14) since the excitation probability of the qubit in thermal equilibrium was measured to be lower than 2%.

The unmonitored evolution of the effect matrix E evolves backward in time according to Eq. (7.11). In our experiments, it reads (in the forward sense)

$$\frac{dE_t}{dt} = i[\frac{\Omega}{2}\sigma_y, E_t] - \frac{\Gamma_\mathrm{d} + \Gamma_\varphi}{2}\mathcal{D}^*[\sigma_z](E_t) - \Gamma_1\mathcal{D}^*[\sigma_-](E_t) \tag{7.15}$$

where $D_i^*(E_t) = L_i^\dagger E_t L_i - (L_i^\dagger L_i E_t - E_t L_i^\dagger L_i)/2$.

8 This is a generalization to mixed states of the historical weak value $\langle A \rangle_w = \langle\psi_f|A|\psi_i\rangle \,/\, \langle\psi_f|\psi_i\rangle$ envisioned by Aharonov [59].

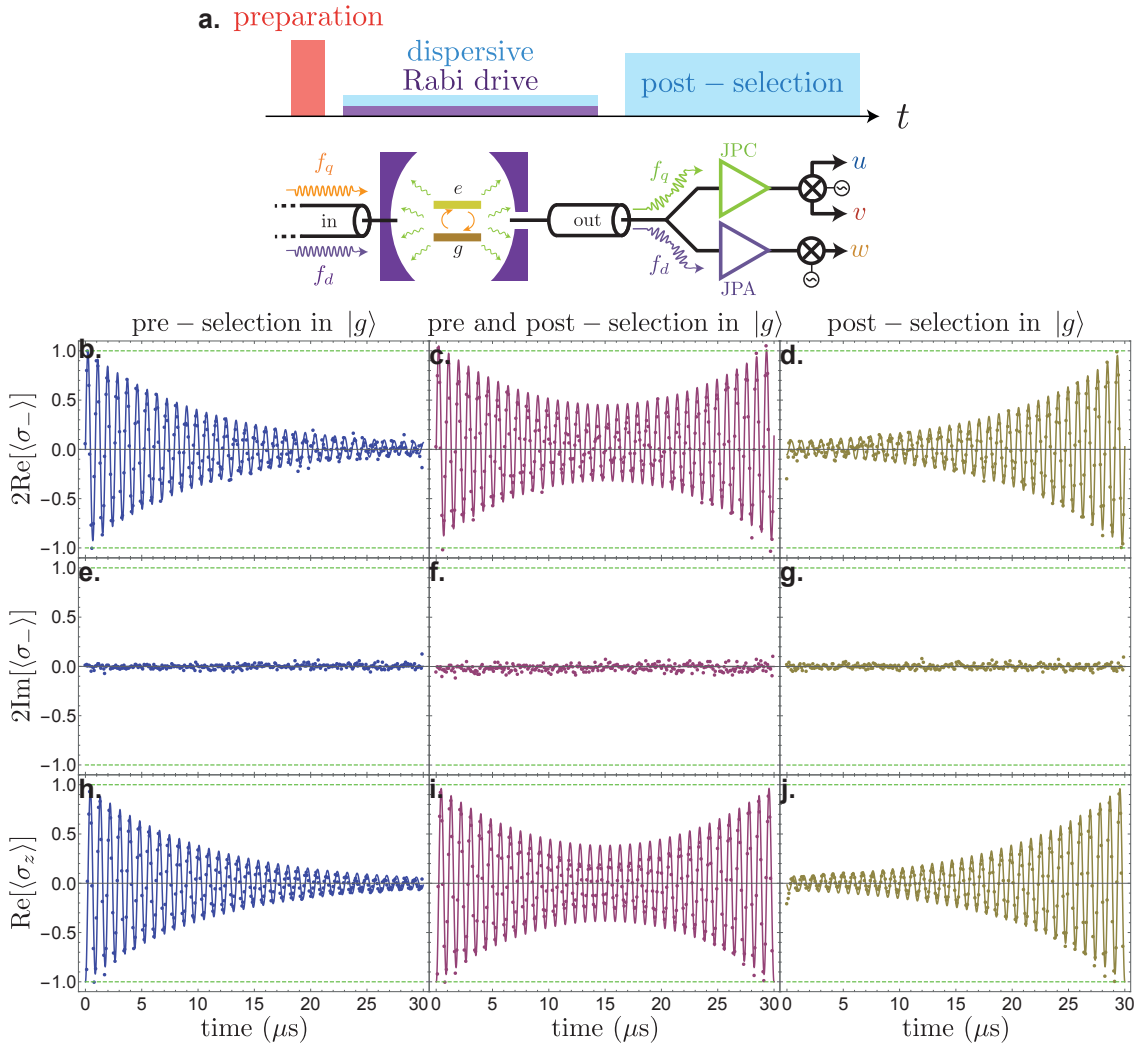

Figure 7.3: **a.** Pulse sequence and measurement setup. The qubit is prepared in $|g\rangle$ or in a statistical mixture of $|g\rangle$ and $|e\rangle$. During the experiment, the qubit is driven by a continuous tone at f_q. The state of the cavity is concurrently probed by sending a tone at f_c leading to the continuous measurement records $w(t)$ in Eq. (7.16). The spontaneous emission of the qubit is recorded at the same time yielding to the records u and v in (7.16). At the end of the experiment we perform a projective measurement of the spin along a given axis of the bloch sphere. In this experiment, we pre and post-select only on $|g\rangle$. **b. e. h.** Pre-selected trajectory. The solid line is the solution of the Lindblad equation (7.14) with the parameters $\Gamma_1 = (10.4\ \mu\mathrm{s})^{-1}$, $\Gamma_\varphi + \Gamma_d = (22\ \mu\mathrm{s})^{-1}$, $\Omega/2\pi = (875\ \mathrm{ns})^{-1}$ while the dots are the measured records $u(t)$, $v(t)$ $w(t)$, here raw averaged on the selected ensemble out of the 36 million realizations of the experiment. In this case $2\mathrm{Re}[\langle\sigma_-\rangle] = \langle\sigma_x\rangle_\rho$ and $2\mathrm{Im}[\langle\sigma_-\rangle] = -\langle\sigma_y\rangle_\rho$ corresponds to the Bloch coordinates. **d. g. j.** Post-selected trajectory (without pre-selection meaning $\rho_0 = \mathbb{1}/2$). The lines are the solutions of the equation (7.15) with the above-mentioned parameters. The average measurements records (dots) are superimposed. In this case, $2\mathrm{Re}[\langle\sigma_-\rangle] = \langle\sigma_x\rangle_E$ and $2\mathrm{Im}[\langle\sigma_-\rangle] = -\langle\sigma_y\rangle_E$ are the Bloch coordinates of the retrodicted quantum state. **c. f. i.** Pre and post-selected trajectory. The solid lines are the prediction of Eq. (7.16) where the density matrix is calculated from the Lindblad equation (7.14) and the effect matrix is obtained from Eq. (7.15) with the same parameters as in the other plots. We observe a good agreement between these *smoothed* measurement records and the experimental records (dots) raw averaged on the pre and post-selected ensembles of trajectories.

The system is post-selected at time T in a state E_T that defines the final condition of Eq. (7.15). Note that Eq. (7.15) is not the exact time symmetric[9] of Eq. (7.14). Although, the decoherence term is symmetric in time $\mathcal{D}^*[\sigma_z](E) = \mathcal{D}[\sigma_z](E)$, the energy dissipation for the effect is $\mathcal{D}^*[\sigma_-](E) \neq \mathcal{D}[\sigma_-](E)$. This last term vanishes when $E = \mathbb{1}/2$ in contrast to the dissipation term of Eq. (7.14) $\mathcal{D}[\sigma_-](\rho)$ which cancels for $\rho = |g\rangle\langle g|$ [85]. In this section, the Rabi rate Ω of the Hamiltonian evolution dominates the decoherence rates of the system. The asymmetry induced by dissipation is therefore not straightforwardly observable.

We can use both the density matrix and the effect matrix to predict the measurement records averaged on a pre and post-selected ensemble of trajectories given in Eq. (7.12)

$$\boxed{\begin{cases} \bar{u}^S(t)dt = \sqrt{2\eta_f\Gamma_1}\mathrm{Re}[\langle\sigma_-\rangle_w]dt \\ \bar{v}^S(t)dt = -\sqrt{2\eta_f\Gamma_1}\mathrm{Im}[\langle\sigma_-\rangle_w]dt \\ \bar{w}^S(t)dt = \sqrt{2\eta_d\Gamma_d}\mathrm{Re}[\langle\sigma_z\rangle_w]dt \end{cases}} \tag{7.16}$$

where the weak value is defined as $\langle A\rangle_w = \mathrm{Tr}[A\rho E]/\mathrm{Tr}[\rho E]$ (see Eq. (7.13)).

A striking feature of the weak values in Eq. (7.16) is that the real and imaginary part functions do not 'commute' with the average $\langle . \rangle_w$. For instance the real part of $\langle\sigma_-\rangle_w$ is not $\langle\sigma_x\rangle_w/2 = \langle\mathrm{Re}[\sigma_-]\rangle_w$ because ρE is not Hermitian. Let us denote $\rho_p = \rho E/\mathrm{Tr}[\rho E]$, we can write

$$\begin{aligned} \mathrm{Re}[\langle\sigma_-\rangle_w] &= \frac{1}{2}\mathrm{Re}[\mathrm{Tr}[\rho_p(\sigma_x - i\sigma_y)]] \\ &= \frac{1}{2}\mathrm{Tr}[\mathrm{Re}[\rho_p]\sigma_x - \mathrm{Im}[\rho_p]\sigma_y]. \\ &\neq \frac{1}{2}\mathrm{Re}[\mathrm{Tr}[\rho_p\sigma_x]] \end{aligned} \tag{7.17}$$

In our detection setup (see Fig. 7.3 **a**), monitoring the fluorescence emitted by a qubit will no longer be equivalent to obtaining information on $\sigma_x = 2\mathrm{Re}[\sigma_-]$ on one quadrature and $\sigma_y = -2\mathrm{Im}[\sigma_-]$ along the other quadrature as it was the case in section 3.3. A pre and post-selected homodyne detection of an electromagnetic wavepacket can thus access the properties of both the real and the imaginary part of the field. This fact is the basis of wavefunction tomography protocols based on weak values [204, 60]. The pre-selected (resp. post-selected) measurement records can be recovered from Eq. (7.16) by setting $E = \mathbb{1}/2$ (resp. $\rho = \mathbb{1}/2$). In this case, u, v and w are proportional to the expectation values of σ_x, σ_y and σ_z for the quantum state ρ (forward estimation) or E (backward estimation).

Pre-selection (resp. post-selection) is experimentally achieved by performing a projective measurement (see chapter 3) at the beginning (resp. at the end) of the experiment along a given axis of the Bloch sphere. Trajectories are averaged conditionally on the final and initial projective measurement outcome revealing the smoothed measurement records (7.16).

In Fig. 7.3, we perform a pre and/or post-selection of a 30 μs long Rabi oscillation. In the pre-selected traces (Fig. 7.3 **b e h**), the qubit is initialized in $|g\rangle$ and then

9 The two equations are not time symmetric as soon as one of the jump operators is not Hermitian nor skew-Hermitian.

experiences usual Rabi oscillations in the presence of weak decoherence. The Bloch vector oscillates around the y axis in the $x-z$ plane and converges toward the center of the Bloch sphere. In the post-selected case (Fig. 7.3 **d g j**), the qubit state starts[10] in $\mathbb{1}/2$ and then experiences time reversed Rabi oscillations before reaching its final state $E_T = |g\rangle\langle g|$. Finally, when the trajectories are both pre and post-selectioned (Fig. 7.3 **c f i**), the amplitude of the oscillation starts to decrease because of the Lindblad super-operator in Eq. (7.14) before increasing again under the action of the adjoint Lindblad operator in Eq. (7.15). The time $t = T/2$ defines a plane of symmetry for the trajectory enlightening the time symmetry of the past quantum state formalism when the dynamics is dominated by a fast Hamiltonian evolution. In the middle of this pre and post-selected average trace, the amplitude of the oscillation (Fig. 7.3 **c i**) is greater than the one for the forward prediction (Fig. 7.3 **b h**) or the backward retrodiction (Fig. 7.3 **d j**). We will demonstrate in the next section that this abnormally high amplitude can even exceed ± 1.

7.2.2 *"Anomalous" weak values*

The denominator of the weak value (7.13) is just the probability for the sequence of future measurement results

$$Tr[\rho_t E_t] = \mathbb{P}[\{y_\tau\}_{t<\tau<T}|\rho_t]/\mathrm{Tr}[\mathbf{K}^*_{y(t_n)} \circ ... \circ \mathbf{K}^*_{y(t_{N-1})}(E_{t_N})]. \tag{7.18}$$

If the future measurement records $\{y_\tau\}_{\tau>t}$ are very 'unlikely' given the density matrix ρ_t at time t, the weak value at this time will be 'large' because of the near orthogonality of ρ_t and E_t. They can even surpass the extremal eigenvalues of the measured operator leading to the 'anomalous' weak values predicted by Aharonov et al. [59]. The observation of these anomalous values has been claimed to contradict macro-realism when using a *non-invasive detector*[11] equivalently to the violation of Leggett-Garg inequality [61, 199, 200, 201]. At a given time t orthogonality of the states ρ_t and E_t is limited by the Lindblad terms in Eq. (7.14) and Eq. (7.15) that reduces the purity[12] of the states for lengthy evolution. We thus reduce the duration of the experiment from 30 μs (Fig. 7.3) to 1.7 μs (Fig. 7.4) to increase the combined effect of pre and post-selection by reducing the effect of decoherence.

In Fig. 7.4, we pre and post-select a trajectory on a very unlikely future outcome (Fig. 7.4 **a**). We observe again a good agreement between the calculated smoothed records (7.16) and the experimental measurement records averaged conditionally on the outcomes of pre and post-selection (Fig. 7.4 **b d**). We emphasize that the measurement records do not correspond to the pre and post-selected expectation of the Pauli observable (see Eq. 7.17) by representing $\mathrm{Re}[\langle\sigma_x\rangle_w]$ as a solid line in Fig. 7.4 **b**. In contrast to Fig. 7.3, the measured signal reaches values beyond ± 1 that are not permitted for only pre or post-selected averages. This is an illustration of the amplifying property

10 We artificially prepare an equal statistical mixture of $|g\rangle$ and $|e\rangle$ by averaging with the appropriate weighting coefficients trajectories pre-selected in $|g\rangle$ and in $|e\rangle$.

11 Our detection setup can be considered as non-invasive as cryogenic circulator isolate the system from the detection setup.

12 Only pure states can be perfectly orthogonal in the Bloch sphere.

of weak values [202, 203, 60]. In this regions, the sensitivity of our detection on small variation of the parameters[13] of the system is increased as the weak values are inversely proportional to the almost vanishing scalar product between ρ_t and E_t. This feature is even more salient when the conditioned records are represented in 3D. As explained in chapter 3, raw averaging the unconditioned measurement records amounts to directly imaging the Bloch vector. When pre and post-selected, the imaged vector norm can now exceed 1 and thus explore the outside of the unit sphere[14] (see Fig. 7.5 **a**).

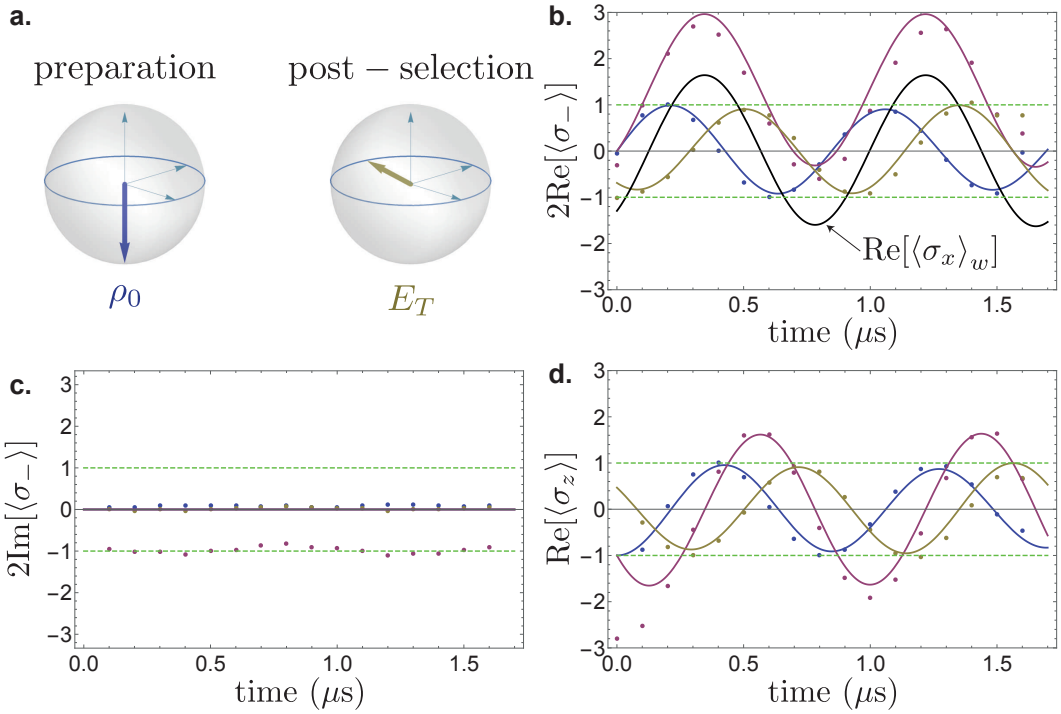

Figure 7.4: **a.** We perform a pre-selection in the ground state $\rho_0 = |g\rangle\langle g|$ and a post-selection in an arbitrarily chosen state E_T such that $(\mathrm{Tr}[\sigma_x E_T], \mathrm{Tr}[\sigma_y E_T], \mathrm{Tr}[\sigma_z E_T]) = (\sin(\theta), 0, -\cos(\theta))$ where $\theta = 238\pi/180$. The pre (dark blue), post (dark yellow), pre and post (purple) selected trace are observed through the measurement records $2\mathrm{Re}[\langle\sigma_-\rangle]$ (Fig. **b**), $2\mathrm{Im}[\langle\sigma_-\rangle]$ (Fig. **c**) and $\mathrm{Re}[\langle\sigma_z\rangle]$ (Fig. **d**). Similarly to Fig. 7.3, the solid lines are predicted from the smoothed measurement record (7.16) calculated from the density matrix and effect matrix obtained from Eq. (7.14) and Eq. (7.15) with the parameters $\Gamma_1 = (11\ \mu\mathrm{s})^{-1}$, $\Gamma_\varphi + \Gamma_d = (12.3\ \mu\mathrm{s})^{-1}$ and $\Omega/2\pi = (850\ \mathrm{ns})^{-1}$. Both Fig. **b** and **d** show values that exceed the range of possible unconditional average values delimited by the green dashed lines. The vector obtained by raw averaging of the three measurement records lies outside of the sphere of radius 1. We additionally represent $\mathrm{Re}[\langle\sigma_x\rangle_w]$ as a black line in Fig. **b** illustrating the stark difference between this quantity and the measured record $2\mathrm{Re}[\langle\sigma_-\rangle_w] = \mathrm{Re}[\langle\sigma_x - i\sigma_y\rangle_w]$ with pre and post-selection. Note that in the experiment, the pre and post-selected trace exhibit an offset in the $v(t)$ record (Fig. **c**) that is not predicted by theory.

13 For instance, a small change in the Rabi rate or in the pre and post-selection fidelities changes dramatically the amplitude of the weak value.

14 This does not contradict the quantum theory as the pre and post-conditioned imaged vector does not correspond to the Bloch vector of a quantum state.

Lastly, we notice that the experimental measurement record v exhibits an almost constant value when pre and post-selected (Fig. 7.4 **c**). This constant offset is not observable with only pre-selection or post-selection and it is not predicted by the past quantum state theory. When pre or post-selecting the trace on states ρ_0 or E_T with non zero $\langle\sigma_y\rangle$, this constant offset remains on top of the observed oscillation of $2\mathrm{Im}[\langle\sigma_-\rangle]$ that is well predicted. We have checked many possible sources of error for that offset but we could not find any experimental mistake (see below).

7.2.3 *Influence of the post-selection*

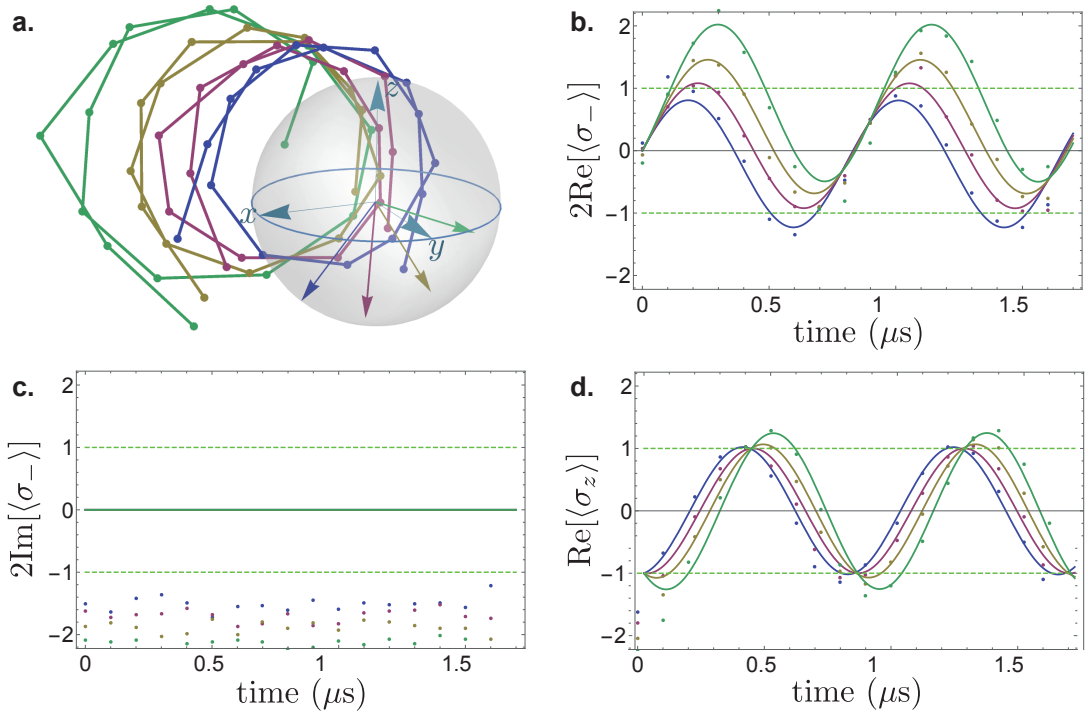

Figure 7.5: Influence of the post-selection on the measured traces. The qubit is initialized in the ground state $|g\rangle$ and post-selected on a state E_T represented by colored Bloch vectors on Fig. **a**. The post-selected states are of the form $(\mathrm{Tr}[\sigma_x E_T], \mathrm{Tr}[\sigma_y E_T], \mathrm{Tr}[\sigma_z E_T]) = (\sin(\theta), 0, -\cos(\theta))$ where $\pi\theta/180 = 40, 4, -32, -68$. We superimpose a 3-dimensional representation of the pre and post-selected measured records that exceed the unit sphere. The color encodes the post-selected state. **b. c. d.** Measured (dots) and predicted (lines) measurement records for the trajectories represented in Fig. **a**. We observe a good agreement with the theory calculated with the parameters $\Gamma_1 = (10.4\ \mu\mathrm{s})^{-1}$, $\Gamma_d + \Gamma_\varphi = (22\ \mu\mathrm{s})^{-1}$ and $\Omega/2\pi = (875\ \mathrm{ns})^{-1}$ except for Fig. **c**. Fig. **b** and **d** exhibits measurement records that exceed the normal eigenvalue range. Note that the experimental offset in Fig. **c** component already noticed in Fig. 7.4 depends on the post-selected state.

The weak value "amplification" can be increased by an appropriate choice of parameters. In Fig. 7.5, we present 1.7 μs long average traces conditioned on both pre and post-selection for various post-selected states. We measure weak values that exceed the normal range but they remain smaller than the one we obtain with the very unlikely

post-selection of Fig. 7.4. Even larger weak values can be obtained by reducing the total duration of the experiment[15] and by increasing the preparation and post-selection fidelities.

Additionally, the constant value (see Fig. 7.5 **c**) already observed in Fig. 7.4 **c** depends on the post-selected state as well. In order to understand this offset that is not predicted by our theory, we carried out several experiments. Here are our conclusion on the behavior of the observed offset with respect to the experimental parameters.

- The offset depends on pre and post-selection as depicted in Fig. 7.5 **c** and it is not observed with only pre or post-selection. For short durations of the experiments, its amplitude seems inversely proportional to the scalar product $\mathrm{Tr}[\rho E]$ between the past and future states revealing the weak value nature of this constant signal.

- For a fixed 'angle' between the Bloch vectors encoding preparation and post-selection, the offset does not seem to be significantly affected by the amplitude of the drive at f_q i.e. at fixed $\mathrm{Tr}[\rho E]$, $\mathrm{Im}[\langle\sigma_-\rangle_w]$ seems independent on Ω.

- This feature cannot be modeled by an error on the preparation or post-selection that would produce nonzero σ_y. A preparation and/or post-selection outside of the $x-z$ plane ($\mathrm{Tr}[\rho\sigma_y] \neq 0$ or $\mathrm{Tr}[E_T\sigma_y] \neq 0$) leads to an oscillating $2\mathrm{Im}[\langle\sigma_-\rangle]$ smoothed record and not a constant offset.

- Discarding the measurement records on the dephasing channel or canceling the probe tone at the frequency of the cavity does not change the measured offset.

- Initializing the system in a maximally mixed state $\rho_0 = \mathbb{1}/2$ before preparation does not prevent an offset when taking into account both pre-selection and post-selection.

- Moving the operating frequency of the quantum limited amplifier used to detect the spontaneous emission (see Fig. 7.3 **a**) away from the frequency of the qubit degrades the signal-to-noise ratio but the offset remains. The offset is not caused by a spurious effect of the JPC.

- Impressively, by inserting a unitary rotation that maps the y component of the qubit onto the z component of the qubit amid the trajectory, the $\mathrm{Im}[\langle\sigma_-\rangle_w]$ offset usually picked up by the fluorescence signal can be detected in the dephasing channel as well.

15 Or by increasing the coherence time and the lifetime of the qubit.

7.3 CONCLUSION

In this chapter, we demonstrated

- that *prediction* and *retrodiction* of the evolution of a qubit that is prepared and post-selected in chosen states using the *past quantum state* formalism describe experimentally relevant situation.
- that our full quantum tomography method can lie outside of the Bloch sphere by combining preparation and post-selection. This is an observation of a *weak value*.
- the apparition of an a *constant signal* on the imaginary quadrature of the fluorescence signal when both pre and post-selecting. That offset is not predicted by theory and it requires further investigation.

Weak values are at the heart of colorful theoretical debate as they are often misunderstood [60]. A way to circumvent this difficulty is to define a smoothed quantum state [213, 214, 215] using the complete available knowledge *a posteriori*. This smoothed quantum state belongs to the operator space as opposed to the past quantum 'state' $\Xi_t = (\rho_t, E_t)$ introduced by Gammelmark et al. [58]. Moreover, such a smoothed estimate made from incomplete observations are predicted to outperform estimates made using full knowledge of the causal quantum state [214]. This might be observed by unraveling quantum trajectories, not only for the density matrix as in chapter 6, but also for the effect matrix [63], for both [64] and for the smoothed quantum state. Manifestations of the interference between initial and final states can be revealed through the statistics of pre and post-selected measurement records such as peaks or dips at half-quantized value of the measurement outputs [216]. Finally, the time asymmetry induced by dissipation could be studied by comparing the statistics of forward and backward quantum trajectories. The arrow of time could emerge by comparing the likelihood of the forward and backward propagation hypotheses [190].

Part III

APPENDIX

A

TRANSMON COUPLED TO A TRANSMISSION LINE

This appendix follows a lecture given by Pierre Rouchon at the *CIRM school : Modeling and Control of Open Quantum Systems* in April 2018. It gives a prototypical derivation of the dynamics of an open quantum system: a transmon qubit coupled to a transmission line modeled as a collection of harmonic oscillators. Special care is given to the treatment of the Markov approximation to obtain the Langevin equation. We also bring to light the fact that the non linearity of the junction is distributed among all the elements of the circuit including the coupling capacitance to the transmission line [82]. This problem is crucial in this thesis because it takes on the problem of relaxation and measurement of an atom by spontaneous emission, which is central for the heterodyne measurement of the energy relaxation of a transmon qubit in our experiments. We show that extra higher order terms appear in the derivation of the input-output relation of an anharmonic oscillator such as the transmon. However, the additional terms give rise to a negligible non linear correction to the dissipation. This effect exactly vanishes for a qubit but it might be of importance for high impedance circuits.

A.1 CLASSICAL EQUATION OF MOTIONS

We start by introducing the classical equations of motion of the system depicted in Fig (A.1). In this description the transmission line was replaced by an infinite collection of discrete $l\Delta, c\Delta$ modes at positions $x = 0, \Delta, 2\Delta, ...$ We also assume that the coupling capacitance C_l satisfies $C_l \ll C$. Together with the Ohmic modeling of the semi-infinite transmission line, this assumption plays the role of the so-called *Markov approximation*.

A.1.1 *Dynamics of the system*

The Lagrangian of the system reads

$$\mathcal{L} = \frac{C}{2}\dot{\Phi}^2 + \frac{C_l}{2}(\dot{\Phi}_0 - \dot{\Phi})^2 + \sum_{r\geq 0}\frac{c\Delta}{2}\dot{\Phi}_r^2 + E_J\cos(\Phi/\varphi_0) - \sum_{r\geq 0}\frac{(\Phi_{r+1}-\Phi_r)^2}{2l\Delta} \quad \text{(A.1)}$$

where the reduced flux quantum is $\varphi_0 = \hbar/2e$. We have the associated conjugated variables

$$\begin{cases} Q = \dfrac{\partial\mathcal{L}}{\partial\dot{\Phi}} = C\dot{\Phi} + C_l(\dot{\Phi} - \Phi_0) \\ q_0 = \dfrac{\partial\mathcal{L}}{\partial\dot{\Phi}_0} = C_l(\dot{\Phi}_0 - \dot{\Phi}) + c\Delta\dot{\Phi}_0 \\ q_r = \dfrac{\partial\mathcal{L}}{\partial\dot{\Phi}_r} = c\Delta\dot{\Phi}_r \end{cases} . \quad \text{(A.2)}$$

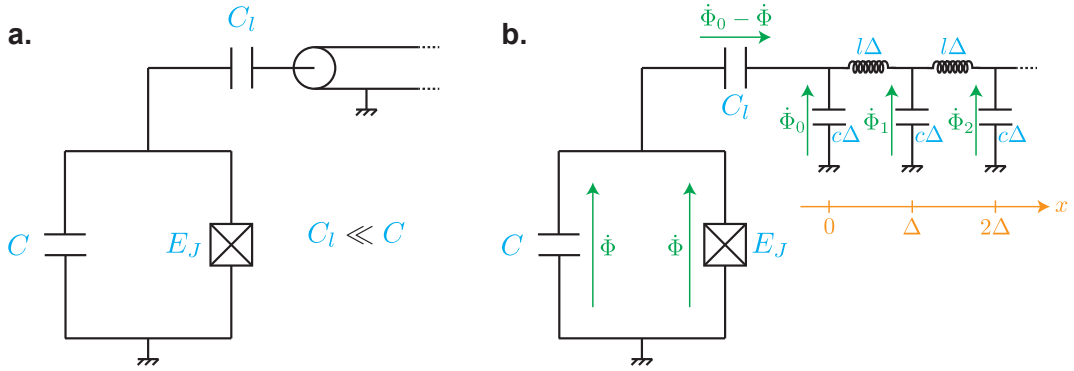

Figure A.1: **a.** A transmon is capacitively coupled to a transmission line by a capacitor C_l. The transmon is composed of a Josephson junction of Josephson energy E_J shunted by a large capacitor C. We neglect the intrinsic capacitance of the junction. We assume that $C_l \ll C$ to ensure that the system can be treated as a well defined system coupled to a zero memory bath. **b.** We decompose the electromagnetic modes of the transmission line in discrete modes spaced by a distance Δ. We denote by l and c the inductance and capacitance per unit length of the transmission line. $\dot{\Phi}$ is the voltage across the junction and $\dot{\Phi}_r$ is the voltage across the r^{th} capacitance of the transmission line.

A Legendre transform of the Lagrangian (A.1) gives the Hamiltonian

$$\begin{aligned}\mathcal{H}(\Phi, Q, \{\Phi_r, q_r\}) &= \frac{\partial \mathcal{L}}{\partial \dot{\Phi}}\dot{\Phi} + \sum_{r\geq 0}\frac{\partial \mathcal{L}}{\partial \dot{\Phi}_r}\dot{\Phi}_r - \mathcal{L} \\ &= \frac{(Q+q_0)^2}{2C} + \frac{q_0^2}{2C_l} + \frac{(\Phi_1-\Phi_0)^2}{2C_l} - E_J\cos(\Phi/\varphi_0) \\ &+ \sum_{r\geq 1}\frac{q_r^2}{2c\Delta} + \frac{(\Phi_{r+1}-\Phi_r)^2}{2l\Delta}.\end{aligned} \tag{A.3}$$

We can then write Hamilton's equations of motion as

$$\begin{cases} \dfrac{d\Phi}{dt} = \dfrac{Q+q_0}{C} \\ \dfrac{dQ}{dt} = -\dfrac{E_J}{\varphi_0}\sin(\Phi/\varphi_0) \\ \dfrac{d\Phi_0}{dt} = \dfrac{q_0}{C_l} + \dfrac{Q+q_0}{C} \\ \dfrac{dq_0}{dt} = \dfrac{\Phi_1-\Phi_0}{l\Delta} \\ \dfrac{d\Phi_r}{dt} = \dfrac{q_r}{c\Delta} \\ \dfrac{dq_r}{dt} = \dfrac{\Phi_{r+1}-2\Phi_r+\Phi_{r-1}}{l\Delta} \end{cases}. \tag{A.4}$$

By combining two equations of (A.4), we have

$$\frac{d^2\Phi_r}{dt^2} = \frac{\Phi_{r+1}-2\Phi_r+\Phi_{r+1}}{lc\Delta^2}. \tag{A.5}$$

In the continuous limit ($\Delta \ll 1$), we can write the flux as a function of position $\Phi_r(t) = \Phi(t, r\Delta)$ where the function $\Phi(t,x)$ satisfies Dalembert's equation with velocity $1/\sqrt{lc}$

$$\frac{\partial^2\Phi}{\partial t^2} = \frac{1}{lc}\frac{\partial^2\Phi}{\partial x^2}. \tag{A.6}$$

The flux along the transmission line can be decomposed into left and right propagating plane waves $\Phi(t,x) = \Phi_{\text{in}}(t+\sqrt{lc}x) + \Phi_{\text{out}}(t-\sqrt{lc}x)$ allowing us to recover the usual input-output relation at $x = 0$

$$\Phi(t,0) = \Phi_{\text{in}}(t) + \Phi_{\text{out}}(t) = \Phi_0(t). \tag{A.7}$$

The derivative of the input-output relation (A.7) reads

$$\dot{\Phi}_{\text{in}}(t) + \dot{\Phi}_{\text{out}}(t) = \dot{\Phi}_0(t) = q_0\left(\frac{1}{C} + \frac{1}{C_l}\right) + \frac{Q}{C}. \tag{A.8}$$

We can approximate the derivative of the charge at position $x = 0$ by

$$\begin{aligned}\frac{dq_0}{dt} = \frac{\Phi_1 - \Phi_0}{l\Delta} &= \frac{\Phi_{\text{in}}(t+\sqrt{lc}\Delta) + \Phi_{\text{out}}(t-\sqrt{lc}\Delta) - (\Phi_{\text{in}}(t) - \Phi_{\text{out}}(t))}{l\Delta} \\ &\simeq \sqrt{\frac{c}{l}}(\dot{\Phi}_{\text{in}}(t) - \dot{\Phi}_{\text{out}}t))\end{aligned}. \tag{A.9}$$

We end up with the following system of coupled equations

$$\begin{cases} \dot{\Phi}_{\text{out}}(t) = -\dot{\Phi}_{\text{in}}(t) + \dfrac{Q+q_0}{C} + \dfrac{q_0}{C_l} \\ \dfrac{dq_0}{dt} = \sqrt{\dfrac{c}{l}}\left(2\dot{\Phi}_{\text{in}}(t) - \left(\dfrac{Q+q_0}{C} + \dfrac{q_0}{C_l}\right)\right) \\ \dfrac{d\Phi}{dt} = \dfrac{Q+q_0}{C} \\ \dfrac{dQ}{dt} = -\dfrac{E_J}{\varphi_0}\sin(\Phi) \end{cases} \tag{A.10}$$

Let us introduce the small parameter $\epsilon = \frac{C_l}{C+C_l}$. We assumed in the situation depicted on Fig. A.1 that ϵ was very small with the so-called *Markov approximation*. We will expand the solutions of the problem of Fig. A.1 up to the first non trivial order in ϵ. From (A.10), the method of 'variation of constants' gives

$$\frac{d(q_0(t)e^{zt/C\epsilon})}{dt} = z\left(2\dot{\Phi}_{\text{in}}(t) - \frac{Q(t)}{C}\right)e^{zt/C\epsilon} \tag{A.11}$$

where $z = \sqrt{\frac{l}{c}}$ is the impedance of the transmission line. An integration between 0 and $+\infty$ leads to

$$\begin{aligned} q_0(t) &= z\int_0^{+\infty} dt'\left(2\dot{\Phi}_{\text{in}}(t') - \frac{Q(t')}{C}\right)e^{-z(t-t')/C\epsilon} \\ &= \epsilon\int_0^{+\infty} e^{-\sigma}(2C\dot{\Phi}_{\text{in}}(t-\epsilon\sigma\tau) - Q(t-\epsilon\sigma\tau))d\sigma \end{aligned} \tag{A.12}$$

where $\tau = Cz$.

A.1.2 *Asymptotic expansion in ϵ*

FIRST ORDER IN ϵ

Let us expand Eq. (A.12) with respect to ϵ. At first order,

$$q_0(t) = \epsilon(2C\dot{\Phi}_{\text{in}}(t) - Q(t)). \tag{A.13}$$

By using this expression with Eq. (A.10), we get

$$\dot{\Phi}_{\text{out}} = -\dot{\Phi}_{\text{in}} + \frac{q_0}{\epsilon C}(1 + O(\epsilon)) + \frac{Q}{C} \tag{A.14}$$

which leads to the trivial input-output relation

$$\dot{\Phi}_{\text{out}}(t) = \dot{\Phi}_{\text{in}}(t). \tag{A.15}$$

There is no information in the reflected signal at first order in ϵ in (A.12), we must go to the second order.

SECOND ORDER IN ϵ

We can expand Q and $\dot{\Phi}_{\text{in}}$ with respect to ϵ

$$\begin{aligned} Q(t - \epsilon\tau\sigma) &= Q(t) - \epsilon\tau\sigma\dot{Q}(t) = Q(t) + \frac{E_J\epsilon\tau\sigma}{\varphi_0}\sin(\Phi(t)/\varphi_0) \\ \dot{\Phi}_{\text{in}}(t) &\simeq \int_0^{+\infty} e^{-\sigma}\dot{\Phi}_{\text{in}}(t - \epsilon\sigma\tau)d\sigma \end{aligned} . \tag{A.16}$$

The dynamics of the system is governed by

$$\begin{cases} \dfrac{d\Phi}{dt} = \dfrac{(1-\epsilon)}{C}Q(t) + \epsilon\left(2\dot{\Phi}_{\text{in}}(t) - \dfrac{\epsilon\tau E_J}{\varphi_0}\sin(\Phi(t))\right) \\ \dfrac{dQ}{dt} = -\dfrac{E_J}{\varphi_0}\sin(\Phi/\varphi_0) \end{cases} \tag{A.17}$$

In the end, the input-output relation now reads

$$\dot{\Phi}_{\text{out}}(t) = \dot{\Phi}_{\text{in}}(t) - \frac{E_J\epsilon\tau}{\varphi_0 C}\sin(\Phi/\varphi_0). \tag{A.18}$$

We clearly see that this input-output is non linear and it gives us information on $\sin(\Phi)$. We will now transpose this equations in the quantum world to recover the input-output relation used in our system and study the impact of the non-linearity of this relation.

A.2 QUANTUM DESCRIPTION

Following [217], the incoming modes propagating along the transmission line can be decomposed as

$$\dot{\varphi}_{\text{in}}(t,x) = \frac{1}{2}\sqrt{\frac{1}{\pi}}\left(\frac{l}{c}\right)^{1/4}\int_0^{\infty}\sqrt{\omega}d\omega\left(a_{\text{in}}(\omega)e^{-i\omega(t+\sqrt{lc}x)} + \text{h.c.}\right). \tag{A.19}$$

with the commutation relation $[a_{\rm in}(\omega), a^\dagger_{\rm in}(\omega')] = \delta(\omega - \omega')$. A difficulty arises in this description because we cannot simply define the temporal mode operators of the transmission line to be

$$b_{\rm in}(t) = \frac{1}{2}\sqrt{\frac{1}{\pi}}\left(\frac{l}{c}\right)^{1/4}\int_0^\infty \sqrt{\omega}d\omega(a_{\rm in}(\omega)e^{-i\omega t}) \tag{A.20}$$

because with this expression the commutation relation is not preserved $[b_{\rm in}(t), b^\dagger_{\rm in}(t')] \neq \delta(t-t')$. In order to respect the commutation relation and thus to get a Markovian environment we need to focus around the resonant frequency of the oscillator $\omega \simeq \Omega$ where $\Omega = \sqrt{\frac{E_J}{C\varphi_0^2}}$ and discard the rapidly oscillating terms.

LINEARIZATION OF THE OSCILLATOR

First, we consider the linearized oscillator and we reintroduce the non linearity afterwards as a perturbation. Let us introduce the variables $\Phi = \Phi_{\rm ZPF}X$ and $Q = Q_{\rm ZPF}P$ with the quadratures of the field $X = a + a^\dagger$ and $P = \frac{a-a^\dagger}{i}$ with $\Phi_{\rm ZPF} = \sqrt{\frac{\hbar Z}{2}} = \frac{\hbar}{2}\left(\frac{1}{E_J C e^2}\right)^{1/4}$, $Q_{\rm ZPF} = \sqrt{\frac{\hbar}{2Z}} = (e^2 C E_J)^{1/4}$ and the dissipation rate $\kappa = \left(\frac{C_l}{C+C_l}\right)^2\sqrt{\frac{l}{c}}\sqrt{\frac{E_J(C+C_l)}{\varphi_0^2}}\Omega$. The linearized system behaves like an harmonic oscillator with a dissipation rate κ and a driving field $X_{\rm in}$

$$\begin{cases} \dot{X} = \Omega P - \kappa X + 2\sqrt{\kappa}X_{\rm in}(t) \\ \dot{P} = -\Omega X \end{cases}. \tag{A.21}$$

In the rotating frame oscillating at the frequency of the harmonic oscillator $a \to \tilde{a}e^{-i\Omega t}$, the equation of evolution of the modes reads

$$\frac{d\tilde{a}}{dt} = -\frac{\kappa}{2}\tilde{a} + \sqrt{\kappa}X_{\rm in}(t)e^{i\Omega t} \tag{A.22}$$

with the driving term

$$\begin{aligned} X_{\rm in}(t)e^{i\Omega t} &\sim \int_0^{+\infty} d\omega \left(a_{\rm in}(\omega)e^{-i(\omega-\Omega)t} + \underbrace{a^\dagger_{\rm in}(\omega)e^{i(\omega+\Omega)t}}_{\text{rotates fast}} \right) \\ &\sim \int_{-\Omega}^{+\infty} d\omega' a_{\rm in}(\omega'+\Omega)e^{-i\omega' t} \\ &\sim \int_{-\infty}^{+\infty} d\omega' a_{\rm in}(\omega'+\Omega)e^{-i\omega' t} \end{aligned} \tag{A.23}$$

where we let the lower bound of the integral go to infinity $-\Omega \to -\infty$ because the integrand oscillate very fast for these values of ω. We finally arrive at the quantum Langevin equation in the RWA of the form

$$\frac{d\tilde{a}}{dt} = -\frac{\kappa}{2}\tilde{a} + \sqrt{\kappa}b_{\rm in}(t). \tag{A.24}$$

But now, the commutation relation for the input $[b_{\rm in}(t), b^\dagger_{\rm in}(t')] = \delta(t-t')$ is preserved by the application of the RWA

$$b_{\rm out}(t) = b_{\rm in}(t) + \sqrt{\kappa}a(t) \tag{A.25}$$

3rd ORDER EXPANSION

We now expand the sine function at a higher order to see the effect of the first non linear term of the sine on the input-output relation $\sin(\Phi/\varphi_0) = (\Phi/\varphi_0) - \frac{1}{6}(\Phi/\varphi_0)^3 = (\Phi/\varphi_0)(1-\eta X^2)$ where $\eta = \frac{1}{6}(\Phi_{\mathrm{ZPF}}/\varphi_0)^2$. We obtain a modified Langevin equation

$$\frac{d\tilde{a}}{dt} = -\frac{\kappa}{2}\tilde{a} + \sqrt{\kappa}b_{\mathrm{in}}(t) + \frac{\eta}{2}(i\Omega - \kappa)(3\tilde{a}^\dagger\tilde{a} + 2)\tilde{a} \tag{A.26}$$

and the corresponding input-output relation

$$b_{\mathrm{out}}(t) = b_{\mathrm{in}}(t) + \sqrt{\kappa}(a + \eta(3a^\dagger a + 2)a). \tag{A.27}$$

The jump operator of the problem is $L = \sqrt{\kappa}(a+\eta(3a^\dagger a+2)a)$ which is non linear in the number of excitations in the transmon. This non linearity will affect both dissipation and measurement as the measurement records and the measurement innovation are calculated from the jump operators. In order to evaluate the impact of this term, let us estimate $\eta = \frac{1}{6}(\Phi_{\mathrm{ZPF}}/\varphi_0)^2 = \frac{1}{6\varphi_0^2}\frac{\hbar Z}{2}$. The electromagnetic mode of a transmon with parameters $E_C \sim h \times 200$ MHz and $E_J \sim h \times 20$ GHz has an impedance $Z \sim 300\Omega$ corresponding to a non linear correction of $\eta \sim 2.3\%$. This correction is thus very small unless if we reach higher impedances. Interestingly in the case of a qubit, this jump operator is strictly equivalent to the linear jump operator ($a^\dagger a^2 = 0$) so the non linear dissipation only renormalizes the relaxation time of the qubit.

A.3 CONCLUSION

In this appendix, we derived the equation of motion of a transmon coupled to a transmission line as well as the input-output relation required to calculate the response function of the system to an external drive. A striking feature is that the non linearity of the junction is distributed over the first modes that compose the transmission line (in the discrete description). The coupling capacitance C_l inherits a part of the non linearity of the junction that leads to a negligible non linear dissipation. This extra term does not play a role for a qubit but it could be of importance for a high impedance circuit.

B

EXPERIMENTAL TECHNIQUES

In this appendix, we detail the fabrication process of the samples used in this thesis. We explain the fabrication of the 2D and 3D transmons introduced in chapter 2 and the Josephson parametric amplifiers JPA and JPC explained in chapter 5. The fabrication protocol of 3D transmon (resp. JPC) was previously developed in our group by Philippe Campagne-Ibarcq [85] (resp. Emmanuel Flurin [40]). In a second section, we give details about the measurement setups including the wiring inside the dilution refrigerator.

B.1 FABRICATION

B.1.1 *Fabrication of JPA and JPC*

B.1.1.1 *Dolan bridges*

The samples are made out of thin films of aluminum deposited on 10×7 mm chips diced from a wafer of high resistivity silicon of thickness 500 μm. We designed the JPA and JPC amplifiers out of resonators in the so-called microstrip geometry [75]. We evaporate 500 nm of gold on the back side of the chip that constitutes the ground plane[1]. The circuit is made of aluminum (Al5N). Its critical temperature $T_C \sim 1.2$ K is well below the operating temperature of the fridge and it is easy to deposit reproducibly. Crucially, aluminum oxide arguably the only material known to create reproducible insulating barrier in Josephson junctions.

We prepare a resist mask composed of a tri-layer MAA/MAA/PMMA. We 'draw' the design of the amplifier with a focused beam of electrons produced by a Scanning Electron Microscope (SEM), which can achieve sub 10 nm resolution. PMMA is a positive electron-sensitive resist (the exposed part is dissolved during development) so we expose the region of the chip where the aluminum will be deposited. MAA is more sensitive than PMMA so it reacts to most of the back-scattered electrons at the interface with the substrate and create an undercut around the exposed areas. This property is used to fabricate a suspended bridge of PMMA with no MAA underneath. This bridge is instrumental in creating an overlap between two layers of aluminum deposited with different angles. We separate the two layers of aluminum by an oxide barrier made by oxidizing the first layer as depicted on Fig. B.1. This method is known as the *Dolan bridge technique* [218] or *shadow evaporation technique*. It is the most commonly used technique to fabricate junction in one evaporation step[2].

1 Before this step, we deposit a thin layer of PMMA on the upper surface of the substrate to protect it from contamination.

2 Other techniques exist such as the 'bridge-free' fabrication [219] but they require a 100 kV e-beam writer.

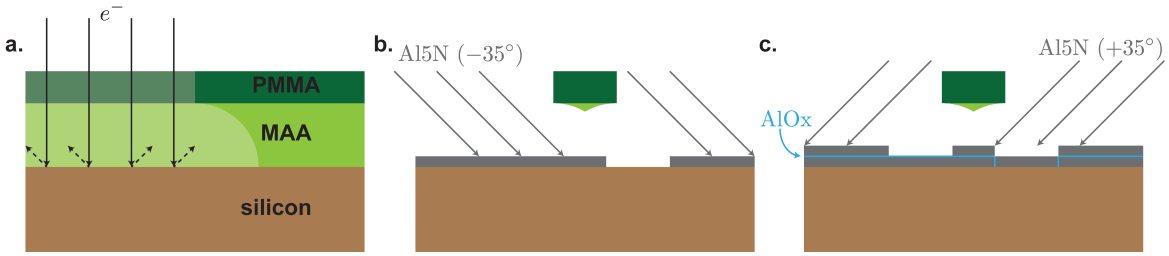

Figure B.1: **a.** An electron beam exposes a Silicon substrate (in brown) covered with a tri-layer MAA/MAA/PMMA (lightgreen/lightgreen/green). After development the exposed region (weak opacity) is removed. **b.** We fabricate a suspended bridge. The bridge is formed by insulating the MAA underneath the PMMA via back-scattering of electrons on the surface of the substrate. A first 100 nm-thick layer of aluminum is deposited with an angle −35°. **c.** This layer is oxidized by the introduction of 20 mBar of oxygen inside the chamber of the evaporator for 7 min. A second 130 nm-thick aluminum layer is deposited with an angle +35°.

In the rest of this section, we describe the exact protocols used to prepare the samples of this thesis. A lot of these steps are crucial to ensure cleanliness of the device and therefore a reliable fabrication with good quality factors.

B.1.1.2 *Cleaning*

We clean all impurities that are deposited of the substrate by the dicing saw.

- Rough acetone cleaning with a cotton swab
- 5 min sonicate in a clean acetone beaker.
- IPA rinsing.
- N_2 drying.
- 10 min of reactive-ion etching (RIE) with an O_2 plasma.

B.1.1.3 *Resist deposition by spin coating*

We deposit a tri-layer MAA/MAA/PMMA

- Pre-bake 2 min à 185°C on a hot plate.
- Three drops of 8.5 MAA EL10.
- Spinning at a speed of 4000 rpm and acceleration of 4000 rpm.s^{-1} for 60 s.
- Bake at 185°C for 3 min on a hot plate.
- Wait for 1 min.
- Three drops of 8.5 MAA EL10.
- Spinning at a speed of 4000 rpm and acceleration of 4000 rpm.s^{-1} for 60 s.

- Bake at 185°C for 3 min on a hot plate.
- Wait for 1 min.
- Three drops of 950 PMMA A6.
- Spinning at a speed of 4000 rpm and acceleration of 4000 rpm.s^{-1} for 60 s.
- Bake at 185°C for 3 min on a hot plate.
- Wait for 1 min.

B.1.1.4 *E-beam lithography*

We realize this crucial step with the Fei Magellan SEM available at ESPCI[3]. The complete pattern is done in a single step lithography. We use two sets of parameters, the first one is used to write the Josephson junction very precisely and the second one is used to write the rest of the circuit with a lower precision.

- We write the junction (typically about 500 nm × 2 μs in area) with an electric current of 9 pA accelerated by a voltage of 25 kV. The magnification is set to 600 with write fields of 100 μm and the pattern is exposed with a dose of 283 μC/cm^2.
- The resonators and coupling capacitances are written with an electric current of 23.5 nA accelerated by a voltage of 25 kV. The magnification is chosen to be 75 with write fields of 800 μm and the pattern is exposed with a dose of 283 μC/cm^2.

B.1.1.5 *Development*

The development step aims at removing the exposed resist before an evaporation of aluminum. A small quantity of resist remaining after development could lead to non radiative loss in the device. The choice of the solution called *developer* used for this step is thus crucial to prevent residues of resist. On the opposite, if the developer is too agressive, large undercuts grow, and may jeopardize the robustness of the Dolan bridge.

We used two different developers, a mixture of MIBK and IPA and a mixture of IPA and H_2O. The former is the most widespread. It leads to a fast but imperfect removal of the resist (see Fig. B.2). In constrat, IPA/H_2O is slow which leads to variation in the development time and it is also very sensitive to variations of temperature.

DEVELOPMENT MIBK/IPA

- 43 s of stirring in a solvent MIBK:IPA (1:3).
- IPA rinsing.
- N_2 drying.

3 École supérieure de physique et de chimie industrielles de la ville de Paris.

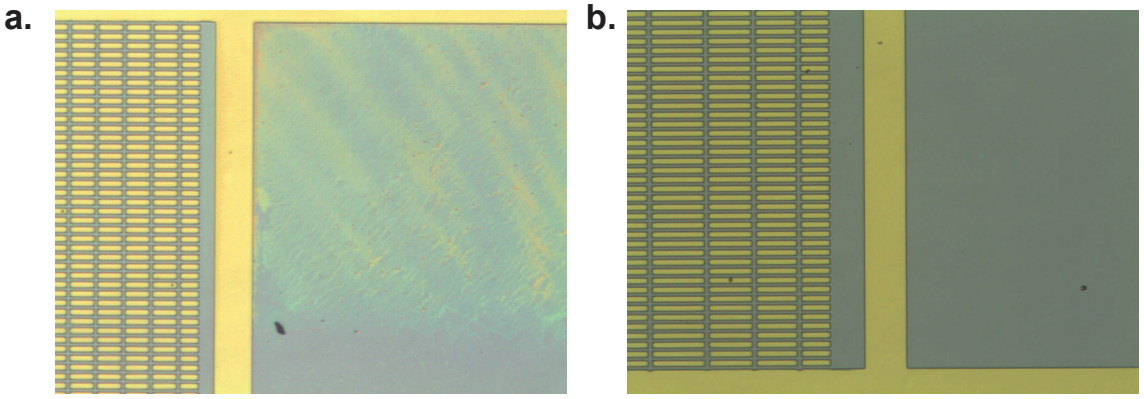

Figure B.2: **a.** Optical image of an area with residues of resist after a MIBK/IPA development. The resist leftovers prevent an homogeneous deposition of aluminum. **b.** Optical image of the same area as in **a** but after a IPA/H_2O development. The residues of resist are gone.

DEVELOPMENT IPA/H_2O

- Between 3 min 30 s et 7 min of stirring in a cold[4] solvent IPA : H_2O (1:3).
- IPA rinsing.
- N_2 drying.

B.1.1.6 *Evaporation and lift-off*

The shadow evaporation technique enables us to create reproducible Josephson junctions by a successive deposition of two aluminum layers (100 nm and 130 nm respectively) interleaved by an oxide barrier. We use University Paris-Diderot clean room facility (see Fig. B.3 **a**) to deposit high purity aluminum. The chip edges are protected with kapton tape to avoid a direct electrical contact between the aluminum and the gold ground plane.

EVAPORATION

- pumping for 45min to reach an evaporation chamber pressure $p \leq 3.10^{-6}$ mbar.
- 2 s of ion etching under $-35°$ (500 V, -100 V, 50 mA, 12 sccn ArO_2).
- 2 s of ion etching under $+35°$.
- Evaporation of the first 130 nm-thick layer of aluminum under an angle of $-35°$ at a rate 1 nm/s .
- 7 min of static oxidation in 20 mbar of Ar : O_2 (80% Ar − 20% O_2)
- Evaporation of the second 100 nm-thick layer of aluminum under an angle of $+35°$ at a rate 1 nm/s .
- Introduction of 40 mbar of ArO_2 before venting.

4 Ideally, the temperature should be fixed at 4.5°C thanks to a temperature controlled water bath.

LIFT-OFF Finally, we remove the non exposed resist with acetone.

- at least 10 min in an acetone bath at 60°C.
- 2 s sonicate in a clean acetone beaker.
- IPA rinsing.
- N_2 drying.

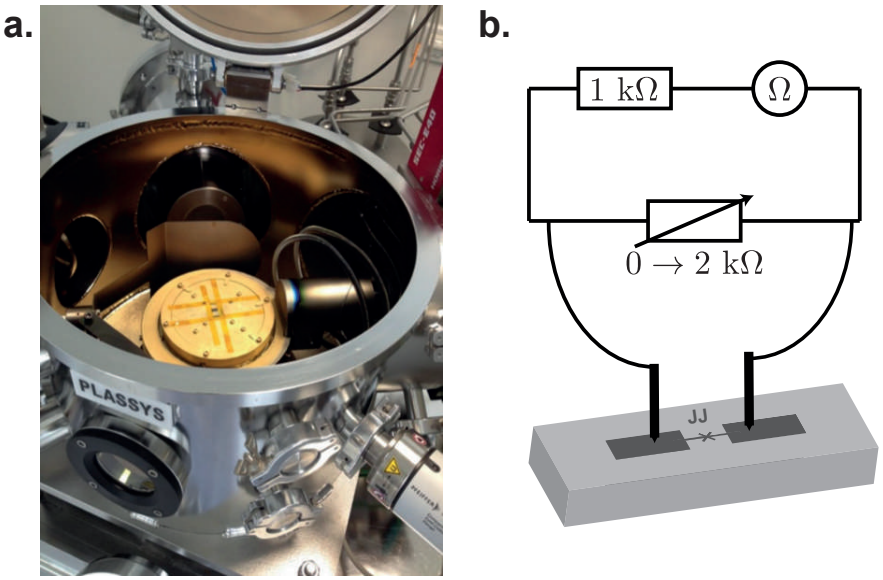

Figure B.3: **a.** Picture of a silicon chip before evaporation in a Plassys machine MEB550S. **b.** Electrical scheme of a wafer prober. A ballast resistor of 1 kΩ protects the sample by limiting the current flowing across the junction. The current is ramped up with a potentiometer.

B.1.1.7 *Wafer probing*

The Ambegaokar-Baratoff relation links the normal state resistance of a junction at zero temperature R_n^0 to the critical current of the junction I_0

$$R_n^0 = \frac{\pi\Delta}{2eI_0} = \frac{\pi\Delta\varphi_0}{2eE_J} \tag{B.1}$$

where e is the elementary charge, Δ is the superconducting gap, $\varphi_0 = \hbar/2e$ is the reduced flux quantum and E_J is the Josephson energy. The superconducting gap is of the order $\Delta \sim 180$ μeV for thin film of aluminum. We estimate the resistance at zero temperature R_n^0 to be approximatively 20% smaller than the room temperature resistance R_n. Measuring the resistance of a Junction at room temperature with the setup of Fig. B.3 **b** gives an estimate on the Josephson energy E_J.

The wafer prober is an essential tool to select devices that are not shorted nor open[5] and that display the closest E_J to the targeted value[6].

5 For a SQUID, measuring twice the expected resistance indicates that one of the junction is an open.

6 The Josephson energy plays an important role in the participation ratio of an amplifier (see chapter 5) or the resonant frequency of a transmon (see chapter 2).

B.1.1.8 *Measured amplifiers*

We fabricated more than 20 JPA and 10 JPC during this thesis work. Some JPCs were characterized and used by Nathanaël Cottet and Sébastien Jezouin for the quantum Maxwell demon experiment [220]. Table B.1 summarizes the measured parameters of the devices that were actually cooled down. The devices dubbed JPA18 and JPCXYZ2 were used to acquire quantum trajectories [221].

Name	$f_r(\varphi_{\text{ext}} = 0)$ (GHz)	p	Q	BW (MHz)	κ_{loss}(MHz)	R_n (kΩ)
JPA5	5.72	22%				
JPA10	11.06	22%				
JPA11	9.23	18%	106			0.35
JPA14	9.42		90	58	46	0.21
JPA17	9.01	2.6%	145	62	1	0.10
JPA18	8.35	2%	190	44	≤ 1	0.08
JPC39	5.40		126	43	≤ 1	
JPC48	5.385		168	32	≤ 1	
JPCXYZ2	5.390		180	30	≤ 1	

Table B.1: Measured amplifiers parameters. The measured parameters are the resonant frequency a zero external flux $f_r(\varphi_{\text{ext}} = 0)$, the participation ratio of the non-linearity p, the quality factor of the resonator Q at zero external flux, the bandwidth without pumping, the internal loss rate κ_{loss} and the resistance of the test junctions at room temperature R_n. The constraints on the parameters of the amplifiers are explained in chapter 5. Several trials and errors were needed to match the frequency of the amplifiers with the frequency of the qubit and cavity. All the measurements shown in this thesis were obtained with JPA18 and JPCXYZ2. The empty squares correspond to parameters that were not measured nor extracted from the measurements.

B.1.2 *3D transmons*

The fabrication procedure of 3D transmons is very similar to the one used to fabricate amplifiers. The main difference lies in the use of C-plane oriented 430 μm-thick sapphire substrate instead of silicon. The substrate is diced into 10 $\times$ 4 mm chips before the fabrication. Let us list the differences with the previously detailed fabrication process

- the bake times are increasing from 3 min to 4 min during spin coating.
- sapphire being an insulator, a 10 nm layer of aluminum is deposited on top of the resist prior to lithography to evacuate charges during the e-beam lithography.

- this thin aluminum layer is removed after e-beam writing and before development by immersion of the chip in a KOH solution[7].
- we deposit a first layer of 35 nm of aluminum (instead of 100 nm) followed by oxidation and a second layer of 100 nm (instead of 130 nm) of aluminum during the evaporation.

The other steps are unchanged. Luckily, the first transmon that we cooled down had sufficiently good coherence times for our experiments. It was used for all the measurements presented in this manuscript.

B.1.3 *2D CPW chips*

We also used 2D circuits composed of several microwave resonators and qubits. The resonators and qubits are patterned in the coplanar waveguide geometry. The associated experiments are still on-going and the results are not presented in the manuscript. Nevertheless, we describe the fabrication process used to make our 2D chips. These chips were fabricated by Théau Peronnin and Raphaël Lescanne at ENS Paris with a process developed jointly with Danijela Marković [149].

After cleaning the wafer, a 150 nm layer of of Nb is deposited on the entire upper surface of the substrate by sputtering. The resonators, geometric inductances and capacitances are patterned by optical lithography with the laser writer available in the clean room at Collège de France. After development, the niobium is dry etched using SF6 to form the 'gaps' of the CPW. Aluminum Josephson junction are written at the end by e-beam lithography. Let us briefly describe the fabrication process.

SPIN COATING

- One drop of S1813.
- Spinning at a speed of 4000 rpm for 60 s.
- Bake at 115°C for 1 min on a hot plate.

OPTICAL LITHOGRAPHY

- We use a microtech LW405-B+ laser writer.
- Exposition at a dose 300 mJ/cm^2.

DEVELOPMENT

- AZ726-MIF for 90 ns
- H_2O rinsing.

7 The concentration of the KOH solution (KOH comes as solid pellets) and the immersion time are not controlled carefully. We simply wait for the visible dissolution of the aluminum layer.

ETCHING

- Reactive ion etching with SF_6 for 2 min.
- Dissolution of the remaining resist in acetone.
- IPA rinsing.
- N_2 drying.

Josephson junctions are then written with the exact same protocol as the one used for 3D transmons.

B.2 MEASUREMENT SETUP

Fig. B.4 is a picture of the inside of the dilution refrigerator used in during this thesis. Our devices are shielded by aluminum foils and placed inside cryoperm boxes. They are thermally anchored at the base plate of the dilution refrigerator at a temperature of 20 mK. The signal coming from room temperature is heavily attenuated at every stage of the refrigerator and filtered by XMA attenuators and home-made eccosorb filters to prevent any thermal noise from reaching the base plate. A special care is taken to thermally anchor all microwave components at every stage. Superconducting NbTi coaxial cables are used on the return lines between base temperature and 4 K to minimize the losses before the HEMT while reducing the heat exchange between these stages. Twisted DC lines are used to current biais coils that are placed above the amplifiers to enable us to match the frequency of the amplifiers with our qubit and cavity.

Fig. B.5 is a diagram of the measurement setup. The qubit-cavity system described throughout this thesis is probed via coaxial transmission lines whose central pin plunge into the 3D cavity. Readout and qubit drive and gate are produced by mixing a few GHz continuous wave with 50 MHz (readout) and 40 MHz (qubit) modulated pulses generated by a Tektronix AWG[8] 5014C. At the output of the cavity, a commercial[9] frequency diplexer routes output signal in the frequency range $DC - 7$ GHz (including qubit frequency) toward a Josephson parametric converter (JPC). The signal in the frequency range 7 GHz $-$ 14 GHz is routed toward a Josephson parametric amplifier (JPA). The JPA is double pumped by two side-bands generated by an IQ mixing of the readout frequency. The two spatially separated detection chains are further amplified by a HEMT[10] at 4 K and at room temperature before down conversion, digitization by an Alazar 9351 ADC board and numerical demodulation. Several cryogenic circulators are used to prevent amplified noise from entering the cavity from the output port and thus degrade the qubit coherence time (see chapter 5).

8 Arbitrary waveform generator.
9 TIGER TGF-A4214-001.
10 Low Noise Factory high electron mobility transistor amplifiers.

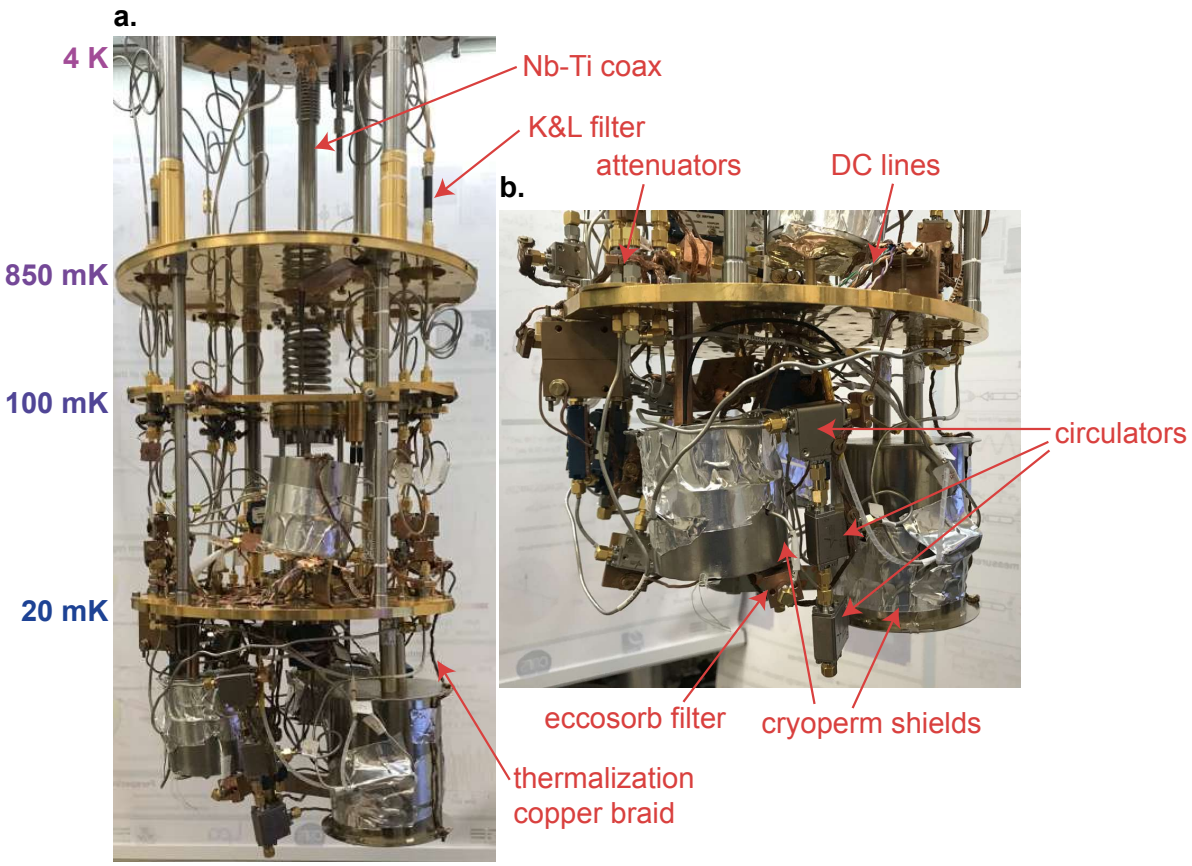

Figure B.4: Wiring of our BlueFors dilution refrigerator for several experiments. **a.** Wiring of the fridge between 4 K and base temperature. The signal coming from room temperature is heavily attenuated and filtered to prevent thermal noise from reaching the base plate. **b.** Zoom on the 20 mK stage. Qubits and amplifiers placed inside cryoperm boxes and thermally anchored to the base plate of the dilution refrigerator with copper braids.

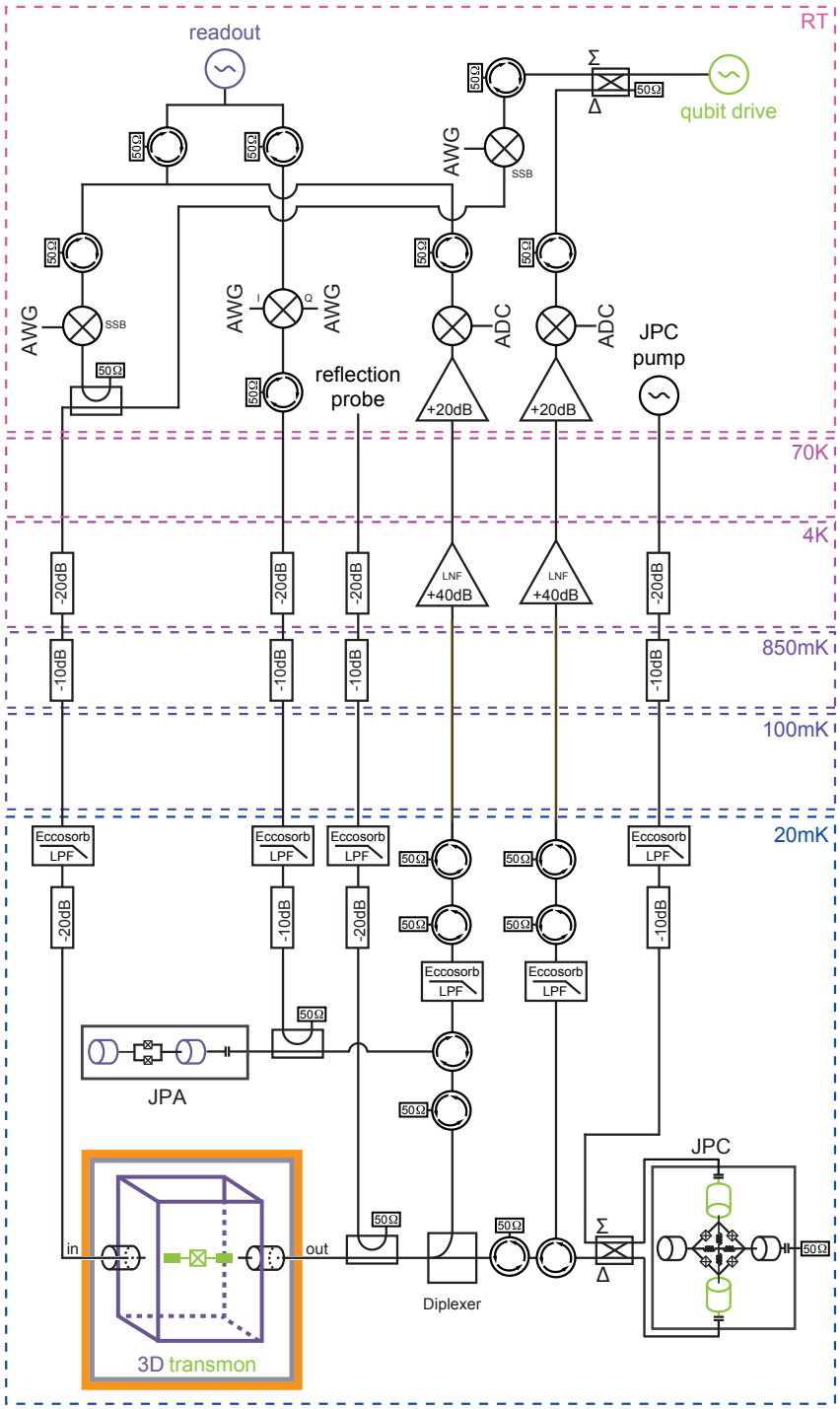

Figure B.5: Schematics of the experimental setup for the quantum trajectories experiment. A single RF source at $f_c - \chi/2 + 50$ MHz is used to readout the cavity by single side band modulation and to generate a two side-band pump for a JPA. The mixed readout signal is sent through the input line which is heavily attenuated (XMA attenuators) and filtered with home made ecosorb filters. At the output of the cavity a commercial frequency diplexer routes the signal toward a Josphson parametric converter (JPC)(frequencies lower than 7 GHz including f_q) or a Josephson parametric amplifier (JPA) (frequencies higher than 7 GHz including f_c). The readout pulse is further amplified by a HEMT routed out of the fridge before down conversion, digitization and numerical demodulation. An additional tone is mixed at 40 MHz and used for qubit rotations and down conversion of the amplified fluorescence field at room. The fluorescence signal is also digitized and demodulated to extract the two associated measurement records.

Part IV

BIBLIOGRAPHY

BIBLIOGRAPHY

[1] A Pais. "Einstein and the quantum theory." In: *Reviews of Modern Physics* 51.4 (1979), pp. 863–914. arXiv: 0510180 [quant-ph] (Cited on page 1).

[2] A Einstein, B Podolsky, and N Rosen. "Can Quantum-Mechanical Description of Physical Reality Be Considered Complete?" In: *Physical Review* 47 (1935), p. 777. arXiv: 0701001 [quant-ph] (Cited on page 1).

[3] David Bohm. "A suggested interpretation of the quantum theory in terms of "hidden" variables. I." In: *Physical Review* (1952). arXiv: 0208158 [quant-ph] (Cited on page 1).

[4] Stuart J Freedman and John F Clauser. "Experimental Test of Local Hidden-Variable Theories." In: *Phys. Rev. Lett.* 28.14 (1972), pp. 938–941 (Cited on page 1).

[5] Alain Aspect, Jean Dalibard, and Gérard Roger. "Experimental Test of Bell's Inequalities Using Time- Varying Analyzers." In: *Physical Review Letters* 49.25 (1982), pp. 1804–1807 (Cited on page 1).

[6] Erwin Schrödinger. *The Present Situation in Quantum Mechanics*. 1980. arXiv: 1206.6024 (Cited on page 1).

[7] Zurek. "Decoherence, einselection, and the quantum origins of the classical." In: *Reviews of Modern Physics* 75.3 (2003), pp. 715–775 (Cited on pages 1, 32).

[8] Max Jammer. *The Philosophy of Quantum Mechanics*. New York: Wiley, 1974 (Cited on page 2).

[9] Lucien Hardy and Robert Spekkens. "Why Physics Needs Quantum Foundations." In: (). arXiv: arXiv:1003.5008v1 (Cited on page 2).

[10] E. Schrödinger. "Are there quantum jumps ?: Part ii." In: *British Journal for the Philosophy of Science* (1952) (Cited on page 2).

[11] Rainer Blatt and David Wineland. *Entangled states of trapped atomic ions*. 2008 (Cited on page 3).

[12] Serge Haroche. "Nobel Lecture: Controlling photons in a box and exploring the quantum to classical boundary." In: *Reviews of Modern Physics* 85 (2013), p. 1083 (Cited on pages 3, 13).

[13] M. H. Devoret et al. "Superconducting circuits for quantum information: An outlook." In: *Science* 339.6124 (2013), pp. 1169–1174. arXiv: 0402594 [cond-mat] (Cited on pages 3, 14).

[14] Leo Kouwenhoven and Charles Marcus. "Quantum dots." In: *Physics World* (1998). arXiv: 1412.1667 (Cited on page 3).

[15] Markus Aspelmeyer, Tobias J. Kippenberg, and Florian Marquardt. "Cavity optomechanics." In: *Reviews of Modern Physics* (2014). arXiv: 1303.0733 (Cited on page 3).

[16] John M. Martinis, Michel H. Devoret, and John Clarke. "Experimental tests for the quantum behavior of a macroscopic degree of freedom: The phase difference across a Josephson junction." In: *Physical Review B* (1987) (Cited on page 3).

[17] Y. Nakamura, Yu. a. Pashkin, and J. S. Tsai. "Coherent control of macroscopic quantum states in a single-Cooper-pair box." In: *Nature* 398.6730 (1999), pp. 786–788. arXiv: 9904003 [cond-mat] (Cited on pages 3, 13, 21).

[18] Uri Vool and Michel Devoret. "Introduction to quantum electromagnetic circuits." In: *International Journal of Circuit Theory and Applications*. 2017. arXiv: 1610.03438 (Cited on page 3).

[19] Jens Koch et al. "Charge-insensitive qubit design derived from the Cooper pair box." In: *Physical Review A - Atomic, Molecular, and Optical Physics* 76.4 (2007), p. 042319. arXiv: 0703002 [cond-mat] (Cited on pages 3, 14, 23, 35, 40).

[20] J. A. Schreier et al. "Suppressing charge noise decoherence in superconducting charge qubits." In: *Physical Review B - Condensed Matter and Materials Physics* 77.18 (2008), p. 180502. arXiv: 0712.3581 (Cited on pages 3, 14, 23).

[21] John M. Martinis. *Qubit metrology for building a fault-tolerant quantum computer*. 2015. arXiv: 1510.01406 (Cited on page 3).

[22] A Wallraff et al. "Strong coupling of a single photon to a superconducting qubit using circuit quantum electrodynamics." In: *Nature* 431 (2004), pp. 162–167 (Cited on pages 4, 13).

[23] P Campagne-Ibarcq et al. "Observing quantum state diffusion by heterodyne detection of fluorescence." In: *Physical Review X* 6.1 (2016), p. 11002. arXiv: 1511.01415 (Cited on pages 4, 6, 45, 98, 105, 115, 129).

[24] M. Naghiloo et al. "Mapping quantum state dynamics in spontaneous emission." In: *Nature Communications* 7.May (2016), pp. 1–7. arXiv: 1512.02307 (Cited on pages 4, 115).

[25] M. Naghiloo et al. "Quantum caustics in resonance-fluorescence trajectories." In: *Physical Review A* (2017). arXiv: 1612.03189 (Cited on pages 4, 6, 98, 115, 132).

[26] M Hatridge et al. "Quantum Back-Action of an Individual Variable-Strength Measurement." In: *Science* 339.6116 (2013), pp. 178–181 (Cited on pages 4, 6, 47, 98).

[27] K W Murch et al. "Observing single quantum trajectories of a superconducting quantum bit." In: *Nature* 502.7470 (2013), pp. 211–214. arXiv: 1305.7270 (Cited on pages 4, 6, 98, 100, 102, 115).

[28] G de Lange et al. "Reversing Quantum Trajectories with Analog Feedback." In: *Physical Review Letters* 112.8 (2014), p. 80501 (Cited on pages 4, 6, 98, 103).

[29] Steven J Weber et al. "Quantum trajectories of superconducting qubits." In: *Comptes Rendus Physique* 17.7 (2016), pp. 766–777 (Cited on pages 4, 6, 98).

[30] P Facchi et al. "Quantum Zeno dynamics." In: *Physics Letters A* 275.1-2 (2000), pp. 12–19 (Cited on pages 5, 115).

[31] J Gough. "Zeno dynamics for open quantum systems." In: *Russian Journal of Mathematical Physics* 21.3 (2014), pp. 337–347 (Cited on pages 5, 115).

[32] B Yurke et al. "Observation of parametric amplification and deamplification in a Josephson parametric amplifier." In: *Physical Review A* 39.5 (1989), p. 2519 (Cited on pages 5, 73, 75).

[33] M A Castellanos-Beltran and K W Lehnert. "Widely tunable parametric amplifier based on a superconducting quantum interference device array resonator." In: *Applied Physics Letters* 91.8 (2007), p. 83509 (Cited on pages 5, 75, 76).

[34] T Yamamoto et al. "Flux-driven Josephson parametric amplifier." In: *Applied Physics Letters* 93.4 (2008), p. 42510 (Cited on pages 5, 75).

[35] Archana Kamal, Adam Marblestone, and Michel Devoret. "Signal-to-pump back action and self-oscillation in double-pump Josephson parametric amplifier." In: *Physical Review B* 79.18 (2009), p. 184301. arXiv: 0902.0007 (Cited on pages 5, 75).

[36] J Y Mutus et al. "Strong environmental coupling in a Josephson parametric amplifier." In: *Applied Physics Letters* 104.26 (2014), p. 263513 (Cited on pages 5, 75).

[37] Christopher Eichler and Andreas Wallraff. "Controlling the dynamic range of a Josephson parametric amplifier." In: *EPJ Quantum Technology* 1.1 (2014), p. 2 (Cited on pages 5, 75).

[38] N Bergeal et al. "Analog information processing at the quantum limit with a Josephson ring modulator." In: *Nature Physics* 6.4 (2010), pp. 296–302 (Cited on pages 5, 81).

[39] N. Roch et al. "Widely Tunable, Nondegenerate Three-Wave Mixing Microwave Device Operating near the Quantum Limit." In: *Physical Review Letters* 108.14 (2012), p. 147701. arXiv: arXiv:1202.1315v1 (Cited on pages 5, 81, 84, 86).

[40] Emmanuel Flurin. "The Josephson Mixer, a Swiss army knife for microwave quantum optics." Theses. ENS, 2014 (Cited on pages 5, 81–83, 90, 91, 155).

[41] N. Gisin and I. C. Percival. "The quantum-state diffusion model applied to open systems." In: *Journal of Physics A: General Physics* 25.21 (1992), pp. 5677–5691 (Cited on pages 6, 97).

[42] H Carmichael. *An Open Systems Approach to Quantum Optics*. Springer Berlin Heidelberg, 1993 (Cited on pages 6, 97).

[43] Christine Guerlin et al. "Progressive field-state collapse and quantum non-demolition photon counting." In: *Nature* 448.7156 (2007), pp. 889–893 (Cited on pages 6, 97).

[44] Howard M Wiseman and G J Milburn. *Quantum Measurement and Control*. Cambridge University Press, 2009 (Cited on pages 6, 36, 41, 97, 99).

[45] Alberto Barchielli and Matteo Gregoratti. *Quantum Trajectories and Measurements in Continuous Time*. Vol. 782. Springer-Verlag Berlin Heidelberg, 2009 (Cited on pages 6, 97).

[46] Alexander N Korotkov. "Quantum Bayesian approach to circuit QED measurement." In: *Les Houches summer school "Quantum Machines" (2011)*. 2011. arXiv: 1111.4016 (Cited on pages 6, 97).

[47] D Ristè et al. "Deterministic entanglement of superconducting qubits by parity measurement and feedback." In: *Nature* 502.7471 (2013), pp. 350–354 (Cited on pages 6, 98).

[48] N. Roch et al. "Observation of measurement-induced entanglement and quantum trajectories of remote superconducting qubits." In: *Physical Review Letters* 112.17 (2014). arXiv: 1402.1868 (Cited on pages 6, 98).

[49] Shay Hacohen-Gourgy et al. "Dynamics of simultaneously measured non-commuting observables." In: *Nature* 538 (2016), p. 491. arXiv: 1608.06652 (Cited on pages 6, 8, 92, 98, 115, 119, 129, 131, 132).

[50] Andrew N. Jordan and Markus Büttiker. "Continuous quantum measurement with independent detector cross correlations." In: *Physical Review Letters* (2005) (Cited on page 8).

[51] Michel Bauer, Denis Bernard, and Antoine Tilloy. "The open quantum Brownian motions." In: *Journal of Statistical Mechanics: Theory and Experiment* 2014.9 (2014). arXiv: 1312.1600 (Cited on pages 8, 123).

[52] J von Neumann and R T Beyer. *Mathematical Foundations of Quantum Mechanics*. Investigations in physics. Princeton University Press, 1996 (Cited on pages 8, 133).

[53] D Bohm. *Quantum Theory*. Dover books in science and mathematics. Dover Publications, 1989 (Cited on pages 8, 133).

[54] Yakir Aharonov, Peter Bergmann, and Joel Lebowitz. "Time Symmetry in the Quantum Process of Measurement." In: *Physical Review* 134.6B (1964), B1410–B1416 (Cited on pages 8, 133).

[55] H. M. Wiseman. "Weak values, quantum trajectories, and the cavity-QED experiment on wave-particle correlation." In: *Physical Review A* 65.3 (2002), p. 32111. arXiv: 0112116 [quant-ph] (Cited on pages 8, 133, 134, 137, 138).

[56] Mankei Tsang. "Optimal waveform estimation for classical and quantum systems via time-symmetric smoothing. II. Applications to atomic magnetometry and Hardy's paradox." In: *Physical Review A* 81.3 (2009), p. 33840 (Cited on pages 8, 133, 134).

[57] Mankei Tsang. "Time-Symmetric Quantum Theory of Smoothing." In: *Physical Review Letters* 102.25 (2009), p. 250403 (Cited on pages 8, 133, 134).

[58] Søren Gammelmark, Brian Julsgaard, and Klaus Mølmer. "Past Quantum States of a Monitored System." In: *Physical Review Letters* 111.16 (2013), p. 160401 (Cited on pages 8, 133, 134, 136, 137, 145).

[59] Yakir Aharonov, David Albert, and Lev Vaidman. "How the result of a measurement of a component of the spin of a spin-1/2 particle can turn out to be 100." In: *Physical Review Letters* 60.14 (1988), pp. 1351–1354 (Cited on pages 9, 133, 138, 141).

[60] Justin Dressel et al. "Colloquium: Understanding quantum weak values: Basics and applications." In: *Reviews of Modern Physics* 86.1 (2014), pp. 307–316. arXiv: 1305.7154 (Cited on pages 9, 133, 134, 140, 142, 145).

[61] Nathan Williams and Andrew Jordan. "Weak Values and the Leggett-Garg Inequality in Solid-State Qubits." In: *Physical Review Letters* 100.2 (2008), p. 26804 (Cited on pages 9, 133, 141).

[62] Philippe Campagne-Ibarcq et al. "Observing interferences between past and future quantum states in resonance fluorescence." In: *Physical Review Letters* 112.18 (2014), pp. 1–5. arXiv: arXiv:1311.5605v1 (Cited on pages 9, 133).

[63] D. Tan et al. "Prediction and retrodiction for a continuously monitored superconducting qubit." In: *Physical Review Letters* 114.9 (2015), p. 6. arXiv: 1409.0510 (Cited on pages 9, 133, 145).

[64] D. Tan et al. "Homodyne monitoring of postselected decay." In: *Physical Review A* (2017). arXiv: 1705.04287 (Cited on pages 9, 133, 145).

[65] David J. Wineland. *Superposition, entanglement, and raising Schrödinger's cat*. 2013 (Cited on page 13).

[66] S Haroche and J Raimond. "Exploring the Quantum: Atoms, Cavities, and Photons." In: *Oxford Graduated Text* (2006), p. 616 (Cited on pages 13, 18, 36, 38, 47, 48).

[67] Hanhee Paik et al. "Observation of High Coherence in Josephson Junction Qubits Measured in a Three-Dimensional Circuit QED Architecture." In: *Physical Review Letters* 107.24 (2011), p. 240501 (Cited on pages 14, 15).

[68] Austin G Fowler et al. "Surface codes: Towards practical large-scale quantum computation." In: *Physical Review A* 86.3 (2012), p. 32324 (Cited on page 14).

[69] Mazyar Mirrahimi et al. "Dynamically protected cat-qubits: a new paradigm for universal quantum computation." In: *New Journal of Physics* 16.4 (2014), p. 45014. arXiv: arXiv:1312.2017v1 (Cited on page 14).

[70] L. Dicarlo et al. "Demonstration of two-qubit algorithms with a superconducting quantum processor." In: *Nature* 460.7252 (2009), pp. 240–244. arXiv: 0903.2030 (Cited on page 14).

[71] R Barends et al. "Superconducting quantum circuits at the surface code threshold for fault tolerance." In: *Nature* 508.7497 (2014), pp. 500–503 (Cited on pages 14, 35).

[72] Matthew Reagor et al. "Reaching 10 ms single photon lifetimes for superconducting aluminum cavities." In: *Applied Physics Letters* 102.19 (2013), p. 192604 (Cited on page 15).

[73] M Devoret. "Quantum fluctuations in electrical circuits." In: *Les Houches* (1995) (Cited on pages 14, 21).

[74] S Girvin. "Circuit QED: superconducting qubits coupled to microwave photons." In: *Quantum Machines: Measurement and Control of Engineered Quantum Systems, Lecture notes of the Les Houches Summer School: volume 96*. Ed. by Michel Devoret et al. Oxford University Press, USA, 2014, p. 113 (Cited on page 14).

[75] D M Pozar. *Microwave Engineering*. Wiley, 2004 (Cited on pages 14, 155).

[76] Matthew Reagor. "Superconducting Cavities for Circuit Quantum Electrodynamics." PhD thesis. 2015 (Cited on pages 14, 19).

[77] John Preskill. "Preskills Lectures." In: *Quantum Computing - Physics 219 Lecture notes* (2001). arXiv: 0101025v2 [arXiv:quant-ph] (Cited on page 18).

[78] Alexandre Blais et al. "Cavity quantum electrodynamics for superconducting electrical circuits: An architecture for quantum computation." In: *Physical Review A* 69.6 (2004), p. 062320. arXiv: 0402216 [cond-mat] (Cited on page 19).

[79] S Kuhr et al. "Ultrahigh finesse Fabry-Perot superconducting resonator." In: *Applied Physics Letters* 90.16 (2007), p. 164101 (Cited on page 19).

[80] V. Bouchiat et al. "Quantum Coherence with a Single Cooper Pair." In: *Physica Scripta* T76.1 (1998), p. 165 (Cited on page 21).

[81] K. W. Lehnert et al. "Measurement of the Excited-State Lifetime of a Microelectronic Circuit." In: *Physical Review Letters* (2003) (Cited on page 21).

[82] Simon E Nigg et al. "Black-box superconducting circuit quantization." In: *Physical Review Letters* 108.24 (2012), p. 240502. arXiv: 1204.0587 (Cited on pages 24, 25, 149).

[83] Firat Solgun, David W. Abraham, and David P. Divincenzo. "Blackbox quantization of superconducting circuits using exact impedance synthesis." In: *Physical Review B - Condensed Matter and Materials Physics* 90.13 (2014). arXiv: 1403.7341 (Cited on page 24).

[84] Moein Malekakhlagh and Hakan E. Türeci. "Origin and implications of an A2 -like contribution in the quantization of circuit-QED systems." In: *Physical Review A* (2016). arXiv: 1506.02773 (Cited on page 24).

[85] Philippe Campagne-Ibarcq. "Measurement back action and feedback in superconducting circuits." Thesis. ENS, 2015 (Cited on pages 24, 47, 61, 105, 137, 140, 155).

[86] Kurtis Lee Geerlings. "Improving Coherence of Superconducting Qubits and Resonators." PhD thesis (Cited on pages 26, 61).

[87] John David Jackson. *Jackson - Classical Electrodynamics (3rd Ed.).pdf*. 1962 (Cited on page 28).

[88] Z Leghtas et al. "Confining the state of light to a quantum manifold by engineered two-photon loss." In: *Science* 347.6224 (2015), pp. 853–857. arXiv: 1412.4633 (Cited on pages 29, 71).

[89] Z. K. Minev et al. "Planar Multilayer Circuit Quantum Electrodynamics." In: *Physical Review Applied* (2016). arXiv: 1509.01619 (Cited on page 29).

[90] S. Touzard et al. "Coherent Oscillations inside a Quantum Manifold Stabilized by Dissipation." In: *Physical Review X* (2018). arXiv: 1705.02401 (Cited on page 29).

[91] J.-M. Raimond. "Exploring the quantum world with photons trapped in cavities and Rydberg atoms." In: *Quantum Machines: Measurement and Control of Engineered Quantum Systems* (2014), pp. 395–426 (Cited on page 29).

[92] M. Nielsen and I. L. Chuang. *Quantum Computation and Quantum Information: 10th Anniversary Edition*. 2010. arXiv: arXiv:1011.1669v3 (Cited on pages 31, 37).

[93] Nicolas Gisin and Ian C Percival. "The quantum state diffusion picture of physical processes." In: *Journal of Physics A* 26 (1993), p. 2245 (Cited on page 32).

[94] David P DiVincenzo. "Fault-tolerant architectures for superconducting qubits." In: *Physica Scripta* T137 (2009), p. 14020 (Cited on page 35).

[95] M D Reed et al. "Fast reset and suppressing spontaneous emission of a superconducting qubit." In: *Applied Physics Letters* 96.20 (2010), p. 203110 (Cited on page 35).

[96] T. Walter et al. "Rapid High-Fidelity Single-Shot Dispersive Readout of Superconducting Qubits." In: *Physical Review Applied* (2017). arXiv: 1701.06933 (Cited on page 35).

[97] Johannes Heinsoo et al. "Rapid High-fidelity Multiplexed Readout of Superconducting Qubits." In: *Physical Review Applied* 10.3 (2018), pp. 1–13. arXiv: 1801.07904 (Cited on page 35).

[98] T. Picot et al. "Role of relaxation in the quantum measurement of a superconducting qubit using a nonlinear oscillator." In: *Physical Review B - Condensed Matter and Materials Physics* (2008). arXiv: 0808.0464 (Cited on page 35).

[99] Daniel Sank et al. "Measurement-Induced State Transitions in a Superconducting Qubit: Beyond the Rotating Wave Approximation." In: *Physical Review Letters* (2016). arXiv: 1606.05721 (Cited on page 35).

[100] I Siddiqi et al. "RF-Driven Josephson Bifurcation Amplifier for Quantum Measurement." In: *Physical Review Letters* 93.20 (2004), p. 207002 (Cited on pages 35, 74).

[101] F Mallet et al. "Single-shot qubit readout in circuit quantum electrodynamics." In: *Nature Physics* 5.11 (2009), pp. 791–795 (Cited on page 35).

[102] M D Reed et al. "High-Fidelity Readout in Circuit Quantum Electrodynamics Using the Jaynes-Cummings Nonlinearity." In: *Physical Review Letters* 105.17 (2010), p. 173601 (Cited on page 35).

[103] Th K. Mavrogordatos et al. "Simultaneous Bistability of a Qubit and Resonator in Circuit Quantum Electrodynamics." In: *Physical Review Letters* 118.4 (2017), pp. 1–5. arXiv: 1611.10354 (Cited on page 35).

[104] I. Pietikäinen et al. "Multilevel Effects in a Driven Generalized Rabi Model." In: *Journal of Low Temperature Physics* 191.5-6 (2018), pp. 354–364. arXiv: 1710.00588 (Cited on page 35).

[105] Raphaël Lescanne et al. "Dynamics of an off-resonantly pumped superconducting qubit in a cavity." In: *arXiv:1805.05198* (2018). arXiv: 1805.05198 (Cited on pages 35, 56, 69).

[106] S. Touzard et al. "Gated conditional displacement readout of superconducting qubits." In: *arXiv:1809.06964* (2018). arXiv: 1809.06964 (Cited on page 35).

[107] Claude Cohen-Tannoudji, Bernard Diu, and Franck Laloe. *Quantum Mechanics - Vol 1 - Cohen-Tannoudji.pdf*. 2006 (Cited on page 36).

[108] Mazyar Mirrahimi and Pierre Rouchon. "Dynamics and Control of Open Quantum Systems." In: 2015 (Cited on pages 36, 108).

[109] A. Uhlmann. "Relative entropy and the Wigner-Yanase-Dyson-Lieb concavity in an interpolation theory." In: *Communications in Mathematical Physics* (1977) (Cited on page 38).

[110] A. Barchielli M. and M. Gregoratti. "Quantum Trajectories and Measurements in Continuous Time: The Diffusive Case." In: *Springer* (2009) (Cited on page 39).

[111] Mark Fox. "Quantum Optics." In: *University of Oxford* (2013). arXiv: arXiv:1011.1669v3 (Cited on pages 39, 45).

[112] A. Wallraff et al. "Approaching unit visibility for control of a superconducting qubit with dispersive readout." In: *Physical Review Letters* (2005). arXiv: 0502645 [cond-mat] (Cited on page 40).

[113] Jay Gambetta et al. "Quantum trajectory approach to circuit QED: Quantum jumps and the Zeno effect." In: *Physical Review A* 77.1 (2008), p. 12112. arXiv: 0709.4264 (Cited on pages 41, 44, 57).

[114] A. A. Clerk et al. "Introduction to quantum noise, measurement, and amplification." In: *Reviews of Modern Physics* 82.2 (2010), pp. 1155–1208. arXiv: 0810.4729 (Cited on page 42).

[115] Vijay, Slichter, and Siddiqi. "Observation of Quantum Jumps in a Superconducting Artificial Atom." In: *Physical Review Letters* 106.11 (2011), p. 110502 (Cited on pages 42, 67).

[116] B Misra and E C G Sudarshan. "The Zeno paradox in quantum theory." In: *Journal of Mathematical Physics* 18.4 (1977), p. 756 (Cited on page 42).

[117] H. J. Carmichael. "Quantum trajectory theory for cascaded open systems." In: *Physical Review Letters* (1993) (Cited on page 45).

[118] R. Bianchetti et al. "Control and tomography of a three level superconducting artificial atom." In: *Physical Review Letters* (2010). arXiv: 1004.5504 (Cited on pages 55, 57, 63, 64, 66).

[119] Michael J. Peterer et al. "Coherence and decay of higher energy levels of a superconducting transmon qubit." In: *Physical Review Letters* (2015). arXiv: 1409.6031 (Cited on pages 55, 63, 64).

[120] A B Klimov et al. "Qutrit quantum computer with trapped ions." In: *Physical Review A - Atomic, Molecular, and Optical Physics* 67.6 (2003), p. 7 (Cited on page 55).

[121] Helle Bechmann-Pasquinucci and Asher Peres. "Quantum cryptography with 3-state systems." In: *Physical Review Letters* (2000). arXiv: 0001083 [quant-ph] (Cited on page 55).

[122] Thomas Durt et al. "Security of quantum key distributions with entangled qudits." In: *Physical Review A - Atomic, Molecular, and Optical Physics* 69.3 (2004), pp. 1–11 (Cited on page 55).

[123] M Pechal et al. "Microwave-controlled generation of shaped single photons in circuit quantum electrodynamics." In: *arxiv:1308.4094* (2013). arXiv: 1308.4094 (Cited on page 55).

[124] Anatoly Kulikov et al. "Realization of a Quantum Random Generator Certified with the Kochen-Specker Theorem." In: *Physical Review Letters* 119.24 (2017), pp. 1–5. arXiv: 1709.03687 (Cited on page 55).

[125] A. A. Abdumalikov et al. "Experimental realization of non-Abelian non-adiabatic geometric gates." In: *Nature* (2013). arXiv: 1304.5186 (Cited on page 55).

[126] Benjamin P. Lanyon et al. "Simplifying quantum logic using higher-dimensional Hilbert spaces." In: *Nature Physics* (2009). arXiv: 0804.0272 (Cited on page 55).

[127] Frederick W. Strauch. "Quantum logic gates for superconducting resonator qudits." In: *Physical Review A - Atomic, Molecular, and Optical Physics* (2011). arXiv: 1108.2984 (Cited on page 55).

[128] Vincent Mourik et al. "Exploring quantum chaos with a single nuclear spin." In: *arXiv:1703.04852* (2017). arXiv: 1703.04852 (Cited on page 55).

[129] A. R. Shlyakhov et al. "Quantum metrology with a transmon qutrit." In: *Physical Review A* (2018). arXiv: 1711.06172 (Cited on page 55).

[130] J. Wenner et al. "Excitation of superconducting qubits from hot nonequilibrium quasiparticles." In: *Physical Review Letters* (2013). arXiv: 1209.1674 (Cited on page 59).

[131] K. Serniak et al. "Hot non-equilibrium quasiparticles in transmon qubits." In: *arXiv:1803.00476* (2018). arXiv: 1803.00476 (Cited on page 61).

[132] Jian Li et al. "Pure dephasing in a superconducting three-level system." In: *Journal of Physics: Conference Series* 400.PART 4 (2012) (Cited on page 62).

[133] Z. Wang et al. "Cavity Attenuators for Superconducting Qubits." In: *arXiv:1807.04849* (2018). arXiv: 1807.04849 (Cited on page 64).

[134] M A Castellanos-Beltran et al. "Amplification and squeezing of quantum noise with a tunable Josephson metamaterial." In: *Nature Physics* 4.12 (2008), pp. 929–931 (Cited on page 71).

[135] N Bergeal et al. "Phase-preserving amplification near the quantum limit with a Josephson ring modulator." In: *Nature* 465.7294 (2010), p. 64 (Cited on pages 71, 85).

[136] C Macklin et al. "A near – quantum-limited Josephson traveling-wave parametric amplifier." In: *Science* 350.September (2015), p. 307 (Cited on pages 71, 86–88, 92).

[137] E. Flurin et al. "Generating Entangled Microwave Radiation Over Two Transmission Lines." In: *Physical Review Letters* 109.18 (2012), p. 183901. arXiv: 1204.0732 (Cited on page 71).

[138] M Pechal et al. "Microwave-Controlled Generation of Shaped Single Photons in Circuit Quantum Electrodynamics." In: *Physical Review X* 041010.4 (2014), pp. 1–9 (Cited on page 71).

[139] E Flurin et al. "Superconducting quantum node for entanglement and storage of microwave radiation." In: *Phys. Rev. Lett.* 114.Umr 8551 (2014), p. 90503. arXiv: arXiv:1401.5622v1 (Cited on page 71).

[140] K W Murch et al. "Cavity-Assisted Quantum Bath Engineering." In: *Physical Review Letters* 109.18 (2012), p. 183602 (Cited on page 71).

[141] Greg Calusine. "Private communication: TWPA Data Sheet." 2017 (Cited on pages 71, 88, 92).

[142] C M Caves. "Quantum limits on noise in linear amplifiers." In: *Physical Review D* 26 (1982), p. 1817 (Cited on page 72).

[143] Ananda Roy and Michel Devoret. *Introduction à l'amplification paramétrique de signaux quantiques par les circuits Josephson*. 2016 (Cited on page 73).

[144] Samuel Boutin et al. "Effect of Higher-Order Nonlinearities on Amplification and Squeezing in Josephson Parametric Amplifiers." In: *Physical Review Applied* (2017). arXiv: 1708.00020 (Cited on pages 74, 92).

[145] Tanay Roy et al. "Broadband parametric amplification with impedance engineering: Beyond the gain-bandwidth product." In: *Applied Physics Letters* 107.26 (2015), pp. 1–12. arXiv: 1510.03065 (Cited on pages 75, 80, 93).

[146] A. Metelmann and A. A. Clerk. "Nonreciprocal quantum interactions and devices via autonomous feedforward." In: *Physical Review A* (2017). arXiv: 1610.06621 (Cited on pages 80, 93).

[147] Christopher Eichler and Andreas Wallraff. "Controlling the dynamic range of a josephson parametric amplifier." In: *EPJ Quantum Technology* 1.1 (2014), pp. 1–10. arXiv: 1305.6583 (Cited on page 80).

[148] A Palacios-Laloy. "Superconducting qubit in a resonator: test of the Leggett-Garg inequality and single-shot readout." PhD thesis. CEA Saclay: Universit{é} Pierre et Marie Curie, Paris 6, 2010 (Cited on page 81).

[149] Danijela Marković. "Applications of the Josephson mixer : ultrastrong coupling , quantum node and injection locking." Theses. ENS, 2018 (Cited on pages 85, 161).

[150] Byeong Ho Eom et al. "A wideband, low-noise superconducting amplifier with high dynamic range." In: *Nature Physics* 8.8 (2012), pp. 623–627. arXiv: 1201.2392 (Cited on pages 86, 87).

[151] O. Yaakobi et al. "Parametric amplification in Josephson junction embedded transmission lines." In: *Physical Review B - Condensed Matter and Materials Physics* (2013). arXiv: arXiv:1308.2951v1 (Cited on page 86).

[152] K O'Brien et al. "Resonant Phase Matching of Josephson Junction Traveling Wave Parametric Amplifiers." In: *Physical Review Letters* 113.15 (2014), p. 157001 (Cited on pages 86, 87).

[153] J. A. Armstrong et al. "Interactions between light waves in a nonlinear dielectric." In: *Physical Review* (1962) (Cited on page 87).

[154] C. Bockstiegel et al. "Development of a broadband NbTiN traveling wave parametric amplifier for MKID readout." In: *Journal of Low Temperature Physics*. 2014 (Cited on page 87).

[155] S Weinreb, M W Pospieszalski, and R Norrod. "Cryogenic, HEMT, low-noise receivers for 1.3 to 43 GHz range." In: *1988., IEEE MTT-S International Microwave Symposium Digest*. IEEE, 1988, pp. 945–948 (Cited on page 90).

[156] Factory Low Noise. *LNF-LNC4_8C datasheet* (Cited on page 90).

[157] P. Campagne-Ibarcq et al. "Using Spontaneous Emission of a Qubit as a Resource for Feedback Control." In: *Physical Review Letters* 117.6 (2016), pp. 1–6. arXiv: 1602.05479 (Cited on page 91).

[158] X. Zhou et al. "High-gain weakly nonlinear flux-modulated Josephson parametric amplifier using a SQUID array." In: *Physical Review B - Condensed Matter and Materials Physics* (2014). arXiv: 1409.5630 (Cited on page 92).

[159] A. Eddins et al. "High-efficiency measurement of an artificial atom embedded in a parametric amplifier." In: *arXiv:1806.05276* (2018). arXiv: 1806.05276 (Cited on pages 93, 127).

[160] N. E. Frattini et al. "3-wave mixing Josephson dipole element." In: *Applied Physics Letters* (2017). arXiv: 1702.00869 (Cited on page 93).

[161] Kamal, Clarke, and Devoret. "Noiseless non-reciprocity in a parametric active device." In: *Nature Physics* 7.4 (2011), pp. 311–315 (Cited on page 93).

[162] Archana Kamal, John Clarke, and Michel H. Devoret. "Gain, directionality, and noise in microwave SQUID amplifiers: Input-output approach." In: *Physical Review B - Condensed Matter and Materials Physics* (2012). arXiv: 1206.4706 (Cited on page 93).

[163] A. Metelmann and A. A. Clerk. "Nonreciprocal photon transmission and amplification via reservoir engineering." In: *Physical Review X* (2015). arXiv: 1502.07274 (Cited on page 93).

[164] G. A. Peterson et al. "Demonstration of efficient nonreciprocity in a microwave optomechanical circuit." In: *Physical Review X* (2017). arXiv: 1703.05269 (Cited on page 93).

[165] Benjamin J. Chapman, Eric I. Rosenthal, and K. W. Lehnert. "Design of an on-chip superconducting microwave circulator with octave bandwidth." In: *arXiv:1809.08747* (2018). arXiv: 1809.08747 (Cited on page 93).

[166] Jean Dalibard et al. "Wave-function approach to dissipative processes in quantum optics." In: *Phys. Rev. Lett.* 68.5 (1992), pp. 580–583 (Cited on page 97).

[167] W G Teich and G Mahler. "Stochastic dynamics of individual quantum systems: Stationary rate equations." In: *Phys. Rev. A* 45.5 (1992), pp. 3300–3318 (Cited on page 97).

[168] H M Wiseman and G J Milburn. "Interpretation of quantum jump and diffusion processes illustrated on the Bloch sphere." In: *Physical Review A* 47.3 (1993), pp. 1652–1666 (Cited on page 97).

[169] Areeya Chantasri et al. "Quantum trajectories and their statistics for remotely entangled quantum bits." In: *Physical Review X* 6.4 (2016). arXiv: 1603.09623 (Cited on pages 98, 115).

[170] Areeya Chantasri et al. "Simultaneous continuous measurement of noncommuting observables: Quantum state correlations." In: *Physical Review A* (2018) (Cited on page 98).

[171] Pierre Rouchon and Jason F. Ralph. "Efficient quantum filtering for quantum feedback control." In: *Physical Review A - Atomic, Molecular, and Optical Physics* (2015). arXiv: 1410.5345 (Cited on page 99).

[172] Alain Sarlette and Pierre Rouchon. "Deterministic submanifolds and analytic solution of the quantum stochastic differential master equation describing a monitored qubit." In: *Journal of Mathematical Physics* 58.6 (2017). arXiv: 1603.05402 (Cited on pages 102, 103, 105, 129).

[173] John Gough. "An Introduction to Quantum Filtering." In: *arXiv:1804.09086v1* (2018). arXiv: arXiv:1804.09086v1 (Cited on page 108).

[174] P Six et al. "Parameter estimation from measurements along quantum trajectories." In: *Decision and Control (CDC), 2015 IEEE 54th Annual Conference on*. IEEE, 2015, pp. 7742–7748 (Cited on page 113).

[175] S. J. Weber et al. "Mapping the optimal route between two quantum states." In: *Nature* 511.7511 (2014), pp. 570–573. arXiv: 1403.4992 (Cited on pages 115, 132).

[176] Steven J. Weber et al. "Trajectoires quantiques de qubits supraconducteurs." In: *Comptes Rendus Physique* 17.7 (2016), pp. 766–777. arXiv: 1506.08165 (Cited on page 115).

[177] Andrew N Jordan et al. "Anatomy of Fluorescence: Quantum trajectory statistics from continuously measuring spontaneous emission." In: *Quantum Studies: Mathematics and Foundations* (2015), p. 15. arXiv: 1511.06677 (Cited on pages 115, 132).

[178] Philippe Lewalle, Areeya Chantasri, and Andrew N. Jordan. "Prediction and characterization of multiple extremal paths in continuously monitored qubits." In: *Physical Review A* (2017). arXiv: 1612.07861 (Cited on page 115).

[179] Yunjin Choi and Andrew N. Jordan. "Operational approach to indirectly measuring the tunneling time." In: *Physical Review A - Atomic, Molecular, and Optical Physics* (2013). arXiv: arXiv:1309.1710v1 (Cited on page 119).

[180] Rusko Ruskov, Alexander N. Korotkov, and Klaus Mølmer. "Qubit state monitoring by measurement of three complementary observables." In: *Physical Review Letters* (2010). arXiv: 1006.2013 (Cited on page 119).

[181] N G Van Kampen. *Stochastic Processes in Physics and Chemistry*. North-Holland Personal Library. Elsevier Science, 2011 (Cited on page 123).

[182] E Guyon et al. *Physical Hydrodynamics*. Physical Hydrodynamics. OUP Oxford, 2001 (Cited on page 123).

[183] Crispin W. Gardiner. *Handbook of stochastic methods: For Physics, Chemistry and the Natural Sciences*. 1996. arXiv: arXiv:1011.1669v3 (Cited on page 124).

[184] Lars Hörmander. "Hypoelliptic second order differential equations." In: *Acta Mathematica* (1967) (Cited on page 128).

[185] Hp Robertson. "The uncertainty principle." In: *Physical Review* (1929) (Cited on page 130).

[186] V B Braginsky et al. *Quantum Measurement*. Cambridge University Press, 1995 (Cited on page 131).

[187] Lorenzo MacCone and Arun K. Pati. "Stronger uncertainty relations for all incompatible observables." In: *Physical Review Letters* (2014). arXiv: 1407.0338 (Cited on page 131).

[188] H. M. Wiseman. "Adaptive phase measurements of optical modes: Going beyond the marginal Q distribution." In: *Physical Review Letters* 75.25 (1995), pp. 4587–4590 (Cited on page 132).

[189] Eliska Greplova, Christian Kraglund Andersen, and Klaus Mølmer. "Quantum parameter estimation with a neural network." In: *arXiv:1711.05238* (2017). arXiv: 1711.05238 (Cited on page 132).

[190] Justin Dressel et al. "Arrow of Time for Continuous Quantum Measurement." In: *Physical Review Letters* (2017). arXiv: 1610.03818 (Cited on pages 132, 145).

[191] Antoine Tilloy, Michel Bauer, and Denis Bernard. "Spikes in quantum trajectories." In: *Physical Review A - Atomic, Molecular, and Optical Physics* 92.5 (2015), pp. 1–7. arXiv: 1510.01232 (Cited on page 132).

[192] Michel Bauer, Denis Bernard, and Antoine Tilloy. "Zooming in on quantum trajectories." In: *Journal of Physics A: Mathematical and Theoretical* 49.10 (2016). arXiv: 1512.02861 (Cited on page 132).

[193] Philippe Lewalle, John Steinmetz, and Andrew N. Jordan. "Chaos in continuously monitored quantum systems: An optimal-path approach." In: *Physical Review A* 98.1 (2018), pp. 1–23. arXiv: 1803.07615 (Cited on page 132).

[194] M. Naghiloo et al. "Thermodynamics along individual trajectories of a quantum bit." In: *arXiv:1703.05885* (2017). arXiv: 1703.05885 (Cited on page 132).

[195] M. Naghiloo et al. "Information Gain and Loss for a Quantum Maxwell's Demon." In: *Physical Review Letters* 121.3 (2018), pp. 1–6. arXiv: 1802.07205 (Cited on page 132).

[196] Cyril Elouard et al. "Stochastic thermodynamics in the quantum regime: From quantum measurement to quantum trajectories." In: *arXiv:1603.07266 [cond-mat, physics:quant-ph]* (2016), pp. 1–8. arXiv: 1603.07266 (Cited on page 132).

[197] Yakir Aharonov and Lev Vaidman. *The two-state vector formalism: An updated review*. 2007. arXiv: 0105101 [quant-ph] (Cited on page 133).

[198] N Ritchie, J Story, and Randall Hulet. "Realization of a measurement of a weak value." In: *Physical Review Letters* 66.9 (1991), pp. 1107–1110 (Cited on page 133).

[199] Agustin Palacios-laloy et al. "Experimental violation of a Bell's inequality in time with weak measurement." In: *Nature Physics* 6.6 (2010), pp. 442–447 (Cited on pages 133, 141).

[200] J P Groen et al. "Partial-Measurement Backaction and Nonclassical Weak Values in a Superconducting Circuit." In: *Physical Review Letters* 111.9 (2013), p. 90506 (Cited on pages 133, 141).

[201] M. E. Goggin et al. "Violation of the Leggett-Garg inequality with weak measurements of photons." In: *Proceedings of the National Academy of Sciences* 108.4 (2011), pp. 1256–1261. arXiv: 1504.02707 (Cited on pages 133, 141).

[202] Onur Hosten and Paul Kwiat. "Observation of the spin hall effect of light via weak measurements." In: *Science (New York, N.Y.)* 319.5864 (2008), pp. 787–790 (Cited on pages 134, 142).

[203] P Dixon et al. "Ultrasensitive Beam Deflection Measurement via Interferometric Weak Value Amplification." In: *Physical Review Letters* 102.17 (2009), p. 173601 (Cited on pages 134, 142).

[204] Jeff S Lundeen et al. "Direct measurement of the quantum wavefunction." In: *Nature* 474.7350 (2011), pp. 188–191 (Cited on pages 134, 140).

[205] Y Aharonov and D Rohrlich. *Quantum Paradoxes: Quantum Theory for the Perplexed*. Physics textbook. Wiley, 2008 (Cited on page 134).

[206] Yakir Aharonov, Sandu Popescu, and Jeff Tollaksen. "A time-symmetric formulation of quantum mechanics." In: *Physics Today* 63.11 (2010), p. 27 (Cited on page 134).

[207] Christopher Ferrie and Joshua Combes. "Weak Value Amplification is Suboptimal for Estimation and Detection." In: *Physical Review Letters* 112.4 (2014), p. 40406 (Cited on page 134).

[208] Christopher Ferrie and Joshua Combes. "How the result of a single coin toss can turn out to be 100 heads." In: *Physical Review Letters* (2014). arXiv: 1403.2362 (Cited on page 134).

[209] Yakir Aharonov and Daniel Rohrlich. "Comment on "How the result of a single coin toss can turn out to be 100 heads"." In: *Physical Review Letters* 113.12 (2014), pp. 1–3. arXiv: 1403.2362 (Cited on page 134).

[210] Aharon Brodutch. "Comment on "How the result of a single coin toss can turn out to be 100 heads"." In: *Physical Review Letters* 113.12 (2014), pp. 1–3. arXiv: 1403.2362 (Cited on page 134).

[211] H. L. Van Trees. *Detection, Estimation, and Modulation Theory*. Vol. 1. Wiley, 2001, pp. 1–687 (Cited on page 134).

[212] P Six et al. "Quantum state tomography with noninstantaneous measurements, imperfections, and decoherence." In: *Phys. Rev. A* 93.1 (2016), p. 12109 (Cited on page 134).

[213] Ivonne Guevara and Howard Wiseman. "Quantum State Smoothing." In: *Physical Review Letters* (2015). arXiv: 1503.02799 (Cited on pages 137, 145).

[214] Luis Pedro García-Pintos and Justin Dressel. "Past observable dynamics of a continuously monitored qubit." In: *Physical Review A* (2017). arXiv: 1708.04362 (Cited on page 145).

[215] Albert Franquet, Yuli V Nazarov, and Hongduo Wei. "Statistics of continuous weak quantum measurement of an arbitrary quantum system with multiple detectors." In: *arXiv:1804.07639* (2018). arXiv: 1804.07639 (Cited on page 145).

[216] A Franquet and Yuli V Nazarov. "Probability distributions of continuous measurement results for conditioned quantum evolution." In: *Physical Review B* 95.8 (2017). arXiv: 1708.05662 (Cited on page 145).

[217] Bernard Yurke and John S. Denker. "Quantum network theory." In: *Physical Review A* (1984) (Cited on page 152).

[218] G. J. Dolan. "Offset masks for lift-off photoprocessing." In: *Applied Physics Letters* (1977) (Cited on page 155).

[219] Florent Lecocq et al. "Junction fabrication by shadow evaporation without a suspended bridge." In: *Nanotechnology* (2011). arXiv: 1101.4576 (Cited on page 155).

[220] Nathanaël Cottet et al. "Observing a quantum Maxwell demon at work." In: *Proceedings of the National Academy of Sciences* 114.29 (2017), pp. 7561–7564. arXiv: 1702.05161 (Cited on page 160).

[221] Q Ficheux et al. "Dynamics of a qubit while simultaneously monitoring its relaxation and dephasing." In: *Nature Communications* 9.1 (2018), p. 1926 (Cited on page 160).

Résumé

Au contraire de sa version classique, une mesure quantique perturbe nécessairement l'état du système. Ainsi, la mesure projective d'un spin-1/2 selon une direction rend parfaitement aléatoire le résultat d'une mesure successive de la composante du même spin le long d'un axe orthogonal. Dans cette thèse, nous discutons des expériences basées sur les circuits supraconducteurs qui permettent de mettre en évidence cette action en retour de la mesure. Nous mesurons en particulier la dynamique d'un qubit supraconducteur dont on révèle simultanément les trois composantes de Bloch x, y et z.

Deux techniques récentes sont utilisées pour réaliser ces enregistrements simultanés. Les composantes x et y sont obtenues par la mesure des deux quadratures du champ de fluorescence émis par le qubit. La composante z est quant à elle obtenue en sondant une cavité non résonante couplée de manière dispersive au qubit. La fréquence de la cavité dépend de l'énergie du qubit et la force de cette dernière mesure peut être ajustée in situ en faisant varier la puissance de la sonde. Ces observations sont rendues possibles grâce aux avancées récentes dans l'amplification ultra-bas bruit des signaux micro-onde grâce aux circuits Josephson. Cette thèse détaille toutes ces techniques à la fois théoriquement et expérimentalement et présente différents résultats annexes inédits.

En présence des mesures simultanées, nous montrons que l'état du système diffuse à l'intérieur de la sphère de Bloch en suivant une marche aléatoire dont les pas obéissent aux lois de l'action en retour de mesures incompatibles. Les trajectoires quantiques associées ont des dynamiques allant du régime diffusif au régime de blocage de Zénon soulignant l'interaction non-triviale des actions en retours des deux mesures incompatibles effectuées. En conditionnant les enregistrements aux résultats d'une mesure projective finale, nous mesurons également les valeurs faibles des composantes de notre qubit et démontrons qu'elles dépassent les valeurs extrémales moyennes. La thèse discute en détail de la statistique des trajectoires obtenues.

Mots Clés

Mécanique quantique, trajectoires quantiques, circuits supraconducteurs

Abstract

In contrast with its classical version, a quantum measurement necessarily disturbs the state of the system. The projective measurement of a spin-1/2 in one direction maximally randomizes the outcome of a following measurement along a perpendicular direction. In this thesis, we discuss experiments on superconducting circuits that allow us to investigate this measurement back-action. In particular, we measure the dynamics of a superconducting qubit whose three Bloch x, y and z components are simultaneously recorded.

Two recent techniques are used to make these simultaneous recordings. The x and y components are obtained by measuring the two quadratures of the fluorescence field emitted by the qubit. Conversely, the z component is accessed by probing an off-resonant cavity dispersively coupled to the qubit. The frequency of the cavity depends on the energy of the qubit and the strength of this last measurement can be tuned from weak to strong in situ by varying the power of the probe. These observations are enabled by recent advances in ultra-low noise microwave amplification using Josephson circuits. This thesis details all these techniques, both theoretically and experimentally, and presents various unpublished additional results.

In the presence of the simultaneous measurements, we show that the state of the system diffuses inside the sphere of Bloch by following a random walk whose steps obey the laws of the back-action of incompatible measurements. The associated quantum trajectories follow a variety of dynamics ranging from diffusion to Zeno blockade. Their peculiar dynamics highlights the non-trivial interplay between the back-action of the two incompatible measurements. By conditioning the records to the outcome of a final projective measurement, we also measure the weak values of the components of the qubit state and demonstrate that they exceed the mean extremal values. The thesis discusses in detail the statistics of the obtained trajectories.

Keywords

Quantum mechanics, quantum trajectories, superconducting circuits